

UNIVERSITY OF SOUTHAMPTON
FACULTY OF ENGINEERING, SCIENCE AND MATHEMATICS
SCHOOL OF ELECTRONICS AND COMPUTER SCIENCE

**Generalized Space-Time Block Coding
for Co-located and Cooperative MIMO Systems**

by

Nan Wu

*A thesis for the degree of
Doctor of Philosophy*

July 2008

SUPERVISOR:
Professor Lajos Hanzo

University of Southampton
Southampton SO17 1BJ
United Kingdom

© Nan Wu 2008

Dedicated to my family

UNIVERSITY OF SOUTHAMPTON

ABSTRACT

Faculty of Engineering, Science and Mathematics

School of Electronics and Computer Science

Doctor of Philosophy

Generalized Space-Time Block Coding

for Co-located and Cooperative MIMO Systems

by Nan Wu

In this thesis, firstly we introduce Linear Dispersion Codes (LDCs) and investigate their applications, characteristics and performance in the context of wireless communications employing multiple antennas. Secondly, the LDCs are combined with the powerful irregular code design concept to create near-capacity Serial Concatenated Codes (SCCs) using iterative decoders.

The application of irregular LDCs is investigated in the context of co-located Multiple-Input Multiple-Output (MIMO) elements using coherent detection. We provide the detailed mathematical representation of various Space-Time Block Codes (STBCs) and unify them using the linear dispersion structure. Furthermore, the sophisticated irregular principle is imposed on both the *outer* and *inner* constituent codes of the SCC scheme. In this way, the resultant scheme becomes capable of operating near the MIMO channel's capacity across a wide range of SNRs, while maintaining an infinitesimally low BER.

The linear dispersion architecture is combined with the irregular design philosophy also in the context of non-coherently detected MIMO systems having co-located antenna elements. The specific link between STBCs and Differential Space-Time Block Codes (DSTBCs) allows us to invoke similar designs for both code families. The resultant Differential Linear Dispersion Codes (DLDCs) demonstrate remarkable flexibility and they subsume existing DSTBC designs found in the literature. The employment of the Cayley transform provides an efficient way of constructing the unitary codewords required by the DLDCs.

Finally, this thesis also investigates the combination of the linear dispersion structure with the irregular code design principle in the context of cooperative MIMO systems. After characterizing the fundamental link between co-located and cooperative MIMO systems, we propose twin-layer Cooperative Linear Dispersion Codes (CLDCs) for the relay-aided cooperative systems. We demonstrate that the irregular design principle can be implemented to the SCC system, despite the fact that the MIMO elements are formed in a distributed fashion.

Acknowledgement

Many people have supported me during my graduate research in diverse ways, without whom the completion of this thesis would be impossible. Only a few words here could not adequately express my appreciation.

My supervisor Professor Lajos Hanzo who has incredible vision and endless energy deserves special attention and many, many thanks. He has guided me to reach milestones that I never imagined reaching. I am grateful for his enthusiasm and encouragement, as well as his patience, which helped me walk through the dark period of my life. I have benefited tremendously by simply observing the ways he worked and by working with him. I also enjoyed the open atmosphere while discussing various technical as well as philosophical issues with him.

I am grateful to my colleges in the Communication group, who enriched my experience for the past three years. I thank Dr. S. X. Ng and Dr. O. Alamri for their generous support during the initial stage of my research. Many thanks to C. Y. Wei, S. Tan, M. El-Hajjar, L. Xu, Dr. J. Akhtman, Dr. L. L. Yang, Professor S. Chen and Dr. R. Maunder for numerous technical discussions. Also many thanks to Denise Harvey for her help in the administrative matters.

As always, I would express my appreciation to my parents Di Wu and Su Gao for their love, unconditional support as well as for their tolerance. Most importantly, they truly exemplify for me how to be a good person, which largely shape my characters and personality. I also feel extremely lucky to live in a big family. Many people give their endless love to me since the day I was born. Special thanks to my dear uncle Dr. N. Gao and his family, who looked after me in every possible way.

Last, my most tender and sincere thanks to my beloved wife, HsiangChi Fang. Her love and optimism gave me the courage and internal peace to face various aspects of life.

List of Publications

Book Chapters:

1. L. Hanzo, **N. Wu**, M. El-Hajjar, and O. Alamri “Advanced Space-Time Coding: Near-Capacity Sphere Packing Modulation, Cooperative Communication and Multi-functional MIMO”, *Wiley-IEEE Press*, Research Monograph under contract

Journal:

1. **N. Wu**, O. Alamri, S. X. Ng and L. Hanzo, “Precoded Sphere Packing Aided Bit-Interleaved Differential Space-Time Coded Modulation Using Iterative Decoding”, *IEEE Transactions on Vehicular Technology*, March 2008, Volume 57, pp. 1311-1316.
2. **N. Wu** and L. Hanzo, “Near-Capacity Irregular Convolutional-Coding Aided Irregular Precoded Linear Dispersion Codes”, *IEEE Transactions on Vehicular Technology*, Submitted, March 2008.
3. **N. Wu** and L. Hanzo, “Coherent Versus Non-Coherent Linear Dispersion Space-Time Codes for Co-located And Cooperative MIMO Systems”, *IEE Communications Magazine*, Submitted, July 2008.
4. D. Yang, **N. Wu**, L. L. Yang and L. Hanzo, “Closed-loop Linear Dispersion Coded Eigen-beam Transmission and its Capacity”, *IEE Electronics Letters*, Submitted, June 2008.

Conference:

1. **N. Wu** and L. Hanzo, “Irregular Precoder-Aided Differential Linear Dispersion Codes”, *IEEE Vehicular Technology Conference*, Singapore, May 11-14, 2008, pp. 285-289.
2. **N. Wu**, T.D. Nguyen, C.Y. Wei, L.L. Yang and L. Hanzo, “Integrated LT Coding, Bit Interleaved Differential Space Time Coding and Sphere Packing Modulation for the Wireless Internet”, *IEEE Vehicular Technology Conference*, Singapore, May 11-14, 2008, pp. 344-348.
3. **N. Wu** and L. Hanzo, “Near-Capacity Irregular Precoded Linear Dispersion Codes”, *IEEE International Conference on Communications*, Beijing, China, May 19-23, 2008, pp. 4501-4505.
4. **N. Wu**, S. Ahmed, O. Alamri, L. L. Yang and L. Hanzo, “A sphere-packing modulated space-frequency diversity aided FFH-assisted DSTBC system” *IEEE Wireless Communications and Networking Conference*, Las Vegas, USA, April 3-6, 2006, Volume 4, pp. 1881-1886.

5. O. Alamri, **N. Wu** and L. Hanzo, “A Differential Turbo Detection Aided Sphere Packing Modulated Space-Time Coding Scheme”, *IEEE Vehicular Technology Conference*, Melbourne, Australia, May 08-10, 2006, Volume 5, pp. 2474-2478.
6. C. Y. Wei, T.D. Nguyen, **N. Wu**, J. Akhtman, L. L. Yang and L. Hanzo, “Luby Transform Coding Aided Iterative Detection for Downlink SDMA Systems”, *IEEE Workshop on Signal Processing Systems*, Shanghai, China, October 17-19, 2007, pp. 397-402.

Contents

Abstract	iii
Declaration of Authorship	iv
Acknowledgement	v
List of Publications	vi
List of Symbols	xiii
1 Introduction	1
1.1 MIMO Techniques	1
1.2 Space-Time Block Codes	3
1.3 Near-Capacity Serial Concatenated Codes	8
1.4 Outline and Novel Contributions	10
1.4.1 Novel Contributions	10
1.4.2 Outline	12
2 Linear Dispersion Codes – An EXIT Chart Perspective	14
2.1 Introduction and Outline	14
2.2 Linear Dispersion Codes	18
2.2.1 Channel Model	18

2.2.2	Linear Dispersion Code Model of [1]	19
2.2.3	Linear Dispersion Code Model of [2]	22
2.2.4	Maximizing the Discrete LDC Capacity	25
2.2.5	Performance Results	27
2.2.6	Summary	34
2.3	Link Between STBCs and LDCs	36
2.3.1	Review of Existing STBC Knowledge	37
2.3.2	Orthogonal STBCs	39
2.3.3	Quasi-Orthogonal Space-Time Block Codes	40
2.3.4	Linear STBCs Based on Amicable Orthogonal Designs	41
2.3.5	Single-Symbol-Decable STBCs Based on QOSTBCs	42
2.3.6	Space-Time Codes Using Time Varying Linear Transformation	43
2.3.7	Threaded Algebraic Space-Time Codes	44
2.3.8	Summary	45
2.4	EXIT Chart Based Design of LDCs	47
2.4.1	Analyzing Iteratively-Detected LDCs	47
2.4.2	Analyzing Iteratively-Detected Precoded LDCs	53
2.4.3	Summary	60
2.5	EXIT Chart Based Design of IrRegular Precoded LDCs	61
2.5.1	RSC-coded IR-PLDC Scheme	62
2.5.1.1	Generating Component Codes for IR-PLDCs	64
2.5.1.2	Maximum-Rate RSC-Coded IR-PLDCs	69
2.5.1.3	Complexity-Constrained RSC-Coded IR-PLDCs	75
2.5.2	IR-PLDCs and IRCCs	80
2.5.3	IRCC-Coded IR-PLDC Scheme	82
2.5.4	Practical Issues of Near-Capacity Designs	86
2.5.5	Summary	87

2.6 Conclusion	89
3 Differential Space-Time Block Codes – A Universal Approach	90
3.1 Introduction and Outline	90
3.2 System Model	92
3.2.1 DPSK System Model for Single Antenna	92
3.2.2 DSTBC System Model for Multiple Antennas	93
3.2.3 Link Between STBCs and DSTBCs	96
3.3 Differential Orthogonal STBCs	97
3.3.1 Differential Alamouti Codes	97
3.3.1.1 Using QAM Constellations	98
3.3.2 DOSTBCs for Four Transmit Antennas	99
3.3.3 DOSTBCs Based on QOSTBCs	100
3.3.4 DOSTBCs Based on LSTBCs and SSD-STBCs	102
3.3.5 Performance Results	103
3.3.6 Summary	107
3.4 Differential Linear Dispersion Codes	108
3.4.1 Evolution to a Linear Structure	109
3.4.2 Differential LDCs Based on the Cayley Transform	110
3.4.2.1 The Cayley Transform	110
3.4.2.2 Differential Encoding/Decoding	112
3.4.2.3 Examples of DLDCs Based on the Cayley Transform	114
3.4.3 Performance Results	116
3.4.4 Summary	120
3.5 RSC-Coded Precoder-Aided DOSTBCs	122
3.5.1 DOSTBC Design With Sphere Packing Modulation	123
3.5.2 System Description	124
3.5.3 EXIT Chart Analysis	126

3.5.4	Performance Results	130
3.6	IRCC-Coded Precoder-Aided DLDCs	132
3.6.1	EXIT Chart Based IR-PDLDC Design	132
3.6.2	Performance Results	136
3.7	Conclusion	139
4	Cooperative Space-Time Block Codes	140
4.1	Introduction and Outline	140
4.2	Twin-Layer Cooperative Linear Dispersion Codes	143
4.2.1	System Model	143
4.2.2	System Assumptions	145
4.2.3	Mathematical Representations	146
4.2.4	Link Between CLDCs and LDCs	151
4.2.5	Performance Results	152
4.3	IRCC-coded Precoder-Aided CLDCs	161
4.3.1	EXIT Chart Based IR-PCLDC Design	164
4.3.2	Performance Results	169
4.4	Conclusion	171
5	Conclusions and Future Research	173
5.1	IR-PLDCs of Co-located MIMO Systems	173
5.2	IR-PDLDCs of Co-located MIMO Systems	176
5.3	IR-PCLDCs of Cooperative MIMO Systems	179
5.4	Linking LDCs, DLDCs and CLDCs	181
5.5	Future Work	186
5.5.1	Adaptive Closed-loop Co-located MIMO Systems	186
5.5.2	Improved Performance Cooperative MIMO Systems	187
Appendices		188

A LDCs' χ for QPSK Modulation	188
B DLDCs' χ for 2PAM Modulation	193
C CLDCs' χ_1 and χ_2 for BPSK Modulation	197
D Weighting Coefficient Vectors λ and γ	202
Glossary	217
Bibliography	221
Subject Index	234
Author Index	237

List of Symbols

- **Matrices and vectors :**

\mathbf{A}_n	The n -th dispersion matrix
\mathbf{B}_n	The n -th dispersion matrix
\mathbf{H}	The Channel State Information (CSI) matrix
\mathbf{I}	The identity matrix
\mathbf{K}	A symbol vector containing Q symbols
\mathbf{K}_n	The n -th symbol vector containing Q symbols
\mathbf{K}_f	All the possible combinations from Q symbols
\mathbf{R}_m	The received signal vector at the m -th relay
\mathbf{S}	The space-time transmission matrix
\mathbf{S}_n	The n -th space-time transmission matrix
\mathbf{S}_Δ	The difference matrix between two distinctive space-time codewords
\mathbf{U}	The reference matrix
\mathbf{V}	The complex-valued AWGN signal matrix
\mathbf{V}_n	The n -th complex-valued AWGN signal matrix
\mathbf{X}_n	The n -th space-time coded matrix
\mathbf{Y}	The received signal matrix at the Base Station
\mathbf{Y}_n	The n -th received signal matrix at the Base Station
\mathbf{Z}_m	The signal vector transmitted from the m -th relay
χ	The Dispersion Character Matrix (DCM) of the co-located MIMO system
χ_1	The DCM characterizing the broadcast interval
χ_2	The DCM characterizing the cooperation interval
λ	The weighting coefficient vector of the <i>inner</i> code of an irregular scheme
γ	The weighting coefficient vector of the <i>outer</i> code of an irregular scheme

- **Variables :**

C_{MIMO}	The coherent MIMO channel's CCMC capacity
C_{MIMO}^{non}	The non-coherent MIMO channel's CCMC capacity
C_{LDC}	The CCMC capacity of a LDC scheme
C_{LDC}^{DCMC}	The DCMC capacity of a LDC scheme
D	The total spatial diversity gain
D_{tx}	The transmit spatial diversity gain
F	The number of legitimate combinations of the vector \mathbf{K}
I_A	The <i>a-priori</i> information input of the <i>inner</i> code

\bar{I}_A	The <i>a-priori</i> information input of the <i>outer</i> code
I_E	The extrinsic information output of the <i>inner</i> code
\bar{I}_E	The extrinsic information output of the <i>outer</i> code
L	The number of constellation points
M	The number of transmit antennas (relays)
N	The number of receive antennas
T	The number of time slots used per block during the transmission
T_1	The number of time slots used per block during the broadcast interval
T_2	The number of time slots used per block during the cooperation interval
Q	The number of symbols transmitted per space time block
k	The number of <i>outer</i> iterations of a serial concatenated code (SCC) scheme
j	The number of <i>inner</i> iterations of a serial concatenated code (SCC) scheme
P	The total number of component codes of an irregular SCC system
P_{out}	The number of <i>outer</i> component codes of an irregular SCC system
P_{in}	The number of <i>inner</i> component codes of an irregular SCC system
s_n	The n -th L -PSK modulated symbol
R_{STBC}	The symbol rate of a STBC scheme
\bar{R}	The code rate of a STBC scheme in (<i>bits/channel use</i>)
α_n	The real part of symbol s_n
β_n	The imaginary part of symbol s_n
\bar{L}	The number of layers within a STBC scheme
θ	The normalization factor
Ξ	The spatial multiplexing gain
ρ	The Signal to Noise Ratio (SNR)
ρ_{SR}	The SNR at the relays
ρ_{RB}	The SNR at the Base Station (BS)
Ω	The standard deviation of a Gaussian distribution in dB
σ_0	The complex Gaussian noise variance at the receiver
σ_{SR}	The complex Gaussian noise variance at the relays
σ_{RB}	The complex Gaussian noise variance at the Base Station
$\varpi(\rho)$	The decoding complexity of an irregular scheme at SNR ρ
η	The minimum rank of \mathbf{S}_Δ
∇_n	The n -th non-zero eigenvalue of \mathbf{S}_Δ
Θ_{2n}^2	The chi-square random variable with dimension $2n$

- **Mathematical operations :**

Σ	Sum operation
\otimes	Kronecker product
$\log[\cdot]$	Logarithm operation
$\max(\cdot)$	The maximum value of a matrix/vector
$\min(\cdot)$	The minimum value of a matrix/vector
$\text{vec}(\cdot)$	Vertical stacking of the columns of a matrix
$\text{row}(\cdot)$	Vertical stacking of the rows of a matrix
$\text{tr}(\cdot)$	Trace operation of a matrix
$QR(\cdot)$	The QR-decomposition of a square matrix
$\det(\cdot)$	The determinant operation
$p(\cdot)$	The probability density function
$\ \cdot\ ^2$	The second order norm
$\text{Real}\{\cdot\}$	Real part of a complex value
$E\{\cdot\}$	Expectation of a random variable
\mathbf{A}^H	Matrix/vector Hermitian adjoint
\mathbf{A}^{-1}	Matrix inverse
\mathbf{A}^T	Matrix/vector transpose
\mathbf{A}^*	Matrix/vector/variable Complex conjugate

- **Symbols :**

\Re^n	n -dimensional real-valued Euclidean space
Π	Interleaver
Π^{-1}	Deinterleaver
Γ_n	The EXIT function of the n -th irregular code
\bar{E}	The total power of a sphere packing symbol
t^{i_1, i_2}	The (i_1, i_2) -th entry of the matrix \mathbf{S}

- **Channel parameters :**

f_d	The normalized Doppler frequency
δ	The spatial correlation coefficient
ω	The degree of channel estimation error in dB
\Im	The channel coherence time

Chapter 1

Introduction

The aim of wireless communications is to support information exchange between people and/or devices at anytime, anywhere and whenever it is necessary. This vision will allow people to operate a virtual office anywhere in the world using a single device with the ability of supporting voice, data as well as video applications, although these applications have different reliability, rate and delay requirements. In order to address these issues, multiple antennas can be employed at both the transmitter and receiver, resulting in Multiple Input Multiple Output (MIMO) systems. The research of MIMO system was inspired by the pioneering work of Foschini [3] [4] and Telatar [5], who predicted remarkable spectral efficiencies.

1.1 MIMO Techniques

Besides employing multiple antennas at the transmitter and receiver as in the conventional 'co-located MIMO systems', a virtual antenna array may also be formed by a group of cooperating relays. The resultant 'cooperative MIMO system' is capable of offering similar degrees of freedom promised by a co-located MIMO system [6] having independently fading antenna elements. In other words, the distributed MIMO elements mimic the functionality of the co-located MIMO elements. Depending on the specific configuration of the MIMO elements, MIMO related techniques can be classified into the following categories:

- Space-Time Coding (STC). When the multiple antennas are separated by about ten times the wave length to ensure the independent fading of the spatially separated signal paths, redundant copies of the data can be transmitted from the multiple antennas. Hence, the multiple antenna aided receiver has the benefit of exploiting the redundancy, which improves the reliability of the wireless link;

- Space-Division Multiple Access (SDMA). SDMA techniques take advantage of the unique user-specific Channel Impulse Responses (CIRs) of the multiple antennas employed at the Base Station (BS), where each antenna may be viewed as being to assist the transmission of a single user. Hence, SDMA continually adapts to the radio environment, allowing us to separate the users, even if they communicate in the same time or frequency slots, provided that their CIRs are accurately estimated.
- Spatial multiplexing. If we transmit a single user's independent and separately encoded data signals from the individual transmit antenna elements, a proportionally increased data rate can be achieved. Hence, we are able to differentiate the streams in the spatial domain, provided that the CIRs are accurately estimated.
- Beamforming. When each element of the antenna array is spaced by half of the wave length, we are capable of creating a pattern of constructive and destructive interference in a specific direction, resulting in angular selectivity.

From another point of view, the advantage of a MIMO channel can be exploited in two ways: to increase the reliability of the system by providing diversity gain and/or to increase the data rate by providing multiplexing gain.

The main concept of diversity is to provide multiple independently fading replicas of the transmitted signal for the receiver with the aid of the MIMO channel. If indeed these replicas are faded independently, it is unlikely that all copies of the transmitted signal are in a deep fade simultaneously. Therefore, the receiver is expected to reliably decode the transmitted signal using these independently faded received signals. To define diversity quantitatively, we use the relationship between the received Signal-to-Noise Ratio (SNR), denoted by ρ , and the associated Bit Error Ratio (BER). Explicitly, a plausible definition of the diversity, or diversity gain, is given by

$$D = - \lim_{\rho \rightarrow \infty} \frac{\log[BER]}{\log[\rho]}, \quad (1.1)$$

where diversity is physically interpreted as the slope of the error probability curve in terms of the received SNR on a logarithmic scale.

In addition to the above-mentioned spatial diversity, diversity can be achieved in both the temporal as well as in the frequency domain. Time-diversity can be achieved with the aid of channel coding and interleaving, where the information is encoded and dispersed over different channel coherence time periods so that the different time-segments of the codewords experience independent fading. Naturally, the provision of time diversity would impose excessive delay on delay-constrained real-time interactive services. Analogously, different replicas of the codeword can be

generated by transmitting redundant information mapped to several parallel channels each having a different carrier frequency, which is achieved at the cost of decreasing the spectral efficiency. Alternatively, spatial diversity is also capable of providing diversity without degrading the spectral efficiency or increasing the delay, by employing multiple antennas at the transmitter and receiver to create spatial-domain replicas, which increases the system's complexity.

On the other hand, the term spatial multiplexing gain refers to the fact that one can use multiple antennas to transmit at a higher rate achieved at the cost of an increased SNR requirement. Since the capacity of a MIMO channel increases upon increasing the SNR [4], it is desirable to design a system that operates near the attainable capacity, where the achievable rate can be increased as the SNR increases. This argument has resulted in the following definition for the spatial multiplexing gain [7]

$$\Xi = \lim_{\rho \rightarrow \infty} \frac{\bar{R}}{\log[\rho]}, \quad (1.2)$$

where \bar{R} is the code rate in *bits/channel use*. In [7], the authors have shown that there is a fundamental tradeoff between the achievable diversity gain D and the attainable multiplexing gain Ξ for a given MIMO channel.

1.2 Space-Time Block Codes

The term spatial diversity includes both the receive diversity provided by multiple receive antennas and the transmit diversity offered by multiple transmit antennas. When considering receive diversity, the independent received signals associated with multiple receive antennas are combined in order to obtain a signal that is passed to a standard demodulator. Combining the received signals can be achieved in several ways, such as by using Selection Combining (SC), Maximal Ratio Combining (MRC) and Equal Gain Combining (EGC) [8], which exhibit different complexity and performance. On the other hand, employing transmit diversity is more desirable in cellular systems, since more space, power and processing capability tend to be available at the transmit side than at the receive side. When the transmitter does not have Channel State Information (CSI), achieving transmit diversity gain requires a combination of spatial and temporal domain STC techniques.

More specifically, STCs can be catalogued into two classes, namely Space-Time Block Codes (STBCs) and Space-Time Trellis Codes (STTCs). The class of STTCs [9] [10] combines the design of modulation, trellis coding as well as space-time coding. In fact, STTCs can be considered as applying Trellis Coded Modulation (TCM) [11] for mapping the information bits to the antenna elements in the context of MIMO channels. However, the design of STTCs is challenging and the complexity imposed by the STTCs may become excessive, especially when used for high-rate

Table 1.1: Major contributions addressing the design of STBCs for co-located MIMO systems.

Author(s)	Contribution
[4] Foschini <i>et. al.</i> 1998, [5] Telatar 1999	Derived the MIMO channel's capacity.
[12] Wittneben, [13] Seshadri <i>et. al.</i> 1993	Proposed the transmit delay diversity scheme.
[14] Alamouti 1998	Discovered a transmit diversity scheme using two transmit antennas and linear receiver processing.
[15] Tarokh <i>et. al.</i> 1999	Generalized Alamouti's scheme for more than two transmit antennas.
[16] Ganesan <i>et. al.</i> 2000	Applied the orthogonal design philosophy in the context of linear dispersion structure.
[17] Jafarkhani 2001	Proposed a quasi-orthogonal design.
[18] Gamal and Damen 2003	Introduced the layered MIMO structure into the STBC design.
[19] [20] Hochwald and Marzetta 2000	Proposed the family of USTM.
[1] Hassibi and Hochwald 2002	Designed LDCs to maximize the ergodic capacity.
[2] Heath <i>et. al.</i> 2002	Designed LDCs to maximize the ergodic capacity and to provide a good BER.
[21] Belfiore <i>et. al.</i> 2005	Designed LDCs having non-vanishing determinant.
[22] Sezgin <i>et. al.</i> 2008	Optimized LDCs for Ricean channels.
[23] Lin <i>et. al.</i> 2008	Optimized LDCs for correlated MIMO channels.

communications. By contrast, the family of STBCs achieves diversity by transmitting carefully designed block matrices associated with relatively low complexity, since trellis decoding is replaced by low-complexity detection. Hence, in this thesis, we focus our attention on the family of STBCs designed for achieving transmit diversity gains, when communicating over frequency-flat Rayleigh fading channels having no CSI available at the transmitter.

Table 1.1 summarized the major contributions to STBCs designed for co-located MIMO systems. The first bandwidth-efficient transmit diversity scheme was proposed in [12], which included the transmit delay diversity scheme of [13] as a special case. It demonstrated that the diversity advantage is proportional to the number of transmit antennas. Then, Foschini *et. al.* [4] and Telatar [5] independently derived the capacity of MIMO systems. They demonstrated that the MIMO channel's capacity increases linearly with the minimum number of transmit and receive antennas, when communicating over independent and identically distributed (i.i.d.) flat Rayleigh channels. The ca-

capacity potential of MIMO systems inspired further research, leading to the discovery of Alamouti's code [14], which achieves the maximum attainable diversity order, despite using low-complexity linear receiver processing for a two-antenna-aided system. In order to create different antenna configurations, this scheme was later generalized in [15] leading to a family, which is referred to as Orthogonal Space-Time Block Codes (OSTBCs). In [16], a linear dispersion structure was introduced for the design of STBCs based on the principle of orthogonal design, which implies each space-time codeword is an orthogonal matrix. In fact, the design philosophy proposed in [16] revealed the flexibility of the linear dispersion structure, since it may be shown that the proposed scheme [16] subsumes the previously designed OSTBCs of [14] [15]. If the orthogonal constraint is relaxed to a degree, the resultant Quasi-Orthogonal Space-Time Block Codes (QOSTBCs) [17] become capable of achieving a higher rate than OSTBCs.

Besides the previously mentioned STBCs based on various orthogonal constraints, Hochwald and Marzetta proposed the family of Unitary Space-Time Modulation (USTM) schemes [19] [20], which jointly design the modulation and space-time coding schemes from an information theoretic perspective. However, USTM schemes are difficult to design for MIMO systems having a large number of antennas, since an excessive number of space-time modulation matrices have to be optimized. Hence, Hassibi and Hochwald [1] proposed the family of Linear Dispersion Codes (LDCs), which is fully specified by a single Dispersion Character Matrix (DCM) regardless of the number of antennas. In their original form, the LDCs [1] were optimized to maximize the ergodic capacity, which also referred to as the Continuous-input Continuous-output Memoryless Channel (CCMC) capacity [24]. Naturally, different optimization criteria can be imposed on the DCM. For example, the authors of [2] specifically designed the LDCs to maximize the ergodic capacity, while maintaining a good BER. On the other hand, LDCs can also be optimized using the so-called determinant criterion [10] invoking the beneficial techniques of Golden codes [21], where having a non-vanishing determinant is promised. Recently, Sezgin [22] and Lin [23] have demonstrated that LDCs were capable of operating in diverse channel conditions, including Ricean channels and spatially correlated MIMO channels.

The above schemes assumed the availability of perfect channel knowledge at the receiver. In practice, however, CSI has to be estimated at the receiver using, for example, training or pilot symbols. Alternatively, blind or differential detection schemes that require no CSI knowledge could be developed. Table 1.2 summarized the major contributions on Differential Space-Time Block Codes (DSTBCs) designed for the co-located MIMO systems. Note that designing differential schemes employing a space-time trellis structure is possible [35], but again this thesis concentrates on the family of DSTBCs having a simple block-based structure. In [25], the authors have shown

Table 1.2: Major contributions addressing the design of DSTBCs for co-located MIMO systems.

Author(s)	Contribution
[25] Zheng and Tse 2003	Derived the capacity of the non-coherent MIMO channel.
[26] Tarokh <i>et. al.</i> 2000	Proposed the differential version of Alamouti's scheme [14].
[27] Nam <i>et. al.</i> 2004	Extended the work of [26] to four antennas.
[28] Zhu <i>et. al.</i> 2005	Designed DSTBCs using the quasi-orthogonal philosophy.
[29] Hochwald <i>et. al.</i> 2000	Introduced the family of DUSTM.
[30] Shokrollahi <i>et. al.</i> 2001	Proposed to design DUSTM using the theory of fixed-point-free groups and their representations.
[31] Oggier 2007	Proposed to design DUSTM based on cyclic algebra [32].
[33] Hassibi <i>et. al.</i> 2002	Designed DUSTM based on the Cayley transform.
[34] Pauli and Lampe 2007	Proposed multiple-symbol differential detectors for DUSTM.

that the non-coherent MIMO channel's capacity approaches the coherent MIMO channel's capacity upon increasing the channel's coherence time, which encouraged researchers to design various DSTBC schemes to fully exploit the potential capacity advantage. First, Tarokh and Jafarkhani [26] proposed a differential encoding/decoding extension of Alamouti's scheme [14], which is restricted to PSK constellations. Later in [27] and [36], this simple scheme was generalized to employ four transmit antennas as well as to use QAM constellations. In [28], the authors demonstrated that the quasi-orthogonal constraint can also be applied and the resultant DSTBCs are capable of operating at a higher rate than the schemes of [26].

From the non-orthogonal design perspective, Hochwald *et. al.* [29] and Hughes [37] independently proposed the family of Differential Unitary Space-Time Modulation (DUSTM) schemes. The design of unitary space-time matrices has been extensively studied in the literature. For example, in order to guarantee a non-vanishing determinant, similar to the philosophy of coherently detected Golden codes [21], fixed-point-free groups¹ were employed [30] to construct DUSTM codewords. However, finite groups do not allow high date rate, which led to consideration of infinite groups, such as employing cyclic algebra [31]. For the detail of the cyclic algebra, we refer to [32] [39], which contains tutorial and useful background for the topic. Alternatively, the Cayley transform [33] provided an efficient way of generating unitary matrices with convenient encoding/decoding process. In terms of the development of the differential decoders, Pauli and

¹Fixed-point-free groups are groups with a unitary representation with no eigenvalue at 1, which yield full diversity codes. The classification of fixed-point-free groups can be found in [30] [38].

Table 1.3: Major contributions addressing the design of CSTBCs for co-operative MIMO systems.

Author(s)	Contribution
[40] Laneman <i>et. al.</i> 2003	Proposed to implement OSTBCs in a distributed fashion.
[41] Jing <i>et. al.</i> 2007	Proposed to employ STBCs based on a quasi-orthogonal design.
[42] Nabar <i>et. al.</i> 2004	Considered the case when the source transmits continuously.
[43] Stauffer <i>et. al.</i> 2007	Investigated the diversity-multiplexing gain tradeoffs.
[44] Liang <i>et. al.</i> 2006	Employed the linear dispersion structure in relay-aided networks.
[45] Yang <i>et. al.</i> 2007	Designed Cooperative STBCs with non-vanishing determinants.
[46] Sendonaris <i>et. al.</i> 2003	Exploited the case, where the relays transmit their own data.
[47] Mahinthan <i>et. al.</i> 2008	Considered the optimal power allocation of the CSTBC schemes.

Lampe [34] have shown that Multiple Symbol Differential Detectors (MSDDs) can be applied at the receiver, which jointly process several blocks of the received symbols.

In many practical scenarios, reliable wireless communications may not be guaranteed, even when multiple antennas have been employed. For example, when large-scale shadow fading contaminates the wireless links, all the channels tend to fade together rather than independently, hence eroding the achievable diversity gain. Therefore, the concept of 'cooperative diversity' has been proposed in the literature aiming for providing diversity using the single antennas of other nodes in the cellular network as relays. More explicitly, Table 1.3 listed the major contributions on Space-time block coding schemes designed for achieving cooperative diversity, which are referred to as Cooperative Space-Time Block Codes (CSTBCs). The transmission regime typically consists of two phases, namely the broadcast interval and the cooperation interval. Apparently, the power allocation strategy between these two intervals becomes a key design issue [47], since it determines the symbol's integrity received at both the relays and the final destination. In [40], the authors exploited cooperative diversity using the repetition and orthogonal space-time algorithms, where the OSTBCs [14] [15] listed in Table 1.1 have been employed. The mutual information and the outage probability of this scheme were analyzed in [48]. Similarly, the QOSTBCs [17] of Table 1.1 can also be implemented in a distributed and cooperative fashion, yielding similar diversity advantages [41]. Furthermore, the concept of linear dispersion used in co-located MIMO systems seen in Table 1.1 can also be 'transplanted' to relay-aided transmissions [44] [49] [50]. Particularly, the family of CSTBCs whose code construction is based on the non-vanishing determinant criterion [45] corresponds to the Golden codes [21] of the family of co-located MIMO systems based on an identical design philosophy.

Table 1.4: Major contributions on near-capacity Serial Concatenated Codes (SCCs) using iterative decoding.

Author(s)	Contribution
[53] Berrou <i>et. al.</i> 1993	Invented turbo codes and showed that efficient decoding of SCCs can be carried out by employing iterative decoding.
[54] Benedetto <i>et. al.</i> 1998	The turbo principle was extended to more general SCCs.
[55] ten Brink <i>et. al.</i> 1998	Employed the turbo principle in BICM-ID schemes.
[56] Divsalar <i>et. al.</i> 2000	Unity-rate precoders were employed for designing low complexity turbo codes suitable for bandwidth and power limited systems.
[57] [58] ten Brink 2000	Proposed the employment of EXIT charts for describing the convergence behaviour of concatenated decoders.
[59] Tüchler 2002	The EXIT chart analysis was extended to three-stage SCCs.
[60] Tüchler <i>et. al.</i> 2002	IRCCs designed based on EXIT charts were proposed as the <i>outer</i> code of a SCC scheme.
[61] Maunder <i>et. al.</i> 2007	Employed a family of IR-VLCs as the <i>outer</i> code of a SCC scheme.
[62] Hochwald <i>et. al.</i> 2003	Designed a convolutional-coded near-capacity STBC scheme for operation at certain specific SNRs.
[63] Zhang <i>et. al.</i> 2007	Proposed a near-capacity LDPC-based BLAST scheme using adaptive modulation.

Provided that the source node is allowed to transmit continuously during both the broadcast and the cooperation intervals, as opposed to the above-mentioned schemes transmitting only using the broadcast interval, the authors of [42] demonstrated that cooperative diversity gains can be achieved at a higher rate. In fact, the diversity-multiplexing gain tradeoff of such CSTBC schemes has been exploited in [43] [51], as a means of evaluating the fundamental limitations of different CSTBCs. If the relays are capable of transmitting their own data as well as of assisting the source node [46] [52], a diversity gain can be achieved for the data of both the source and of the relays. This scheme is referred as a 'user-cooperation' arrangement in the literature.

1.3 Near-Capacity Serial Concatenated Codes

The search for a practical system that is capable of achieving the potential capacity promised by MIMO systems is not straightforward. However, the discovery of turbo codes [53] demonstrated

that efficient iterative decoding of concatenated codes can be carried out at a manageable complexity by employing simple constituent codes. In [54], the 'turbo principle' was extended to Serial Concatenated Codes (SCCs). A SCC aided system usually requires some form of *outer* channel code that provides redundancy and interleavers ensure that the extrinsic information used is uncorrelated with the intrinsic information, but also to guard against bursts of transmission errors, interference, and additive receiver noise. The *outer* channel code can be an arbitrary code that may be decoded using Soft Inputs and Soft Outputs (SISO). Hence, convolutional codes [64], turbo codes [53] and Low Density Parity Check (LDPC) [65] codes become natural candidates. In order to exploit the benefit of multiple antenna elements, STBCs are often employed as the *inner* code that transmits symbols containing redundancy introduced by the *outer* code. Bit-Interleaved Coded Modulation using Iterative Decoding (BICM-ID) [55] scheme constituted an early attempt in the literature in order to achieve a low BER with the aid of iterative decoding. Later, a variety of SCC systems aiming for achieving near capacity operation have been proposed [62] [63] [66]. For example, the LDPC-based Bell Labs' Layered-Space-Time (BLAST) system [63] achieved near-capacity operation by employing adaptive modulation. The convolutional coded STBC schemes of [62] [66] also demonstrated near-capacity performance at certain SNRs.

In order to investigate the convergence behaviour of iterative decoders in the context of SCCs, the flow of extrinsic information through the SISO decoders can be visualized with the aid of EXtrinsic Information Transfer (EXIT) charts [55] [57]. An open tunnel in the EXIT chart indicates that an infinitesimally low BER may be achieved by an iterative receiver using a sufficient number of iterations. It was observed in [60] [67] that for the *A Posteriori* Probability (APP) based outer decoders, the area under the EXIT curves can be approximated by the associated code rate. This relationship was later formally shown in [68] for the family of Binary Erasure Channels (BECs). This is referred to as the 'area property' [60] in the literature. The EXIT chart analysis was later extended to SCC systems having three-stage decoders [59].

It has been demonstrated in [60] [69] that SCCs benefit from having an open convergence tunnel, when IrRegular Convolutional Codes (IRCCs) were adopted as the *outer* channel code, since IRCCs exhibited flexible EXIT characteristics [60]. Alternatively, the family of IrRegular Variable Length Codes (IR-VLCs) proposed in [61] also provided the ability of shaping the *outer* code's EXIT curve. However, SCCs employing irregular *outer* codes are unable to operate at low BERs, where the associated convergence tunnel is closed. Hence, in [70] the authors demonstrated that the employment of a unity-rate precoder [56] will facilitate convergence to the top right corner of the EXIT chart, therefore an infinitesimally low BER can be achieved for SNRs exceeding a certain threshold.

1.4 Outline and Novel Contributions

1.4.1 Novel Contributions

The diversity-oriented STBCs listed in Tables 1.1 demonstrate striking similarities. Firstly, all the schemes are based on either an orthogonal design philosophy, such as the OSTBCs and QOSTBCs or non-orthogonal structures, i.e. USTMs and LDCs. Secondly, the flexibility of the family of LDCs allows us to optimize them using different criteria [1] [2] [21]. These key observations assisted us in making the following contributions [71] [72]:

Contribution 1. *In order to unify the family of orthogonal and non-orthogonal STBC designs, we proposed to employ the linear dispersion structure of LDCs. This unified structure enables us to examine existing STBCs from a novel perspective. More explicitly, we characterized the linkage between existing STBCs found in the open literature and LDCs in terms of both their mathematical representations and their design philosophies. Furthermore, we proposed to optimize the LDCs from a capacity maximization perspective, namely by maximizing the LDCs' Discrete-input Continuous-output Memoryless Channel (DCMC) capacity.*

The existing DSTBC schemes found in the open literature tackled the non-coherent detection design challenge from various perspectives, as summarized in Table 1.2. However, we observe in Table 1.2 that the orthogonal and non-orthogonal philosophies remain the distinguishing features of various designs. Motivated by the above-mentioned unified LDC architecture, we were able to make the following contributions [70] [73]:

Contribution 2. *We demonstrated the fundamental relationship between STBCs and DSTBCs, which enables us to extend the STBC design philosophy to DSTBCs. Furthermore, the Cayley transform [33] was introduced as an efficient way of constructing unitary matrices for their description. The resultant Differential Linear Dispersion Codes (DLDCs) based on the Cayley transform exhibited similar characteristics to those of their coherently detected LDC counterparts.*

The family of CSTBCs listed in Table 1.3 illustrated the efforts devoted to the design of cooperative MIMO systems. Again, Table 1.3 demonstrated that the design of CSTBCs was dominated by various orthogonal or non-orthogonal design philosophies. For example, Laneman's scheme [40] can be considered as the 'cooperative' version of the orthogonal scheme of [15]. This observation assisted us in making the following contributions:

Contribution 3. *The fundamental relationship between co-located and cooperative MIMO systems has been investigated, which is facilitated by the establishment of the broadcast interval.*

In other words, CSTBCs are designed to provide spatial diversity with the aid of a two-phase transmission regime. Hence, we proposed the family of twin-layer Cooperative Linear Dispersion Codes (CLDCs), which inherited the flexible linear dispersion structure and were specifically designed to exploit the above-mentioned two-phase transmission regime.

To the best of our knowledge, there is no public literature comparing STBCs, DSTBCs and CSTBCs within a unified framework at the time of writing. Hence, we offered the following additional contributions:

Contribution 4. *We constructed a general simulation platform in order to carry out a quantitative comparison between LDCs, DLDCs and CLDCs, since all of them are based on the linear dispersion structure. Our investigations suggested that the family of LDCs is suitable for co-located MIMO systems employing coherent detection. The class of DLDCs is more applicable, when no CSI is available at the receiver. When relay-aided cooperative transmission is necessary to avoid the performance erosion imposed by shadow fading, our specifically designed twin-layer CLDCs are more beneficial.*

Another design objective of this thesis is to implement practical SCC schemes associated with infinitesimally low BERs, which are capable of operating near the attainable capacity across a wide range of SNRs. As reviewed in Section 1.3, it is entirely feasible for SCCs to achieve near-capacity performance using iterative decoding [62]. The employment of a unity-rate precoder [56] facilitates maintaining an infinitesimally low BER above a certain SNR threshold. Moreover, the employment of EXIT charts [57] [58] allows us to precisely predict and control the convergence behaviour of a SCC scheme. Facilitated by the flexibility of the IRCCs [60] in terms of shaping the outer code's EXIT curve, SCCs can operate within 1dB of the attainable capacity. However, there are no SCCs capable of near-capacity operations across a wide range of SNRs, owing to the lack of flexibility concerning the design of *inner* code. Hence, we focus our attention on the last 'missing' piece of a sophisticated SCC scheme, namely that of designing an *inner* code having flexible EXIT characteristics. More explicitly, the contributions are:

Contribution 5. *We enhanced the ingenious concept of irregular coding [60] and extended its ability to a much broader system design. More explicitly, the irregular design principle was applied in the context of the inner code of a SCC scheme. The resultant inner IrRegular Precoded LDC (IR-PLDC) scheme facilitates the system's near-capacity operation across a wide range of SNRs. Similarly, we proposed the IR-DLDCs for non-coherent MIMO systems and IR-CLDCs for cooperative MIMO systems.*

1.4.2 Outline

In this section we provide an overview of the remainder of this thesis.

- In Chapter 2, we investigate the theory and design of LDCs for co-located MIMO systems and propose a novel irregular near-capacity scheme using LDCs as the *inner* constituent code of a SCC. Section 2.2 presents LDC models suitable for describing OSTBCs and for non-orthogonal STBCs. Furthermore, a novel method of optimizing the LDCs according to their DCMC capacities is proposed. In Section 2.3, the relationship between various STBCs and LDCs is exploited in detail, demonstrating the flexibility of the linear dispersion framework. Table 2.3 specifically characterizes the evolution of STBCs in terms of their rate, diversity and flexibility. As far as channel-coded schemes concerned, Section 2.4 investigates various design issues related to two-stage concatenated convolutional coded LDCs as well as to three-stage precoder-assisted LDCs with the aid of EXIT chart, including their maximum achievable throughput and their iteration parameters. Section 2.5 investigates the irregular code design principle originally derived for IRCCs and employs a similar concept to design a family of IrRegular Precoded Linear Dispersion Codes (IR-PLDCs) as the *inner* constituent code of a SCC. In Sections 2.5.1 to 2.5.3, different degrees of irregularity are imposed on both the *inner* IR-PLDCs and the *outer* IRCCs.
- In Chapter 3, we exploit the linear dispersion structure in the context of non-coherently detected MIMO systems as well as characterize the effective throughput achieved by an irregular SCC scheme. In Section 3.2, the multi-antenna aided DSTBC's system architecture is derived from the conventional single-antenna aided Differential Phase Shift Keying (DPSK) scheme, followed by the characterization of the fundamental relationship between STBCs and DSTBCs in Section 3.2.3. After characterizing the performance of DSTBCs based on various orthogonal constraints in Section 3.3, Section 3.4 proposes the family of DLDCs based on the Cayley transform. In Section 3.5, we introduce the concept of Sphere Packing (SP) modulation [70] and jointly design the SP modulation and DSTBCs. The convolutional-coded SP-aided DSTBC scheme of Figure 3.18 is capable of approaching the attainable capacity at a specific SNR. Finally, in Section 3.6 the irregular design philosophy is imposed on both the *inner* and *outer* codes. Again, the resultant IRCC-coded IrRegular Precoded Differential Linear Dispersion Codes (IR-PDLDCs) of Figure 3.25 has the potential of operating near the attainable capacity across a wide range of SNRs.
- In Chapter 4, we apply the linear dispersion structure to the family of relay-aided cooperative schemes and characterize the maximum achievable throughput achieved by the irregular sys-

tem. More explicitly, Section 4.1 justifies the need for cooperation and portrays the system architecture in Figure 4.2. The mathematical model of the proposed twin-layer CLDCs as well as the rationale of the assumptions are discussed in Sections 4.2.1 to 4.2.3. The fundamental link between LDCs and CLDCs is exploited in Section 4.2.4, followed by their achievable performance recorded in Section 4.2.5. Similarly, we impose the irregular design philosophy in the context of cooperative MIMO systems in Section 4.3. The resultant IRCC-coded IrRegular Precoded Cooperative Linear Dispersion Codes (IR-PCLDCs) of Figure 4.16 become capable of achieving a flexible effective throughput according to the SNR encountered, while maintaining an infinitesimally low BER.

- Finally, Chapter 5 compares the findings of the previous chapters and draw the conclusions along with suggestions for future research.

Chapter 2

Linear Dispersion Codes – An EXIT Chart Perspective

2.1 Introduction and Outline

The design of coding schemes for the MIMO systems of Figure 2.1 operating at high SNRs¹ involves a tradeoff between the achievable rate at which the system’s capacity increases and the rate at which the error probability decays [7]. This inherent tradeoff provides a distinction between transmit diversity schemes like the family of Orthogonal Space-Time Block Codes (OSTBCs) [15] that sacrifice the achievable throughput in exchange for maximum reliability and the class of Spatial Division Multiplexing (SDM) arrangements, such as those belonging to Bell Labs’ Layered-Space-Time (BLAST) architecture [74]. SDM schemes are capable of supporting transmission rates close to the MIMO channel’s capacity, but do so without fully benefiting from the diversity potential of the channel. Since OSTBCs and BLAST schemes were designed for achieving the two extremes of the tradeoff scale, there is considerable interest in developing design methods for schemes that provide different trade-offs in terms of the achievable throughput and the error probability, which are applicable for employment in a broad range of antenna configurations. In other words, the space-time transmission matrix \mathbf{S} in Figure 2.1 provides a total of $(M \times T)$ transmission slots, when considering both the spatial and temporal domains. The design of Space-Time Block Codes (STBCs) aims for answering the question of how to use the available resources most efficiently.

Unitary Space-Time Modulation (USTM) was proposed independently by Hughes [37] and Hochwald [19] [20] in an early attempt to design flexible STBCs that are capable of achieving the highest attainable diversity gain. Instead of specifically designing either the modulation schemes or

¹High SNRs represent the SNR region, where the AWGN no longer dominates the system’s achievable performance.

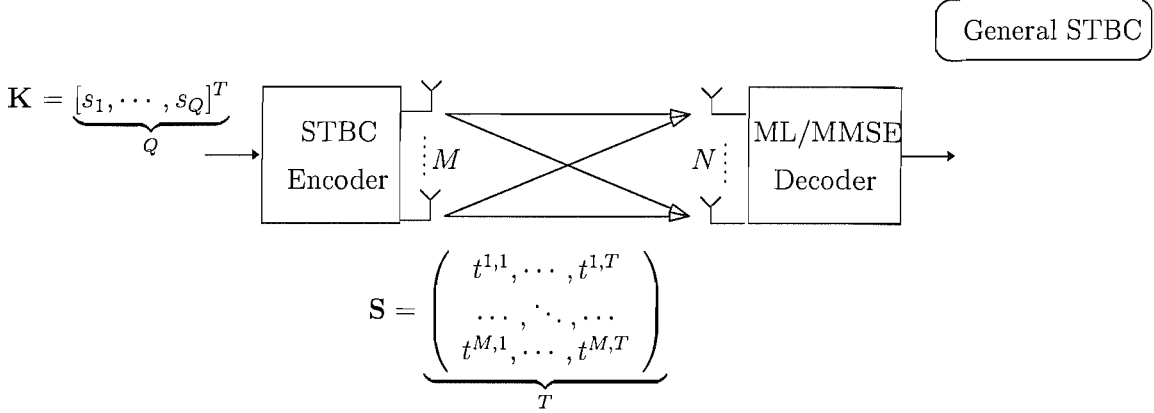


Figure 2.1: Schematic of MIMO system equipped with M transmit and N receive antenna, when transmitting Q symbols over T time slots using the space-time matrix \mathbf{S} .

the inner structure of the space time transmission matrix \mathbf{S} of Figure 2.1, the philosophy of USTM [19] [37] is to directly maximize the mutual information between \mathbf{S} and the received signal matrix \mathbf{Y} . However, the complexity of the optimization increases exponentially with both the number of antennas and the throughput. Hence, the problem of designing simple STBCs that exhibiting both high-throughput and full-diversity remains to be tackled.

The set of Linear Dispersion Codes (LDCs), first proposed by Hochwald and Hassibi [1], constitutes a wide-ranging class of space-time block codes exhibiting diverse characteristics. Hence, this family encompasses numerous existing schemes, providing a natural framework in which such design problems can be posed. While some recently developed codes, such as the Threaded Algebraic Space-Time Block Codes (TASTBCs) [75] as well as Time Variant Linear Transformation (TVLT) codes [76] and those proposed in [77], possess many desirable features, they remain a subset of the LDC framework. Given the generality of the LDC framework and the high degrees of design freedom, the focus of this chapter is on the design and further development based on LDCs.

The revolutionary concept of LDCs [1] invokes a matrix-based linear modulation framework seen in Figures 2.2 and 2.3, where each space-time transmission matrix \mathbf{S} is generated by a linear combination of so-called dispersion matrices and the weights of the components are determined by the transmitted symbol vector \mathbf{K} of Figure 2.1. These figures will be revisited in more depth during our further discourse. The structure of the dispersion matrices is governed by the so-called Dispersion Character Matrix (DCM) χ to be outlined in detail in Equation (2.16) and the Appendix A. The dispersion matrices can be designed to maximize the ergodic MIMO capacity [4] as it will be further highlighted in Section 2.2. However, the LDCs proposed in [1] only optimized the ergodic capacity, which did not necessarily guarantee that a low error probability was achievable [2] [78]. It is often exploited that the probability of a codeword error can be upper bounded by the largest

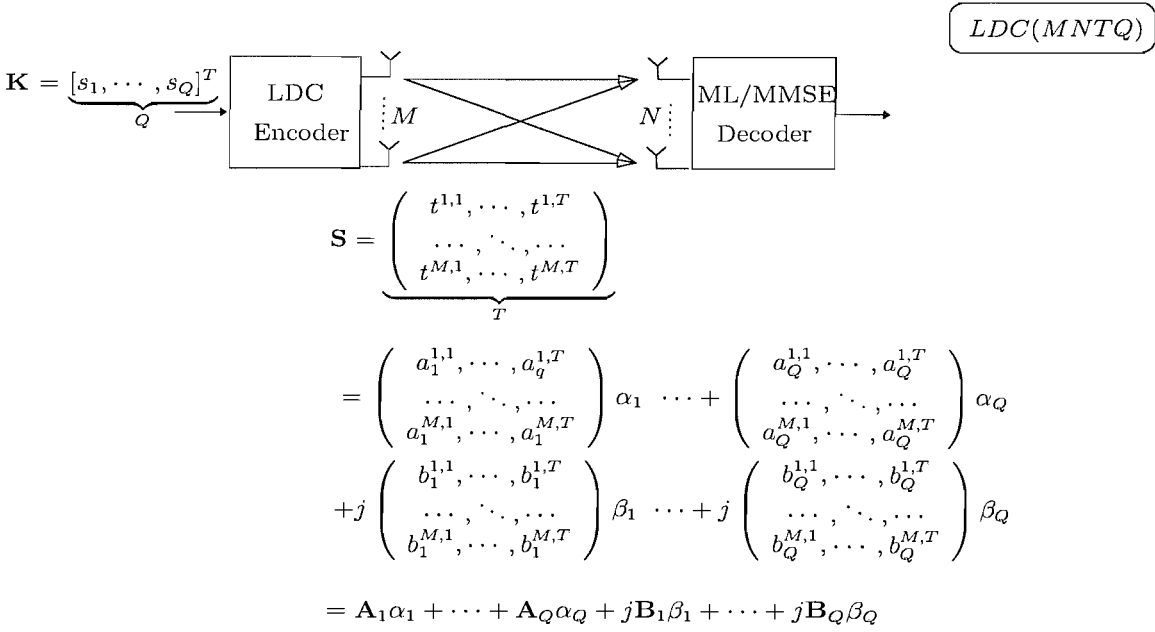


Figure 2.2: Schematic of a MIMO system equipped with M transmit and N receive antennas employing the $\text{LDC}(MNTQ)$ structure of [1], while transmitting Q symbols over T time slots using the space-time matrix \mathbf{S} .

Pairwise Symbol Error Probability (PSEP) [24]. Therefore, LDCs minimizing the maximum PSEP based on frame theory [79] were proposed in [2]. On the other hand, LDCs can be optimized using the determinant criterion [10] using the same technique of the Golden code [21] [80].

The achievable ergodic capacity of the LDCs [1] [2] [78] is also referred to as the Continuous-input Continuous-output Memoryless Channel (CCMC) capacity [24], where the channel's input is assumed to be a continuous-amplitude discrete-time Gaussian-distributed signal and the capacity is restricted only by either the signalling energy or the bandwidth. Therefore, we will refer to the CCMC capacity as the unrestricted bound. Naturally, in practice the channel's input is constituted by non-Gaussian symbols, although in certain circumstances, when for example high-order Quadrature Amplitude Modulation (QAM) aided symbols are transmitted over multiple Orthogonal Frequency-Division Multiplexing (OFDM) carriers this assumption becomes valid owing to the central limit theorem. In the more realistic context of discrete-amplitude Phase-Shift Keying (PSK) and QAM signals, we encounter a Discrete-input Continuous-output Memoryless Channel (DCMC). Therefore, the DCMC capacity is more pertinent in the design of practical channel-coded modulation schemes. We will demonstrate in Section 2.2 that LDCs achieving the same CCMC capacity may attain a different DCMC capacity. Therefore, we propose an optimization method that is capable of maximizing both the CCMC and DCMC capacity of the LDCs at the same time.

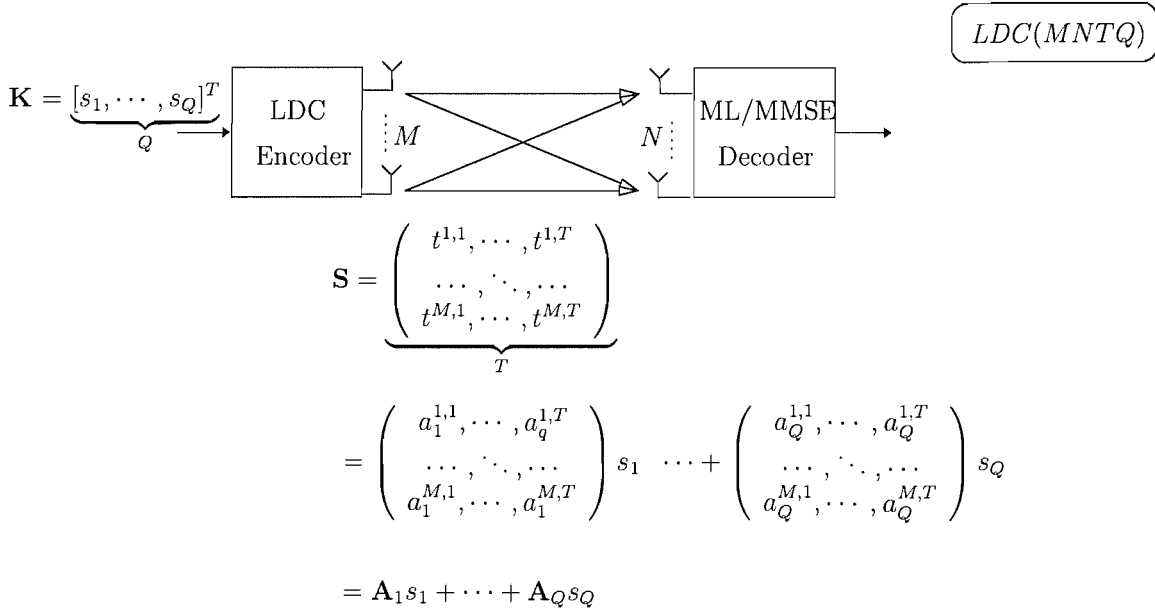


Figure 2.3: Schematic of a MIMO system equipped with M transmit and N receive antennas employing the $LDC(MNTQ)$ structure of [2], while transmitting Q symbols over T time slots using the space-time matrix \mathbf{S} .

Serial Concatenated Codes (SCCs) are capable of attaining an infinitesimally low BER, while maintaining a manageable decoding complexity. The discovery of 'turbo codes' [53] [64] considerably improved the attainable performance gains of concatenated codes by exchanging extrinsic information between concatenated component codes. Since LDCs have the ability to approach the potential capacity of MIMO systems, it is natural to serially concatenate for example a simple convolutional channel code as the *outer* code and LDCs employed as the *inner* code in order to approach the MIMO capacity, while having a near error-free BER performance. The concept of 'irregularity' was proposed in [60] [69] for SCCs, when IrRegular Convolutional Codes (IRCCs) were adopted as the *outer* channel code. Since IRCCs exhibited flexible EXIT characteristics [60], shaping the *outer* code's EXIT curve in order to match the *inner* code's EXIT curve becomes possible. However, near capacity IRCC schemes may require an excessive number of iterations at the receiver to achieve an infinitesimally low BER, which may exceed the affordable complexity budget of mobile handsets.

Motivated by the above-mentioned flexibility of the irregular *outer* code design philosophy, in this chapter we circumvent the IRCC-related *outer* code limitations by proposing IrRegular Precoded Linear Dispersion Codes (IR-PLDCs) as the *inner* rather than *outer* code and serially concatenate the resultant IR-PLDCs with regular/irregular *outer* channel codes in order to achieve an infinitesimally low BER, when employing iterative decoders. The novel contributions of this chapter are listed as follows [71] [72].

- LDCs are optimized by maximizing both the CCMC and DCMC capacity;
- The links between existing STBCs and LDCs are explored, and the necessary condition for STBCs to achieve both high-rate and full-diversity is investigated;
- We investigate the maximum achievable throughput of precoded LDCs with the aid of EXIT charts, when using both Maximum Likelihood (ML) and Minimum Mean Squared Error (MMSE) detectors;
- We propose IR-PLDCs as the *inner* code of SCCs and employ regular/irregular convolutional codes as the *outer* code. Hence, the resultant SCCs become capable of operating near the attainable MIMO channel capacity for a wide range of SNRs.²

The outline of this chapter is as follows. Section 2.2 presents the system models and the optimization of the LDCs, followed by the achievable performance in terms of their capacity and attainable BER. Section 2.3 characterizes the link between existing STBCs found in the open literature and LDCs in terms of both mathematical representations and design philosophy. In Section 2.4, the EXIT chart analysis of LDCs is provided in order to characterize the convergence behaviour of the serial concatenated scheme with/without unity-rate precoders. Section 2.5 presents the detailed design of the proposed IR-PLDCs with the aid of EXIT charts, when a simple *outer* code is employed. Furthermore, Section 2.5.2 compares the IRCCs and the proposed IR-PLDCs, where the irregularity is imposed in the *outer* and *inner* codes, respectively. In order to further illustrate the irregular concept, in Section 2.5.3 we propose an IRCC-coded IR-PLDC scheme, where the irregularity is evenly distributed between the *inner* and *outer* codes. Finally, the concluding remarks are provided in Section 2.6.

2.2 Linear Dispersion Codes

2.2.1 Channel Model

A MIMO communication system equipped with M transmit antennas and N receive antennas is illustrated in Figure 2.1. The space-time encoder takes the input symbol vector $\mathbf{K} = [s_1, s_2, \dots, s_Q]^T$ and generates a transmission matrix \mathbf{S} , which is transmitted synchronously through the propagation environment using M antennas. The signal received at each antenna is therefore given by a superposition of M transmitted signals corrupted both by Additive White Gaussian Noise (AWGN) and

²The operational SNR region of the proposed irregular scheme can be extended to any SNR values, provided that sufficiently diverse set of codes are adopted as the component codes.

multiplicative fading. When the Space-Time (ST) transmission matrix \mathbf{S} spans T symbol intervals, the received signal matrix $\mathbf{Y} \in \mathbb{C}^{N \times T}$ can be written as follow:

$$\mathbf{Y} = \mathbf{HS} + \mathbf{V}, \quad (2.1)$$

where $\mathbf{V} \in \mathbb{C}^{N \times T}$ represents realizations of an i.i.d. complex AWGN process with zero-mean and variance σ_0^2 determined by the associated SNR ρ . The Channel Impulse Response (CIR) matrix $\mathbf{H} \in \mathbb{C}^{N \times M}$ is assumed to be constant during a space-time codeword of T symbol periods and change independently from one ST matrix to the next, which corresponds to experiencing quasi-static fading. Each entry of \mathbf{H} represents the fading coefficient between a transmit-receive antenna pair. We will assume that the scattering imposed by the propagation environment is sufficiently rich for the channel coefficients to be modelled as i.i.d. zero-mean complex-valued Gaussian random variables having a common variance of 0.5 per real dimension. The entries of the channel matrix are assumed to be known to the receiver, but not to the transmitter. The space-time transmission matrix $\mathbf{S} \in \mathbb{C}^{M \times T}$ is given by

$$\mathbf{S} = \begin{pmatrix} t^{1,1} & \dots & t^{1,T} \\ t^{2,1} & \dots & t^{2,T} \\ \vdots & \ddots & \vdots \\ t^{M,1} & \dots & t^{M,T} \end{pmatrix}, \quad (2.2)$$

where t^{i_1, i_2} denotes the signal transmitted from the i_1 -th antenna in the i_2 -th time slot. We are concerned with designing the signal matrix \mathbf{S} obeying the power constraint $E\{tr(\mathbf{SS}^H)\} = T$, to ensure that the total transmission power is constant.

Given an arbitrary signal constellation, we follow [10] and define the symbol rate of a STBC having the structure of Figure 2.1 by

$$R_{STBC} = \frac{Q}{T}. \quad (2.3)$$

Under this definition, a rate-two code corresponds to a STBC transmits on average two symbols per channel use. For example, Alamouti's twin-antenna \mathbf{G}_2 code [14] has a rate of $R_{\mathbf{G}_2} = \frac{Q}{T} = 1$.

2.2.2 Linear Dispersion Code Model of [1]

Let us assume that each space-time transmission matrix \mathbf{S} formulated in Equation (2.2) represents the linear combination of Q space-time symbols, such as for example L -PSK or L -QAM symbols, which are dispersed over both space and time with the motivation of exploiting both the spatial and temporal diversity, as seen in Figure 2.2. We simply refer to this structure as Linear Dispersion Code (LDC). Hence, \mathbf{S} obeys

$$\mathbf{S} = \sum_{q=1}^Q (\mathbf{A}_q \alpha_q + j \mathbf{B}_q \beta_q), \quad (2.4)$$

where α_q and β_q are the real and imaginary parts of symbol s_q having a variance of 0.5, while \mathbf{A}_q and \mathbf{B}_q are real-valued or complex-valued dispersion matrices. We normalize \mathbf{S} to $E\{tr(\mathbf{S}^H\mathbf{S})\} = T$, which limits the total transmit power of the ST codeword. It may be readily shown that this normalization imposes the following normalization on the set of matrices \mathbf{A}_q and \mathbf{B}_q

$$\sum_{q=1}^Q (tr(\mathbf{A}_q^H \mathbf{A}_q) + tr(\mathbf{B}_q^H \mathbf{B}_q)) = 2T. \quad (2.5)$$

The idea behind the decoding of LDCs is to exploit the linearity of Equation (2.4) with respect to the variables. More explicitly, denote the real part of the received signal matrix \mathbf{Y} by \mathbf{Y}_R and the imaginary part by \mathbf{Y}_I . Similarly, we introduce the notations \mathbf{H}_R , \mathbf{H}_I , \mathbf{V}_R , \mathbf{V}_I and denote the i -th columns of these matrices by $y_{R,i}$, $y_{I,i}$, $h_{R,i}$, $h_{I,i}$, $v_{R,i}$ and $v_{I,i}$. Let us also define

$$\bar{\mathbf{A}}_q = \begin{bmatrix} \mathbf{A}_{R,q} & -\mathbf{A}_{I,q} \\ \mathbf{A}_{I,q} & \mathbf{A}_{R,q} \end{bmatrix}, \bar{\mathbf{B}}_q = \begin{bmatrix} -\mathbf{B}_{I,q} & -\mathbf{B}_{R,q} \\ \mathbf{B}_{R,q} & -\mathbf{B}_{I,q} \end{bmatrix}, \underline{\mathbf{h}}_i = \begin{bmatrix} h_{R,i} \\ h_{I,i} \end{bmatrix}, \quad (2.6)$$

where we have $\bar{\mathbf{A}}_q \in \zeta^{2T \times 2M}$, $\bar{\mathbf{B}}_q \in \zeta^{2T \times 2M}$ and $\underline{\mathbf{h}}_i \in \zeta^{2M \times 1}$. Furthermore, define

$$\bar{\mathbf{H}} = \begin{bmatrix} \bar{\mathbf{A}}_1 \underline{\mathbf{h}}_1 & \bar{\mathbf{B}}_1 \underline{\mathbf{h}}_1 & \cdots & \bar{\mathbf{A}}_Q \underline{\mathbf{h}}_1 & \bar{\mathbf{B}}_Q \underline{\mathbf{h}}_1 \\ \vdots & \vdots & \ddots & \vdots & \vdots \\ \bar{\mathbf{A}}_1 \underline{\mathbf{h}}_N & \bar{\mathbf{B}}_1 \underline{\mathbf{h}}_N & \cdots & \bar{\mathbf{A}}_Q \underline{\mathbf{h}}_N & \bar{\mathbf{B}}_Q \underline{\mathbf{h}}_N \end{bmatrix}, \quad (2.7)$$

where we have $\bar{\mathbf{H}} \in \zeta^{2NT \times 2Q}$.

Then the whole system can be represented by [1]

$$\begin{bmatrix} y_{R,1} \\ y_{I,1} \\ \vdots \\ y_{R,N} \\ y_{I,N} \end{bmatrix} = \bar{\mathbf{H}} \begin{bmatrix} \alpha_1 \\ \beta_1 \\ \vdots \\ \alpha_Q \\ \beta_Q \end{bmatrix} + \begin{bmatrix} v_{R,1} \\ v_{I,1} \\ \vdots \\ v_{R,N} \\ v_{I,N} \end{bmatrix}, \quad (2.8)$$

where the matrix noting the received signal has a size of $(2NT \times 1)$, while the matrix hosting the transmitted symbols is of size $(2Q \times 1)$. The resultant equivalent channel $\bar{\mathbf{H}}$ is known to the receiver, because the CIR matrix \mathbf{H} and the dispersion matrices \mathbf{A}_q and \mathbf{B}_q are available to the receiver. Equation (2.8) explicitly portrays the linear relation between the equivalent channel's the input and output vectors. Therefore, ML and MMSE detectors as well as sphere decoders [81] can be readily employed to recover the Q transmitted symbols.

The dispersion matrices \mathbf{A}_q and \mathbf{B}_q of Figure 2.2 can be specifically designed to maximize the mutual information between the equivalent transmit and receive vectors in Equation (2.8). This

guarantees that the resultant LDCs minimize the potential mutual information penalty. This design procedure can be formalized as follows [1]. .

Given the equivalent MIMO channel matrix $\bar{\mathbf{H}}$ of Equation (2.7), the achievable capacity C_{LDC} of this MIMO system employing LDCs at SNR ρ is given by [1]

$$C_{LDC}(\rho, M, N, T, Q) = \max_{A_q, B_q} \left(\frac{1}{2T} E \left\{ \log_2 \left[\det \left(\mathbf{I} + \frac{\rho}{M} \bar{\mathbf{H}} \bar{\mathbf{H}}^H \right) \right] \right\} \right), \quad (2.9)$$

where \mathbf{I} denotes an identity matrix having a size of $(2NT \times 2NT)$. Choosing \mathbf{A}_q and \mathbf{B}_q in order to maximize C_{LDC} for a given Q , subject to one of the following constraints:

- $\sum_{q=1}^Q (tr(\mathbf{A}_q^H \mathbf{A}_q) + tr(\mathbf{B}_q^H \mathbf{B}_q)) = 2T$, which represents our total transmission power constraint to be satisfied during T time slots;
- $tr(\mathbf{A}_q^H \mathbf{A}_q) = tr(\mathbf{B}_q^H \mathbf{B}_q) = \frac{T}{Q}$, $q = 1, \dots, Q$, implying that each ST signal component is transmitted with the same overall power from the M antennas during the T consecutive time slots, which corresponds to T channel activations;
- $\mathbf{A}_q^H \mathbf{A}_q = \mathbf{B}_q^H \mathbf{B}_q = \frac{T}{MQ} \mathbf{I}$, $q = 1, \dots, Q$, indicating that α_q and β_q are dispersed with equal energy in all spatial and temporal dimensions.

We now continue by offering a few remarks concerning this model.

1. Clearly, the mutual information achieved by the LDC obeying Equation (2.9) is less than or equal to the MIMO channel capacity C_{MIMO} of [4]

$$C_{MIMO}(\rho, M, N) = E \left\{ \log_2 \left[\det \left(\mathbf{I} + \frac{\rho}{M} \mathbf{H} \mathbf{H}^H \right) \right] \right\}, \quad (2.10)$$

where identity matrix \mathbf{I} have a size of $(N \times N)$. The corresponding lower bound can be derived [4]:

$$C_{MIMO}(\rho, M, N) \geq \min(M, N) \log_2 \left[\frac{\rho}{M} \right] + \sum_{i=\max(M, N)-\min(M, N)+1}^{\max(M, N)} E \left\{ \log_2 [\Theta_{2i}^2] \right\}, \quad (2.11)$$

where Θ_{2i}^2 is a chi-square distributed random variable with dimension $2i$. Moreover, this lower bound is asymptotically tight at high SNRs. We observe that this is equivalent to the capacity of $\min(M, N)$ sub-channels. In other words, the multiple antenna aided channel has $\min(M, N)$ degrees of freedom to communicate.

2. The solution of Equation (2.9) subject to any of the above-mentioned three constraints is non-unique. The judicious choice of the dispersion matrices allows LDCs to satisfy other criteria, such as for example the rank criterion [10] detailed in Section 2.3.1 without sacrificing mutual information.

3. The optimization stipulated in Equation (2.9) is carried out for a specific SNR ρ , although the authors of [1] argue that the optimization process insensitive to the specific value of ρ in the range of $\rho \geq 20$ and the resultant LDCs generally perform well over a wide SNR range.
4. This design criterion is not directly linked with the diversity design criterion given in [10], therefore, it does not guarantee good BER performance.

The general LDC model of Figure 2.2 is suitable for us to demonstrate that LDCs subsume the existing class of STBCs based on orthogonal designs. Since the conjugate operations seen in Equation (2.30) constitute the key feature of Alamouti scheme [14], as well as of other STBCs based on orthogonal constraints, it required the real and imaginary parts of the transmitted symbols to be modulated separately. However, for non-orthogonal STBCs, we do not have significant performance differences between separately modulated and in-phase/quadrature-phase combined modulated codes. Therefore, in order to simplify the related discussions as well as to reduce the size of the equivalent channel matrix $\tilde{\mathbf{H}}$ of Equation (2.7), another LDC model is presented in the next section.

2.2.3 Linear Dispersion Code Model of [2]

The schematic of the LDCs using the model of [2] is illustrated in Figure 2.3. Given the vector $\mathbf{K} = [s_1, s_2, \dots, s_Q]^T$ of Figure 2.3, the transmitted space-time matrix \mathbf{S} may be defined as [2]

$$\mathbf{S} = \sum_{q=1}^Q \mathbf{A}_q s_q, \quad (2.12)$$

which is visualized in Figure 2.4. More explicitly, each symbol s_q is dispersed to the M spatial- and T temporal dimensions using a specific dispersion matrix \mathbf{A}_q and the transmission space-time codeword \mathbf{S} is attained by the linear combination of all the weighted dispersion matrices, as seen in Figure 2.4.

Therefore, the codeword is uniquely and unambiguously determined by the set of dispersion matrices \mathbf{A}_q that are known to both the transmitter as well as the receiver. Note that in contrast to Equation (2.4), this model modulates the real and imaginary parts of the symbols using the same dispersion matrix \mathbf{A}_q , rather than using another dispersion matrix \mathbf{B}_q . The transmitted codewords should satisfy the power constraint given by

$$tr\left(\sum_{q=1}^Q \mathbf{A}_q^H \mathbf{A}_q\right) = T. \quad (2.13)$$

More strictly, each spatial and temporal slot should be allocated the same transmission power of

$$tr(\mathbf{A}_q^H \mathbf{A}_q) = \frac{T}{Q}. \quad (2.14)$$

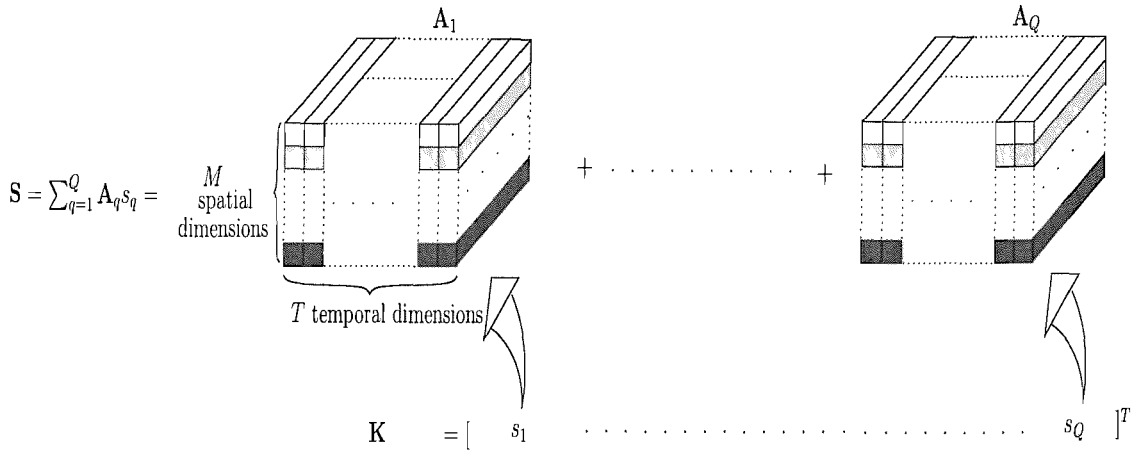


Figure 2.4: The space-time codeword \mathbf{S} formulated based on Equation (2.12).

Similarly to Equation (2.8), it is desirable to rewrite the input-output matrix relationship of Equation (2.1) in an equivalent vectorial form. Define the $vec()$ operation as the vertical stacking of the columns of an arbitrary matrix. Subjecting both sides of Equation (2.1) to the $vec()$ operation gives the equivalent system matrix:

$$\bar{\mathbf{Y}} = \bar{\mathbf{H}}\chi\mathbf{K} + \bar{\mathbf{V}}, \quad (2.15)$$

where $\bar{\mathbf{Y}} \in \zeta^{NT \times 1}$, $\bar{\mathbf{H}} \in \zeta^{NT \times MT}$, $\chi \in \zeta^{MT \times Q}$, $\mathbf{K} \in \zeta^{Q \times 1}$ and $\bar{\mathbf{V}} \in \zeta^{NT \times 1}$. More explicitly, χ is referred to as the Dispersion Character Matrix (DCM), which is defined as

$$\chi = [vec(\mathbf{A}_1), vec(\mathbf{A}_2), \dots, vec(\mathbf{A}_Q)], \quad (2.16)$$

while $\bar{\mathbf{H}}$ in Equation (2.15) is given by

$$\bar{\mathbf{H}} = \mathbf{I} \otimes \mathbf{H}, \quad (2.17)$$

where \otimes denotes the Kronecker product and \mathbf{I} is the identity matrix having a size of $(T \times T)$. The ML estimation of the transmitted signal vector \mathbf{K} is formulated as:

$$\bar{\mathbf{K}} = arg\{\min(||\bar{\mathbf{Y}} - \bar{\mathbf{H}}\chi\mathbf{K}_f||^2)\}, \quad (2.18)$$

where \mathbf{K}_f denotes all the possible combinations of the Q transmitted symbols.

Using the equivalent input-output relationship of Equation (2.15) and applying the results of [5], the ergodic capacity of the LDCs subjected to quasi-static Rayleigh fading is given by

$$C_{LDC}(\rho, M, N, T, Q) = \max_{tr(\chi\chi^H)} \frac{1}{T} E\{\log[\det(\mathbf{I} + \rho\bar{\mathbf{H}}\chi\chi^H\bar{\mathbf{H}}^H)]\}, \quad (2.19)$$

where \mathbf{I} has a size of $(NT \times NT)$.

The equivalent system model of Equation (2.15) is important, because it provides an insightful view of the LDC structure. More explicitly, when transmitting $\mathbf{S} \in \zeta^{M \times T}$ over a MIMO channel

$\mathbf{H} \in \mathbb{C}^{N \times M}$, it is equivalent to the transmission of the corresponding symbol vector \mathbf{K} over an equivalent MIMO channel $\tilde{\mathbf{H}}\chi \in \mathbb{C}^{NT \times Q}$. Applying the lower bound of Equation (2.11) to the equivalent MIMO channel $\tilde{\mathbf{H}}\chi$, it can be shown that the capacity achieved by LDCs spanning T time slots is determined by $\min(NT, Q)$. Therefore, when we have $Q \geq MT$, there will be no further improvement of LDC's CCMC capacity of Equation (2.19).

The optimization procedure of Equation (2.9) may be used to find near-capacity LDCs by exhaustively searching the entire design space of LDCs. The resultant solution is not guaranteed to be the global maximum of the cost function. However, by maximizing the ergodic capacity of Equation (2.19), it is possible to obtain a near-capacity LDC by choosing Q according to M and T . More explicitly, upon substituting $Q \geq MT$ into Equation (2.19) and ensuring that

$$\chi\chi^H = \frac{1}{M}\mathbf{I}, \quad (2.20)$$

which satisfies the power constraint of $\text{tr}(\chi\chi^H) = T$, we arrive at an equivalent channel in the form of the $(M \times N)$ -element MIMO channel of Equation (2.10). Since the Q transmitted symbols hosted by the vector \mathbf{K} of Figure 2.3 are jointly decoded as in Equation (2.18), the decoding complexity increases exponentially with Q . Hence, it is sufficient to choose $Q = MT$ rather than $Q > MT$ to achieve full the CCMC capacity of Equation (2.10).

In many practical scenarios, it may be desirable to maintain $Q < MT$ in order to reduce the decoding complexity, memory and latency or to satisfy various throughput constraints. To accommodate these constraints, χ can be designed by removing the appropriate number of columns from a scaled unitary matrix to arrive at a DCM χ that satisfies:

$$\chi^H\chi = \frac{T}{Q}\mathbf{I}. \quad (2.21)$$

Typically, when we have $Q < MT$, there is a loss of ergodic capacity, since it is no longer possible to exploit all the degrees of freedom $\min(NT, Q)$ of Equation (2.11) provided by the equivalent MIMO channel $\tilde{\mathbf{H}}\chi$.

This structure of LDCs guarantees to approach the MIMO channel's capacity quantified in Equation (2.10), depending on the specific choice of Q and T . It does not, however, guarantee a good performance in terms of error probability. By minimizing the maximum PSEP [10] of Equation (2.26), the authors of [2] optimized LDCs that achieve both high rates and full diversity.

We now make a range of further remarks concerning this model.

- LDCs are suitable for arbitrary transmit and receive antenna configurations, combined with arbitrary modulation schemes;

- LDCs are capable of transforming an $(M \times N)$ -antenna MIMO system into a $(Q \times NT)$ -element equivalent MIMO system by exploiting their inherent linearity;
- Since the real and imaginary parts of the transmitted symbols are dispersed using different dispersion matrices obeying the LDC model of Figure 2.2, the size of the equivalent MIMO system is $(2Q \times 2NT)$, as explicitly shown in Equation (2.8). The non-orthogonal model of Equation (2.15) reduces the equivalent model to a size of $(Q \times NT)$;
- All the dispersion matrices \mathbf{A}_q of Equation (2.12) can be described with the aid of a single DCM χ characterized in Equation (2.16);
- The LDC's equivalent CIR of Equation (2.15) can be appropriately adjusted by employing different DCM χ ;
- **Theorem 1.** When we have $Q \geq MT$, any dispersion character matrix χ satisfying Equation (2.20) is an optimal LDC which is capable of approaching the MIMO channel's capacity. For the proof of the theorem please refer to [2];
- **Theorem 2.** When we have $Q < MT$, the ergodic capacity is approached within a margin which is in proportional to $\frac{Q}{T}$. For the proof of the theorem please refer to [2];
- **Theorem 3.** The diversity order of the LDC scheme is less than or equal to $N \cdot \min(M, T)$. This implies that increasing T beyond M does not provide any further advantage in terms of an increased spatial transmit diversity, where the receive diversity is determined by N alone. For the proof of the theorem please refer to [2].

2.2.4 Maximizing the Discrete LDC Capacity

In order to generate a DCM χ defined in Equation (2.16), a random search algorithm was adopted [2]. To elaborate a little further, the random search algorithm of [2] randomly generates a matrix χ from some specific distribution, for example the Gaussian distribution, to satisfy the capacity constraint formulated in Theorems 1 and 2. Then, the corresponding diversity order and the coding gain is maximized by checking the *rank* and *determinant* criteria [10] detailed in Section 2.3.1, when performing an exhaustive search through the entire set of legitimate dispersion matrices.

The random search algorithm has the advantage of providing a wide variety of legitimate LDCs and typically provides a good performance [2]. In fact, codes obtained using a random dispersion character matrix often perform well without checking the *rank* and the *determinant* criteria. Since the search is random, they are unable to guarantee finding the maximum of the determinant function of Equation (2.27).

In this section, we adopt the aforementioned random search algorithm to optimize LDCs by maximizing the corresponding DCMC capacity. The rationale and advantage of optimizing the DCMC capacity are listed as follows:

- We will demonstrate in Figures 2.6 and 2.7 that a set of LDCs achieving identical CCMC capacity may attain a different DCMC capacity. Therefore, it is more pertinent to directly maximize the LDC's DCMC capacity.
- The LDCs that achieve a higher DCMC capacity at a certain SNR typically exhibit a good BER performance in the high-SNR region, since achieving a higher DCMC capacity implies that they are capable of providing a higher integrity as a result of their higher diversity gain and coding gain;
- The proposed optimization procedure is capable of taking into account different modulated signal constellations, such as specific L -PSK or L -QAM constellations. Hence, the total number of legitimate ST symbol vectors \mathbf{K} is $F = L^Q$.

The conditional probability of receiving $\bar{\mathbf{Y}}$ of Equation (2.15), given a signal vector K_f for $f \in (1, \dots, F)$ transmitted over a slowly Rayleigh fading channel is determined by the Probability Density Function (PDF) of the noise, as seen below [82]:

$$p(\bar{\mathbf{Y}}|K_f) = \frac{1}{(\sqrt{\pi\sigma_0^2})^{2N}} \cdot \exp\left(-\frac{||\bar{\mathbf{Y}} - \bar{\mathbf{H}}\chi K_f||^2}{\sigma_0^2}\right). \quad (2.22)$$

The DCMC capacity of the ML-detected MIMO system using L -QAM or L -PSK signalling, when we have the equivalent CIR $\bar{\mathbf{H}}\chi$ of Equation (2.15), is given by:

$$C_{LDC}^{DCMC} = \frac{1}{T} \max_{p(K_1), \dots, p(K_F)} \sum_{f=1}^F \int_{-\infty}^{\infty} \dots \int_{-\infty}^{\infty} p(\bar{\mathbf{Y}}|K_f) p(K_f) \cdot \log_2 \left[\frac{p(\bar{\mathbf{Y}}|K_f)}{\sum_{g=1}^F p(\bar{\mathbf{Y}}|K_g) p(K_g)} \right] d\bar{\mathbf{Y}} \quad (bits/sym/Hz), \quad (2.23)$$

where the right hand side of Equation (2.23) is maximized, when we have equiprobable ST symbols obeying $p(K_f) = \frac{1}{F}$ for $f = 1, \dots, F$. Furthermore, Equation (2.23) can be simplified as [82]

$$C_{LDC}^{DCMC} = \frac{1}{T} \left(\log_2[F] - \frac{1}{F} \sum_{f=1}^F E \left\{ \log_2 \left[\sum_{g=1}^F \exp(\Psi_{f,g}) | K_f \right] \right\} \right), \quad (2.24)$$

where $\Psi_{f,g}$ within the curly-bracketed expectation value of Equation (2.24) is given by:

$$\Psi_{f,g} = -||\bar{\mathbf{H}}\chi(K_f - K_g) + \bar{\mathbf{V}}||^2 + ||\bar{\mathbf{V}}||^2. \quad (2.25)$$

Since the equivalent system model represents the transmission regime of T time slots, the DCMC capacity of LDCs has to be divided by T , as seen in Equations (2.23) and (2.24).

Given the DCMC capacity of the LDC($MNTQ$) family, the following random search algorithm can be derived:

1. Randomly generate the complex-valued matrix $\bar{\chi} \in \zeta^{MT \times MT}$ using the Gaussian distribution.
2. If we arrange the system to satisfy $Q \geq MT$, the candidate DCM has to be a unitary matrix according to Theorem 1. It has been shown in [83] that a complex-valued matrix can be factored into the product of a unitary matrix and an upper triangular matrix using the QR decomposition [83]. Thus, a random dispersion character matrix can be obtained by $\chi = \frac{1}{\sqrt{M}} QR(\bar{\chi})$, which satisfies Equation (2.20).
3. By contrast, if we confine the LDC schemes to $Q < MT$, the DCM χ has to satisfy Equation (2.21) and it can be generated by retaining the first Q columns of the unitary matrix obtained using the QR decomposition of $\sqrt{\frac{T}{Q}} QR(\bar{\chi})$.
4. Having searched through the entire set of legitimate dispersion character matrices, we choose that particular one, which maximizes the DCMC capacity of Equation (2.24).

The LDCs generated by the above algorithm are sufficiently diverse to represent the entire legitimate space and additionally they are capable of maximizing the DCMC capacity. We found that 100,000 random searches are typically sufficient for generating LDCs exhibiting a good BER performance. Furthermore, Appendix A summarizes all the DCMs χ derived for the LDCs used in this chapter.

2.2.5 Performance Results

In this section, we present our simulation results for characterizing LDCs having different parameters and quantify their capacity with the aid of Theorems 1, 2 and 3. For the moment, we concentrate on the achievable LDC performance in terms of the attainable ergodic capacity and BER. Gray labelling was assumed for the bit-to-symbol mapping and an ML detector using Equation (2.18) was employed. Quadrature Phase Shift Keying (QPSK) modulation was employed in all the simulations. The LDC structure of Figure 2.3 was adopted in our simulations and the DCMs were generated using the DCMC maximization method presented in Section 2.2.4.

Figure 2.5 portrays the BER performance of LDCs having rates of $R_{LDC}=0.5, 1, 1.5, 2, 2.5$ and 3, which were adjusted by fixing (MNT) while gradually increasing Q . Observe from the shape of the curves in Figure 2.5 that all the codes do achieve the maximum diversity order of $D = 4$

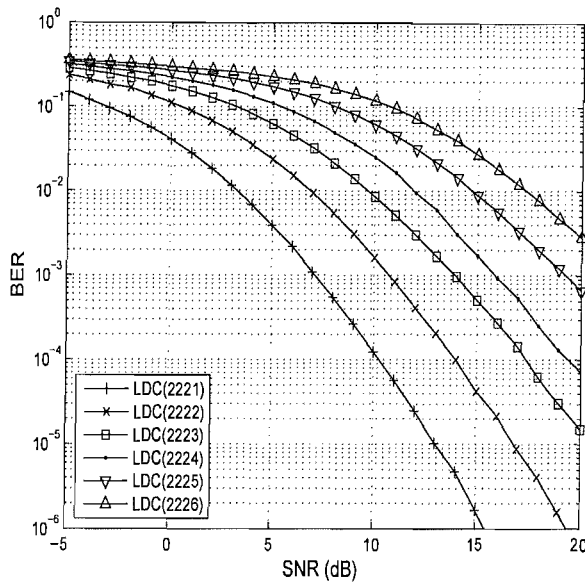


Figure 2.5: BER of a family of QPSK modulated LDCs obeying the structure of Figure 2.3 having $M = 2, N = 2, T = 2$ and $Q = 1, 2, 3, 4, 5, 6$ using an ML detector, when transmitting over i.i.d. Rayleigh-fading channels.

that a (2×2) -element MIMO system is capable of providing. Owing to the power constraint of Equation (2.13), the average transmit energy of each symbol was decreased when increasing Q , which results in a BER degradation. The ML detector jointly and simultaneously decodes the Q symbols of the vector \mathbf{K} seen in Figure 2.3. When we have $Q = 1$, the transmitted signal is a single element in a two-dimensional (2D) space obeying Equation (2.15). Since Gray labelling is used, the minimum Euclidean distance is maximized. However, when we have $Q > 1$, since each transmitted symbol is expected to fade independently, as seen in Equations (2.8) and (2.15), there is no guarantee that Gray mapping will ensure that the maximum minimum Euclidean distance is maximized within the $2Q$ -dimensional space.

The corresponding achievable CCMC capacity of LDCs having $M = 2, N = 2, T = 2$ and $Q = 1, 2, 3, 4, 5, 6$ using an ML detector is shown in Figure 2.6. The MIMO channel capacity of Equation (2.10) is also shown as an upper bound. Observe that LDCs having $Q \geq MT = 4$ have already achieved the maximum attainable diversity order of $D = 4$ and the MIMO channel capacity of Equation (2.10). Therefore, there is no point in selecting $Q > MT$ in terms of the achievable CCMC capacity of Equation (2.19), especially since this will increase the decoding complexity. In case of $Q < MT$, observe in Figure 2.6 that the CCMC capacity increases proportionally to $\frac{Q}{T}$, as stated in Theorem 2.

The achievable DCMC capacity of LDCs having $M = 2, N = 2, T = 2$ and $Q = 1, 2, 3, 4, 5, 6$ using an ML detector is shown in Figure 2.7 as plotted according to Equation (2.23). Recall that

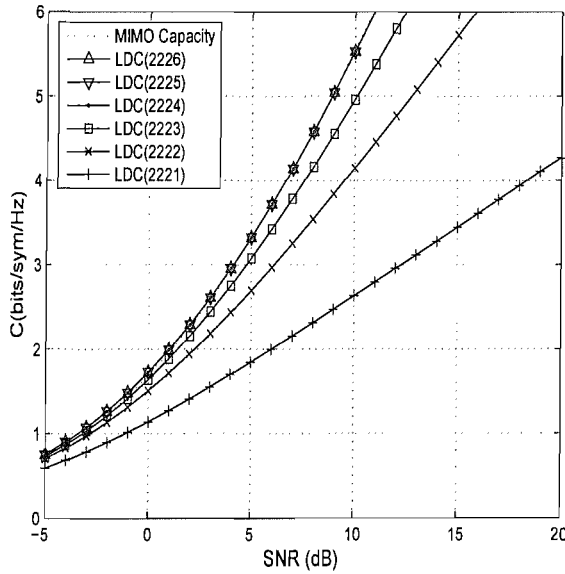


Figure 2.6: CCMC capacity comparison of a family of LDCs obeying the structure of Figure 2.3 having $M = 2$, $N = 2$, $T = 2$ and $Q = 1, 2, 3, 4, 5, 6$ using an ML detector, as plotted from Equation (2.9).

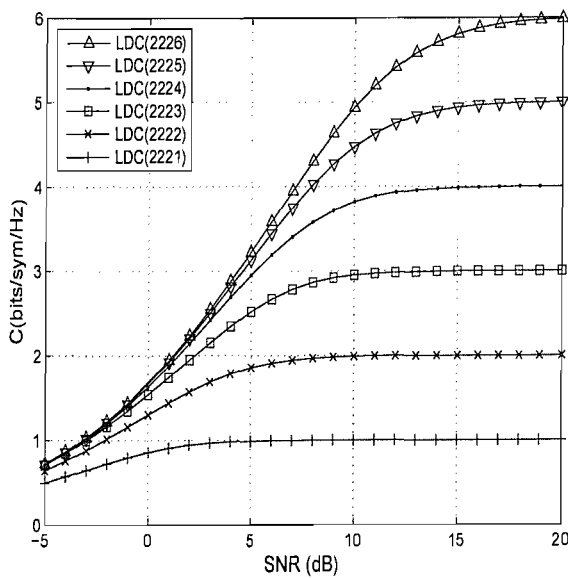


Figure 2.7: DCMC capacity comparison of LDCs obeying the structure of Figure 2.3 having $M = 2$, $N = 2$, $T = 2$ and $Q = 1, 2, 3, 4, 5, 6$ using an ML detector, as plotted from Equation (2.23), where QPSK modulation was employed.

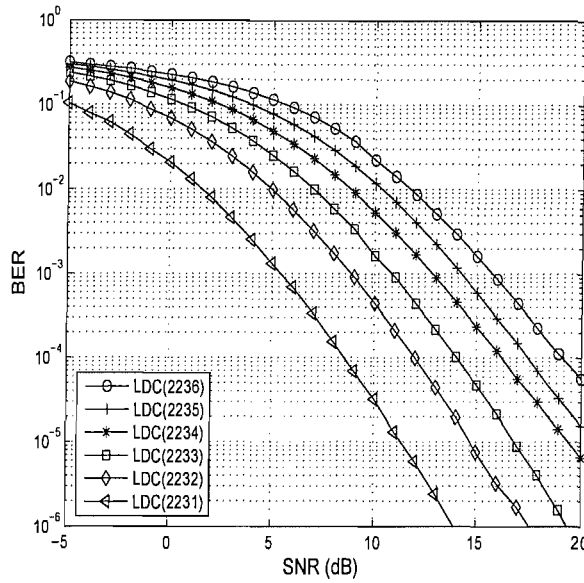


Figure 2.8: BER of a family of QPSK modulated LDCs obeying the structure of Figure 2.3 having $M = 2$, $N = 2$, $T = 3$ and $Q = 1, 2, 3, 4, 5, 6$ using an ML detector, when transmitting over i.i.d. Rayleigh-fading channels.

when we have $Q \geq MT$, the CCMC MIMO channel capacity has already been achieved as seen in Figure 2.6. By contrast, Figure 2.7 demonstrates that the DCMC capacity calculated using Equation (2.23) increases with Q , even when we have $Q > MT$. Naturally, it is possible to further improve the throughput of the system by transmitting more bits per symbol, or by using higher order modulation schemes.

Figure 2.8 shows the BER performance of a group of QPSK modulated LDCs having $M = 2$, $N = 2$, $T = 3$ and $Q = 1, 2, 3, 4, 5, 6$ using an ML detector. Again, a BER degradation is observed upon increasing the number of symbols transmitted per space-time block. Compared to the family of LDCs having $T = 2$ and characterized in Figure 2.5, the group of LDCs characterized in Figure 2.8 has the same spatial diversity order of $D = 4$. This observation is supported by Theorem 3, where the transmit diversity order is determined by $\min(M, T)$. However, it is still interesting to observe that the identical-rate LDC pairs of [LDC(2222), LDC(2233)] and [LDC(2224), LDC(2236)] characterized in Figures 2.5 and 2.8 exhibit near identical BER performance.

Furthermore, Figure 2.9 characterizes the DCMC capacity achieved by the equal-rate LDC pairs of [LDC(2222), LDC(2233)] and [LDC(2224), LDC(2236)] using an ML detector in conjunction with QPSK modulation. Not surprisingly, according to Equation (2.23), these equal-rate equal-diversity-order LDCs achieve the same DCMC capacity. This implies that increasing T and maintaining $T > M$, while fixing the rate to $R_{LDC} = \frac{Q}{T}$, do not benefit the system in terms of an improved BER performance and increased achievable capacity. In fact, maintaining the minimum

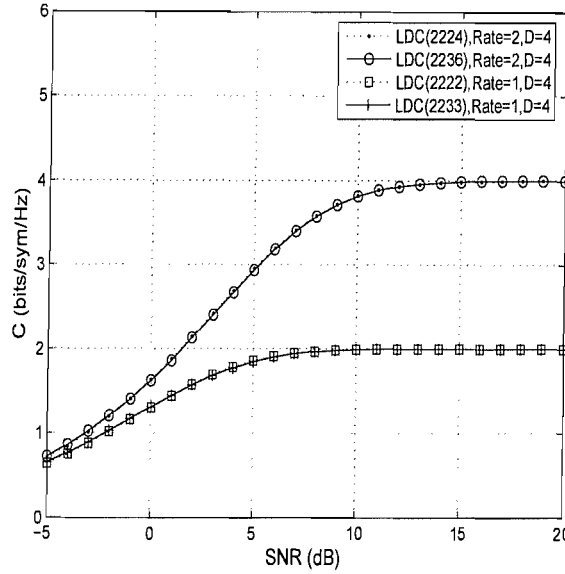


Figure 2.9: DCMC capacity comparison of QPSK modulated equal-rate LDC pairs [LDC(2222), LDC(2233)] and [LDC(2224), LDC(2236)] obeying the structure of Figure 2.3 using an ML detector, as evaluated from Equation (2.23).

value of T is desirable due to the associated complexity considerations.

Figure 2.10 quantifies the achievable BER performance of the QPSK modulated equal-rate LDCs pairs [LDC(2212), LDC(2224)] obeying the structure of Figure 2.3 using an ML detector, when transmitting over i.i.d. Rayleigh-fading channels. According to Theorem 3, the LDC(2212) scheme achieves $D = 2$, whereas $D = 4$ diversity gain is achievable using the LDC(2224) scheme. The BER performance recorded in Figure 2.10 demonstrates a clear gap between these schemes in the high-SNR region.

The CCMC and DCMC capacity achieved by the LDC(2212) and LDC(2224) schemes plotted using Equations (2.9) and (2.23) are shown in Figure 2.11. According to Theorem 1, the only requirement for LDCs to achieve full MIMO channel's capacity is that the DCM χ has to be a unitary. Therefore, despite different diversity orders were achieved by the LDC(2212) and LDC(2224) schemes, they attain the same CCMC capacity. However, the LDC(2224) arrangement has a higher DCMC capacity characterized in Equation (2.23) in the SNR region of $5dB < \rho < 15dB$, since having a higher spatial diversity order provides a higher degree of protection, as shown in Figure 2.10.

Based on the discussions above as well as on Theorems 1, 2, 3, our observations may be summarized as follows:

Corollary 1. *A group of LDCs ($MNTQ$) having M transmit and N receive antennas as well as a*

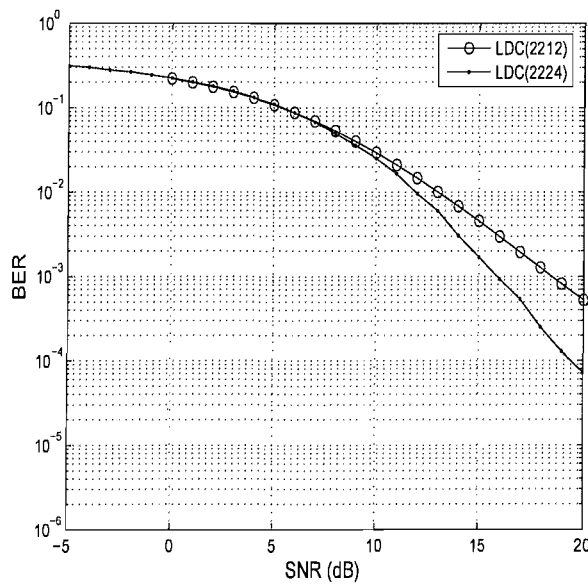


Figure 2.10: BER of QPSK modulated equal-rate LDC pairs [LDC(2212), LDC(2224)] obeying the structure of Figure 2.3 using an ML detector, when transmitting over i.i.d. Rayleigh-fading channels.

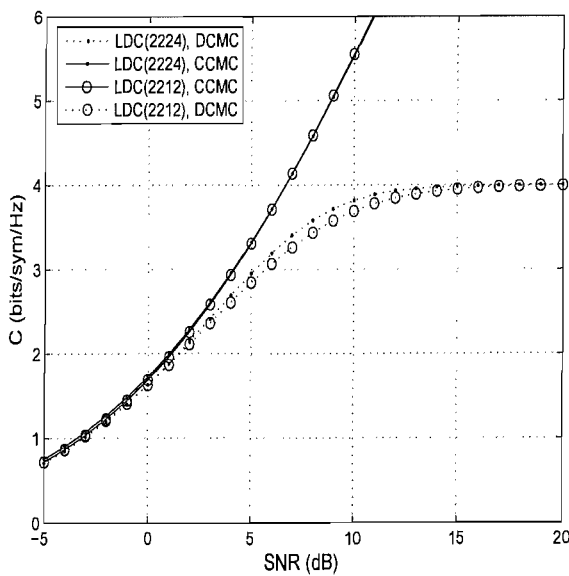


Figure 2.11: The CCMC and DCMC capacity of equal-rate LDC pairs [LDC(2212), LDC(2224)] obeying the structure of Figure 2.3 using an ML detector, as plotted using Equations (2.9) and (2.23). For plotting the DCMC capacity, QPSK modulation was employed.

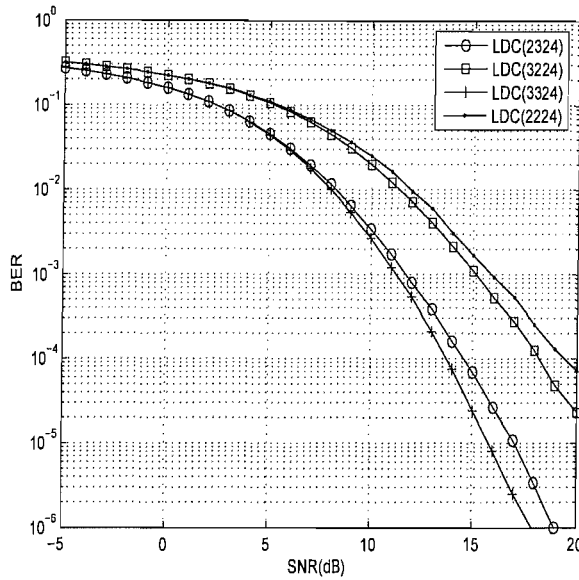


Figure 2.12: BER of a family of QPSK modulated LDCs obeying the structure of Figure 2.3 having $M = 2, 3$, $N = 2, 3$, $T = 2$ and $Q = 4$ using an ML detector, when transmitting over i.i.d. Rayleigh-fading channels.

fixed rate of $\frac{Q}{T}$ ($T > M$), exhibits the same diversity order and the same capacity. Consequently, they have an identical rate and an identical BER performance.

Figure 2.12 plots the BER performance of a group of QPSK modulated LDCs having the same fixed rate of $R_{LDC} = 2$, while using different MIMO antenna structures. Here, the LDC(2224) scheme is used as the benchmark. When increasing the number of transmit antennas to $M = 3$, according to Theorem 3, the LDC(3224) scheme exhibits the same diversity order of $D = 4$. However, the increased value of M enables the LDC(3224) arrangement to achieve a better coding gain, as shown in Figure 2.12. On the other hand, when increasing N to 3, the LDC(2324) arrangement achieved a diversity order of $D = 6$, which resulted in a significant SNR gain in Figure 2.12. Again, when an additional transmit antenna is employed compared to the LDC(2324) scheme, the resultant LDC(3324) arrangement demonstrated a better coding gain.

The capacity associated with changing the number of transmit and receive antennas is portrayed in Figure 2.13. Observe that the LDCs associated with $N = 3$, which have a higher diversity order also achieved a substantially higher CCMC/DCMC capacity, compared to the LDCs having $N = 2$. On the other hand, the effect of employing more transmit antennas ($M \geq T$), which results in an increased coding gain in Figure 2.12 is insignificant in terms of the increased achievable capacity, as quantified in Figure 2.13.

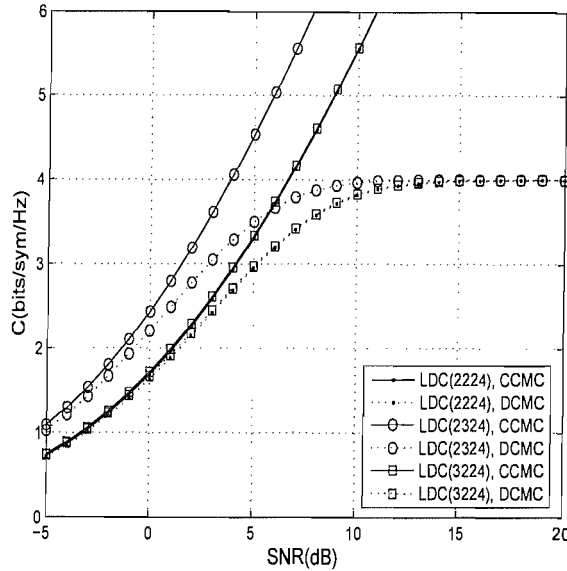


Figure 2.13: The CCMC and DCMC capacity of LDCs having $M = 2, 3$, $N = 2, 3$, $T = 2$ and $Q = 4$ obeying the structure of Figure 2.3 using an ML detector, as plotted using Equations (2.9) and (2.23). For plotting the DCMC capacity, QPSK modulation was employed.

2.2.6 Summary

In this section, we characterize the performance of the LDCs presented in Section 2.2.5 in terms of the effective throughput and the coding gains, where the latter is defined as the SNR difference, expressed in dBs, at a BER of 10^{-4} between various LDCs and the identical throughput single-antenna-aided systems.

Figure 2.14 characterizes the effective throughput against the SNR required to achieve $\text{BER} = 10^{-4}$ for a group of LDCs having $N = 1, 2, 3, 4$ receive and $M = 2$ transmit antennas using $T = 2$ time slots to transmit $Q = 1$ symbols per space-time block. An increased effective throughput was achieved by employing high-order modulation schemes, rather than by increasing the value of Q . For this particular group of LDC(2N21), 9.5dB is required for increasing the effective throughput from 0.5 to 2 (bits/sym/Hz).

Figure 2.15 plots the SNR requirement against the number of receive antennas N for a family of LDCs having $T = 2$, $Q = 4$ to achieve $\text{BER} = 10^{-4}$. For a given number of receive antennas N , the advantage of employing $M = 2, 3, 4$ transmit antennas is up to 6.5dB compared to that of the single antenna scheme, which increases gradually, as the total spatial diversity order is increased from $D = 2$ to $D = 4$. Also observe in Figure 2.15 that increasing N significantly reduces the SNR required to achieve $\text{BER} = 10^{-4}$, when we fix the number of transmit antennas M . In fact, the resultant SNR advantage of increasing N from 1 to 5 is about 25dB.

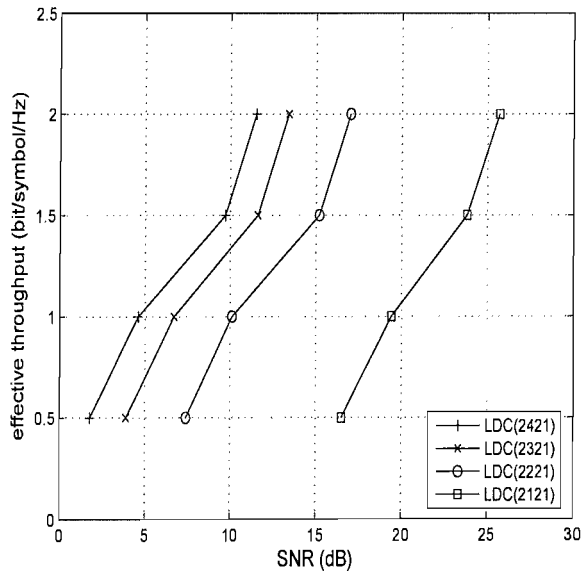


Figure 2.14: Effective throughput recorded at $\text{BER} = 10^{-4}$ of a family of LDCs obeying the structure of Figure 2.3 having $M = 2$, $N = 1, 2, 3, 4$, $T = 2$ and $Q = 1$ $\text{BER} = 10^{-4}$, when employing QPSK modulation in conjunction with an ML detector.

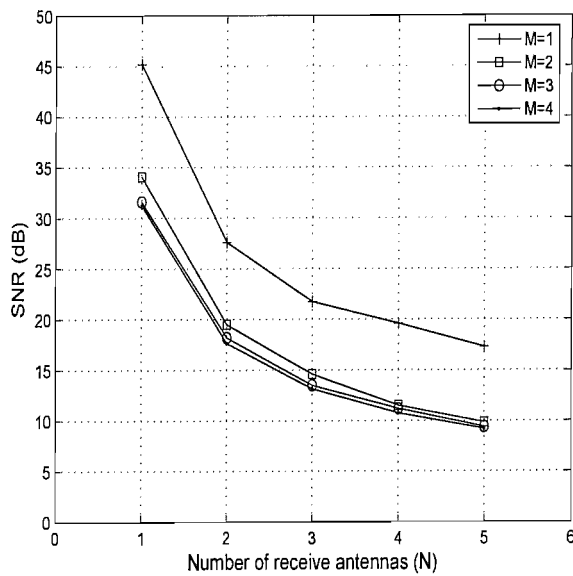


Figure 2.15: SNRs for a family of LDC schemes obeying the structure of Figure 2.3 having $M = 1, 2, 3, 4$, $N = 1, 2, 3, 4, 5$, $T = 2$ and $Q = 4$ to achieve $\text{BER} = 10^{-4}$, when employing QPSK modulation in conjunction with an ML detector.

Table 2.1: Coding gains of a family of LDCs have an effective throughput of 1 (bits/sym/Hz).

LDC	Diversity order	Modulation	Coding Gain
LDC(2211)	2	BPSK	17.5dB
LDC(2221)	4	QPSK	23.9dB
LDC(2222)	4	BPSK	23.65dB
LDC(2231)	4	8PSK	20.8dB
LDC(2233)	4	BPSK	23.7dB

Table 2.2: Coding gains of a family of LDCs have an effective throughput of 2 (bits/sym/Hz).

LDC	Diversity order	Modulation	Coding Gain
LDC(2211)	2	QPSK	17.7dB
LDC(2212)	2	BPSK	17.4dB
LDC(2221)	4	16QAM	19.9dB
LDC(2222)	4	QPSK	23.0dB
LDC(2224)	4	BPSK	23.3dB
LDC(2231)	4	64QAM	16.0dB
LDC(2232)	4	8PSK	20.7dB
LDC(2233)	4	QPSK	23.0dB

Furthermore, Tables 2.1 and 2.2 characterize the coding gains of a family of LDCs having an effective throughput of 1 and 2 (bits/sym/Hz) respectively, compared to the single antenna system having the identical effective throughput. The corresponding modulation schemes employed are also listed in Tables 2.1 and 2.2. More particularly, for schemes having an effective throughput of 1 (bits/sym/Hz), the largest coding gain is observed, when LDC(2233) was employed in conjunction with Binary Phase Shift Keying (BPSK) modulation, while the BPSK-modulated LDC(2224) arrangement is achieved the highest coding gain for an effective throughput of 2 (bits/sym/Hz).

2.3 Link Between STBCs and LDCs

This section firstly continues our discourse by reviewing main results in the state-of-art literature related to STBCs, including the so-called *rank criterion* [10], the *determinant criterion* [10], the diversity versus multiplexing gain tradeoff [7] and the diversity versus rate tradeoff [84]. Secondly, we investigate the relationship between all the major representatives of STBCs reported in the open

literature and LDCs from both mathematical and design concept perspectives.

2.3.1 Review of Existing STBC Knowledge

The PSEP of mistaking a space-time transmission matrix \mathbf{S} of Equation (2.2) for another matrix $\bar{\mathbf{S}}$, denoted as $p(\bar{\mathbf{S}} \rightarrow \mathbf{S})$, depends only on the distance between the two matrices after transmission through the channel and the noise power, which is upper bounded by [10]:

$$p(\bar{\mathbf{S}} \rightarrow \mathbf{S}) \leq \frac{1}{(\nabla_1 \cdots \nabla_\eta)^N} \cdot \left(\frac{\rho}{4M}\right)^{\eta N}. \quad (2.26)$$

- **Rank Criterion** [10]. Observe in Equation (2.26) that $(\frac{\rho}{4M})^{\eta N}$ dominates how fast the error decays with the SNR and the total diversity order is determined by ηN . More explicitly, the transmit diversity order of a STBC scheme equals to the minimum rank η of the difference matrix $\mathbf{S}_\Delta = (\mathbf{S} - \bar{\mathbf{S}})$. Accordingly, η has to be found by searching through all distinct codeword pairs \mathbf{S} and $\bar{\mathbf{S}}$, where $\bar{\mathbf{S}} \neq \mathbf{S}$.
- **Determinant Criterion** [10]. Also observe in Equation (2.26) that $\frac{1}{(\nabla_1 \cdots \nabla_\eta)^N}$ has to be minimized, which determines the coding gain of a STBC scheme. Furthermore, the determinant criterion states the minimum of

$$(\nabla_1 \cdots \nabla_\eta) \quad (2.27)$$

evaluated over all distinct ST codeword pairs determines the achievable coding gain and must be maximized, where the coefficients ∇_i are the non-zero eigenvalues of $\mathbf{S}_\Delta \mathbf{S}_\Delta^H$.

- **Full-diversity.** Using the average PSEP analysis technique of Equation (2.26), it follows that the maximum attainable diversity order of a STBC scheme designed for an $(M \times N)$ -element MIMO system is [10] [85]

$$D_{full} = MN, \quad (2.28)$$

which implies the ST difference matrix \mathbf{S}_Δ should have full rank.

- **Full-rate.**³ Since it is possible to transmit up to one 'independent' symbol per antenna per time slot, the symbol rate could be

$$R_{full} = M. \quad (2.29)$$

³At this stage it is important to contrast the above-mentioned full-rate, full-diversity schemes, which were primarily conceived for providing transmit and receive diversity against the family of Spatial Division Multiplexing (SDM) MIMO that were contrived for attaining a multiplexing gain, although they may also provide some diversity gain. The terminology of full-rate and full-diversity schemes is typically invoked in the context of STCs, although quantifying the throughput and diversity gain of SDM schemes would also be beneficial. Nonetheless to the best of our knowledge, no parallel terminology has been used in the context of SDM schemes.

Note that LDCs obeying Equation (2.12) are capable of achieving a rate $R_{LDC} > M$, since the transmission matrix is the weighted sum of all the symbols as exemplified in Figures 2.5, 2.6 and 2.8. However, the terminology 'full-rate' remains useful in the discussion of a STBC scheme's CCMC capacity. For example, we have demonstrated in Equation (2.19) that when the LDC's rate $R_{LDC} \geq M$, there is no further improvement in terms of the achievable CCMC capacity. On the other hand, using the term 'full-rate' is inappropriate for quantifying the DCMC capacity, since the corresponding capacity increases upon increasing the rate, as seen in Figure 2.7.

- **Diversity Multiplexing Gain Tradeoff.** The authors of [7] showed that for a MIMO channel, there is a fundamental tradeoff between the achievable diversity gain and the attainable multiplexing gain. More explicitly, achieving a higher spatial multiplexing gain comes at the price of sacrificing diversity gain, when employing a continuous-valued signal alphabet that grows linearly with the logarithm of the SNR. In other words, the diversity and multiplexing gain tradeoff quantifies how fast the rate of a STBC scheme can increase with the SNRs, while having a certain diversity order. According to the multiplexing gain definition of Equation (1.2), any scheme employing a fixed rate modulation scheme has a zero multiplexing gain, since at high SNRs, any fixed rate constitutes only a vanishing fraction of the achievable capacity.
- **Rate Diversity Tradeoff.** In [84] [86], the authors argued that in MIMO systems, one can also increase the attainable transmission rate at the expense of a certain loss in the diversity gain, which reflects the associated rate versus diversity tradeoff. This tradeoff is characterized by $R_{STBC} \leq M - D_{tx} + 1$ [84], where D_{tx} denotes the spatial transmit diversity order. With the aid of recent advances in high-rate full-diversity STBCs [2] [77] [87], it has been shown that it is not necessary to sacrifice rate in order to achieve diversity and vice versa. However, considering the rate versus diversity tradeoff is still valuable for the analysis of STBCs obeying a certain structure, which is characterized by the so-called transmit symbol separability defined as follows.

Definition 1. *Transmit Symbol Separability (TSS):*

- *If all the entries of the transmitted ST signal matrix \mathbf{S} constitute a transformed version⁴ of a single rather than several symbols from a specific modulated signal constellation, then this STBC is said to obey the property of full TSS.*

⁴Transformation includes scalar multiplication, Hermitian transpose and conjugate operation.

- If *some* of the entries in the transmitted ST signal matrix \mathbf{S} are constituted by a combination of several symbols from a specific modulated signal constellation, then the STBC is said to obey the property of partial TSS.
- If *all* the entries in the transmitted ST matrix \mathbf{S} are constituted by a combination of several symbols from a specific modulated constellation, then the STBC is deemed to be non-separable.

For example, the STBC scheme transmitting the signal $(\frac{1}{\sqrt{2}}s_1 + \frac{1}{\sqrt{2}}s_2)$ is non-separable, while Alamouti's scheme [14] transmits either $\pm s_1$ or $\pm s_1^*$ and hence exhibits full TSS. Let us now consider the family of STBCs from a TSS perspective in more detail.

Intuition: If a STBC scheme exhibits full TSS, then there exists a tradeoff between the maximum rate and the maximum achievable spatial diversity. If a STBC scheme has the property of partial TSS or it is non-separable, it has the potential of simultaneously achieving both a high throughput and full diversity.

Discussion: When full TSS is maintained, each transmitted symbol only contains the information of its own. Therefore, there is a tradeoff between increasing the achievable rate by sending more independent symbols and increasing the diversity by transmitting redundant information. For example, Alamouti's STBC and the classic V-BLAST scheme achieve two extremes, respectively. On the other hand, even when partial TSS is maintained, some of the transmitted symbols may carry information related to multiple symbols, then it is possible to achieve some grade of diversity, despite operating at high-rate. Furthermore, the family of STBCs does not maintain TSS, but nonetheless has the potential of simultaneously achieving both a high throughput and full diversity.

2.3.2 Orthogonal STBCs

STBCs based on orthogonal designs in order to achieve full spatial diversity were first proposed in [14], and later were generalized in [15]. The philosophy behind Orthogonal STBCs (OSTBCs) is that each transmission space-time signal matrix \mathbf{S} satisfies an orthogonality constraint. The orthogonality embedded in \mathbf{S} enables the receiver to decouple the transmitted multi-antenna-coded symbol streams into independent symbols. Thus, simple ML detection can be carried out. Unfortunately, STBCs satisfying the orthogonality constraint exist for only a few specific choices of the parameters ($MNTQ$) and they do not achieve the ergodic capacity of Equation (2.10), especially not when multiple receive antennas are employed.

For example, given a symbol vector $\mathbf{K} = [s_1, s_2]^T$, the simple \mathbf{G}_2 space-time code of [15] can

be written as

$$\begin{aligned}
\mathbf{G}_2 &= \begin{pmatrix} s_1 & s_2 \\ -s_2^* & s_1^* \end{pmatrix} \\
&= \begin{pmatrix} \alpha_1 & 0 \\ 0 & \alpha_1 \end{pmatrix} + j \begin{pmatrix} \beta_1 & 0 \\ 0 & -\beta_1 \end{pmatrix} + \begin{pmatrix} 0 & \alpha_2 \\ -\alpha_2 & 0 \end{pmatrix} + j \begin{pmatrix} 0 & \beta_2 \\ \beta_2 & 0 \end{pmatrix} \\
&= \begin{pmatrix} 1 & 0 \\ 0 & 1 \end{pmatrix} \alpha_1 + j \begin{pmatrix} 1 & 0 \\ 0 & -1 \end{pmatrix} \beta_1 + \begin{pmatrix} 0 & 1 \\ -1 & 0 \end{pmatrix} \alpha_2 + j \begin{pmatrix} 0 & 1 \\ 1 & 0 \end{pmatrix} \beta_2 \\
&= \mathbf{A}_1 \alpha_1 + j \mathbf{B}_1 \beta_1 + \mathbf{A}_2 \alpha_2 + j \mathbf{B}_2 \beta_2,
\end{aligned} \tag{2.30}$$

where $s_1 = \alpha_1 + j\beta_1$ and $s_2 = \alpha_2 + j\beta_2$. Observe that Equation (2.30) is fully characterized by the LDC structure of Figure 2.2. Following the similar disassemble process of Equation (2.30), it may be readily shown that other OSTBCs such as the \mathbf{G}_3 , \mathbf{G}_4 , \mathbf{H}_3 and \mathbf{H}_4 schemes of [15] can also be fully specified by the dispersion structure of Figure 2.2.

From the perspective of LDCs, the family of OSTBCs disperses each multi-antenna ST symbol to specific spatial and temporal slots according to a certain pattern, as seen in Equation (2.30). The pattern is fully characterized by the orthogonality of the dispersion matrices. Hence, both full TSS as well as simple ML detection are guaranteed.

It is worth mentioning that the OSTBCs \mathbf{H}_3 and \mathbf{H}_4 [15] exhibit partial TSS, whereas their counterparts \mathbf{G}_3 and \mathbf{G}_4 [15] possess the property of full TSS. Therefore, \mathbf{H}_3 and \mathbf{H}_4 achieve a higher rate than the \mathbf{G}_3 and \mathbf{G}_4 codes, although none of them are capable of achieving a symbol rate higher than 1.

2.3.3 Quasi-Orthogonal Space-Time Block Codes

The main benefits of an orthogonal design are their simple decoding and full transmit diversity potential. When relaxing the simple separate decoding property of the multi-antenna streams, a potentially higher rate can be achieved. In [17], the family of the so-called Quasi-Orthogonal Space-Time Block Codes (QOSTBCs) was proposed for the sake of pursuing high-rate transmission, while maintaining a certain diversity order. The class of QOSTBCs is capable of decoupling the symbol streams into groups, where each decoding group contains two symbols rather than a single symbol. Hence, a higher ML decoding complexity is imposed compared to that of the OSTBCs.

The construction of QOSTBCs can be directly derived from that of OSTBCs. For example, a

(4×4) -antenna QOSTBC codeword matrix is given by [17]:

$$\mathbf{S} = \begin{pmatrix} \mathbf{G}_2(s_1, s_2) & \mathbf{G}_2(s_3, s_4) \\ -\mathbf{G}_2(s_3, s_4)^* & \mathbf{G}_2(s_1, s_2)^* \end{pmatrix}. \quad (2.31)$$

Therefore, it is straight-forward to rewrite the QOSTBC transmission matrix of Equation (2.31) using the LDC structure of Figure 2.2 following the same procedure as in the context of Equation (2.30). Compared to the \mathbf{G}_4 OSTBC code of [15], the QOSTBC of Equation (2.31) achieves twice the symbol rate at the cost of sacrificing half of the transmit diversity order, which constitutes a manifestation of the rate versus diversity tradeoff formulated in the context of Property 1.

Clearly, the LDC structure of Figure 2.2 subsumes the family of QOSTBCs. Similarly to OSTBCs, QOSTBCs disperse each multi-antenna ST symbol to specific space-time slots obeying the relaxed orthogonality constraint. Observe from Equation (2.31) that full TSS is also ensured, which implies that the class of QOSTBCs obeys the rate versus diversity tradeoff.

In later works of [88] [89], the idea of constellation rotation was introduced in order to overcome the potential diversity loss. However, the associated diversity gain improvement accrued from modulation diversity [90], rather than from the spatial diversity addressed in this treatise.

2.3.4 Linear STBCs Based on Amicable Orthogonal Designs

Although QOSTBCs exhibit a higher design flexibility than OSTBCs, they are still unsuitable for MIMO systems having flexible $(MNTQ)$ parameter combinations and they are unable to achieve full diversity. The further pursuit of full-diversity STBCs leads to the design of Linear Space-Time Block Codes (LSTBCs) [16] [91] [92] [93], which are defined as:

$$\mathbf{S} = \sum_{q=1}^Q (\alpha_q \mathbf{A}_q + j\beta_q \mathbf{B}_q). \quad (2.32)$$

The philosophy behind LSTBCs is to find specific orthogonal dispersion matrices \mathbf{A}_q and \mathbf{B}_q , which are capable of separating Q transmitted symbols at the receiver. In other words, Q symbols are mapped to M number of transmit antennas with the aid of a set of orthogonal matrices.

To accomplish this design goal, the dispersion matrices designed for real-valued symbols have to satisfy the following requirement [16]

$$\mathbf{A}_{i_1} \mathbf{A}_i^H = \mathbf{I} \quad (i = i_1), \quad (2.33)$$

$$\mathbf{A}_{i_1} \mathbf{A}_i^H = -\mathbf{A}_i \mathbf{A}_{i_1}^H \quad (i \neq i_1), \quad (2.34)$$

where $i, i_1 = 1, 2, \dots, Q$. Full spatial diversity order is guaranteed by Equation (2.33), while Equation (2.34) ensures that the set of dispersion matrices are orthogonal to each other. For complex-

valued modulated symbols, the dispersion matrices \mathbf{A}_q and \mathbf{B}_q should satisfy [16]

$$\begin{aligned}\mathbf{A}_{i_1} \mathbf{A}_i^H &= \mathbf{I}, \\ \mathbf{B}_{i_1} \mathbf{B}_i^H &= \mathbf{I}, \quad (i = i_1),\end{aligned}\tag{2.35}$$

$$\begin{aligned}\mathbf{A}_{i_1} \mathbf{A}_i^H &= -\mathbf{A}_i \mathbf{A}_{i_1}^H, \\ \mathbf{B}_{i_1} \mathbf{B}_i^H &= -\mathbf{B}_i \mathbf{B}_{i_1}^H, \quad (i \neq i_1),\end{aligned}\tag{2.36}$$

$$\mathbf{A}_{i_1} \mathbf{B}_i^H = \mathbf{B}_i \mathbf{A}_{i_1}^H, \quad (1 < i, i_1 < Q).\tag{2.37}$$

Equation (2.35) ensures that full spatial transmit diversity order can be achieved and Equation (2.36) ensures the orthogonality within the dispersion matrices \mathbf{A}_i and \mathbf{B}_i . The orthogonality between the dispersion matrices \mathbf{A}_i and \mathbf{B}_i is guaranteed by Equation (2.37).

Recall that the family of OSTBCs discussed in Section 2.3.2 obey the orthogonal constraint of

$$\mathbf{S} \mathbf{S}^H = \mathbf{I}.\tag{2.38}$$

If the LSTBCs obeying the structure of Equation (2.32) satisfy the orthogonal constraint of Equation (2.38), it can be shown that the set dispersion matrices of \mathbf{A}_q and \mathbf{B}_q has to satisfy Equations (2.35), (2.36) and (2.37). The design of such set of matrices is referred to as *amicable orthogonal* design and more details can be found in [94]. In other words, LSTBCs constitute a family of LDCs obeying the structure of Figure 2.2 that satisfy the orthogonality constraint of Equation (2.38). Thus, it becomes clear that the LSTBCs have to obey the rate versus diversity tradeoff, owing to their full TSS property, as stated in Property 1.

2.3.5 Single-Symbol-Decodable STBCs Based on QOSTBCs

Observe in Equations (2.35), (2.36) and (2.37) that the orthogonality imposed enables the transmitted ST symbol streams to be separated by a set of dispersion matrices \mathbf{A}_q and \mathbf{B}_q . However, ensuring the orthogonality for each of the Q transmitted symbols according to Equation (2.37) may not be necessary, if the real and imaginary parts of a transmitted ST symbol are jointly detected. If we eliminate this constraint, the requirement for the set of the dispersion matrices becomes [95]

$$\mathbf{A}_{i_1} \mathbf{A}_i^H = -\mathbf{A}_i \mathbf{A}_{i_1}^H, \quad \mathbf{B}_{i_1} \mathbf{B}_i^H = -\mathbf{B}_i \mathbf{B}_{i_1}^H \quad (i \neq i_1),\tag{2.39}$$

$$\mathbf{A}_{i_1} \mathbf{B}_i^H = \mathbf{B}_i \mathbf{A}_{i_1}^H \quad (i \neq i_1).\tag{2.40}$$

Compared to Equation (2.37), Equation (2.40) excludes the scenarios, where $i = i_1$, which eliminates the orthogonality within each transmitted symbols of Figure 2.2. In the open literature, STBCs obeying Equations (2.39) and (2.40) are referred as Single-Symbol-Decodable Space-Time Block Codes (SSD-STBCs) [94] [95].

From another point of view, SSD-STBCs constitute the class of LDCs having the structure of Figure 2.2 that obeys the constraints of Equations (2.39) and (2.40). Consequently, the full TSS property is maintained, which inevitably imposes the rate versus diversity tradeoff.

Note that the STBCs presented in Sections 2.3.2 to 2.3.5 can be characterized using the LDC structure of Figure 2.2, since they all possess some degrees of orthogonality. However, the orthogonality imposed not only restricts the design of STBCs, but imposed the rate versus diversity tradeoff [86] characterized by having the property of full TSS.

2.3.6 Space-Time Codes Using Time Varying Linear Transformation

For the sake of achieving a high throughput⁵ and full diversity in the context of STBCs, the authors of [76] proposed a class of STBCs employing unitary a Time Variant Linear Transformation (TVLT).

A TVLT code can be represented using the notation of $\text{TVLT}(M, N, T, MT)$, where the MT symbols mapped to the M antennas are transmitted using T time slots and received by N antennas. Hence, maintaining a symbol rate of $R = M$. More explicitly, a TVLT scheme firstly separates MT symbols into T layers, each contains M symbols. Note that these MT number of symbols are correlated, as opposed to independent symbols in the previous discussions. Then, each layer is separately modulated by a specific vector for transmission in a single time slot. For example, a $\text{TVLT}(2224)$ scheme disperses a layer containing coded symbols s_1 and s_2 during the first time slot and disperses the other layer containing coded symbols s_3 and s_4 during the second time slot. This process is expressed as follows:

$$\mathbf{S} = \begin{pmatrix} a_1^{11} & 0 \\ a_1^{21} & 0 \end{pmatrix} s_1 + \begin{pmatrix} a_2^{11} & 0 \\ a_2^{21} & 0 \end{pmatrix} s_2 + \begin{pmatrix} 0 & a_3^{12} \\ 0 & a_3^{22} \end{pmatrix} s_3 + \begin{pmatrix} 0 & a_4^{12} \\ 0 & a_4^{22} \end{pmatrix} s_4, \quad (2.41)$$

where a_q^{ij} denotes the entries of the dispersion matrices \mathbf{A}_q of Equation (2.12). Furthermore, the rank criterion [10] discussed in Section 2.3.1 states that the minimum rank of the difference matrix $\mathbf{S}_\Delta = (\mathbf{S} - \bar{\mathbf{S}})$ equals to the transmit diversity order of a STBC scheme. For the $\text{TVLT}(2224)$ example of Equation (2.41), the difference transmission matrix is given by:

$$\mathbf{S}_\Delta = \begin{pmatrix} a_1^{11} & 0 \\ a_1^{21} & 0 \end{pmatrix} s_{1\Delta} + \begin{pmatrix} a_2^{11} & 0 \\ a_2^{21} & 0 \end{pmatrix} s_{2\Delta} + \begin{pmatrix} 0 & a_3^{12} \\ 0 & a_3^{22} \end{pmatrix} s_{3\Delta} + \begin{pmatrix} 0 & a_4^{12} \\ 0 & a_4^{22} \end{pmatrix} s_{4\Delta}. \quad (2.42)$$

Observe in Equation (2.42) that maintaining full transmit diversity is guaranteed, as long as the non-zero columns of the dispersion matrices are independent of each other. Note that the decoder has to

⁵High throughput refers to a STBC scheme having a throughput higher than one symbol per channel use.

jointly decode all the symbols in order to achieve full diversity, since all the symbols are correlated with each other. In other words, if each layer is decoded separately, no diversity advantage can be gained.

Clearly, the class of TVLT codes obeying similar structure as to Equation (2.41) constitute a subset of LDCs following the schematic of Figure 2.3. The TVLT codes can be obtained using the LDC model of Equation (2.12), under the constraint of dispersing each layer to a single time slot. In other words, different layers are separated using time-division.

2.3.7 Threaded Algebraic Space-Time Codes

Recently, another family of STBCs has been proposed in order to achieve both high-throughput and full diversity, which is referred as to Threaded Algebraic Space-Time Block Codes (TASTBCs) [18] [75] [96]. The main rationale behind this framework is to partition the Q symbols into L ($L \leq M$) layers and disperse each layer to a $(M \times 1)$ -element vector with the aid of a set of dispersion matrices. The resultant vector is arranged diagonally into the space-time transmission matrix \mathbf{S} of Figure 2.1 in order to span across the entire spatial domains encompassed by the TASTBC design. The $(M \times 1)$ -element dispersed vector is referred as a 'thread' in [18]. The L number of dispersed vectors are designed to be 'orthogonal' to each other by employing an appropriately chosen scaling factor [18].

In order to expound a little further, we use the well-known \mathbf{G}_2 space-time matrix to demonstrate the philosophy of TASTBCs, where a \mathbf{G}_2 is given by

$$\mathbf{G}_2 = \begin{pmatrix} s_1 & s_2 \\ -s_2^* & s_1^* \end{pmatrix}. \quad (2.43)$$

With a small modification, Alamouti's scheme can be written as follows:

$$\mathbf{G}_2 = \begin{pmatrix} s_1 & \sqrt{-1} \cdot s_2 \\ \sqrt{-1} \cdot s_2^* & s_1^* \end{pmatrix}. \quad (2.44)$$

It is straightforward to verify that the modified representation seen in Equation (2.44) has the same properties as the original Alamouti scheme of Equation (2.43). However, the modified representation portrayed in Equation (2.44) falls within the scope of TASTBCs. More particularly, the first sub-stream containing the information symbol s_1 is dispersed by:

$$L_1 = \begin{pmatrix} s_1 \\ s_1^* \end{pmatrix} = \begin{pmatrix} 1 \\ 1 \end{pmatrix} \alpha_1 + j \begin{pmatrix} 1 \\ -1 \end{pmatrix} \beta_1. \quad (2.45)$$

Table 2.3: Diversity, rate, complexity and design flexibility comparisons for various STBCs.

STBC	Rate	Diversity	TSS	Complexity	Orthogonality	Flexibility
OSTBC [10]	≤ 1	MN	full	1	full	minimum
LSTBC [16]	≤ 1	MN	full	1	full	\downarrow
SSD-STBC [94]	1	$MN/2$	full	1	\downarrow	\downarrow
QOSTBC [17]	1	$MN/2$	full	2	\downarrow	\downarrow
TVLT [76]	M	MN	partial	M	\downarrow	\downarrow
TASTBC [18]	M	MN	partial	M	\downarrow	\downarrow
LDC [1] [2]	M	MN	non	Q	non	maximum

Similarly, the second sub-stream containing symbol s_2 is dispersed by:

$$\hat{L}_2 = \sqrt{-1} \cdot \begin{pmatrix} s_2 \\ s_2^* \end{pmatrix} = \sqrt{-1} \cdot \begin{pmatrix} 1 \\ 1 \end{pmatrix} \alpha_2 + j\sqrt{-1} \cdot \begin{pmatrix} 1 \\ -1 \end{pmatrix} \beta_2. \quad (2.46)$$

Note that in this case $\sqrt{-1}$ is the aforementioned scaling factor, which guarantees the orthogonality between two threads or layers.

The example of Equations (2.45) and (2.46) demonstrates that TASTBCs can be fully characterized by the general LDC structure of Figure 2.2. More explicitly, the orthogonality imposed on the space-time codeword \mathbf{S} of Figure 2.2 restricts each layer of TASTBCs to only partially explore the ST recourses available. By contrast, LDC schemes disperse each information layer to all the space-time dimensions available.

It is also interesting to compare the TVLT and TASTBC schemes. They all share the same concept of dividing the Q symbols into layers and then disperse each layer independently. The separation of the layers is achieved by time division for TVLT schemes, whereas the TASTBC arrangements employ a unique scaling factor for differentiating and separating the layers, which was $\sqrt{-1}$ in the example of Equations (2.45) and (2.46).

2.3.8 Summary

Sections 2.3.2 to 2.3.7 demonstrated that the family of OSTBCs, QOSTBCs, LSTBCs, SSD-STBCs, TVLTs and TASTBCs can be described using the unified structure of LDCs provided in Figures 2.2 and 2.3, where $\text{LDC}(MNTQ)$ represents a MIMO system employing M transmit and N receive antennas, transmitting Q symbols using T time slots. All of the representatives of this LDC family imposed different degrees of 'orthogonality' on the general LDC framework of

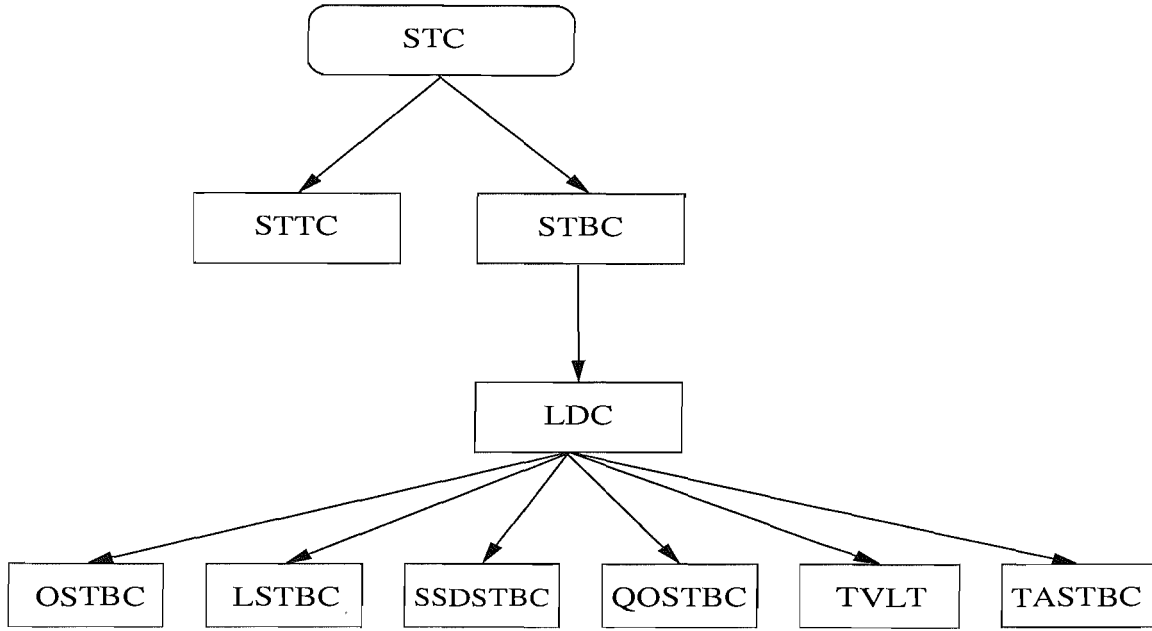


Figure 2.16: Classification of Space-Time Coding (STC) techniques.

Figures 2.2 and 2.3. In this section, we compare the above-mentioned STBCs in terms of their diversity order, rate as well as complexity and characterize the evolution of STBCs.

Assuming that symbol-based ML decoding is used and the same modulation scheme is employed by all the STBCs considered, the decoding complexity ω imposed is associated with the number of symbols decoded at a time. The associated design flexibility can be quantified in terms of the number of practical MIMO solutions for a specific parameter combination of (M, N, T, Q) .

Table 2.3 listed the rate, diversity and estimated decoding complexity of the diverse STBCs that have been discussed in Sections 2.3.2 to 2.3.7. Let us now continue with their brief characterization.

- Maintaining at least partial TSS constitutes a necessary condition for the design of high-throughput, full-diversity STBCs. In simple physical terms, the TSS characterizes the degree of inter-dependence among the symbols within the transmitted space-time matrix \mathbf{S} . If each transmitted signal encapsulates the information of more than one information symbol, then high-throughput and full-diversity can be potentially achieved at the same time. By contrast, if each transmitted signal encapsulates a single original input symbol's information, then the corresponding STBCs can only achieve either full diversity or a rate $R_{STBC} \leq 1$, as shown in Table 2.3.
- When decreasing the degree of orthogonality embedded in the space-time matrix \mathbf{S} of Figure 2.1, typically the degree of design flexibility is increased. For example, the OSTBC design of Section 2.3.2 enjoys simple single-symbol ML decoding as a result of its full or-

thogonality. However, it has a very limited choice of dispersion matrices and the number of transmit antennas supported is restricted. By contrast, LDCs' flexible structure of Figure 2.3 potentially facilitates an unlimited number of dispersion matrices for arbitrary MIMO antenna configurations, as shown in Equation (2.19).

- Observe from Table 2.3 that the degree of TSS is useful for characterizing the decoding complexity imposed. For example, high-rate full-diversity LDCs of [2] have to jointly decode Q symbols per space-time block. On the other hand, for example, the QOSTBCs of Section 2.3.3 is capable of separating the symbols into two-symbol decoding pairs, owing to their orthogonality.
- The flexibility of LDCs is also related to the number of space-time slots used by each symbol. For example, Equation (2.41) demonstrates the structure of TVLT [76] codes, which disperse each layer merely to M out of the total MT number of space-time slots, whereas LDCs ensure that each space-time slot contains information related to all the information symbols, as characterized in Equation (2.12).

Finally, as illustrated in Figure 2.16, we portray the family of LDCs as a prominent class of space-time processing techniques, uniting the class STBCs [64]. More explicitly, the family of Space-Time Coding (STC) may be classified in two major categories, namely STBCs and Space-Time Trellis Codes (STTCs) [10] [64] [97]. The general LDC structure of Figures 2.2 and 2.3 is capable of providing diverse solutions to meet the challenge of achieving both full-diversity and high-throughput. Hence, LDCs subsume many existing space-time block coding schemes, as seen in Figure 2.16.

2.4 EXIT Chart Based Design of LDCs

2.4.1 Analyzing Iteratively-Detected LDCs

This section analyzes a serial-concatenated channel-coded LDC scheme using iterative decoding. The system design is approached from a capacity maximization perspective with the aid of EXIT charts. More explicitly, the EXIT chart analysis enables us to estimate the maximum achievable rate of the proposed channel-coded LDC scheme using both ML and MMSE detectors, when employing the LDCs optimized in Section 2.2.4. Provided the capacity results illustrated in Section 2.2.5, we will demonstrate how far the serial concatenated system operates from LDC's DCMC capacity.

Figure 2.17 plots the schematic of a serial concatenated RSC-encoded LDC system employing

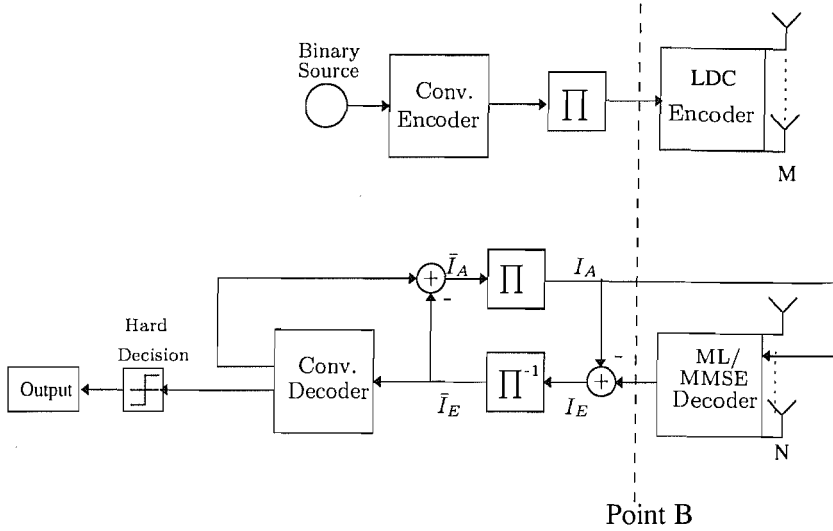


Figure 2.17: Schematic of a serial concatenated RSC-coded LDC system employing iterative decoding.

Table 2.4: System parameters for the RSC-coded LDC system of Figure 2.17.

Modulation	QPSK
Mapping	Gray mapping
Regular Outer Channel Code	RSC(2,1,5)
Interleaver Length	10^6 bits

iterative decoding. The information bits are firstly encoded by a convolution code. Here a simple half-rate Recursive Systematic Convolutional (RSC) code was used. Then, the interleaved bits are fed into the LDC encoder of Figure 2.17. The LDC block also incorporates bit-to-symbol mapping using Gray labelling. The dispersion operation maps each symbol vector \mathbf{K} containing Q symbols to the space-time transmission matrix \mathbf{S} defined in Equation (2.12). At the receiver, extrinsic information is exchanged between the SISO ML/MMSE and RSC detectors. More details about how the extrinsic information is calculated can be found in [98] and the references within. This simple SCC scheme employing iterative decoders has the advantage of exploring both the spatial diversity provided by the LDCs and the temporal diversity offered by the RSC code. To show the exchange of extrinsic information, the right hand side of Point B seen in Figure 2.17 is considered as the *inner* code and the left side is the *outer* code.

The EXIT chart of the half-rate RSC-coded LDC(2224) scheme of Figure 2.17 having a diversity order of $D = 4$ and using an ML decoder is shown in Figure 2.18. In this thesis, I_A denotes the *a-priori* information available for the *inner* code, which is provided by the extrinsic output of the *outer* code \bar{I}_A . By contrast, I_E denotes the extrinsic output of the *inner* code, which also con-

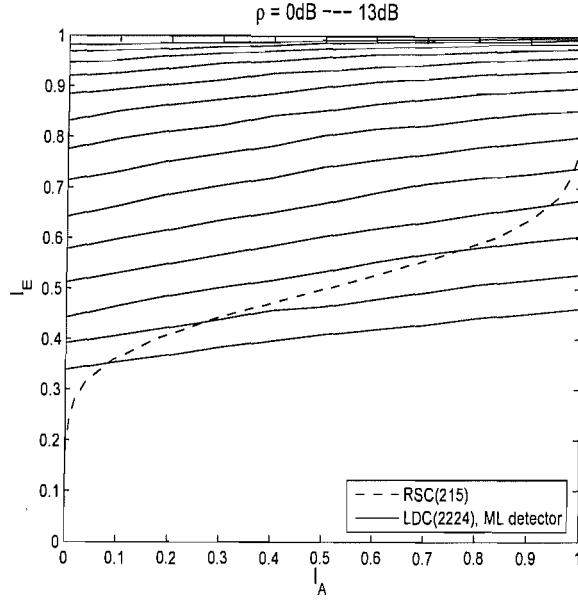


Figure 2.18: EXIT chart of the RSC-coded LDC(2224) scheme of Figure 2.17 having a diversity order of $D=4$, when using the system parameters outlined in Table 2.4 and employing an **ML detector**.

tributes to the *a-priori* input for the *outer* code \bar{I}_E . Observe that the intersection points of the *inner* and *outer* EXIT curves approach $I_A = 1.0$, as the SNR increases, where an infinitesimally low BER is expected.

Figure 2.19 shows the EXIT chart of the RSC(215)-coded LDC(2224) scheme having a diversity order of $D = 4$ and using an MMSE detector. Note that the area under the EXIT curves using the MMSE detector is smaller than that of its ML detection counterpart of Figure 2.18 for any given SNR.

The so-called 'area property' [68] [99] of EXIT charts may be formulated by stating that the area under the *outer* RSC code's EXIT curve is approximately equal to its code rate R_{out} . Thus, if we assume that the area under the EXIT curve of an *outer* code can be perfectly matched to the area under the *inner* code's EXIT curve at any SNR ρ , then it is possible to approximate the **maximum achievable rate** of a serial concatenated scheme by evaluating the area under the EXIT curves, given the rate of the *inner* block R_{in} , which is expressed as:

$$C(\rho) = \log_2(L) \cdot R_{in} \cdot R_{out}, \quad (2.47)$$

where R_{out} is approximated by the area under the *inner* code's EXIT curve and L -PSK or L -QAM modulation is used.

Using Equation (2.47), we are able to plot the maximum achievable rates of the proposed serial concatenated RSC-coded LDC(2224) scheme using both ML and MMSE detectors in Figure 2.20.

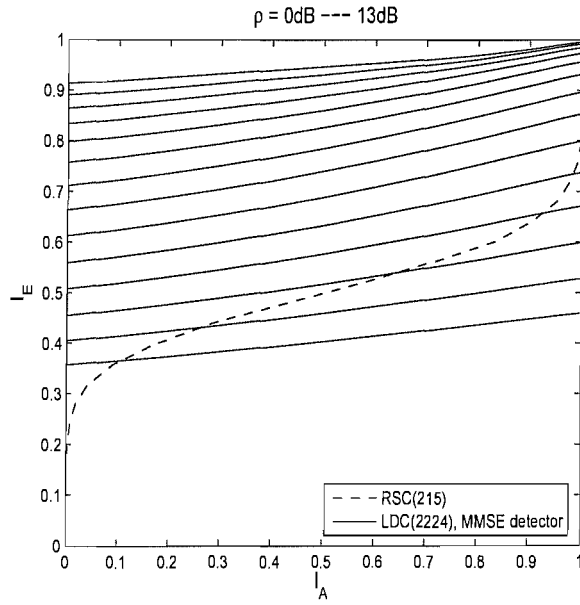


Figure 2.19: EXIT chart of the RSC-coded LDC(2224) scheme of Figure 2.17 having a diversity order of $D=4$, when using the system parameters outlined in Table 2.4 and employing an **MMSE detector**.

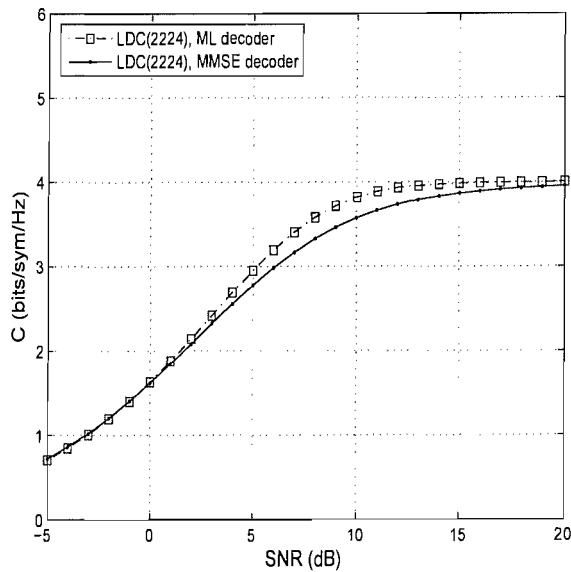


Figure 2.20: Maximum achievable rates comparison of RSC-coded LDC(2224) scheme of Figure 2.17, when using the system parameters outlined in Table 2.4 and employing ML/MMSE detectors.

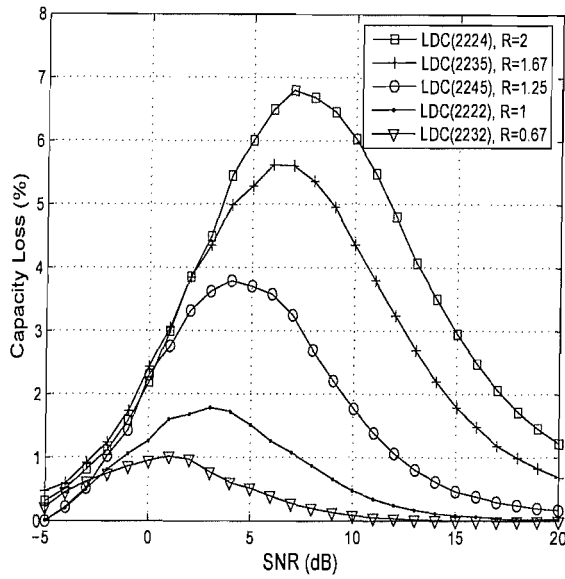


Figure 2.21: MMSE detector's maximum achievable rate loss for a group of RSC-coded LDC schemes of Figure 2.17, when using the system parameters outlined in Table 2.4.

Observe that the system employing ML detection achieved a higher rate across the entire SNR region, since more decoding complexity was invested. Note that the achieved rate loss associated with employing an MMSE detector compared to the ML detector is not constant. The maximum rate loss was recorded at about $\rho = 7$ dB. It is interesting to compare LDC(2224) scheme's maximum achievable rates employing an ML detector to its DCMC capacity curve plotted in Figure 2.7, which appear to be identical. This observation implies that it is feasible to achieving the MIMO channel's capacity using a SCC scheme under the assumption of using a variable-rate *outer* code.

In order to illustrate a little further, Figure 2.21 quantifies the MMSE decoder's maximum achievable rate loss compared to that of the ML detector using the above-mentioned EXIT-aided method as a function of the SNR. For the rate-two LDC(2224) scheme, the peak of the bell-shaped capacity loss curve appears at $\rho = 7$ dB, where approximately 6.8% throughput is lost. When lower rate LDCs were employed, the rate loss was decreased and the peak of the curves gradually shifted to lower SNRs, as seen in Figure 2.21.

Ideally, in order to achieve an infinitesimally low BER, the *inner* and *outer* EXIT curves should only intersect at the $(I_A, I_E) = (1.0, 1.0)$ point. If this condition is satisfied, then a so-called convergence tunnel [57] appears in the EXIT chart. Even if there is no open tunnel in the EXIT chart leading to the $(1.0, 1.0)$ point, but the two curves intersect at a point close to $I_A = 1.0$, then a sufficiently low BER may still be achievable. Observe in Figure 2.19 that the intersection of *inner* and *outer* EXIT curves takes place before reaching the $I_A = 1.0$ point, unless the SNR is sufficiently high.

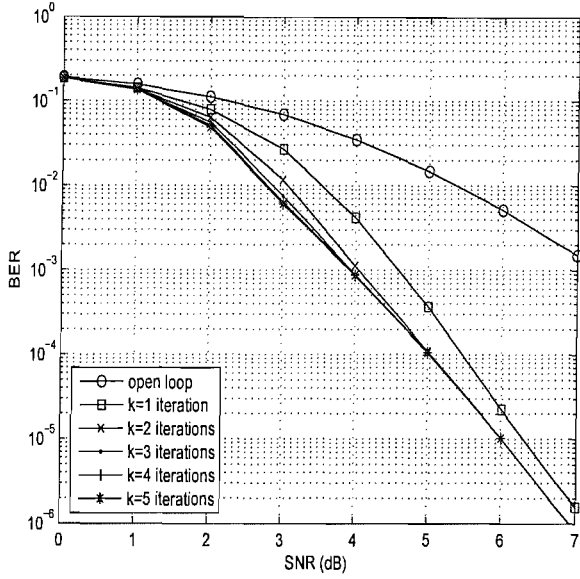


Figure 2.22: BER performance of the RSC-coded LDC(2224) scheme of Figure 2.17 having a diversity order of $D=4$, when using the system parameters outlined in Table 2.4 and employing an MMSE detector.

In Figure 2.22, we characterize the BER performance of the RSC(215)-coded LDC(2224) having a diversity order of $D=4$, while using QPSK modulation in conjunction with an MMSE decoder. Since the slope of the EXIT curves shown in Figure 2.19 is relatively low, the SCC scheme of Figure 2.17 reaches the best attainable performance after $k = 4$ iterations. The BER illustrated in Figure 2.22 gradually decreases upon increasing the SNRs, which corresponds to the fact that the *inner* and *outer* EXIT curves' intersection point shifts to $(1.0, 1.0)$ point on the EXIT chart with the SNRs, as seen in Figure 2.19.

Figure 2.23 compares the EXIT curves of RSC(215)-coded LDC schemes of Figure 2.17 having $M = 2$, $N = 2$, $T = 2$ and $Q = 1, 2, 3, 4$, when employing QPSK modulation in conjunction with an MMSE decoder. Observe that when Q increases, the area under the EXIT chart decreases. It is also interesting to observe in Figure 2.23 that the curves become more and more horizontal, when Q is decreased. In fact, when we have $Q = 1$, the EXIT curve becomes a horizontal line. Recall that Gray mapping is employed for the information symbols, hence for the case of $Q = 1$, there is no extrinsic information induced improvement, as the *a-priori* information increases. However, when we have $Q > 1$, each transmitted symbol is subjected to independent fading, and hence Gray mapping may no longer guarantee the largest Euclidean distance in a $2Q$ -dimensional space. Therefore, the resultant EXIT curves' slope is expected to increase, as Q increases.

Despite its good BER performance, this simple convolutional coded LDC scheme of Figure 2.17 has a deficiency. More explicitly, the flatness of the EXIT curves recorded in Figure 2.23

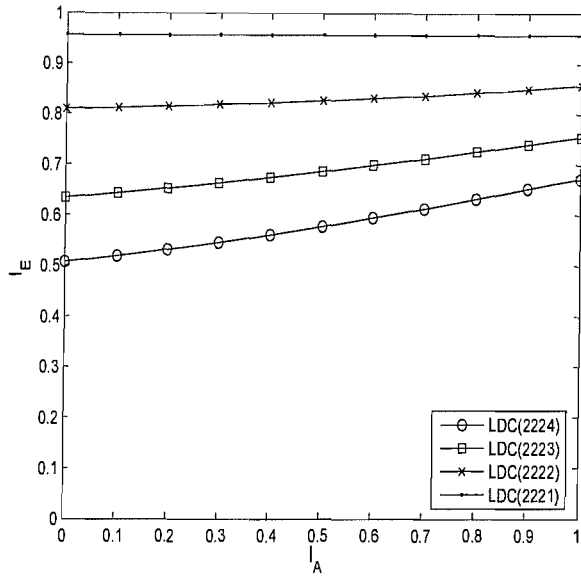


Figure 2.23: EXIT chart comparison for the RSC-coded LDC(222Q) schemes of Figure 2.17 at $\rho = 3\text{dB}$, when using the system parameters outlined in Table 2.4 and employing an MMSE detector.

prevents the intersection from reaching the $(I_A, I_E) = (1.0, 1.0)$ point. Therefore, an infinitesimally low BER can only be achieved at high SNRs. Driven by the desire of designing iterative decoding aided LDCs having an infinitesimally low BER, the family of convolutional-coded precoder-aided LDCs is proposed in the next section.

2.4.2 Analyzing Iteratively-Detected Precoded LDCs

When the channel is classified as non-recursive, such as the system of Figure 2.17, implying that it has a finite-duration CIR, then the achievable iteration gain of the receiver remains limited, since there is a limited interleaver gain [100]. However, the channel can be rendered to appear recursive to the receiver, thus resulting in an infinite impulsive response and hence resulting in a useful interleaver gain by invoking a recursive *inner* encoder [56], namely a unity-rate precoder. Therefore, this section investigates the characteristics and performance of a RSC-coded and precoder-aided LDC system portrayed in Figure 2.24.

Compared to the non-precoded scheme of Figure 2.17, a rate-1 precoder is placed between the convolutional encoding block and the LDC encoder, complemented by a second interleaver. The resultant schematic constitutes a three-stage system, where the extrinsic information is passed through the three decoder blocks according to a pre-defined activation order. Block-1 of Figure 2.24, namely the MMSE/ML decoder, receives its input information from the MIMO channel and its feedback

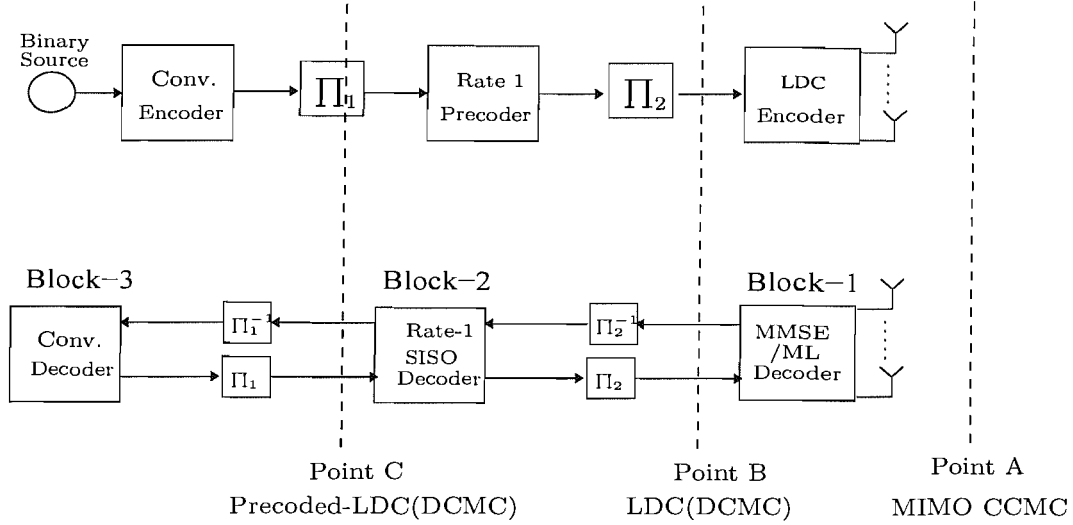


Figure 2.24: Schematic of a three-stage RSC-coded and precoder-aided LDCs using iterative decoding.

information from the precoder's decoder. The intermediate Block-2 of Figure 2.24 benefits from the information provided by both the convolutional decoder and the LDC decoder. Its two outputs are forward to the surrounding blocks at its both sides, respectively. An extrinsic information exchange cycle between Block-1 and Block-2 of Figure 2.24 is defined as an *inner* iteration. The third decoding block, namely the convolutional decoder exchanges information with the precoder. Hence, a single associated extrinsic information exchange cycle between the precoder's decoder and the convolutional decoder is referred to as an *outer* iteration.

Let us briefly discuss the features of the system structure of Figure 2.24. For example, if the system is split into two constituent parts at Point B of Figure 2.24, Block-1 has the same EXIT characteristics as the two-stage system of Figure 2.17, where the $(I_A, I_E) = (1.0, 1.0)$ point cannot be reached at all, unless the associated SNR is sufficiently high. However, if the system is split at Point C of Figure 2.24, we will demonstrate at a later stage that the *inner* Precoded Linear Dispersion Codes (PLDCs) become capable of reaching the $(I_A, I_E) = (1.0, 1.0)$ point. Observe furthermore in Figure 2.24 that the equivalent channel at Point C is recursive i.e. has an Infinite Impulse Response (IIR) as a benefit of using the precoder, whereas the equivalent channel at Point B is non-recursive.

It was argued for example in [101] that the activation order of the decoding blocks of a three-stage system substantially affects both the achievable performance as well as the detection complexity imposed at the receiver. The decoding activation order of the proposed three-stage system of Figure 2.24 is set to $[(\text{Block-1}, \text{Block-2})^{j+1}, \text{Block-3}]^{k+1}$, where j and k are the number of *inner* and *outer* iterations, respectively. More explicitly, $(j + 1)$ iterations are invoked between Block-1

Table 2.5: System parameters for the three-stage RSC-coded and precoder-aided LDC system of Figure 2.24.

Modulation	QPSK
Mapping	Gray mapping
Regular Outer Channel Code	RSC(2,1,5)
Interleaver Length	10^6 bits
Detector	MMSE
Precoder Rate	1

and Block-2 of Figure 2.24, followed by exchanging their joint extrinsic information with Block-3 ($k + 1$) times. We propose to answer the question of how many *inner* iterations per *outer* iteration are necessary, from the capacity approaching perspective. Ideally, a small value of j is desirable in the interest of minimizing the overall decoding complexity. In order to carry out a comparison between the non-precoded scheme of Figure 2.17 and the precoded schemes of Figure 2.24, in our forthcoming investigations a half-rate RSC(215) code is employed as the *outer* code and the length of the interleaver is set to 10^6 bits.

Figure 2.25 plots the EXIT chart of the three-stage RSC(215)-coded PLDC(2224) scheme of Figure 2.24, when using $j = 0$ *inner* iterations and the associated decoding trajectory was recorded at $\rho = 5$ dB. Observe that the employment of the precoder facilitates the converge of all the *inner* EXIT curves to the $(I_A, I_E) = (1.0, 1.0)$ point, since the precoder is capable of gleaning extrinsic information from all the bits within a frame. By contrast, for the non-precoded scheme of Figure 2.17, the extrinsic information can only be extracted from the bits within a single information symbol. The decoding trajectory shown at $\rho = 5$ dB required $k = 6$ *outer* iterations to achieve an infinitesimally low BER.

When $j = 1$ *inner* iteration is employed in the three-stage RSC(215)-coded PLDC (2224) scheme of Figure 2.24, the corresponding EXIT chart is plotted in Figure 2.26. Observe that the area under the EXIT curves is higher than that of the system employing $j = 0$ *inner* iterations, as characterized previously in Figure 2.25, which implies having potentially increased maximum achievable rates. Note that the increased-area open EXIT tunnel between the *inner* and *outer* code's EXIT curves benefits the decoding trajectory recorded at $\rho = 5$ dB, since only $k = 4$ *outer* iterations are necessary to converge to the $(I_A, I_E) = (1.0, 1.0)$ point.

Figure 2.27 quantifies the maximum achievable rates for the three-stage memory-one precoder-aided LDC (PLDC) schemes of Figure 2.24 having different rates in conjunction with different

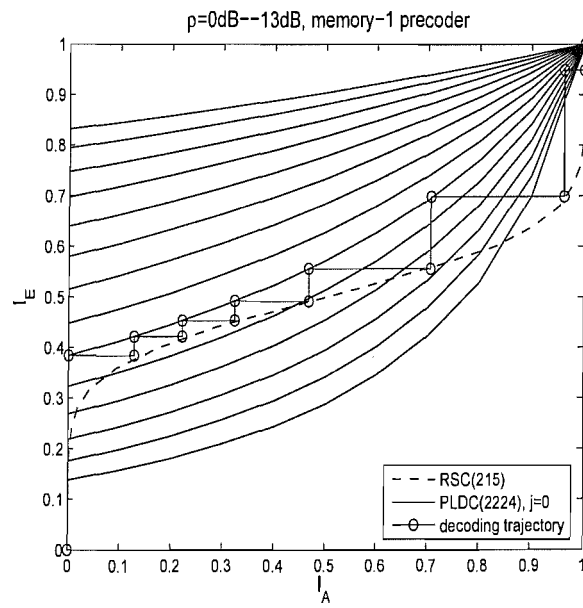


Figure 2.25: EXIT chart of the RSC-coded memory-one precoder-aided LDC(2224) scheme of Figure 2.24 employing $j = 0$ inner iterations, when using the system parameters outlined in Table 2.5 and the decoding trajectory was recorded at $\rho = 5\text{dB}$.

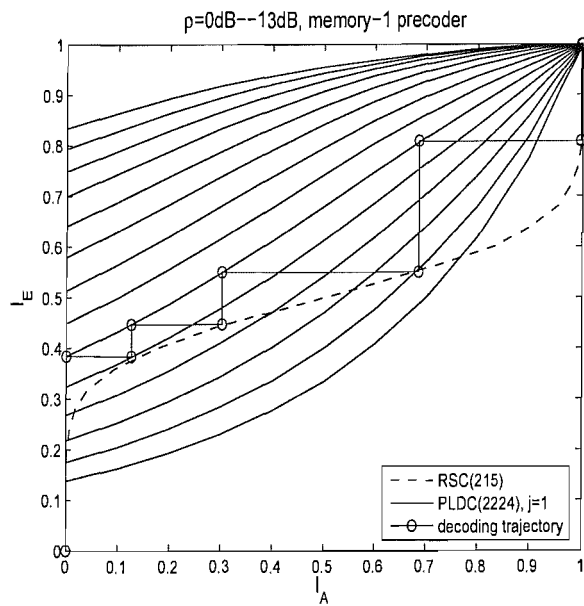


Figure 2.26: EXIT chart of the RSC-coded memory-one precoder-aided LDC(2224) scheme of Figure 2.24 employing $j = 1$ inner iterations, when using the system parameters outlined in Table 2.5 and the decoding trajectory was recorded at $\rho = 5\text{dB}$.

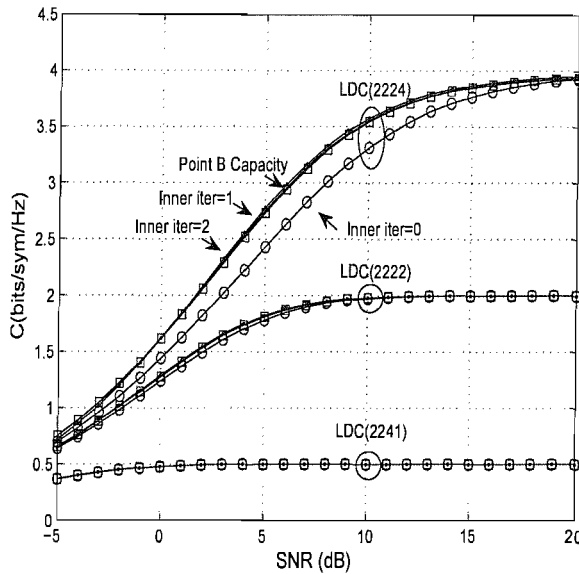


Figure 2.27: Comparison of the maximum achievable rates recorded at Point C of Figure 2.24 for the various PLDC schemes having $j = 0, 1, 2$ inner iterations, when using the system parameters outlined in Table 2.5.

number of *inner* iterations j . For each set of comparisons, the LDC's capacity measured at Point B of Figure 2.24 is plotted as the benchmark. For the rate $R_{2224} = 2$ scheme, a substantial maximum achievable rate gap is observed between the LDC scheme measured at Point B of Figure 2.24 and the corresponding PLDC scheme recorded at Point C of Figure 2.24, when the number of *inner* iterations is $j = 0$. However, when we have $j = 1$, the aforementioned rate loss is eliminated and a further increase of j has only a modest additional rate improvement. In fact, the maximum achievable rate loss is less than 1%, when we have $j = 1$. For the PLDC(2222) scheme having a rate of $R_{2222} = 1$, we observe in Figure 2.27 that although the aforementioned maximum achievable rate loss compared to the associated LDC's achievable capacity is still present, when employing $j = 0$ *inner* iterations, the associated discrepancy is narrower than that seen for the PLDC(2224) scheme. Observe in Figure 2.27 for the PLDC(2241) scheme having a rate of $R_{2241} = 0.25$ that there is no maximum achievable rate loss even in the absence of *inner* iterations.

The above observations are related to the EXIT characteristics of the LDC's MMSE decoding block, which is shown in Figure 2.23. When a single symbol is transmitted, i.e. we have $Q = 1$, the EXIT curve is a horizontal line. Therefore, regardless of the number of *inner* iteration employed, Block-1 of Figure 2.24 always outputs the identical extrinsic information. When Q is increased, the EXIT curves of Block-1 seen in Figure 2.23 become more steep, therefore higher extrinsic information can be obtained upon increasing the *a-priori* information by using a higher number of *inner* iterations. Therefore, the resultant maximum achievable rate observed in Figure 2.27 at Point

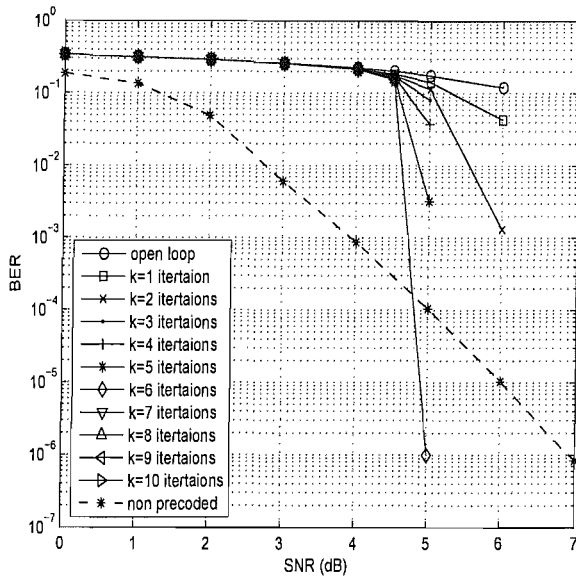


Figure 2.28: BER performance of the three-stage RSC-coded memory-one precoder-aided LDC(2224) scheme of Figure 2.24 employing $j = 0$ inner iterations, when using the system parameters outlined in Table 2.5.

C of Figure 2.24 has an increasing gap with respect to the one observed at Point B, when a higher number of symbols Q is transmitted by each LDC block.

Figure 2.28 characterizes the achievable BER performance of the three-stage RSC(215)-coded memory-1 precoder-aided LDC(2224) scheme using $j = 0$ *inner* iteration. The EXIT chart of Figure 2.25 predicted that an open convergence tunnel will be formed at $\rho = 5$ dB, which is evidenced by the BER performance of Figure 2.28, where $k = 6$ *outer* iterations were required to achieve an infinitesimally low BER. The comparison of Figures 2.22 and 2.28 reveals that the precoded scheme is capable of achieving a lower BER in the high-SNR region, compared to its non-precoded counterpart. When employing $j = 1$ *inner* iterations, the corresponding BER performance is plotted in Figure 2.29. This scheme reached the so-called turbo-cliff associated with an infinitesimally low BER at about $\rho = 4.2$ dB using $k = 10$ iterations, where a 0.8dB SNR gain is achieved compared to the scheme employing $j = 0$ *inner* iteration. Again, Figures 2.28 and 2.29 proves that by rendering the equivalent channel response to be recursive using a precoder [56], the achievable BER performance can be improved.

Another advantage of employing a precoder is that by changing the generator polynomial and/or the precoder's memory size, it is possible to shape the EXIT curves without changing the area below them. The schematic of the unity-rate precoder having different memories is portrayed in Figure 2.30. The generator polynomial characterized in octal form determines the portion of the connections in Figure 2.30.

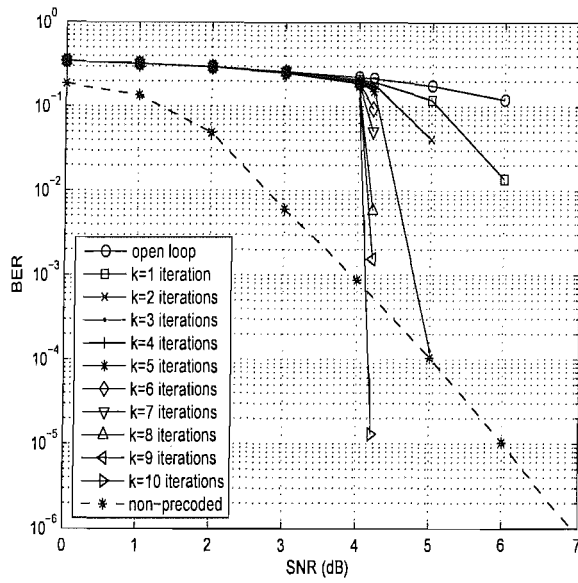


Figure 2.29: BER performance of the three-stage RSC-coded memory-one precoder-aided LDC(2224) scheme of Figure 2.24 employing $j = 1$ inner iterations, when using the system parameters outlined in Table 2.5.

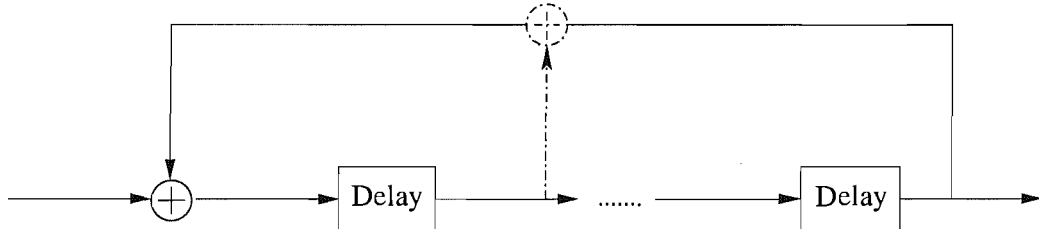


Figure 2.30: Schematic of the unity-rate precoder having different memories.

Figure 2.31 portrays the EXIT curves of the three-stage unity-rate precoder-aided LDC(2221) scheme having various precoder memories and polynomials at $\rho = -1$ dB. Observe that the area under the EXIT curve is constant to 0.79 for all the curves, although their shapes are different. Note that the memory-one precoder has the highest I_E starting point at the left on the ordinate axis of Figure 2.31, when we have $I_A = 0$. By contrast, higher-memory precoded systems have an EXIT curve starting at a significantly lower I_E value, although they are capable of benefiting from the extrinsic information more substantially in the middle range of I_A , as seen in Figure 2.31. Therefore, for the precoded LDC scheme of Figure 2.24, employing the simplest memory-1 precoder of Figure 2.30 is sufficient to attain the lowest BER [70].

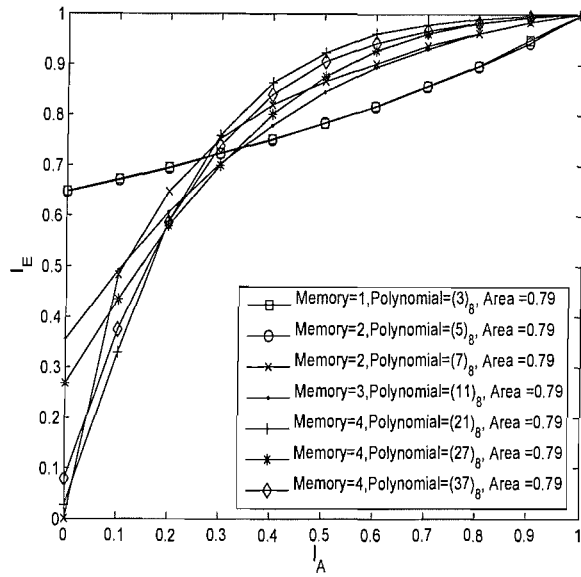


Figure 2.31: EXIT chart comparison of the three-stage RSC-coded PLDC(2221) scheme of Figure 2.24 having different precoder memories and polynomials of Figure 2.30 at $\rho = -1\text{dB}$, when using the system parameters outlined in Table 2.5.

2.4.3 Summary

This section summarizes the coding advantage of the proposed serial concatenated schemes operating with/without the memory-1 precoders, as portrayed in Figures 2.17 and 2.24, respectively. For the half-rate RSC(215)-coded schemes of Figures 2.17 and 2.24, the LDC(2224) scheme using QPSK modulation in conjunction with an MMSE detector was employed. Therefore, the resultant effective throughput is 1 (bits/sym/Hz). The uncoded LDC(2224) scheme using BPSK modulation having the identical throughput was used as a benchmark. The coding gain was recorded between the uncoded scheme and the RSC(215)-coded LDC scheme at both $\text{BER} = 10^{-4}$ and 10^{-5} from Figures 2.22, 2.28 and 2.29.

Table 2.6 summarizes the coding gains of the two-stage non-precoded system of Figure 2.17 and the three-stage precoded LDC(2224) scheme of Figure 2.24 as well as the number of *inner* and *outer* iterations required to achieve the target BER. At BER of 10^{-4} , an increased coding gain is observed, when a higher decoding complexity was invested in terms of employing precoders and increasing the number of *inner* iterations. Note that the advantage of employing a memory-1 precoder having a single *inner* iteration over the non-precoded scheme is 0.8dB. By contrast, the precoding advantage increased to 1.7dB, when the coding gain was quantified at BER of 10^{-5} . In conclusion, the RSC-coded precoder-aided LDC scheme of Figure 2.24 outperforms the non-precoded scheme of Figure 2.17 in the low-BER region.

Table 2.6: Coding gains of the RSC(215)-coded LDC(2224) scheme with/without a memory-1 precoder having an effective throughput of 1 (bits/sym/Hz).

	Number of <i>inner</i> iterations (j)	Number of <i>outer</i> iterations (k)	at BER of 10^{-4}	at BER of 10^{-5}
Two-stage system of Figure 2.17	0	5	9.3dB	11.8dB
Three-stage system of Figure 2.24	0	10	9.5dB	12.9dB
Three-stage system of Figure 2.24	1	10	10.1dB	13.5dB

2.5 EXIT Chart Based Design of IrRegular Precoded LDCs

The EXIT chart analysis of the SCCs of Section 2.4 have demonstrated that the *inner* and *outer* codes' EXIT curves determine the achievable BER performance, given a specific SNR. Naturally, it is desirable to precisely control both the shape of the EXIT curves as well as the area below them, which can be achieved by the introduction of the irregular design principle detailed in this section.

More explicitly, when irregularity is imposed on the *outer* code of a SCC, the authors of [60] have shown that the outer EXIT curve can be designed to closely match to that of the *inner* code. Furthermore, in this section, we propose novel IrRegular Precoded Linear Dispersion Codes (IR-PLDCs) as the *inner* code of a SCC scheme, so that shaping the *inner* code's EXIT curve becomes feasible. The throughput of the SCC system is determined by the rate R_{out} of the *outer* channel code, the rate R_{in} of the IR-PLDC and the modulation scheme employed. Since unity-rate precoders are used, R_{in} is purely determined by the rate of the LDCs employed. The SCC scheme employing the IR-PLDC as the *inner* code is designed under the following assumptions:

- QPSK modulation is employed by all the component codes of the proposed IR-PLDC scheme, although employing different modulation schemes is equally feasible;
- Rate-1 precoders are employed by all the component codes of the IR-PLDC, since lower-rate precoders introduce a capacity loss;
- The receiver has the knowledge of the DCMs as well as the weighting coefficients and knows when to activate a specific component code.

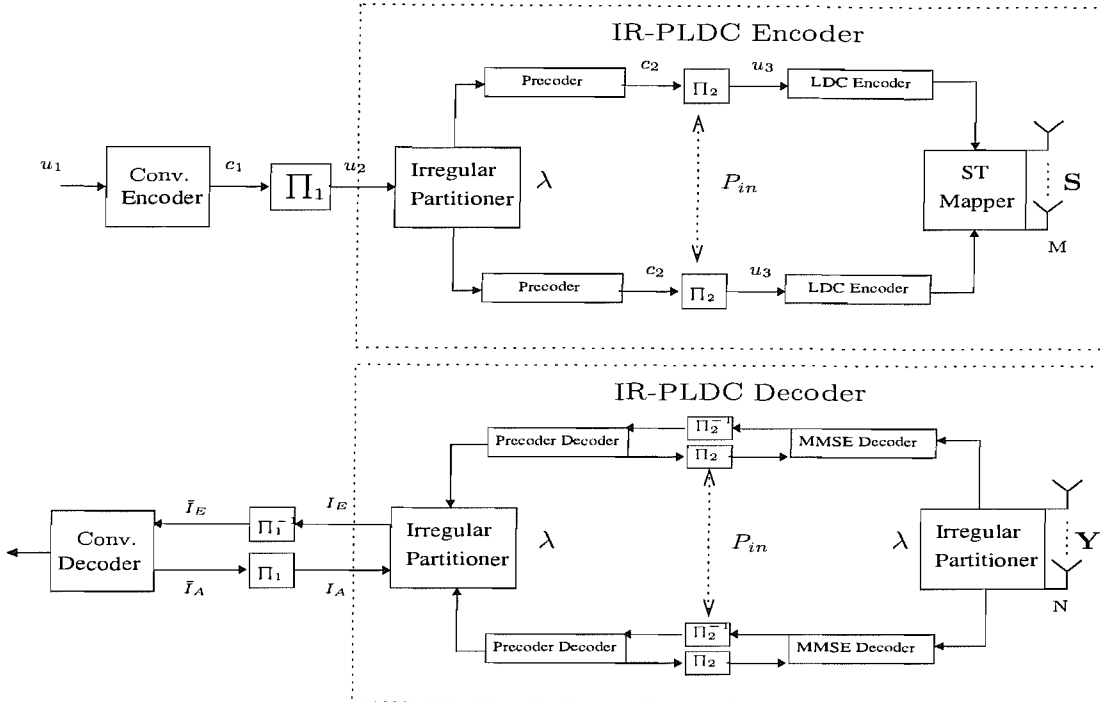


Figure 2.32: Schematic of the serial concatenated RSC-coded IR-PLDC system using iterative decoding.

2.5.1 RSC-coded IR-PLDC Scheme

Figure 2.32 portrays the system model of the proposed serially concatenated RSC-coded IR-PLDC scheme. At the transmitter, a frame of information bits u_1 is encoded by a simple RSC encoder. Then the encoded bits c_1 are interleaved by a random interleaver, yielding the *outer* encoded bits u_2 . Then the 'irregular partitioner' of Figure 2.32 feeds the appropriately selected fraction of u_2 into the various PLDC component codes according to a predefined weighting coefficient vector λ . The *inner* IR-PLDC contains P_{in} number of component codes. The unity-rate precoders may exhibit different EXIT characteristics by employing different memories and generator polynomials, as seen in Figure 2.30. However, for the proposed system of Figure 2.32, memory-1 precoders are employed for all the PLDC components. More explicitly, within each PLDC encoder, the resultant precoded bits c_2 are interleaved by a second interleaver, yielding the interleaved bits u_3 , which are fed to the bit-to-symbol mapper inside the LDC block of Figure 2.32. After QPSK modulation and space-time dispersion, the space-time transmission matrix \mathbf{S} of Equation (2.12) is mapped to the $(M \times T)$ spatial and temporal dimensions by the 'ST mapper' and transmitted over the uncorrelated Rayleigh fading channel contaminated by AWGN at each receive antenna.

At the receiver of Figure 2.32, again the 'irregular partitioner' determines the portion of the received signal matrices \mathbf{Y} and the *a-priori* information to each PLDC decoders, according to the weighting coefficient vector λ . Then, an iterative decoding structure is employed, where extrinsic

information is exchanged between three SISO modules, namely the MMSE detector, the precoder and the *outer* RSC decoder in a number of consecutive iterations. To be specific, in Figure 2.32, I_A denotes the *a-priori* information for the IR-PLDC represented in terms of Log-Likelihood Ratio (LLR), where I_E denotes the extrinsic information output of the *inner* code also expressed in terms of LLR. We use \bar{I}_A and \bar{I}_E to represent the *a-priori* input and extrinsic output of the *outer* RSC decoder, respectively. Note that the intermediate rate-1 precoder processes two *a-priori* inputs arriving from the MMSE detector and the *outer* decoder and generates two extrinsic outputs as well. Since the activation of different PLDC components is implemented by employing different dispersion matrices, the hardware cost is modest low.

In our forthcoming EXIT chart analysis, the precoders' decoders and the MMSE decoders are considered as a single *inner* decoding block, namely the IR-PLDC's decoder of Figure 2.32. The advantage of this representation is that the IR-PLDC's extrinsic information output I_E is only determined by the received signal matrix \mathbf{Y} and the *a-priori* input I_A , but remains unaffected by the extrinsic information exchange between the precoder's decoder and the MMSE detector. Thus, the three-stage system can be projected into a two-stage system and hence the conventional two-dimensional EXIT chart analysis [57] [68] is applicable.

Following the approach of [102], we now carry out the EXIT chart analysis of the proposed RSC-coded IR-PLDC system. The *inner* IR-PLDC block has an *a-priori* input given by I_A and the channel output \mathbf{Y} of Figure 2.32. Thus the corresponding EXIT functions are:

$$I_E = \Gamma_{u_2}[I_A, \rho], \quad (2.48)$$

and for the *outer* RSC code the EXIT function is:

$$\bar{I}_E = \Gamma_{c_1}[\bar{I}_A]. \quad (2.49)$$

According to the area properties [67] of EXIT charts introduced in Section 2.4.1, the area under the EXIT curve of an *outer* code is approximately equal to $(1 - R_{out})$. More explicitly, we have

$$R_{out} \approx 1 - \int_0^1 \Gamma_{c_1}(i) di, \quad (2.50)$$

suggesting that a higher rate code has a lower area under its EXIT curve. This observation is the rationale behind the design of IRCCs proposed in [60], where the aim is to minimize the area of the open EXIT tunnel, because this facilitates a near-capacity operation. However, we will demonstrate in Section 2.5.1.1 that in contrast to IRCCs, the area under the *inner* IR-PLDC code's EXIT curve does not have a linear relationship with its code rate. This property results in a different design procedure and objective of the IR-PLDCs in comparison to the IRCCs.

2.5.1.1 Generating Component Codes for IR-PLDCs

The employment of irregular codes was proposed by Tüchler and Hagenauer [60] [69], where IR-CCs were used as an *outer* channel code. IRCCs are constituted by a family of convolutional codes having different code rates. They were specifically designed with the aid of EXIT charts [58], for the sake of improving the convergence behaviour of iteratively decoded systems. In [60], the authors have proved that the aggregate EXIT function of an irregular code containing P component codes can be obtained from the linear combination of that of its component codes, under the assumption that the PDF of the LLRs is symmetric and continuous. More explicitly, the EXIT function of an irregular code is given by

$$\Gamma_{ir} = \sum_{i=1}^P \lambda_i \Gamma_i(I_{input}), \quad (2.51)$$

where λ_i represents the weighting coefficients of the i -th component having transfer function Γ_i .

Inspired by the above-mentioned beneficial properties of an irregular system, in this section, we propose an IR-PLDC scheme for employment as our *inner* rather than *outer* code for the SCC system. The EXIT function of the proposed IR-PLDC scheme is constituted by the superimposed combination of its component codes' EXIT functions determined by Equation (2.51). Clearly, each PLDC component's EXIT curve as well as the corresponding weighting coefficient vector λ play a crucial role in shaping the resultant aggregate EXIT function. Each component PLDC of the proposed IR-PLDC scheme of Figure 2.32 is constituted by an independent LDC combined with a unity-rate precoder. Different PLDC rates can be obtained by varying the number of transmitted symbols Q and the number of time slots T used per space-time block. Naturally, maintaining low values of Q and T is desirable for the sake of maintaining a low encoding/decoding complexity.

For example, in order to design an *inner* IR-PLDC coding scheme containing $P_{in} = 11$ components for a MIMO configuration having $M = 2$ transmit and $N = 2$ receive antennas, we commence by setting $T = 2$. Hence, all the components have the potential of achieving the maximum diversity order of $D = 4$ according to Theorem 3. By setting $Q = 1$, we are able to optimize the DCMC capacity of LDC(2221) using Equation (2.24). Consequently, more components can be obtained by gradually increasing the Q value to increase the rate. The limit of $Q \leq MT$ is imposed for the sake of maintaining a low complexity, although employing a higher value of Q is equally feasible. Hence, by increasing the value of T and maximizing the corresponding DCMC capacity of each LDC, we can generate a set of beneficial LDCs. Again, low Q and T values are desirable for the sake of maintaining a low complexity. The resultant $P_{in} = 11$ component codes designed for our IR-PLDC scheme are listed in Table 2.7.

Hence, for a MIMO system associated with M transmit and N receive antennas, the univer-

Table 2.7: The $P_{in} = 11$ number of LDC component codes of the IR-PLDC scheme of Figure 2.32 generated for a MIMO system having $M = 2$ and $N = 2$ antennas and employing QPSK modulation and an MMSE detector, where the complexity is quantified in terms of the number of addition and multiplication operations required to calculate a single LLR value in the logarithmic domain.

Index	M	N	T	Q	R_{LDC}	Inner Iteration	Complexity
0	2	2	2	1	0.5	0	1571
1	\vdots	\vdots	\vdots	2	1	1	4086
2	\vdots	\vdots	\vdots	3	1.5	1	5030
3	\vdots	\vdots	\vdots	4	2	1	5974
4	\vdots	\vdots	3	1	0.33	0	3285
5	\vdots	\vdots	\vdots	2	0.67	1	8562
6	\vdots	\vdots	\vdots	4	1.33	1	12546
7	\vdots	\vdots	\vdots	5	1.67	1	14538
8	\vdots	\vdots	4	1	0.25	0	5639
9	\vdots	\vdots	\vdots	3	0.75	1	18126
10	\vdots	\vdots	\vdots	5	1.25	1	24974

sal algorithm of generating P_{in} component codes for an IR-PLDC scheme can be formulated as follows:

- Step 1. Set the number of time slots to $T = M$ in order to ensure that all the resultant component LDCs have the same maximum achievable diversity order of $N \cdot \min(M, T)$, as argued in Theorem 3;
- Step 2. Set $Q = 1$ and find the specific LDCs by searching through the entire set of legitimate codes, which maximize the DCMC capacity of Equation (2.24);
- Step 3. Set $Q := Q + 1$ for the sake of increasing the attainable throughput and repeat the above optimization procedure using Equation (2.24), until the maximum number of transmitted symbols reaches $Q = MT$;
- Step 4. If the LDC having a rate of $R_{LDC} = \frac{Q}{T}$ existed, discard the current code having the same rate but a larger value of Q and T , for the sake of minimizing the complexity according to Corollary 1;
- Step 5. If the number of component codes found is less than P_{in} , then set $T := T + 1$ and

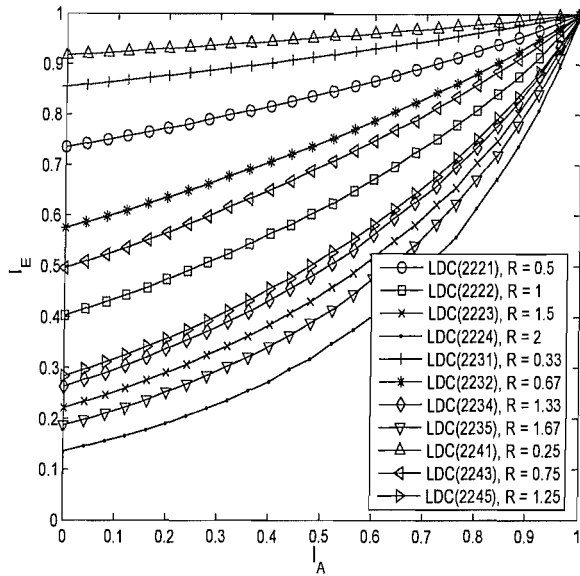


Figure 2.33: EXIT chart of the $P_{in} = 11$ PLDCs of Table 2.7 at $\rho = 0\text{dB}$ using memory one precoders, which are used as component codes for the proposed IR-PLDC scheme of Figure 2.32.

proceed to Step 2. Otherwise, terminate the search process.

Naturally, the resultant code rates may not be evenly distributed, owing to having a limited number of legitimate combinations of T and Q .

Since unity-rate precoders are employed, the rate of each PLDC block is equal to the component LDC's rate. The number of *inner* iterations listed in Table 2.7 quantifies the number of iterations carried out between the precoder and the MMSE detector, which was optimized from the capacity approaching perspective, as detailed explained in Figure 2.27. The component codes generated from the above-mentioned algorithm ensure that the resultant P_{in} number of component codes have the lowest possible complexity. More explicitly, the complexity of each PLDC component code is jointly determined by the precoder's decoding complexity, the MMSE detector's complexity and the number of *inner* iterations. In order to quantify the complexity in a unified manner, we count the number of addition and multiplication operations required to calculate a single LLR value in the logarithmic domain. Since the number of addition and multiplication operations can be quantified in terms of the so-called Add-Compare-Select (ACS) arithmetic operations, the complexity of each PLDC component is quantified by the ACS operations per LLR computation. Observe in Table 2.7 that when the value of T is fixed, the complexity is increased by increasing the value of Q . Furthermore, increasing the value of T typically resulted in a substantially increased complexity.

Figure 2.33 shows the EXIT charts of the above-mentioned $P_{in} = 11$ component PLDCs of Table 2.7 at $\rho = 0\text{dB}$ using memory one precoders, which are used as component codes for the

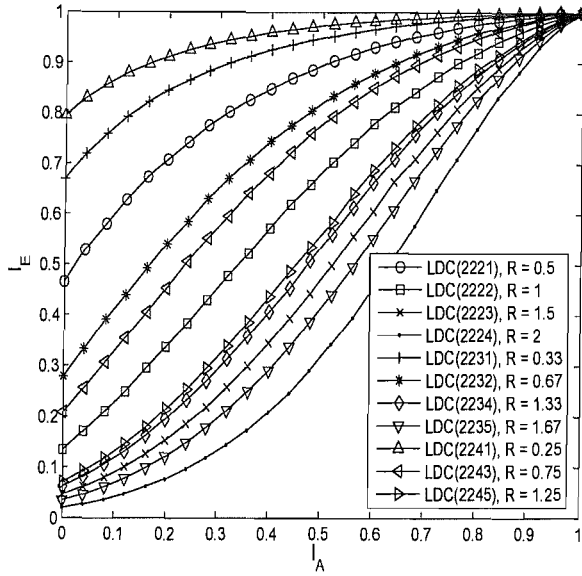


Figure 2.34: EXIT chart of the $P_{in} = 11$ PLDCs of Table 2.7 at $\rho = 0\text{dB}$ using memory **three** precoders, which are used as component codes for the proposed IR-PLDC scheme of Figure 2.32.

proposed IR-PLDC scheme of Figure 2.32. The shape of all the EXIT curves is similar, since they are all combined with the memory one precoders. Furthermore, Figure 2.34 portrays the EXIT curves of the same set of LDC component codes of Table 2.7 in conjunction with memory three precoders. Clearly, although changing the size of the precoder's memory does not affect the area under the curves, it has a substantial impact on the shape of the curves. It is worth mentioning at this stage that a sufficiently diverse set of curves is necessary for employment in a flexible IR-PLDC scheme for the sake of maximizing the achievable rates as well as minimizing the detector's complexity.

Figure 2.35 quantifies the maximum achievable rates of the *inner* IR-PLDC scheme of Figure 2.32 using the EXIT charts of the $P_{in} = 11$ memory-1 precoder-aided LDC component codes listed in Table 2.7. Recall from Section 2.4.1 that the maximum achievable rate is attained using Equation (2.47) under the assumption of having perfectly matched *inner* and *outer* EXIT curves, which results in an infinitesimally low EXIT tunnel area. Observe in Figure 2.35 that a high-rate PLDC component code is capable of attaining a high maximum achievable rate. However, this does not necessarily imply imposing a higher complexity. For example, Table 2.7 shows that the PLDC(2224) scheme imposes a substantially lower complexity than that of the PLDC(2235) arrangement, since the former scheme maintains lower T and Q values.

Let us use λ_i , $i = (1, 2, \dots, P_{in})$ represents the specific fraction of I_E conveying the corresponding extrinsic information, which are fed into the IR-PLDC encoders/decoders of Figure 2.32.

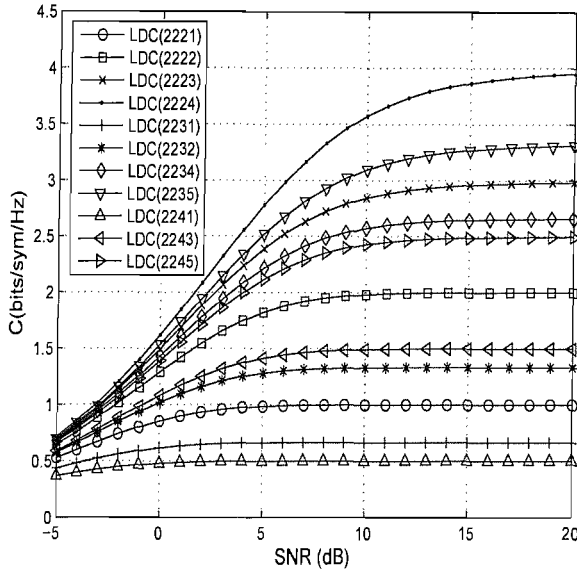


Figure 2.35: Maximum achievable rates of the $P_{in} = 11$ PLDCs listed in Table 2.7 as the component codes for the proposed IR-PLDC scheme of Figure 2.32, when employing QPSK modulation as well as an MMSE detector.

Therefore, the weighting coefficients $\lambda = [\lambda_1, \dots, \lambda_{P_{in}}]$ have to satisfy

$$\sum_{i=1}^{P_{in}} \lambda_i = 1 \quad \lambda_i \in [0, 1], \quad (2.52)$$

and the aggregate rate R_{in} of the *inner* IR-PLDC scheme is given by:

$$\frac{1}{R_{in}} = \sum_{i=1}^{P_{in}} \lambda_i \frac{1}{R_{(i, LDC)}}. \quad (2.53)$$

In order to further illustrate the flexibility provided by the IR-PLDCs using the weighting coefficient vector λ , Figure 2.36 plots the possible number of combinations against the *inner* IR-PLDC scheme's rate R_{in} given in Equation (2.53), under the assumption that we have $\lambda_i \in [0, 0.1, 0.2, \dots, 0.9, 1]$. The bell-shaped distribution of Figure 2.36 exhibits a peak at approximately $R_{in} = 0.8$. At extremely low and high rates in the vicinity of $R_{in} = 0.25$ and $R_{in} = 2$, respectively, the number of legitimate combinations gradually reduced, owing to the lack of irregularity. Again, Figure 2.36 was generated using an exhaustive search for the weighting coefficient vector λ having a step size of 0.1 under the constraint of Equation (2.52).

Figure 2.37 attempts to characterize the flexibility of the IR-PLDC scheme of Figure 2.32 in terms of the associated area under the EXIT curves at $\rho = -1$ dB by plotting a group of IR-PLDC's EXIT charts having different weighting coefficient vectors. Note that all the IR-PLDCs' EXIT curves plotted in Figure 2.37 maintain an identical aggregate rate of $R_{in} = 0.85$. Figure 2.36 has revealed that there are around 17,500 possibilities, given the weighting coefficients $\lambda_i \in [0, 0.1,$

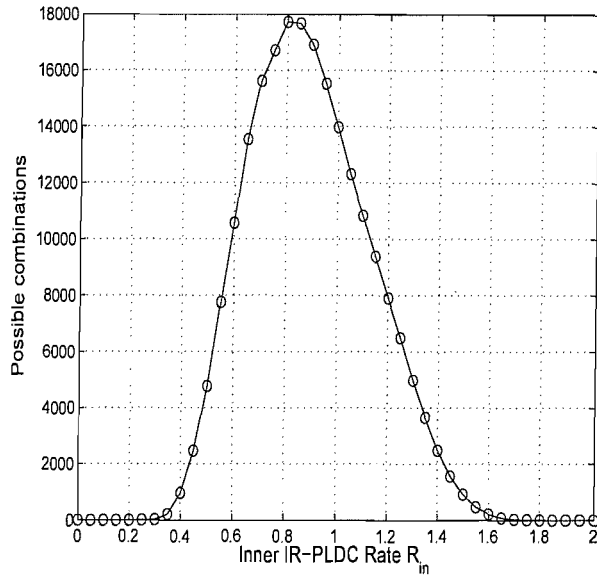


Figure 2.36: The number of possible combinations for the IR-PLDC scheme of Figure 2.32 against its rate using the $P_{in} = 11$ component codes listed in Table 2.7, where $\lambda_i \in [0, 0.1, 0.2, \dots, 1]$.

0.2, ..., 0.9, 1]. Figure 2.37 merely illustrates 12 EXIT curves out of the total 17,500 possible combinations. Observe in Figure 2.37 that the area under the curves exhibits a significant variation, which implies that the MIMO channel's capacity achieved by the IR-PLDC using different weighting coefficient vector λ is different, despite the fact that they share the same aggregate rate $R_{in} = 0.85$.

In conclusion, the *outer* code's 'area property' of Equation (2.50) reflects a linear relationship between its rate R_{out} and the area under the EXIT curve, hence the area under the EXIT curves of the IRCC scheme [60] is equal to the aggregate rate, regardless of the shape of the curves. By contrast, the proposed *inner* IR-PLDC scheme of Figure 2.32 does not obey the linear property, since the area under the EXIT curve quantifies the MIMO channel's capacity achieved using an IR-PLDC scheme and its rate is given by Equation (2.53). Our arguments are further justified by Figure 2.37.

2.5.1.2 Maximum-Rate RSC-Coded IR-PLDCs

The channel-coded IR-PLDC system of Figure 2.32 employs a simple RSC code ($P_{out} = 1$) as the *outer* code, while using the $P_{in} = 11$ component codes characterized in Table 2.7 as the *inner* code. Hence, we have a total number of $P = P_{in} + P_{out} = 12$ component codes. Each PLDC component processes a fraction of the input information according to its weighting coefficient λ_i , which has to satisfy Equation (2.52) and the resultant aggregate *inner* code rate R_{in} is given by Equation (2.53).

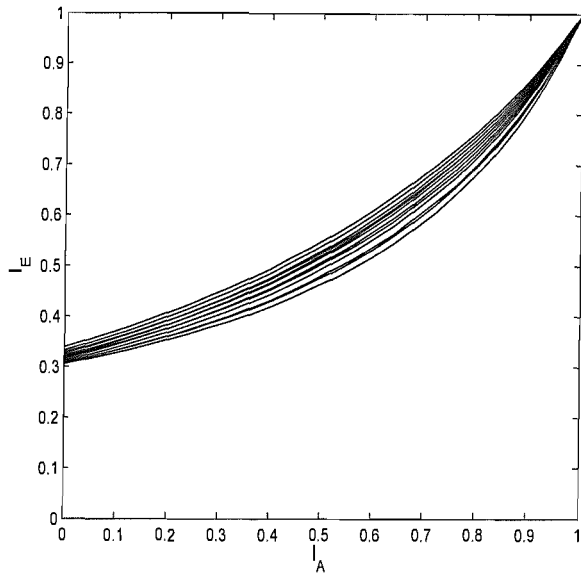


Figure 2.37: A group of EXIT charts of the IR-PLDC scheme of Figure 2.32 using the component codes of Table 2.7 at $\rho = -1\text{dB}$, while having a fixed rate $R_{in} = 0.85$ achieved by employing different weighting coefficient vectors λ .

In order to achieve an infinitesimally low BER at a specific SNR, an open EXIT tunnel should exist in the EXIT chart. Assuming that each component code's EXIT curve is represented by l points, the EXIT function Γ_{irr} at SNR ρ of the IR-PLDC should be optimized by 'maximizing' the square of the EXIT chart matching error function given by:

$$J(\lambda_1, \dots, \lambda_{P_{in}}) = \int_0^1 e(\rho)^2 d\rho, \quad (2.54)$$

where the function $e(\rho)$ is the distance between the *inner* and *outer* EXIT curves subjected to the constraints imposed by Equation (2.52).

The gradient search method of maximizing $J(\lambda_1, \dots, \lambda_{P_{in}})$ of Equation (2.54) is similar to the algorithm proposed in [60]. More explicitly, the algorithm starts by setting the *inner* code rate R_{in} to the minimum value. If the set of weighting coefficients maximizing the area expression of Equation (2.54) is generated using the gradient search method of [60] and an open EXIT tunnel exists, R_{in} is increased by a small amount. The algorithm terminates at the highest possible R_{in} value, where an open convergence tunnel may no longer be found.

The reason that our proposed *inner* IR-PLDC scheme is seeking the solutions 'maximizing' the area expression of $J(\lambda_1, \dots, \lambda_P)$ is justified as follows. The benefit of employing irregular *inner* or *outer* codes for an iteratively-detected scheme is to maximize the achievable rates. When using IRCCs as an *outer* code, minimizing the EXIT tunnel area corresponds to maximizing the achievable rate, owing to the area property discussed in Section 2.4.1. In other words, IRCCs are

Table 2.8: Design comparison of irregular schemes using either IRCCs having $\gamma = [\gamma_1, \dots, \gamma_{P_{out}}]$ or IR-PLDCs having $\lambda = [\lambda_1, \dots, \lambda_{P_{in}}]$, where the weighting coefficient vectors γ and λ quantify the fraction of bits encoded by each component code.

	IRCC	IR-PLDC
Design objective	Maximizing the achievable rates	
Component codes generated by	Puncturing a mother code	Varying T and Q
Area and rate relationship	Unique	Non-unique
Interleaver length requirement	High	Modest
Error function of Equation (2.54)	Minimizing	Maximizing
Aggregate code rate	$\frac{1}{R_{out}} = \sum_{i=1}^{P_{out}} \gamma_i \frac{1}{R_{i,ircc}}$	$\frac{1}{R_{in}} = \sum_{i=1}^{P_{in}} \lambda_i \frac{1}{R_{i,ldc}}$

Table 2.9: System parameters for the RSC-coded IR-PLDC system of Figure 2.32.

Modulation	QPSK
Mapping	Gray mapping
Regular Outer Channel Code	RSC(2,1,3)
IrRegular Outer Channel Code	IRCCs [60]
Interleaver Length	10^6 bits
Detector	MMSE
Precoder Rate	1
Precoder Memory	1

designed to find an *outer* EXIT curve that matches a given *inner* EXIT curve as close as possible by maximizing the area under the EXIT curve. However, there is no one-to-one relationship between the *inner* aggregate rate R_{in} and the associated area under the EXIT curves. Consequently, the IR-PLDC scheme offers multiple area values under its EXIT curves for a given rate, as illustrated in Figure 2.37. Larger EXIT tunnel area potentially requires less *outer* iterations to achieve an infinitesimally low BER. Therefore, given an *outer* code, the design criterion for the *inner* IR-PLDC is to maximize the achievable rate, while having an infinitesimally low BER, which corresponds to **maximizing the inner code rate R_{in} and simultaneously maximizing the EXIT tunnel area according to Equation (2.54)**, since the latter minimizes the number of iterations required. A detailed comparison of designing the proposed *inner* IR-PLDC and the IRCC of [60] as an *outer* code is provided in Table 2.8.

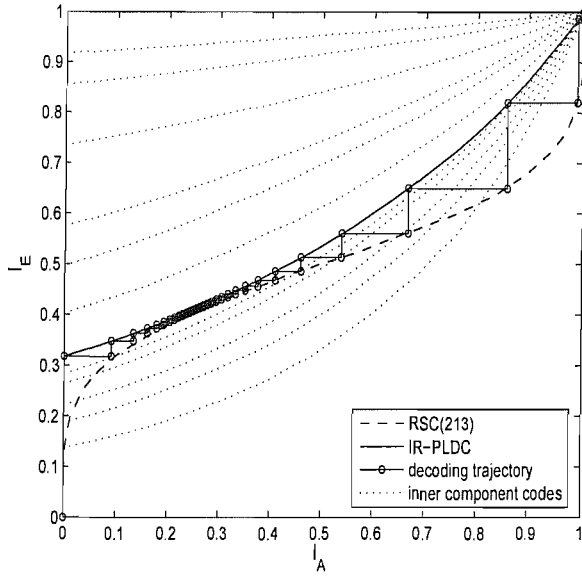


Figure 2.38: EXIT chart and the decoding trajectory of the RSC-coded IR-PLDC scheme of Figure 2.32 recorded at $\rho = 0\text{dB}$, when using the system parameters outlined in Table 2.9.

In the previous iteratively detected schemes in Sections 2.4.1 and 2.4.2, half-rate RSC(215) code is employed. It is natural to ask the question whether it is possible to employ an even simpler RSC code to reduce the decoding complexity, while operating near MIMO channel's capacity. Hence, we designed our IR-PLDC system for a half-rate RSC(213) code, which has a decoding complexity of 217 ACS operations per LLR value compared to the 841 ACS operations imposed by the RSC(215) code. It is also worth mentioning that when plotting the EXIT chart, it is often assumed that the distribution of the LLRs is Gaussian, which is only sufficiently accurate, when a high interleaver length is used in the schematic of Figure 2.32. In the context of the RSC(213) code, the Gaussian assumption of the EXIT chart becomes easier to satisfy in conjunction with a shorter interleaver, since the RSC(213) code imposes correlation over a factor of $\frac{3}{5}$ shorter segment of the encoded bit stream.

Figure 2.38 presents the EXIT charts and the corresponding decoding trajectory of the RSC(213)-coded IR-PLDC scheme of Figure 2.32 designed for operating at $\rho = 0\text{dB}$, when using QPSK modulation in conjunction with an MMSE detector. The dotted lines are the EXIT curves of the $P_{in} = 11$ component codes of Table 2.7 and the solid line represents the EXIT curve of the *inner* IR-PLDC having the weighting coefficients given in Table D.1 of Appendix D. The resultant throughput of the system is $C(0\text{dB}) = 1.1392$ (bits/sym/Hz), according to Equation (2.47). By maximizing R_{in} as well as maximizing the open EXIT tunnel area of Equation (2.54), the optimized EXIT curves of Figure 2.38 exhibit a significant tunnel area, where the decoding trajectory of Figure 2.38 shows that $k = 29$ *outer* iterations were required.

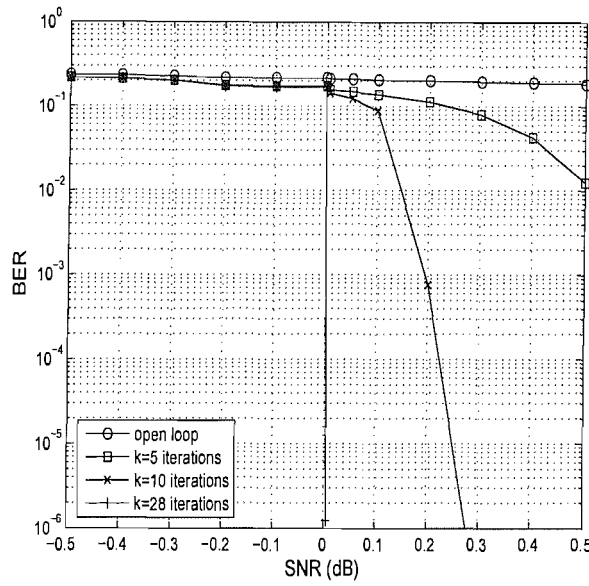


Figure 2.39: BER of the RSC-coded IR-PLDC scheme of Figure 2.32 that designed to achieve an infinitesimally low BER at $\rho = 0$ dB, when using the system parameters outlined in Table 2.9.

The corresponding BER of the RSC(213)-coded IR-PLDC system of Figure 2.32 designed for achieving an infinitesimally low BER at $\rho = 0$ dB using QPSK modulation is shown in Figure 2.39. There is a turbo cliff at $\rho = 0$ dB, when $k = 29$ *outer* iterations were carried out between the RSC(213) decoder and the IR-PLDC decoder. Note that the complexity required for achieving an infinitesimally low BER at $\rho = 0$ dB is quantified in terms of the number of ACS operations per LLR value. Given the number of *outer* iterations and the complexity of each PLDC component of Table 2.7 combined with the RSC(213) decoder requires 217 ACS operations, the total decoding complexity per LLR value was evaluated by considering the number of iterations as well as each component's complexity as follows:

$$\omega(0dB) = 29 \cdot (0.146 \cdot 8562 + 0.034 \cdot 18126 + 0.82 \cdot 12546 + 217) = 3.5876 \times 10^5. \quad (2.55)$$

Naturally, the same design process can be extended to other SNR values. Figure 2.40 plots the maximum rates achieved by the proposed IR-PLDC scheme of Figure 2.32, when half-rate RSC(213) and RSC(215) codes were employed. Each point in Figure 2.40 was designed to achieve the maximum rate with the aid of specific weighting coefficients, which are listed in Tables D.1 and D.2 of Appendix D. The dotted lines of Figure 2.40 quantify the maximum achievable rates of the $P_{in} = 11$ component codes of Table 2.7. By simply adjusting the fraction of information fed into each components, as seen in Tables D.1 and D.2, the proposed system of Figure 2.32 employing irregular *inner* codes becomes capable of operating across a wide range of SNRs. Figure 2.40 clearly demonstrates the variation of the maximum rate, when encounters different-SNR scenarios.

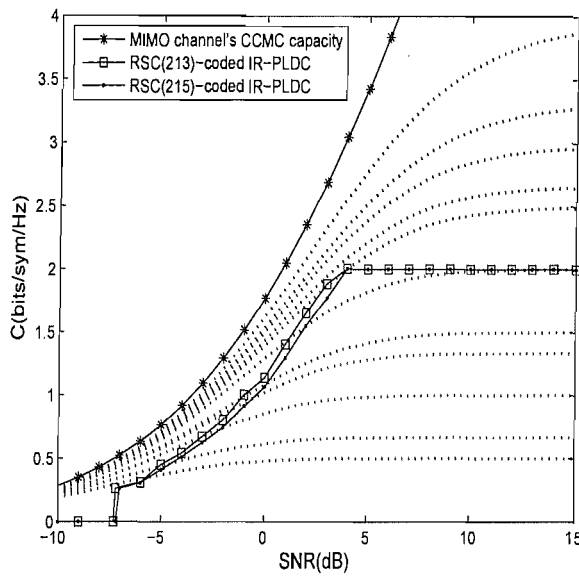


Figure 2.40: The maximum rates achieved by the IR-PLDC schemes of Figure 2.32 using RSC(213) and RSC(215) codes according to Tables D.1 and D.2, when using the system parameters outlined in Table 2.9.

Also observe in Figure 2.40 that the IR-PLDC scheme employing the RSC(213) code is capable of achieving a higher maximum rate compared to the system employing the RSC(215) code, which is about 2.5dB away from MIMO channel's capacity. Compared to the EXIT curve of the RSC(215) code seen in Figure 2.17, the RSC(213) code's EXIT curve of Figure 2.38 has a lower I_E value for abscissa values of $I_A < 0.5$ and a higher I_E value in the rest of the abscissa range. The resultant shape of the *outer* EXIT curve forms a larger open EXIT tunnel area and hence enables the *inner* IR-PLDC code to provide a higher aggregate rate for the serial concatenated system. This implies that having a beneficial shape for the EXIT curves plays a more influential role in determining the achievable rates of the system, than having a larger minimum distance, as it becomes explicit by comparing the performance of the RSC(213) and RSC(215) coded systems.

Tables D.1 and D.2 in Appendix D list the weighting coefficient vector λ for the IR-PLDC scheme of Figure 2.32 required for achieving maximum rates ranging from $\rho = -7$ dB to $\rho = 4$ dB, when the RSC(213) and RSC(215) codes were employed, respectively. The $P_{in} = 11$ component codes are listed from low-rate to high-rate components, where an entry of '0' implies that the specific PLDC component is inactivated during the transmission process. Observe further in Tables D.1 and D.2 that increasing the system's maximum rate upon increasing the SNR is achieved by appropriately adjusting the weighting coefficient vector λ . However, when we have $\rho = 4$ dB in Table D.1, the maximum-rate PLDC component having a rate of $R_{3,LDC} = 2$ has already fully activated, which means that it has a weighting coefficient of $\lambda_3 = 1$. Therefore, no more rate

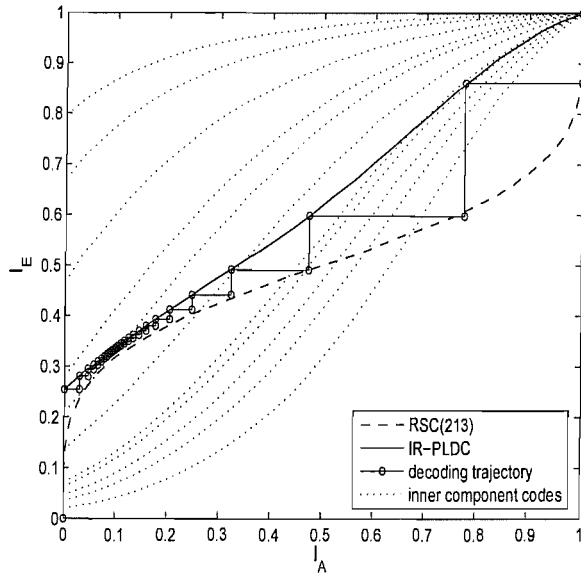


Figure 2.41: EXIT chart and the decoding trajectory of the RSC-code IR-PLDC scheme of Figure 2.32 having a precoder memory of **three** recorded at $\rho = 0\text{dB}$, when using the system parameters outlined in Table 2.9.

increase is observed in Figure 2.40, when we have $\rho > 4\text{dB}$. Naturally, further rate improvements can be achieved, if higher-rate PLDC components are employed.

An alternative way of changing the shape of the EXIT curves is constituted by changing the precoder's memory size and/or the generator polynomials for the system of Figure 2.32. Previously, Figure 2.31 has indicated that changing the rate-1 precoder's memory and generator polynomial does not change the area under the corresponding EXIT curves. Hence, Figure 2.41 portrays both the EXIT curves and the decoding trajectory of the IR-PLDC scheme of Figure 2.32 at $\rho = 0\text{dB}$ using the RSC(213) code, when the precoder's memory size was increased to three. Compared to Figure 2.38, the EXIT curves of Figure 2.41 are more steep. However, in this particular case, increasing the precoder's memory size does not benefit the system in terms of its maximum achievable rate, which is $C(0\text{dB}) = 0.7908$ (bits/sym/Hz), while $C(0\text{dB}) = 1.1392$ (bits/sym/Hz) was achieved for the IR-PLDC schemes having precoder memory size of one. Again, Figure 2.41 demonstrates that the shape of the *inner* and *outer* EXIT curves exhibits an influential role in the EXIT chart based design. The corresponding BER performance is shown in Figure 2.42.

2.5.1.3 Complexity-Constrained RSC-Coded IR-PLDCs

Figures 2.38 and 2.41 have characterized a number of IR-PLDC designs contrived for achieving the maximum throughput across SNRs. Observe from Equation (2.55) that an excessive amount

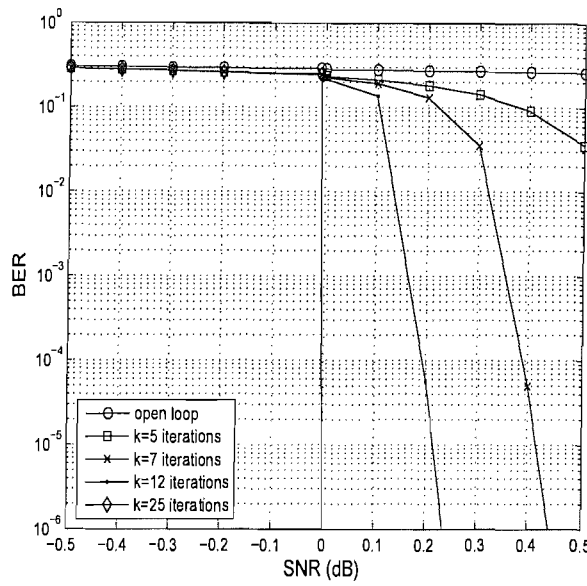


Figure 2.42: BER of the RSC-coded IR-PLDC scheme of Figure 2.32 having a precoder memory of three that designed to achieve an infinitesimally low BER at $\rho = 0\text{dB}$, when using the system parameters outlined in Table 2.9.

of complexity is required to decode each information bit. However, the mobile handsets normally can not afford such high complexity. Therefore, this section investigates the IR-PLDC designs of Figure 2.32 that are capable of achieving the maximum possible rate under a certain complexity constraint.

The total decoding complexity is constituted by two contributions. Firstly, the particular fraction of bits λ_i fed into each component code as well as each component's own complexity quantified in Table 2.7. Secondly, the number of *outer* iterations k required for reaching the $(1.0, 1.0)$ point on the EXIT chart constitutes a linear complexity factor. Observe from Figure 2.38 that the IR-PLDC schemes designed for maximizing the achievable rate often result in a high decoding complexity, which is associated with a narrow EXIT tunnel. These high-complexity designs may be suitable for the base station. The flexibility of the IR-PLDCs also allows us to derive designs for mobile handsets, where the affordable complexity is more limited. We refer to this as a 'complexity-constrained' design.

For the above-mentioned 'maximum-rate' schemes, the design problem was formulated in Equation (2.54) and a gradient search [60] can be performed to find the most suitable weighting coefficient vector λ . However, for the 'complexity-constrained' scheme, we are looking for the maximum achievable rate under a specific complexity constraint, which requires an extended search for the weighting coefficient vector λ . More specifically, the complexity of an IR-PLDC

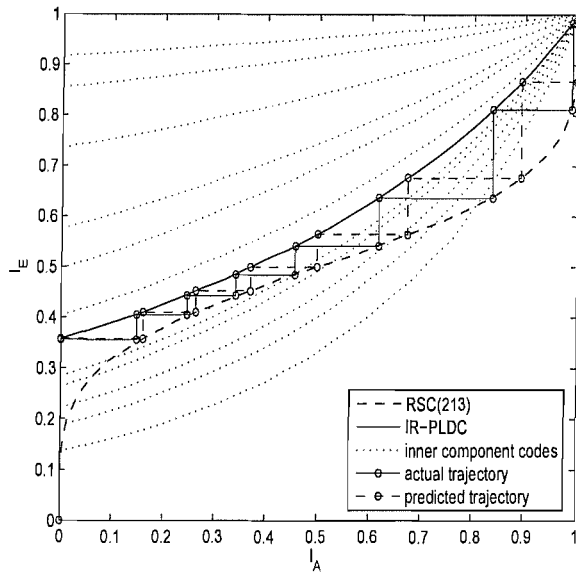


Figure 2.43: EXIT chart and the (predicted) decoding trajectory of the 'complexity-constrained' RSC-coded IR-PLDC scheme of Figure 2.32 at $\rho = 0\text{dB}$, when using the system parameters outlined in Table 2.9.

scheme employing an RSC code at SNR ρ is restricted by:

$$k \cdot (\varpi_1\lambda_1 + \varpi_2\lambda_2 \dots + \varpi_P\lambda_P + \varpi_{RSC}) \leq \varpi_{target}, \quad (2.56)$$

where ϖ_i is the complexity of the i -th component code quantified in Table 2.7. The number of decoding iterations k required to achieve an infinitesimally low BER is predicted using a predicted decoding trajectory illustrated in Figure 2.43.

In the following design example, we optimize the IR-PLDC scheme of Figure 2.32 employing a half-rate RSC(213) code as our *outer* code at $\rho = 0\text{dB}$. The complexity imposed at the receiver is restricted by $\varpi_{213,c}(0\text{dB}) \leq \frac{1}{10}\varpi_{213}(0\text{dB}) = 0.35876 \times 10^5$ ACS operations per LLR value.

Figure 2.43 shows the EXIT curves of our 'complexity-constrained' IR-PLDC scheme as well as the predicted decoding trajectory using interpolation and the actual decoding trajectory recorded using simulation. Firstly, a wider convergence tunnel is observed in Figure 2.43 compared to that of Figure 2.38, hence the number of decoding iterations can be effectively reduced. Furthermore, there is a difference between the predicted decoding trajectory generated using interpolation and the actual trajectory recorded using simulation. The accuracy of the match between the decoding trajectory and the EXIT chart is dependent on the validity of the assumption of the LLRs' Gaussian distribution, which requires an infinite interleaver length. If the assumption has a limited accuracy, the actual decoding trajectory may exhibit an 'overshoot' problem. In this design example, the first interleaver Π_1 of Figure 2.32 is set to have a length of 10^6 bits and the length of the second

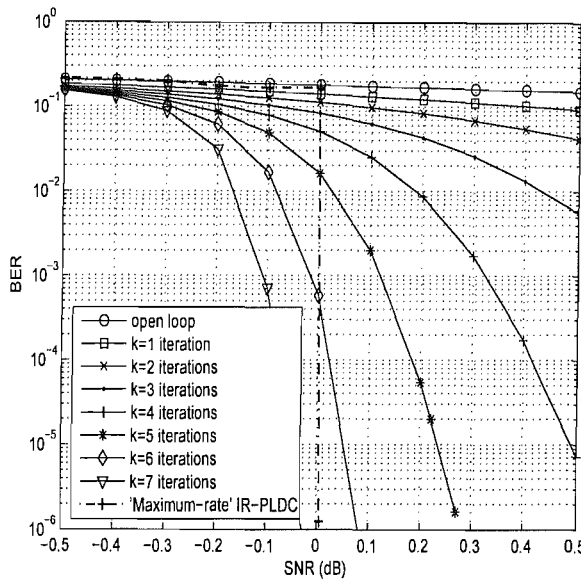


Figure 2.44: BER of the 'complexity-constrained' RSC-coded IR-PLDC scheme of Figure 2.32 designed for achieving an infinitesimally low BER at $\rho = 0\text{dB}$, when using the system parameters outlined in Table 2.9.

interleaver Π_2 is equal to the corresponding number of bits fed into each component code. Note in Figure 2.43 that although no substantial 'overshoot' is visible, the resultant predicted and the actually encountered decoding trajectories exhibit an obvious difference after a few iterations. However, we may state that the number of decoding iterations predicted k using interpolation is sufficiently accurate. The results of our further investigations included here suggest that unless encountering narrow EXIT tunnels, where more than $k = 15$ iterations are necessary, the predicted number of iterations using EXIT chart based interpolation is typically quite accurate. On the other hand, when aiming for low-complexity designs, the 'wide EXIT tunnel assumption' is usually satisfied and hence the aforementioned inaccurate prediction is not encountered.

Furthermore, a rate of $C(0\text{dB})=1.10929$ (bits/sym/Hz) is achieved in Figure 2.43, where the rate loss recorded is insignificant, compared to the maximum achievable rate of $C(0\text{dB}) = 1.1392$ (bits/sym/Hz) recorded for the previous 'maximum-rate' design at $\rho = 0\text{dB}$. As a benefit of this 'complexity-constrained' design, only about 10% of the decoding complexity of the 'maximum-rate' design is imposed. The actual decoding complexity is:

$$\begin{aligned}\varpi_{213,c}(0\text{dB}) &= 7 \cdot (0.83 \cdot 4086 + 0.17 \cdot 5974 + 217) \\ &= 0.3237 \times 10^5 < 0.35876 \times 10^5,\end{aligned}\tag{2.57}$$

where the weighting coefficient vector is given by $\lambda = [0, 0.83, 0, 0.17, 0, 0, 0, 0, 0, 0]$.

Figure 2.44 portrays the BER performance of the RSC(213)-coded IR-PLDC scheme designed

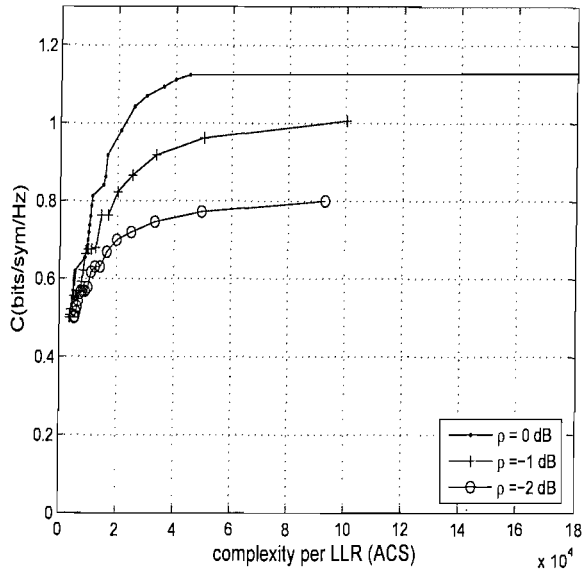


Figure 2.45: Maximum achievable rates against the required decoding complexity of the RSC-coded IR-PLDC schemes of Figure 2.32 at $\rho = -2, -1, 0$ dB, when using the system parameters outlined in Table 2.9.

for satisfying the complexity constraint of Equation (2.56), when using QPSK modulation in conjunction with an MMSE detector. Recall that this system was designed for maintaining an infinitesimally low BER at $\rho = 0$ dB and $k = 7$ *outer* iterations were required by the system to achieve an infinitesimally low BER. In contrast to the previous 'maximum-rate' design of Figure 2.39, where a sharp turbo-cliff BER was observed, the BER of the complexity-constrained schemes dropped more gradually, owing to having a wider EXIT tunnel.

In order to elaborate a little further, Figure 2.45 quantifies the maximum achievable rate of the 'complexity-constrained' RSC-coded IR-PLDC scheme of Figure 2.32 having various complexity constraints. The minimum complexity required to enable the system to operate at $\rho = -2, -1$ and 0 dB is about 3576 ACS arithmetic operations, where a throughput of 0.5 was achieved in Figure 2.45. At the minimum decoding complexity point, the *inner* IR-PLDC only activates the minimum-complexity PLDC component of PLDC(2221) with a weighting coefficient $\lambda_0 = 1$. As a result of investing more complexity, a higher rate becomes achievable in conjunction with more complex PLDC components, while operating at a certain SNR ρ . Note that in the vicinity of the cliff region, the system becomes capable of approaching the performance of the maximum-rate design at a significant complexity reduction, as evidenced in Figures 2.43 and 2.44.

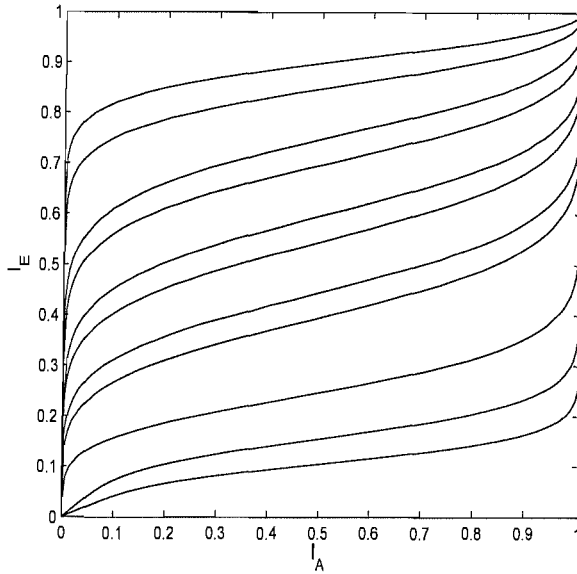


Figure 2.46: EXIT charts of the IRCC scheme having $P_{out} = 11$ component codes.

2.5.2 IR-PLDCs and IRCCs

Since both irregular *inner* schemes, such as IR-PLDCs and irregular *outer* schemes, i.e. IRCCs have the ability of providing flexible EXIT curves, it is natural to investigate further in order to explore the difference between these two approaches.

In this section, we provide a detailed comparison of the IRCCs and IR-PLDCs in terms of the maximum achievable rates and the working SNR region. We adopt the RSC(213)-coded IR-PLDC scheme having a total number of $P = P_{in} + P_{out} = 11 + 1 = 12$ components, which has been extensively demonstrated in Section 2.5.1.2. Since the IR-PLDC component codes have a maximum rate of $R_{3,LDC} = 2$, the resultant maximum rate of the RSC(213)-coded IR-PLDC scheme of Figure 2.32 is limited to 2 (bits/sym/Hz) using QPSK modulation, as seen in Figure 2.40.

For a fair comparison, we also set the maximum rate of the a IRCC-coded PLDC scheme to 2 (bits/sym/Hz), when QPSK modulation is employed. Furthermore, an IRCC scheme constituted by a set of $P_{out} = 11$ component codes was constructed in [69] from a systematic half-rate memory-4 mother code defined by the octally represented generator polynomials of $(23, 35)_8$. Hence, we have a total number of $P = P_{in} + P_{out} = 1 + 11 = 12$ components. The EXIT chart characteristic of the resultant $P_{out} = 11$ IRCC component codes is shown in Figure 2.46, where the rates of the codes are $R_{i,IRCC} = [0.1, 0.15, 0.25, 0.4, 0.45, 0.55, 0.6, 0.7, 0.75, 0.85, 0.9]$, respectively. Each component encodes a specific fraction of the incoming bit stream, as quantified by the weighting coefficient vector $\gamma = [\gamma_1, \dots, \gamma_{P_{out}}]$. Hence, the weighting coefficient vector γ is optimized with the aid of the iterative algorithm in [60], so that the EXIT curve of the resultant IRCC closely

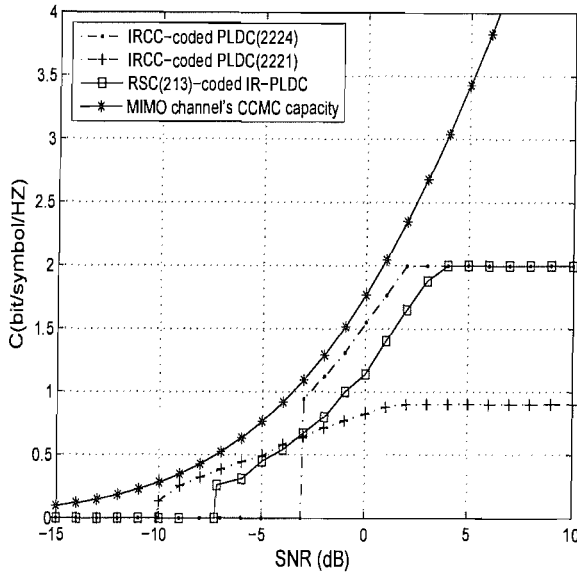


Figure 2.47: Maximum achievable rates plotted according to Tables D.3 and D.4 for the IRCC-coded schemes using PLDC(2224) and PLDC(2221) as the inner codes, when using the system parameters outlined in Table 2.9.

matches that of the *inner* code.

Figure 2.47 portrays the maximum achievable rates achieved by the IRCC-coded schemes using PLDC(2224) or PLDC(2221) as the *inner* codes according to Tables D.3 and D.4 in Appendix D, when employing QPSK modulation as well as an MMSE detector. The maximum achievable rates of the corresponding RSC(213)-coded IR-PLDC scheme configured according to Table D.1 is also plotted as the benchmark. When a rate-two PLDC(2224) code is employed, the resultant IRCC-coded scheme becomes capable of operating about 0.9dB away from the MIMO channel's capacity of Equation (2.10), but no open EXIT tunnel is formed until we have $\rho \geq -3$ dB, which implies that it fails to function adequately in the low SNR region. By contrast, when we use the half-rate PLDC(2221) arrangement as our *inner* code, the system performs adequately for SNRs in excess of $\rho = -10$ dB, as seen in Figure 2.47. However, this scheme suffers from a rate loss in the high SNR region, because the *inner* PLDC(2221) code fails to operate near the MIMO capacity. By contrast, the RSC(213)-coded IR-PLDC scheme operates about 2.5dB away from the MIMO channel's capacity for SNRs spanning from $\rho = -7$ dB to $\rho = 4$ dB.

In conclusion, the IRCC-coded schemes are capable of operating about 0.9dB away from the MIMO channel's capacity in either high-SNR or low-SNR region, but fail to operate across a number of SNRs. On the other hand, although the IR-PLDC aided scheme operates about 2.5dB away from the MIMO channel's capacity, it can work in a wider SNR region.

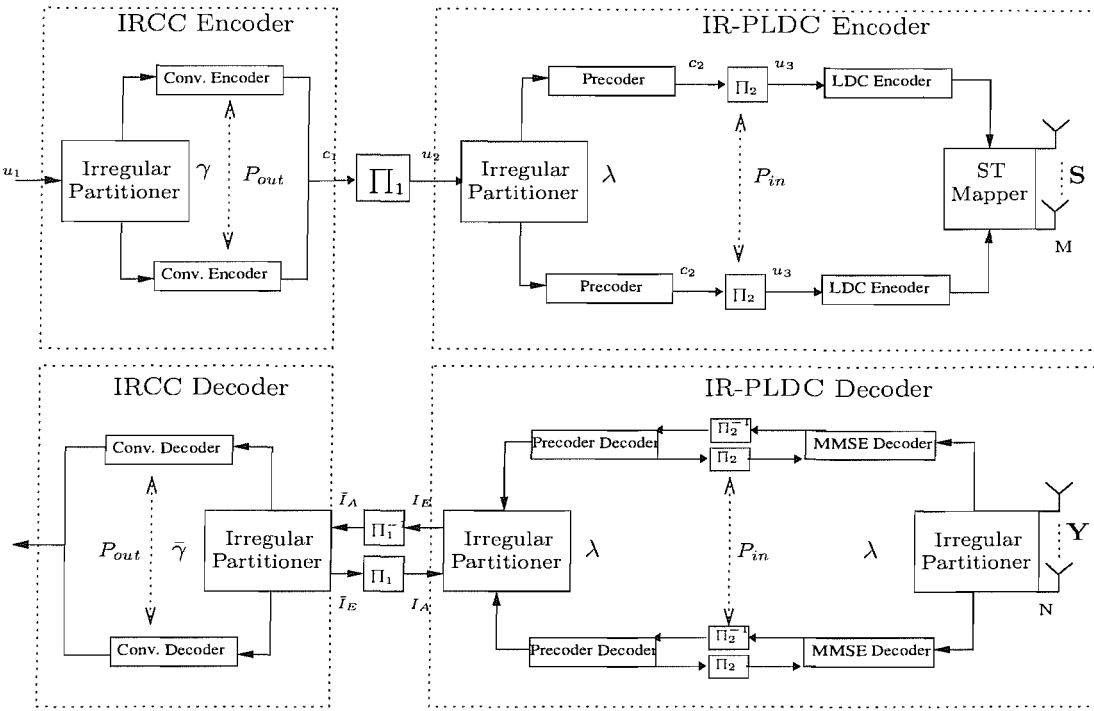


Figure 2.48: Schematic of the serial concatenated IRCC-coded IR-PLDC using iterative decoding.

2.5.3 IRCC-Coded IR-PLDC Scheme

It is desirable to have a flexible system that is capable of working close to the MIMO channel's capacity and at the same time operating across a wide SNR region. Figure 2.47 have demonstrated that either IRCCs or IR-PLDCs are only capable of satisfying one of these design objectives. In this section, we will demonstrate that by serially concatenating the IRCCs [60] and the proposed IR-PLDCs, such ambitious design objectives can be fulfilled at the same time.

Figure 2.48 portrays the schematic of the proposed IRCC-coded IR-PLDC scheme. The receiver is assumed to have the knowledge of the weighting coefficient vectors γ and λ , as well as that of the set of DCMs. The 'irregular partitioner' of Figure 2.48 feeds the required fraction of bits into the relevant component codes, according to the corresponding weighting coefficient vectors. For the sake of having a fair comparison to the schemes illustrated in Section 2.5.2, in the following design example, we consider a MIMO system equipped with $M = 2$ transmit as well as $N = 2$ receive antennas and a total number of $P = 12$ component codes are used, where we have $P_{out} = 6$ IRCC component codes and $P_{in} = 6$ IR-PLDC component codes. More specifically, the IRCC component codes of Figure 2.46 having a rate of $R_{i,IRCC} = [0.1, 0.25, 0.4, 0.55, 0.7, 0.9]$ and the IR-PLDC component codes having a rate of $R_{i,LDC} = [0.33, 0.5, 0.67, 1, 1.5, 2]$ in Table 2.7 were employed. Note that IRCC encoder's 'irregular partitioner' of Figure 2.48 is based on the weighting coefficient vector $\gamma = [\gamma_1, \dots, \gamma_{P_{out}}]$, whereas the 'irregular partitioner' of

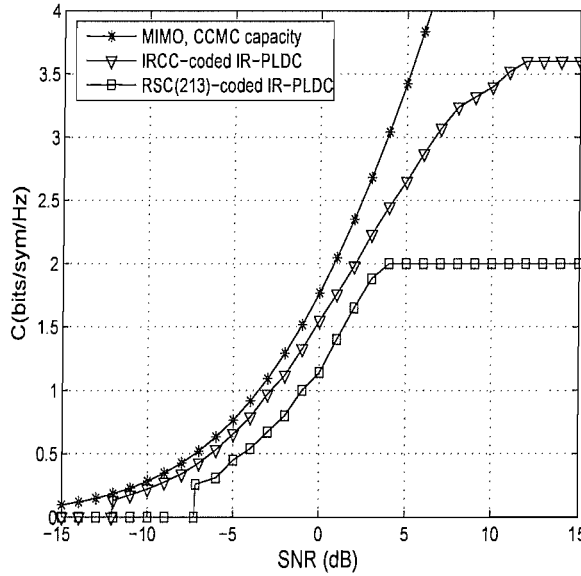


Figure 2.49: Maximum achievable rates plotted according to Tables D.5 and D.6 for the IRCC-coded IR-PLDC schemes of Figure 2.48, when using the system parameters outlined in Table 2.9.

IRCC's decoder is determined by another vector $\bar{\gamma} = [\bar{\gamma}_1, \dots, \bar{\gamma}_{P_{out}}]$. That is because γ quantifies the fraction of incoming information bits, while $\bar{\gamma}$ quantifies the fraction of incoming LLRs and they are related by:

$$\bar{\gamma}_i = \frac{\gamma_i \times R_{out}}{R_{i,IRCC}}, \quad i = 1, \dots, P_{out} \quad (2.58)$$

We run an exhaustive search operation for all the possible combinations of γ and λ under the following constraints:

- An open convergence tunnel must exist between the *inner* and *outer* EXIT curves in order to achieve an infinitesimally BER, provided that the aid of the decoding trajectory arrives at the top right corner of the EXIT chart;
- The throughput $C(\rho) = \log_2(L) \cdot R_{in} \cdot R_{out}$ has to be maximized;
- The resultant open EXIT tunnel area has to be maximized, for the sake of minimizing the number iterations required;
- $\gamma_1 + \gamma_2 + \dots + \gamma_{P_{out}} = 1$ and $\lambda_1 + \lambda_2 + \dots + \lambda_{P_{in}} = 1$.

The exhaustive search is set to have a step-size of 0.05.

Figure 2.49 plots the maximum rates achieved by the IRCC-coded IR-PLDC scheme of Figure 2.48 according to Tables D.5 and D.6, when QPSK modulation in conjunction with an MMSE detector were employed. The corresponding maximum achievable rates of the RSC(213)-coded

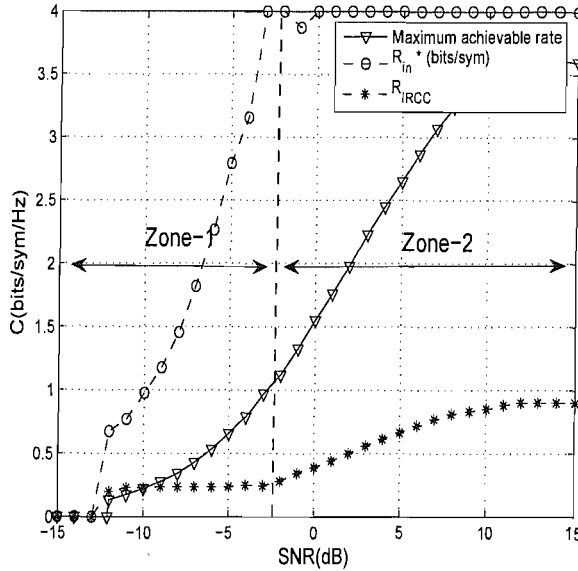


Figure 2.50: Inner throughput $\log_2(L) \cdot R_{in}$ and outer rate R_{out} for the IRCC-coded IR-PLDC scheme of Figure 2.48 to achieve maximum rate according to Tables D.5 and D.6, when using the system parameters outlined in Table 2.9.

IR-PLDC scheme of Figure 2.32 was also presented as the benchmark, which also employed $P = 12$ component codes. Observe in Figure 2.49 that employing an irregular design at both the *inner* and the *outer* codes enables the system to achieve an infinitesimally low BER for SNR starting from as low as $\rho = -12$ dB. Furthermore, the double-side EXIT matching based scheme is capable of operating about 0.9dB from the MIMO channel's CCMC capacity quantified in Equation (2.10). Note that when we have $\rho > 2$ dB, the IRCC-coded IR-PLDC scheme of Figure 2.48 begins to gradually deviate from the MIMO capacity, owing to lack of high-rate IR-PLDC components. Naturally, the dispense observed in the high-SNR region can be eliminated, when adopting high-rate PLDCs as the component codes.

In order to illustrate this phenomenon a little further, Figure 2.50 characterizes the effect of the *inner* throughput $\log_2(L) \cdot R_{in}$ and the *outer* rate R_{out} of the IRCC-coded IR-PLDC scheme of Figure 2.48 designed for achieving the maximum rate according to Tables D.5 and D.6, when QPSK modulation and an MMSE detector were employed. The operating SNR range may be divided into two zones around $\rho = 3$ dB. Observe in Figure 2.50 that in the low-SNR region, namely in Zone-1, the proposed scheme achieved a near-capacity throughput owing to the flexibility provided by the IR-PLDCs. By contrast, when we have high SNRs, i.e. in Zone-2, the maximum rate is achieved by increasing the rate of the IRCC scheme. This observation further justifies the results presented in Figure 2.47.

As far as the decoding complexity is concerned, the original IRCC scheme of [69] imposed a

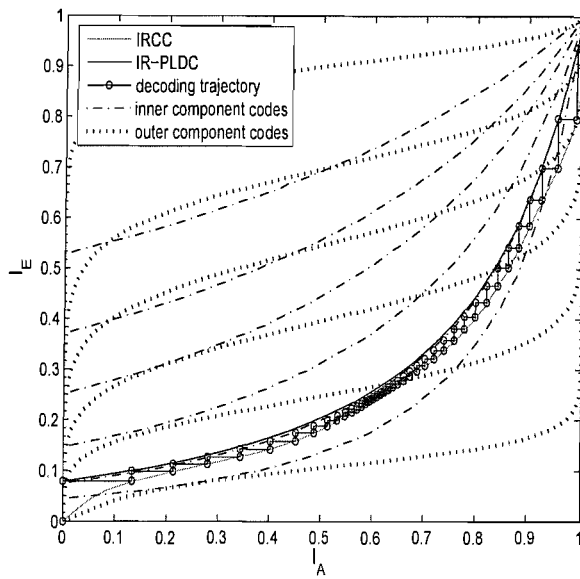


Figure 2.51: EXIT chart and the decoding trajectory of the IRCC-coded IR-PLDC scheme of Figure 2.48 at $\rho = -4\text{dB}$ according to Tables D.5 and D.6, when using the system parameters outlined in Table 2.9.

potentially excessive complexity in the low-rate region, owing to the additional generator polynomials. However, flexible rates of the IRCC-coded IR-PLDC scheme of Figure 2.48 in the low-SNR region are achieved by adjusting the IR-PLDC's rate, where the associated complexity is low, as seen in Figure 2.50. In Zone-2, since high-rate IRCC components are activated, the overall decoding complexity is still manageable, despite the fact that the IR-PLDC scheme's complexity is increased.

The weighting coefficient vectors γ and λ of the IRCC and IR-PLDC schemes optimized for achieving the maximum aggregate rates are listed in Tables D.5 and D.6 of Appendix D. Observe in Table D.6 that typically only two components of the *inner* IR-PLDC are activated, while a number of IRCC components are required for the sake of minimizing the open EXIT tunnel area according to Table D.5. For example, when we have $\rho = 6\text{dB}$, only $P_{out} + P_{in} = 2 + 2 = 4$ out of the total of $P = 12$ components were activated. As a result of having a limited range of EXIT curve shapes, the superimposed EXIT curves cannot be accurately matched, thus we observe that the system is operating about 1.6dB away from the MIMO capacity at $\rho = 6\text{dB}$. By contrast, in the low-SNR region, i.e. when we have $\rho = -4\text{dB}$, $P_{out} + P_{in} = 5 + 2 = 7$ component codes were activated. Hence, a more accurate EXIT curve matching becomes possible. The resultant system operates 0.9dB away from the MIMO capacity, as seen in Figure 2.49.

Figure 2.51 portrays both the EXIT curves and the decoding trajectory of the IRCC-coded IR-PLDC scheme of Figure 2.48 recorded at $\rho = -4\text{dB}$ using QPSK modulation, when an MMSE

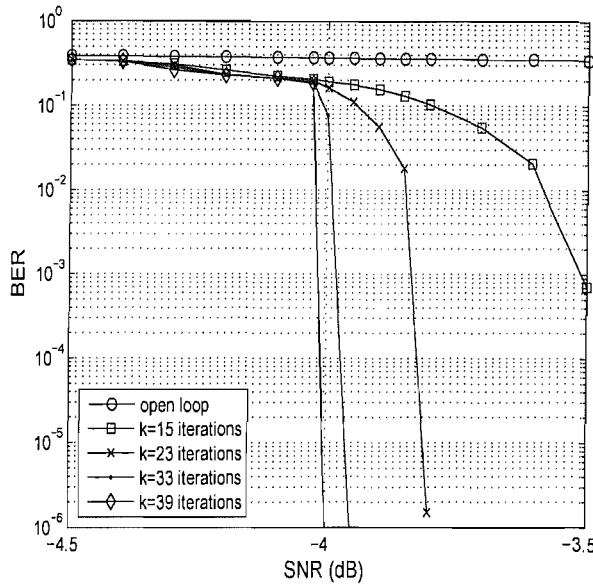


Figure 2.52: BER of the IRCC-coded IR-PLDC scheme of Figure 2.48 that designed to achieve an infinitesimally low BER at $\rho = -4\text{dB}$ according to Tables D.5 and D.6, when using the system parameters outlined in Table 2.9.

detector was employed. The corresponding weighting coefficients are given in Tables D.5 and D.6. Observe in Figure 2.51 that an extremely narrow EXIT tunnel was formed, which required $k = 39$ *outer* iterations to reach the $(I_A, I_E) = (1.0, 1.0)$ point. The associated BER curve is plotted in Figure 2.52.

2.5.4 Practical Issues of Near-Capacity Designs

Using EXIT charts [57] [58] as our design tools, Section 2.5.3 illustrated that practical near-capacity SCC schemes can be designed based on the irregular principle. It was shown in [68] for the BECs that near-capacity operations require the inner and outer codes' EXIT curve shapes to closely match each other. There is experimental evidence that this is also valid for other types of channels. Furthermore, this property may be phrased as having an accurately matching pair of EXIT curves, which results in an infinitesimally low, but still marginally open EXIT-chart 'tunnel'. Naturally, having a narrow EXIT-tunnel typically requires a sufficiently large number of extrinsic information exchanges between the decoder components. Consequently, the decoding complexity increases linearly with the number of *outer* iterations. Furthermore, the component codes may require complex decoders in order to operate at a high throughput, as seen in Figure 2.51. In practical systems, tolerating a high decoding complexity may not be affordable, especially not for mobile handsets. Therefore, the 'complexity-constrained' scheme of Section 2.5.1.3 was proposed in order to maximize the attainable throughput under a given complexity constraint. By maintaining a relatively

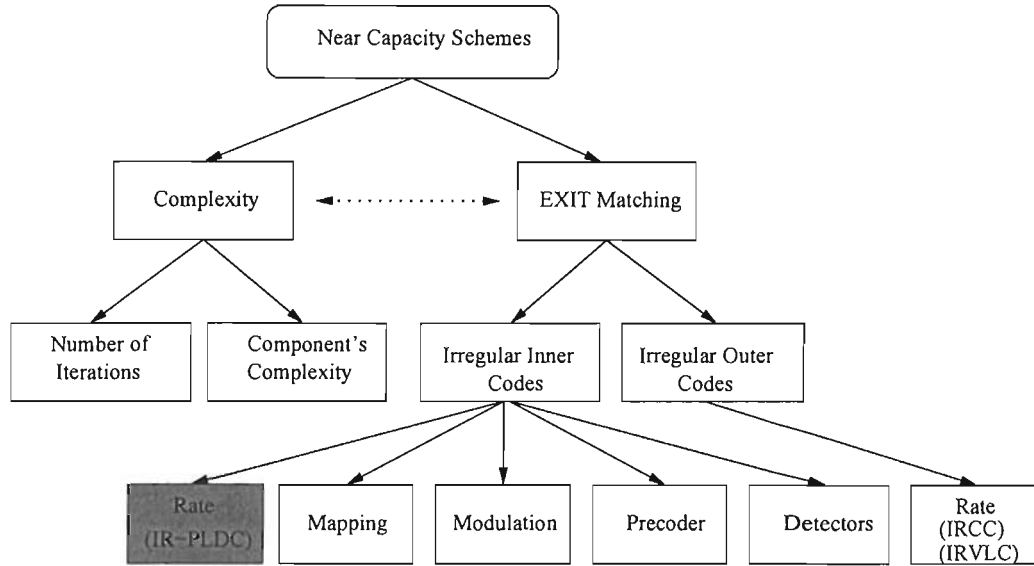


Figure 2.53: Factors affecting the design of near-capacity schemes using irregular principle.

large open EXIT tunnel, we are able to precisely control the number of iterations to be carried out.

On the other hand, in order to accurately predict and control the extrinsic information flow between the *inner* and *outer* decoders, the Probability Density Function (PDF) of the LLR values is assumed to be Gaussian, which is guaranteed by having a high interleaver length of 10^6 bits for the irregular system design of Figure 2.48. The EXIT charts also analyze the LLR values based on the Gaussian assumption, where the associated decoding delay becomes high. If an interleaver having a shorter length is adopted, the PDF of the LLRs may change dramatically, which renders the extrinsic information flow more correlated, because the LLR's PDF becomes affected by both the number of *outer* iterations and by the specific decoder employed. Nonetheless, at the time of writing there are no tools in the open literature for the analysis and design of iterative decoding schemes having time-variant LLR PDFs.

2.5.5 Summary

In order to pursue the design objective of operating in the vicinity of the MIMO channel's capacity across a wide range of SNRs, irregular system designs are necessary. In Sections 2.5.1 to 2.5.3, we have demonstrated the design process of irregular systems using IR-PLDCs and/or IRCCs. The factors affecting the design of near-capacity schemes using the irregular approach are summarized in Figure 2.53, where the decoding complexity and the EXIT matching accuracy of *inner* and *outer* EXIT curves are two main design factors. More specifically, the matching of the *inner* and *outer* code's EXIT curves quantifies the maximum achievable rate, which is dependent on the affordable complexity. The specific shape of the EXIT curves is also related to the decoding complexity.

For example, if the *inner* and *outer* EXIT curves are matched while having a high gradient, a large number of iterations are required to achieve an infinitesimally low BER. On the other hand, if the matched pair of EXIT curves are near-horizontal, a low number of iterations is required. The relationship between “EXIT Matching” and “Complexity” is represented by the dotted line in Figure 2.53.

Irregular schemes are suitable for accurate EXIT curve matching, since they are capable of providing EXIT curves with flexible characteristics. The design of irregular *outer* codes can be accomplished for example by using IRCCs [60] [69] or IrRegular Variable Length Codes (IR-VLCs) [61], where irregularity is achieved by employing various code rates. The area property quantified in Equation (2.50) suggests that maximizing the achievable rate corresponds to minimizing the open EXIT tunnel area. By contrast, the irregularity of the *inner* code can be created in various ways, as seen in Figure 2.53. The IR-PLDC approach proposed in this chapter creates a diverse set of EXIT curves using different rates, as exemplified in Figures 2.33 and 2.34. There are two main differences between the irregular *inner* and *outer* schemes. Firstly, the *inner* code’s EXIT curves are affected by the SNR encountered. In other words, there is a different set of *inner* EXIT curves for each SNR value. This property further explains the reason that IRCC schemes may facilitate operation closer to the MIMO channel’s capacity than IR-PLDCs within a certain SNR region, as evidenced in Figure 2.47. Secondly, the IR-PLDC scheme has a non-unique relationship between its aggregate rate R_{in} of Equation (2.53) and the area under the EXIT curves, which was demonstrated in Figure 2.37. Hence, our optimization objective is to maximize the achievable rate as well as maximize the open EXIT tunnel area. However, the employment of the IR-PLDCs potentially facilitates the resultant scheme to operate across a wide SNR range, as seen in Figure 2.49.

Figure 2.53 also lists other techniques of creating a diverse set of EXIT curves in the context of irregular *inner* codes. For example, changing the precoder’s memories and/or the generator polynomials is capable of effectively changing the shape of the EXIT curves without affecting the area under them, as illustrated in Figure 2.31. Another possible approach of changing the EXIT curves’ shape, while maintaining the same area is to employ different mapping schemes for each component [98] [103]. Obviously, employing different modulation schemes for each component code can also adjust the effective throughput of the system. Hence, a diverse set of EXIT curve shapes can be generated. When the decoding complexity is taken into account, the *inner* code’s irregularity can be complemented by using various detectors, such as ML, MMSE, Serial Interference Cancellation (SIC) and Parallel Interference Cancellation (PIC) detectors. Finally, it is important to point out the set of the techniques seen in Figure 2.53 can be jointly employed to create an even more diverse *inner* irregularity.

2.6 Conclusion

In this chapter, after illustrating the challenge of designing STBCs, we have demonstrated the family of LDCs has a general framework to accommodate different design objectives of STBCs. Furthermore, a novel method of optimizing the LDCs is proposed based on their DCMC capacity, as seen in Section 2.2.4. In Section 2.4.1, we investigated the performance of two-stage serial concatenated LDCs, with the aid of EXIT charts. The employment of precoders for the sake of achieving an infinitesimally low BER was also investigated in Section 2.4.2, while approaching the maximum achievable rate.

Motivated by the flexibility of the LDC complied with its near-capacity performance potential, Section 2.5.1.2 proposed a novel IR-PLDC scheme that is capable of approaching the MIMO capacity across a wide range of SNRs, as demonstrated from Figures 2.38 to 2.42, when combined with a simple *outer* channel coder. Figure 2.40 showed that the proposed RSC(213)-coded IR-PLDC scheme is capable of operating about 2.5dB from the MIMO channel's capacity. In the situation where the affordable decoding complexity is limited, Section 2.5.1.3 proposed a 'complexity-constrained' IR-PLDC scheme, which was designed with the aid of EXIT charts and maximizing the attainable throughput under a specific complexity constraint. After the detailed examination of the advantages and drawbacks of irregular *inner* and *outer* encoding schemes in Section 2.5.2, Section 2.5.3 proposed an IRCC-coded IR-PLDC scheme, which is capable of operating about 0.9dB from the MIMO channel's capacity, while achieving an infinitesimally low BER.

Chapter 3

Differential Space-Time Block Codes – A Universal Approach

3.1 Introduction and Outline

The primary focus of the codes discussed in Chapter 2 has been the case, where only the receiver has the knowledge of the Channel’s Impulse Response (CIR). In practice, the knowledge of the CIR is typically acquired using a channel sounding sequence. However, an excessive number of training symbols may be required, especially when numerous antennas are involved. Hence precious transmit power as well as valuable bandwidth is wasted. For example, a (4×4) antenna aided system requires the estimation of 16 channels, which imposes a high complexity in comparison to the idealized coherently detected system benefitting from perfect CIR estimation. Moreover, since the total transmit energy is shared by the multiple antennas, the energy available for training symbols is reduced compared to single antenna aided systems, which typically results in an increased channel estimation error. Furthermore, when the mobile travels at a high speed, the channel’s complex envelope varies dramatically, thus accurate MIMO channel estimation becomes a challenging task. Therefore, differentially encoded space-time schemes invoking non-coherent detection have been proposed in the literature.

The evolution of Differential Space-Time Block Codes (DSTBCs) can be divided into two categories. More specifically, the family of Differential Orthogonal Space-Time Block Codes (DOSTBCs), which facilitates low-complexity decoding. Similar to their coherent counterparts [14] [15] [85], the class of DOSTBCs also inherits restrictions owing to the orthogonal structure. Another family of DSTBCs is referred as Differential Unitary Space-Time Modulation (DUSTM) in the literature, which was proposed independently by Hochwald [20] [29] and Hughes [37]. This par-

ticular branch of DSTBCs has the advantage of supporting an arbitrary number of transmit and receive antennas. However, the number of space-time matrices to be designed grows exponentially with the effective throughput, which renders the design of such a large set of space-time matrices challenging. Nevertheless, a number of efforts have been reported in the literature to simplify the design problem by imposing different constraints [104] [105] [106].

In this chapter, the philosophy of LDCs is extended to the differential encoding domain. The resultant family of Differential Linear Dispersion Codes (DLDCs) constitutes a unified framework for describing all the DSTBCs found in the open literature and hence subsumes both DOSTBCs and DUSTMs. More explicitly, the novel contributions of this chapter are listed as follows [70] [73].

- The family of DSTBCs designed for dispensing with pilot-based MIMO channel estimation is investigated. More explicitly, the DSTBC schemes found in the literature and listed in Table 1.2 are unified using a general framework;
- By characterizing the fundamental link between STBCs and DSTBCs, we are able to extend the LDC structure into the differential encoding domain, so that flexible system configurations maintaining a dynamically reconfigurable throughput are achievable;
- We propose a family of full-diversity DLDCs based on the Cayley transform [33], where the unitary matrices having a linear structure can be constructed;
- We design turbo-detected channel-coded DSTBCs that are capable of achieving an infinitesimally low BER, while operating at low SNRs.

The outline of this chapter is as follows. Section 3.2 presents a universal system model for all the DSTBC schemes found in the literature, which is generalized by extending the single-antenna aided Differential Phase Shift Keying (DPSK) modulation scheme. Hence, the fundamental challenge of designing DSTBCs is outlined. Section 3.3 examines the family of DOSTBCs and explicitly shows how the orthogonality imposed may limit their applications. Hence, Section 3.4 proposes a novel class of DSTBCs, namely DLDCs based on the Cayley transform. In Section 3.5, we amalgamate Sphere Packing (SP) modulation with the DOSTBC design and propose a turbo-detected SP-aided DOSTBC scheme, aiming for operating at as low SNRs as possible at a given throughput. Facilitated by the design flexibility provided by the IRCC-coded IR-PLDCs of Chapter 2, Section 3.6 proposes a novel IRCC-coded IrRegular Precoded Differential Linear Dispersion Codes (IR-PDLDCs), which operates at high rates across a wide range of SNRs. We focus our attention on the specific restrictions introduced by the differential encoding structure, when designing the irregular system having multiple component codes. Finally, our concluding remarks are provided in Section 3.7.

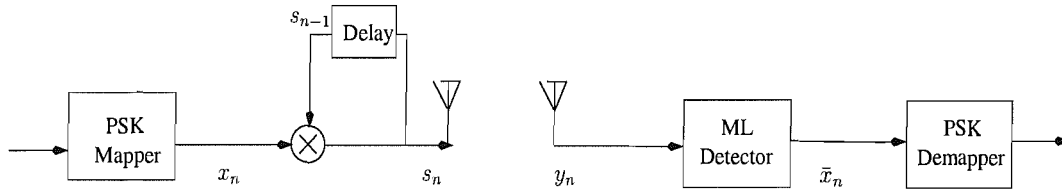


Figure 3.1: Schematic of the single-antenna aided DPSK scheme.

3.2 System Model

Before presenting the detailed design of DSTBCs, the concept of differential coding schemes designed for single transmit antenna scenarios is briefly reviewed [107]. Later in this section, we will generalize the single-antenna model to the MIMO environment and illustrate the specific constraints imposed by the differential encoding structure.

3.2.1 DPSK System Model for Single Antenna

Figure 3.1 portrays the schematic of the conventional DPSK modulation [107] designed for the single antenna aided systems. After the information bits have been mapped to a L -PSK symbol x_n , the n -th transmitted symbol s_n generated using differential encoding is given by:

$$\begin{cases} s_n = x_n & (n = 1), \\ s_n = s_{n-1} \cdot x_n & (n > 1). \end{cases} \quad (3.1)$$

The first symbol is an arbitrary reference symbol, which does not contain any information. Each differentially encoded symbol s_n is then transmitted over $T = 1$ time slot. At the receiver side, the corresponding received signal y_n seen in Figure 3.1 becomes:

$$y_n = h_{1,1} s_n + v_n, \quad (3.2)$$

where $h_{1,1}$ represents the CIR between the single transmit and receive antenna pair and v_n denotes the zero-mean complex-valued Gaussian random variable with variance σ_0^2 determined by SNR ρ .

Since the transmitted signals depend on each other, the ML detector of Figure 3.1 is capable of detecting the information bearing symbols x_n from successive received signals y_n . More explicitly, by combining Equations (3.1) and (3.2) we may have:

$$\begin{aligned} y_n &= h_{1,1} s_{n-1} x_n + v_n \\ &= (y_{n-1} - v_{n-1}) x_n + v_n \\ &= y_{n-1} x_n + \underbrace{v_n - v_{n-1} x_n}_{\hat{v}_n} \\ &= y_{n-1} x_n + \hat{v}_n. \end{aligned} \quad (3.3)$$

Observe in Equation (3.3) that x_n is related to the received signal y_n by the previous received signal y_{n-1} , thus the estimated symbol \bar{x}_n of Figure 3.1 can be obtained using ML estimation and it is given by:

$$\bar{x}_n = \arg \left\{ \min_{x_n \in L\text{-PSK}} (|y_n - y_{n-1}x_n|^2) \right\}. \quad (3.4)$$

Note that the equivalent noise \hat{v}_n of Equation (3.3) has a variance of $2\sigma_0^2$, which is responsible for the well-known 3dB SNR loss compared to its coherently detected counterpart having perfect CIR information.

The properties of the single-antenna aided DPSK scheme are summarized as follows:

- The information is differentially encoded between successive transmission symbols, thus the information can be recovered without the knowledge of the CIR, provided that it does not change substantially between them;
- A 3dB performance penalty is expected compared to its coherently detected counterpart, owing to the doubled noise variance encountered during the differential detection;
- The transmitted symbol s_n generated by differential encoding using Equation (3.1) remains an L -PSK symbol.

Following a similar design philosophy, the differentially encoded structure can be generalized to MIMO applications.

3.2.2 DSTBC System Model for Multiple Antennas

We consider a MIMO wireless communication system equipped with M transmit as well as N receive antennas, which transmits a signal matrix \mathbf{S}_n containing Q symbols during T time slots, as seen in Figure 3.2. During the transmission, the n -th block of information bits is mapped to a symbol vector $\mathbf{K}_n = [s_n^1, \dots, s_n^Q]^T$ containing Q symbols drawn from an L -PSK constellation. Then, \mathbf{K}_n is further coded by the 'Space-Time Coding' block of Figure 3.2, where the resultant space-time coded matrix \mathbf{X}_n spans M spatial- and T temporal-slots. Note that the mapping between \mathbf{K}_n and \mathbf{X}_n is unique. In order to avoid channel estimation, the information has to be encoded into consecutive transmission matrices and the differentially encoded transmission matrix \mathbf{S}_n is given by:

$$\begin{cases} \mathbf{S}_n = \mathbf{U}_n & (n = 1), \\ \mathbf{S}_n = \mathbf{S}_{n-1} \cdot \mathbf{X}_n & (n > 1), \end{cases} \quad (3.5)$$

where \mathbf{U}_n is the reference matrix containing dummy information. The matrix multiplication of Equation (3.5) requires \mathbf{X}_n to be a unitary matrix. Hence, we have $T = M$ and $\mathbf{U}_n \in \mathbb{C}^{M \times M}$,

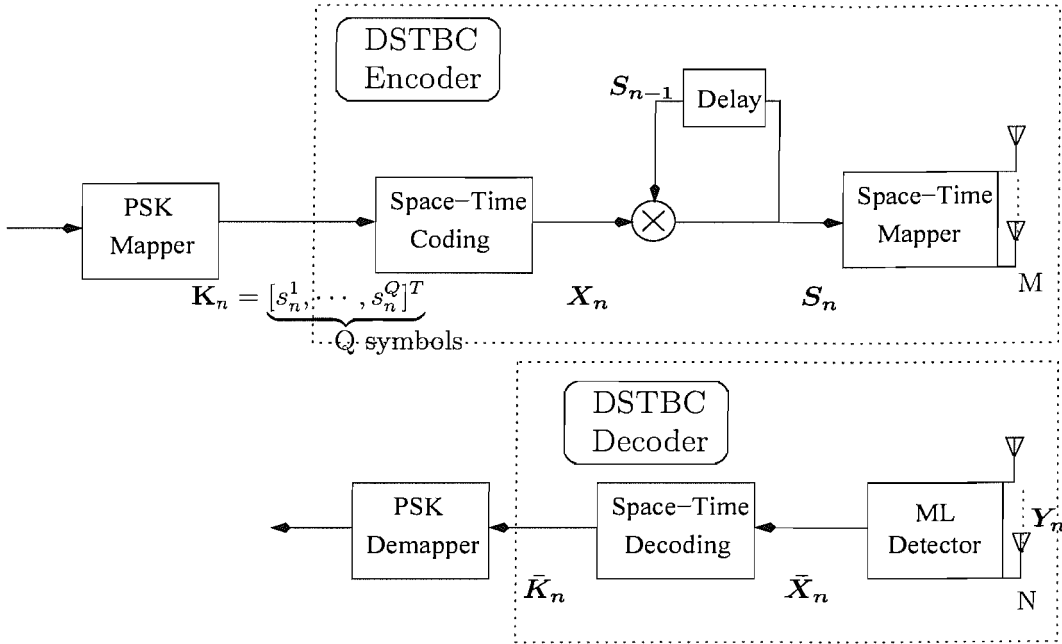


Figure 3.2: Schematic of a MIMO system equipped with M transmit and N receive antennas and employs DSTBCs, while transmitting Q symbols over T time slots using a differentially encoded space-time matrix \mathbf{S}_n .

$$\mathbf{X}_n \in \zeta^{M \times M} \text{ and } \mathbf{S}_n \in \zeta^{M \times M}.$$

The n -th received signal matrix \mathbf{Y}_n having a size of $(N \times M)$ elements becomes:

$$\mathbf{Y}_n = \mathbf{H}_n \mathbf{S}_n + \mathbf{V}_n, \quad (3.6)$$

where $\mathbf{V}_n \in \zeta^{N \times M}$ is assumed to be having independent samples of a zero-mean complex-valued Gaussian random process with variance σ_0^2 determined by SNR ρ . More importantly, $\mathbf{H}_n \in \zeta^{N \times M}$ represents the Rayleigh fading coefficients. We will assume that the scattering imposed by the propagation environment is sufficiently rich for each channel coefficients to be modelled as an i.i.d. zero-mean complex-valued Gaussian random variable having a common variance of 0.5 per real-valued dimension. Each channel of a transmit-receive antenna pair is assumed to be constant over T channel uses, which is then faded before the transmission of another block. The temporal correlation within each channel is governed by the normalized Doppler frequency f_d .

If the MIMO channel fades slowly, after combining Equations (3.5) and (3.6), we obtain:

$$\begin{aligned}
 \mathbf{Y}_n &= \mathbf{H}_n \mathbf{S}_{n-1} \mathbf{X}_n + \mathbf{V}_n \\
 &= (\mathbf{Y}_{n-1} - \mathbf{V}_{n-1}) \mathbf{X}_n + \mathbf{V}_n \\
 &= \mathbf{Y}_{n-1} \mathbf{X}_n + \underbrace{\mathbf{V}_n - \mathbf{V}_{n-1} \mathbf{X}_n}_{\hat{\mathbf{V}}_n}.
 \end{aligned} \quad (3.7)$$

Note that the CIR matrix \mathbf{H}_n does not appear in the above equation. This implies that as long as

the channel is approximately constant for $2T$ channel uses, the differential transmission scheme permits decoding without knowing the CIR.

Furthermore, the differential encoding of Equation (3.5) restricts the set of matrices \mathbf{X}_n to be unitary, otherwise, the product $\mathbf{S}_n = \mathbf{X}_n \mathbf{X}_{n-1} \cdots \mathbf{X}_1$ can go to zero, infinity, or both in different spatial and temporal directions. Moreover, when \mathbf{X}_n is unitary, the additive noise term

$$\hat{\mathbf{V}}_n = \mathbf{V}_n - \mathbf{V}_{n-1} \mathbf{X}_n \quad (3.8)$$

is statistically independent of \mathbf{X}_n having a variance of $2\sigma_0^2 \cdot \mathbf{I}$, which imposes the well-known 3dB penalty. Since the additive noise term $\hat{\mathbf{V}}_n$ has independent complex Gaussian entries, the ML detector of Figure 3.2 stacks two consecutive received matrices \mathbf{Y}_{n-1} and \mathbf{Y}_n and the information bearing matrix \mathbf{X}_n can be estimated using:

$$\bar{\mathbf{X}}_n = \arg \left\{ \min_{\mathbf{X}_n \in F} (||\mathbf{Y}_n - \mathbf{Y}_{n-1} \mathbf{X}_n||^2) \right\}, \quad (3.9)$$

given all the probabilities of \mathbf{X}_n . In fact, since each information vector \mathbf{K}_n contains Q symbols selected from the L -PSK constellation, the total number of information vector is:

$$F = L^Q. \quad (3.10)$$

Then, the 'space-time decoding' block of Figure 3.2 can recover the corresponding symbol vector \mathbf{K}_n by exploring the one-to-one relationship between \mathbf{K}_n and \mathbf{X}_n .

The employment of differential 'modulation' schemes, such as DPSK, enables the single-antenna-aided system to recover the transmitted information without the knowledge of the CIR. However, when extra spatial-dimension becomes available, owing to the employment of multiple antennas at both the transmitter and the receiver, the information can be differentially encoded using the previous symbols as reference in both the spatial and temporal dimensions, instead of using the classic differentially encoded modulation schemes. Hence, the symbols transmitted in the DSTBC system of Figure 3.2 are drawn from an L -PSK constellation, rather than from a 'Differential' L -PSK.

We now continue by offering a few remarks concerning the general DSTBC model of Figure 3.2.

- Compared to the single-antenna aided DPSK scheme, the DSTBC scheme of Figure 3.2 employs space-time block coding to explore all the available spatial and temporal slots.
- In order to carry out the differential encoding of Equation (3.5), the set of space-time coded matrices \mathbf{X}_n has to be unitary.

- The design of DSTBC is separated from the design of modulation, as seen in Figure 3.2. Hence, various modulation schemes can be employed.

3.2.3 Link Between STBCs and DSTBCs

Compared to the general STBC framework of Figure 2.1, the DSTBC structure portrayed in Figure 3.2 introduces a differential encoding unit, in order to forgo the burden of channel estimation. However, the differential encoding structure imposes a unitary constraint on the resultant space-time coded matrices. **In other words, the challenge of designing DSTBCs can be described as that of designing a family of STBCs, where all the space-time matrices are unitary.** From this point of view, it is straightforward to verify that DSTBCs inherit all the properties of STBCs. Most importantly, the *rank criterion* and *determinant criterion* detailed in Section 2.3.1 can be used to maximize the achievable spatial diversity gain and coding gain.

For the coherently detected STBCs, we assumed that the receiver evaluated the CIR with the aid of training sequences and that the channel coefficients are statistically independent under these conditions. We have shown in Equation (2.11) that for large SNRs ρ the coherent detection based MIMO capacity C_{MIMO} is approximately

$$C_{MIMO} \approx \min(M, N) \cdot \log_2 \left[\frac{\rho}{M} \right], \quad (\text{bits/sym/Hz}) \quad (3.11)$$

which implies that the capacity gain of the coherent-detection-aided multiple-antenna-assisted channel is $\min(M, N)$ (bits/sym/Hz) for every 3dB increase in the SNR. In order to address the scenario where the receiver has no *a-priori* channel knowledge apart from the AWGN variance, Zheng and Tse [25] found the capacity of this non-coherent channel scenario to be:

$$C_{MIMO}^{non} \approx \bar{M} \left(1 - \frac{\bar{M}}{\mathfrak{I}} \right) \cdot \log_2 \left[\frac{\rho}{\bar{M}} \right], \quad (\text{bits/sym/Hz}) \quad (3.12)$$

where $\bar{M} = \min(M, N, \mathfrak{I}/2)$ and \mathfrak{I} is the number of signalling intervals over which the channel may be deemed to be static. In [108], a detailed mutual information analysis is carried out between the coherent USTMs [19] and the non-coherent DUSTMs [29] under the assumption of $\mathfrak{I} = 2T$.

Equation (3.12) suggests that the capacity of the non-coherent MIMO channel is affected by its coherence time \mathfrak{I} . More explicitly, the non-coherent capacity of Equation (3.12) approaches the coherent capacity of Equation (3.11) upon increasing \mathfrak{I} and $\mathfrak{I} > 2M$. Note that this model assumes that the channel is constant for \mathfrak{I} signalling intervals and changes independently before the next. However, in our model presented in Section 3.2.2, we consider more realistic scenarios, where the complex-valued CIR taps remain constant for $\mathfrak{I} = M$ channel uses and the temporal correlation is governed by the normalized Doppler frequency f_d . Since there is no closed-form representation of the CCMC capacity and DCMC capacity of the non-coherent channel, it is difficult to

directly optimize DSTBCs from the capacity maximization perspective. Therefore, in this chapter we employ the conventional *rank criterion* and *determinant criterion* to optimize DSTBCs, rather than adopting a capacity-based approach in order to operate under various channel conditions.

3.3 Differential Orthogonal STBCs

In this section, we will demonstrate the philosophy of DSTBCs based on orthogonal design, namely the family of DOSTBCs. Similar to the OSTBCs detailed in Sections 2.3.2 to 2.3.5, the DOSTBCs' orthogonality facilitates low-complexity ML detection at the receivers. Inevitably, the orthogonal structure imposes various restrictions on the design of the space-time coded matrices \mathbf{X}_n of Figure 3.2.

3.3.1 Differential Alamouti Codes

We commence our discussion from the well-known Alamouti scheme [14], where $M = 2$ transmit antennas are employed. To simplify our discussion, the case of using $N = 1$ receive antenna is considered, although employing multiple receive antennas is straightforward. For example, given two arbitrary L -PSK symbols t^1 and t^2 , a \mathbf{G}_2 [14] space-time matrix can be written as:

$$\mathbf{G}_2(t^1, t^2) = \begin{pmatrix} t^1 & -t^{2*} \\ t^2 & t^{1*} \end{pmatrix}, \quad (3.13)$$

which is a unitary matrix.

The differential encoding method of [26] used for generating the n -th ($n > 1$) transmission matrix \mathbf{S}_n of Figure 3.2 using the incoming L -PSK symbol vector $\mathbf{K}_n = [s_n^1, s_n^2]^T$ can be written as:

$$\begin{pmatrix} t_n^1 & -t_n^{2*} \\ t_n^2 & t_n^{1*} \end{pmatrix} = \begin{pmatrix} t_{n-1}^1 & -t_{n-1}^{2*} \\ t_{n-1}^2 & t_{n-1}^{1*} \end{pmatrix} \cdot \begin{pmatrix} s_n^1 & -s_n^{2*} \\ s_n^2 & s_n^{1*} \end{pmatrix}, \quad (3.14)$$

which can be represented as:

$$\underbrace{\mathbf{G}_2(t_n^1, t_n^2)}_{\mathbf{S}_n} = \underbrace{\mathbf{G}_2(t_{n-1}^1, t_{n-1}^2)}_{\mathbf{S}_{n-1}} \cdot \underbrace{\mathbf{G}_2(s_n^1, s_n^2)}_{\mathbf{X}_n}. \quad (3.15)$$

The reference matrix \mathbf{U}_n ($n = 1$) transmitted during the first signalling block is also a \mathbf{G}_2 matrix obeying Equation (3.13), which contains two arbitrary symbols. When comparing Equation (3.15) to the general DSTBC encoding scheme of Equation (3.5), we observe that the challenge of designing a set of unitary space-time matrices \mathbf{X}_n is tackled by employing the well-known \mathbf{G}_2 matrices. Thus, low-complexity ML detection becomes feasible.

The received signal matrix \mathbf{Y}_n of Figure 3.2 can be written as $\mathbf{Y}_n = [y_n^1, y_n^2]$, where y_n^i denotes the received signal during the i -th time slot of the n -th block. Consequently, the orthogonal structure enables the receiver to decouple the symbol streams into independent symbols using linear combination, which is expressed as [26]:

$$\begin{pmatrix} \bar{s}_n^1 \\ \bar{s}_n^2 \end{pmatrix} = \begin{pmatrix} y_{n-1}^{1*} & y_{n-1}^2 \\ y_{n-1}^{2*} & -y_{n-1}^1 \end{pmatrix} \cdot \begin{pmatrix} y_n^1 \\ y_n^2 \end{pmatrix}. \quad (3.16)$$

Hence, the decoding statistics \bar{s}_n^1 and \bar{s}_n^2 may be expressed as:

$$\bar{s}_n^1 = (|h_{1,1}|^2 + |h_{1,2}|^2)(|t_{n-1}^1|^2 + |t_{n-1}^2|^2)s_n^1 + \hat{v}_n^1, \quad (3.17)$$

$$\bar{s}_n^2 = (|h_{1,1}|^2 + |h_{1,2}|^2)(|t_{n-1}^1|^2 + |t_{n-1}^2|^2)s_n^2 + \hat{v}_n^2, \quad (3.18)$$

where \hat{v}_n^i represents the i -th combined noise component encountered during the n -th received signal block. The employment of an L -PSK constellation together with the orthogonality constraint ensures that the term $(|t_{n-1}^1|^2 + |t_{n-1}^2|^2)$ remains a constant value. Hence, single-symbol ML decoding can be performed, provided that the channel's output power factor of $(|h_{1,1}|^2 + |h_{1,2}|^2)$ can be estimated. The estimation of the channel's output power requires a significantly lower complexity than that of the CIR itself. Observe that a transmit diversity order of $D_{tx} = 2$ has been achieved, since the chances are that even if $|h_{1,1}|^2$ is small, the independently faded $|h_{1,2}|^2$ value may not be.

3.3.1.1 Using QAM Constellations

As more bits are transmitted per channel use with the aid of higher-order constellations, the SNR disadvantage of L -PSK over L -QAM increases [24]. In order to reduce the associated SNR penalty, DSTBCs based on Alamouti's STBC using QAM constellations were proposed [36], which increase the minimum Euclidean distance compared to that of the identical-throughput PSK constellation.

The differential encoding process of [36] used to generate the n -th ($n > 1$) transmission matrix \mathbf{S}_n of Figure 3.2 employing the incoming L -QAM symbol vector $\mathbf{K}_n = [s_n^1, s_n^2]^T$ can be rewritten as:

$$\begin{pmatrix} t_n^1 & -t_n^{2*} \\ t_n^2 & t_n^{1*} \end{pmatrix} = \frac{1}{\theta} \begin{pmatrix} t_{n-1}^1 & -t_{n-1}^{2*} \\ t_{n-1}^2 & t_{n-1}^{1*} \end{pmatrix} \cdot \begin{pmatrix} s_n^1 & -s_n^{2*} \\ s_n^2 & s_n^{1*} \end{pmatrix}. \quad (3.19)$$

The difference between Equations (3.15) and (3.19) is the presence of the normalization factor given by $\theta = \sqrt{|t_{n-1}^1|^2 + |t_{n-1}^2|^2}$. Since QAM constellations does not maintain a constant modulus, the discrete amplitude of the symbols may render the peak power of the transmitted signals after differential encoding to become infinity or zero. Therefore, the introduction of the normalization

factor θ is necessary. Furthermore, Equation (3.19) can be expressed as follows:

$$\underbrace{\mathbf{G}_2(t_n^1, t_n^2)}_{\mathbf{S}_n} = \frac{1}{\theta} \cdot \underbrace{\mathbf{G}_2(t_{n-1}^1, t_{n-1}^2)}_{\mathbf{S}_{n-1}} \cdot \underbrace{\mathbf{G}_2(s_n^1, s_n^2)}_{\mathbf{X}_n}. \quad (3.20)$$

Again, the received signal matrix \mathbf{Y}_n is related to the transmission matrix \mathbf{S}_n using Equation (3.6), where we have $\mathbf{Y}_n = [y_n^1, y_n^2]$. The receiver employs the linear combination process of Equation (3.16) to derive the following decision statistics:

$$\bar{s}_n^1 = (|h_{1,1}|^2 + |h_{1,2}|^2) \cdot \theta \cdot s_n^1 + \hat{\sigma}_n^1, \quad (3.21)$$

$$\bar{s}_n^2 = (|h_{1,1}|^2 + |h_{1,2}|^2) \cdot \theta \cdot s_n^2 + \hat{\sigma}_n^2, \quad (3.22)$$

which implies that in addition to estimating the channel's output power ($|h_{1,1}|^2 + |h_{1,2}|^2$), the normalization factor θ also has to be estimated. According to [36], the normalization factor θ can be estimated by exploiting the knowledge of the received signal's auto-correlation function given by:

$$\theta \approx \sqrt{\mathbf{Y}_n \mathbf{Y}_n^H / (|h_{1,1}|^2 + |h_{1,2}|^2)}. \quad (3.23)$$

Hence, again simple ML estimation can be performed to recover the transmitted QAM symbols.

3.3.2 DOSTBCs for Four Transmit Antennas

Retaining the property of low-complexity single-stream ML detection is desirable, especially for systems employing a high number of transmit antennas. There are a number of solutions in the literature [27] [109], which are capable of achieving full spatial diversity. However, these reported schemes only work for real-valued constellations, such as BPSK. Let us now assume that we have $M = 4$ transmit and $N = 1$ receive antennas. The well-known $\mathbf{G}_4(t^1, t^2, t^3, t^4)$ space-time matrix of [15] [109] is defined as:

$$\mathbf{G}_4(t^1, t^2, t^3, t^4) = \begin{pmatrix} t^1 & t^2 & t^3 & t^4 \\ t^2 & -t^1 & -t^4 & t^3 \\ t^3 & t^4 & -t^1 & -t^2 \\ t^4 & -t^3 & t^2 & -t^1 \end{pmatrix}, \quad (3.24)$$

where we only retain the first four out of the eight time slots of the original \mathbf{G}_4 matrix, owing to the unitary constraint required by the differential encoding process.

Following the two-antenna based philosophy of Equation (3.15), given the symbol vector $\mathbf{K}_n = [s_n^1, s_n^2, s_n^3, s_n^4]^T$, the differential encoding of the original work [27] can be rewritten as:

$$\underbrace{\mathbf{G}_4(t_n^1, t_n^2, t_n^3, t_n^4)}_{\mathbf{S}_n} = \underbrace{\mathbf{G}_4(t_{n-1}^1, t_{n-1}^2, t_{n-1}^3, t_{n-1}^4)}_{\mathbf{S}_{n-1}} \cdot \underbrace{\mathbf{G}_4(s_n^1, s_n^2, s_n^3, s_n^4)}_{\mathbf{X}_n}. \quad (3.25)$$

Again, the transmission matrix \mathbf{S}_n and the set of space-time coded matrices \mathbf{X}_n all accrue form the unitary matrix \mathbf{G}_4 of Equation (3.24). The reference matrix $\mathbf{U}_n = \mathbf{G}_4(t_n^1, t_n^2, t_n^3, t_n^4)$ transmits four arbitrary BPSK symbols during the first signalling block of channel use.

After receiving the n -th signal matrix $\mathbf{Y}_n = [y_n^1, y_n^2, y_n^3, y_n^4]$, the orthogonality of the \mathbf{G}_4 scheme enables the receiver to separate the transmitted MIMO symbol streams into single decodable symbols after the following linear combination:

$$\begin{pmatrix} \bar{s}_n^1 \\ \bar{s}_n^2 \\ \bar{s}_n^3 \\ \bar{s}_n^4 \end{pmatrix} = \begin{pmatrix} y_{n-1}^1 & y_{n-1}^2 & y_{n-1}^3 & y_{n-1}^4 \\ -y_{n-1}^2 & y_{n-1}^1 & y_{n-1}^4 & -y_{n-1}^3 \\ -y_{n-1}^3 & -y_{n-1}^4 & y_{n-1}^1 & y_{n-1}^2 \\ -y_{n-1}^4 & y_{n-1}^3 & -y_{n-1}^2 & y_{n-1}^1 \end{pmatrix} \cdot \begin{pmatrix} y_n^1 \\ y_n^2 \\ y_n^3 \\ y_n^4 \end{pmatrix}. \quad (3.26)$$

Hence, the i -th ($i = 1, 2, 3, 4$) decision statistics can be derived by:

$$\bar{s}_n^i = (|h_{1,1}|^2 + |h_{1,2}|^2 + |h_{1,3}|^2 + |h_{1,4}|^2)s_n^i + \hat{\sigma}_n^i, \quad (3.27)$$

where a transmit diversity order of $D_{tx} = 4$ is attained.

Again, note that the original \mathbf{G}_4 matrix in [15] occupies eight time slots, but the \mathbf{G}_4 matrix adopted in Equation (3.24) only preserves the first four rows in the interest of satisfying the unitary constraint of Equation (3.5). The absence of the conjugate complex operation in \mathbf{G}_4 of Equation (3.24) prevents the transmission of complex-valued symbols, since the presence of the conjugation is essential for decoupling the complex-valued transmitted symbols. As an alternative, the simple sub-optimum method of [27] is adopted, which merges the two real-valued dimensions constituted by two transmit antennas into the real and imaginary part and then both of the resultant complex-valued symbols of $s_n^1 + is_n^2$ and $s_n^3 + is_n^4$ are transmitted by the four antennas. For each antenna, Pulse Amplitude Modulation (PAM) is employed.

3.3.3 DOSTBCs Based on QOSTBCs

In order to support high-rate communications, while benefitting from simple ML detection, the family of Differential Quasi-Orthogonal Space-Time Block Codes (DQOSTBCs) was proposed in [28] [110].

In order to support complex-valued modulated constellations in the context of four-antenna aided DSTBCs, the family of DQOSTBCs relax the orthogonality of the space-time matrix. Hence, the transmitted MIMO symbol streams can only be decoupled into a combination of a number of symbols, rather than into individual symbols, where each symbol-combination contains two

symbols. More explicitly, a (4×4) -element QOSTBC matrix [17] is defined as follows:

$$\mathbf{G}_{Q4}(t^1, t^2, t^3, t^4) = \begin{pmatrix} t^1 & -t^{2*} & t^3 & -t^{4*} \\ t^2 & t^{1*} & t^4 & t^{3*} \\ -t^{3*} & t^4 & t^{1*} & -t^2 \\ -t^{4*} & -t^3 & t^{2*} & t^1 \end{pmatrix} = \begin{pmatrix} \mathbf{G}_2(t^1, t^2) & \mathbf{G}_2(t^3, t^4) \\ -\mathbf{G}_2^*(t^3, t^4) & \mathbf{G}_2^*(t^1, t^2) \end{pmatrix}. \quad (3.28)$$

Observe that \mathbf{G}_{Q4} of Equation (3.28) is constructed using \mathbf{G}_2 matrices. Compared to the \mathbf{G}_4 matrix of Equation (3.24) employed for real-valued DOSTBCs, \mathbf{G}_{Q4} of Equation (3.28) introduces the conjugate operation, which potentially enables the employment of complex-valued constellations. In other words, \mathbf{G}_{Q4} of Equation (3.28) can be considered as the 'complex-valued' version of \mathbf{G}_4 , which is capable of supporting a high throughput.

Given a symbol vector $\mathbf{K}_n = [s_n^1, s_n^2, s_n^3, s_n^4]^T$ and assuming that $s_n^1, s_n^2, s_n^3, s_n^4$ are drawn from the same L -PSK constellation, the differential encoding process [110] of generating the n -th transmission matrix \mathbf{S}_n can be expressed as:

$$\underbrace{\mathbf{G}_{Q4}(t_n^1, t_n^2, t_n^3, t_n^4)}_{\mathbf{S}_n} = \underbrace{\mathbf{G}_{Q4}(t_{n-1}^1, t_{n-1}^2, t_{n-1}^3, t_{n-1}^4)}_{\mathbf{S}_{n-1}} \cdot \underbrace{\mathbf{G}_{Q4}(s_n^1, s_n^2, s_n^3, s_n^4)}_{\mathbf{X}_n}. \quad (3.29)$$

It is necessary to point out that although \mathbf{G}_{Q4} of Equation (3.28) itself is not a unitary matrix, it is constructed from the unitary matrix \mathbf{G}_2 of Equation (3.13). Hence, the multiplicative operation of Equation (3.29) is still valid.

Given the received signal matrix $\mathbf{Y}_n = [y_n^1, y_n^2, y_n^3, y_n^4]$, the receiver performs the following linear operations:

$$\begin{pmatrix} \bar{s}_n^1 \\ \bar{s}_n^2 \\ \bar{s}_n^3 \\ \bar{s}_n^4 \end{pmatrix} = \begin{pmatrix} y_{n-1}^1 & y_{n-1}^2 & y_{n-1}^3 & y_{n-1}^4 \\ -y_{n-1}^{2*} & -y_{n-1}^{1*} & y_{n-1}^{4*} & -y_{n-1}^{3*} \\ y_{n-1}^{3*} & y_{n-1}^{4*} & -y_{n-1}^{1*} & -y_{n-1}^{2*} \\ y_{n-1}^4 & -y_{n-1}^3 & -y_{n-1}^2 & y_{n-1}^1 \end{pmatrix} \begin{pmatrix} y_n^1 \\ y_n^{2*} \\ y_n^{3*} \\ y_n^4 \end{pmatrix}. \quad (3.30)$$

If we define

$$\phi_1 = |s_n^1|^2 + |s_n^2|^2 + |s_n^3|^2 + |s_n^4|^2, \quad (3.31)$$

$$\phi_2 = 2\text{real}\{s_n^1 s_n^{4*} - s_n^2 s_n^{3*}\}, \quad (3.32)$$

$$\phi_3 = |h_{1,1}|^2 + |h_{2,1}|^2 + |h_{3,1}|^2 + |h_{4,1}|^2, \quad (3.33)$$

$$\phi_4 = 2\text{real}\{h_{1,1} h_{4,1}^* - h_{2,1} h_{3,1}^*\}, \quad (3.34)$$

as well as

$$\psi_1 = \phi_1 \phi_3 + \phi_2 \phi_4, \quad (3.35)$$

$$\psi_2 = \phi_1 \phi_4 + \phi_2 \phi_3, \quad (3.36)$$

the resultant decision statistics after the linear combination of Equation (3.30) becomes:

$$\bar{s}_n^1 = \psi_1 s_n^1 + \psi_2 s_n^4 + \hat{\sigma}_n^1, \quad (3.37)$$

$$\bar{s}_n^2 = \psi_1 s_n^2 - \psi_2 s_n^3 + \hat{\sigma}_n^2, \quad (3.38)$$

$$\bar{s}_n^3 = \psi_1 s_n^3 - \psi_2 s_n^2 + \hat{\sigma}_n^3, \quad (3.39)$$

$$\bar{s}_n^4 = \psi_1 s_n^4 + \psi_2 s_n^1 + \hat{\sigma}_n^4, \quad (3.40)$$

where $\hat{\sigma}_n^i$ denotes the corresponding combined noise. Observe that the transmit symbols have been separated into two streams, namely $[s_n^1, s_n^4]$ and $[s_n^2, s_n^3]$. Hence, ML decoding can be employed to jointly decode each symbol group. In other words, DOSTBCs based on the quasi-orthogonal matrix can be considered as an alternative design, which achieves a higher rate than the DOSTBCs based on the orthogonal structure with a higher decoding complexity.

Note that the factor ϕ_1 of Equation (3.31) is a constant value, given that an L -PSK constellation is employed, while ϕ_3 of Equation (3.33) contributes the fourth spatial diversity order. However, the existence of ϕ_2 and ϕ_4 as the result of the relaxed orthogonality imposes interference on the decision statistics of Equations (3.37), (3.38), (3.39), (3.40), which potentially degrades the attainable diversity advantage. In fact, DQOSTBCs can only achieve second-order spatial transmit diversity [28] for a MIMO system employing $M = 4$ transmit antennas.

Recall that as mentioned in Section 2.3.3, QOSTBCs are capable of achieving full diversity by introducing a constellation rotation [89] [90]. Similarly, this technique can also be applied to the family of DQOSTBCs. For example, the symbol pair $[s_n^1, s_n^4]$ is chosen from the conventional L -PSK constellation, whereas the symbols $[s_n^2, s_n^3]$ are chosen from the L -PSK constellation rotated by $\pi/4$ degrees. However, the diversity gain improvement accrues from the modulation diversity [90], rather than from the spatial diversity addressed in this chapter.

3.3.4 DOSTBCs Based on LSTBCs and SSD-STBCs

The family of coherently detected LSTBCs [91] detailed in Section 2.3.4 based on the so-called dispersion structure of Equation (2.32), is another candidate to design the set of space-time coded matrices \mathbf{X}_n of Figure 3.2. We refer to as the Differential Linear Space-Time Block Codes (DL-STBCs). The orthogonality of the set of dispersion matrices guarantees that the L -PSK symbols transmitted in parallel can be decoupled into individual single-stream symbols.

More explicitly, given the n -th symbol vector $\mathbf{K}_n = [s_n^1, s_n^2, \dots, s_n^Q]^T$ containing Q single-stream symbols, the corresponding space-time coded matrix \mathbf{X}_n may be expressed as:

$$\mathbf{X}_n = \sum_{q=1}^Q (\alpha_n^q \mathbf{A}_q + j\beta_n^q \mathbf{B}_q), \quad (3.41)$$

where $s_n^q = \alpha_n^q + j\beta_n^q$. The dispersion matrices \mathbf{A}_q and \mathbf{B}_q have a size of $(M \times M)$ elements. According to Section 2.3.4, in order for the dispersion matrices to facilitate the separation of the transmission symbols, the set of matrices has to satisfy:

$$\begin{aligned} \mathbf{A}_{i_1} \mathbf{A}_i^H &= \mathbf{I}, \\ \mathbf{B}_{i_1} \mathbf{B}_i^H &= \mathbf{I}, \quad (i = i_1) \end{aligned} \quad (3.42)$$

$$\begin{aligned} \mathbf{A}_{i_1} \mathbf{A}_i^H &= -\mathbf{A}_i \mathbf{A}_{i_1}^H, \\ \mathbf{B}_{i_1} \mathbf{B}_i^H &= -\mathbf{B}_i \mathbf{B}_{i_1}^H, \quad (i \neq i_1) \end{aligned} \quad (3.43)$$

$$\mathbf{A}_{i_1} \mathbf{B}_i^H = \mathbf{B}_i \mathbf{A}_{i_1}^H. \quad (1 < i, i_1 < Q) \quad (3.44)$$

It is straightforward to check that under the above orthogonality constraints \mathbf{X}_n is always a unitary matrix. Hence, the differential encoding of Equation (3.5) can be performed. The reference matrix is given by $\mathbf{U}_n = \mathbf{I}$, where \mathbf{I} denotes an identity matrix having a size of $(M \times M)$.

Again, the orthogonality of the dispersion matrices allow as to avoid the joint detection of Q symbols. Instead, each transmitted symbol can be estimated individually by calculating [111]:

$$\bar{s}_n^q = \arg \left\{ \min_{s_n^q \in L-PSK} (Real\{tr(\mathbf{Y}_n^H \mathbf{Y}^{n-1} \mathbf{A}_q)\} \alpha_n^q + Real\{tr(\mathbf{Y}_n^H \mathbf{Y}^{n-1} j \mathbf{B}_q)\} \beta_n^q) \right\}. \quad (3.45)$$

The so-called Single-Symbol Decodable STBCs (SSD-STBCs) detailed in Section 2.3.5 obey the same dispersion structure as that of LSTBCs. Furthermore, these two class of STBCs share the same set of constraints on the dispersion matrices expressed as in Equations (3.42), (3.43) and (3.44). The only difference is that SSD-STBCs require $i \neq i_1$ in Equation (3.44). It is plausible that the resultant space-time coded matrices \mathbf{X}_n remain unitary, therefore the standard differential encoding/decoding processes are still applicable. The resultant schemes are often referred to as Differential Single-Symbol-Decodable Space-Time Block Codes (DSSD-STBCs) [112] in the literature.

3.3.5 Performance Results

This section presents the BER simulation results for the DOSTBC schemes outlined in Sections 3.3.1 to 3.3.4. All the system parameters are listed in Table 3.1, unless otherwise specified.

Figure 3.3 portrays the BER performance of a family of DOSTBCs having $M = 2$ transmit and $N = 1$ receive antennas employing various modulation schemes, when communicating over i.i.d. Rayleigh fading channels having a normalized Doppler frequency of $f_d = 10^{-3}$. The orthogonal generator matrices of Equations (3.13) and (3.19) were used. In order to gauge the achievable BER performance, the coherently detected Alamouti's scheme [14] using BPSK modulation is

Table 3.1: System parameters for the DOSTBC scheme of Figure 3.2.

Modulation	L -PSK or L -QAM
Mapping	Gray mapping
Number of transmit antennas (M)	2
Number of receive antennas (N)	1
Normalized Doppler frequency	$f_d = 10^{-2}$ or 10^{-3}
Detector	ML of Equation (3.9)

plotted as the benchmark. Observe in Figure 3.3 that the DOSTBC scheme employing BPSK modulation suffers a 3dB SNR loss compared to its coherent counterpart, owing to the doubled noise variance discussed in Section 3.2. Naturally, DOSTBCs employing high-order modulation schemes require more transmit power in order to maintain a certain BER performance. Observe in Figure 3.3 further that all the curves exhibit similar shapes, which implies that all of them are capable of achieving a full transmit diversity order of $D_{tx} = 2$. The SNR advantage of L -QAM over the corresponding L -PSK constellation render the QAM scheme our preferred choice in the case of high rate communications, which is a benefit of having larger distances among the QAM constellation points at a given average power.

Figure 3.4 characterizes the family of DOSTBCs using the generator matrices of Equations (3.13) and (3.24) employing $M = 1, 2, 3, 4$ transmit and $N = 1$ receive antennas, when communicating over Rayleigh fading channels having a normalized Doppler frequency of $f_d = 10^{-3}$. The corresponding differential encoding/decoding processes are described in Sections 3.3.1 to 3.3.4. Observe that a diversity order of $D = 1, 2, 3$ and 4 is achieved, respectively. Unsurprisingly, less transmit power is required for DOSTBCs having a higher order diversity to maintain a specific BER level, which is a benefit of the higher complexity associated with the increased number of antennas.

Figure 3.5 characterizes a class of BPSK modulated DOSTBCs using the generator matrix of Equation (3.13) employing $M = 2$ transmit and $N = 1, 2, 3, 4$ receive antennas, for transmission over Rayleigh fading channels encountering a normalized Doppler frequency of $f_d = 10^{-3}$. Observe that the increased number of receive antennas substantially boost the total attainable spatial diversity, since a diversity order of $D = 2, 4, 6, 8$ is achieved.

The effect of temporal channel correlation is quantified in Figure 3.6, where we employ a BPSK modulated DOSTBC scheme having $M = 2$ transmit and $N = 1$ receive antennas. The grade of temporal channel correlation is governed by the normalized Doppler frequencies f_d . Ideally, the differential decoding procedure requires two consecutive transmission blocks to experience the

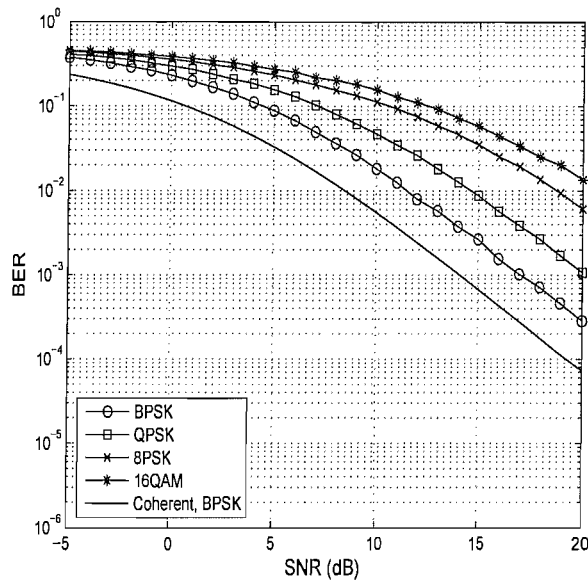


Figure 3.3: BER of a family of DOSTBCs of Figure 3.2 using the generator matrices of Equations (3.13) and (3.19), when employing various modulation schemes and communicating over i.i.d. Rayleigh fading channels having $f_d = 10^{-3}$. All the system parameters were summarized in Table 3.1.

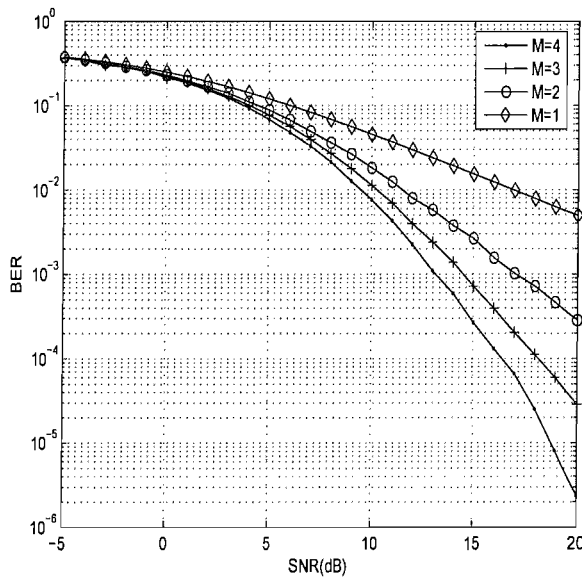


Figure 3.4: BER of a family of BPSK modulated DOSTBCs of Figure 3.2 using the generator matrices of Equations (3.13) and (3.24) having $M = 1, 2, 3, 4$ and $N = 1$ antennas, when communicating over i.i.d. Rayleigh fading channels having $f_d = 10^{-3}$. All the system parameters were summarized in Table 3.1.

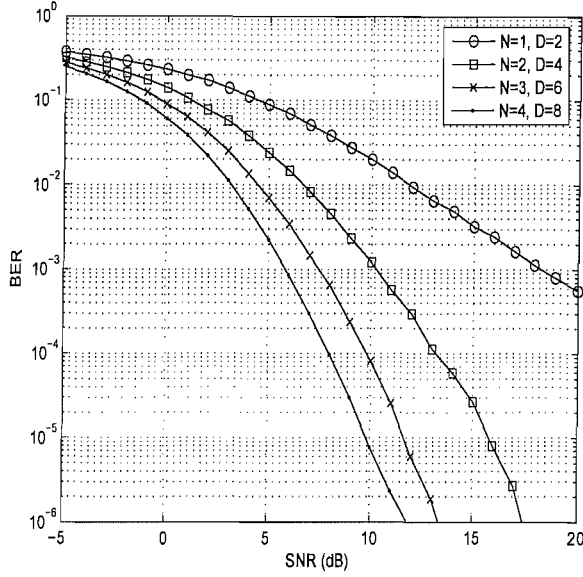


Figure 3.5: BER of a family of BPSK modulated DOSTBCs of Figure 3.2 using the generator matrix of Equation (3.13) employing $M = 2$ transmit and $N = 1, 2, 3, 4$ receive antennas, when communicating over i.i.d. Rayleigh fading channels having $f_d = 10^{-3}$. All the system parameters were summarized in Table 3.1.

same fading envelope. For example, when each block occupies $T = 2$ time slots, the fading has to be constant for four time slots, while for the four transmit antenna aided DOSTBC requiring $T = 4$ time slots, a constant fading envelope has to be experienced for eight time slots. However, when we encounter a rapidly fading environment, this requirement may not be satisfied. Figure 3.6 explicitly plots the BER degradation imposed by rapid fading. When the channels exhibit relatively slow fading, i.e. $f_d = 10^{-3}$, the best attainable BER performance is recorded. On the other hand, when the normalized fading rate reaches $f_d = 10^{-2}$, a significant BER degradation has already been observed. As to very rapid fading, such as $f_d = 0.04$, a BER floor above 10^{-2} has occurred. This implies that MIMO channels having a high coherence time \Im potentially improve the performance of DOSTBCs in comparison to rapid fading. Indeed, the non-coherent MIMO channel's capacity of Equation (3.12) approaches the coherent MIMO channel's capacity expressed in Equation (3.11), when the value of \Im is increased.

All the above results are based on the assumption that all the channels are faded independently. However, this assumption may not be readily satisfied, owing to the lack of sufficient antenna spacing at the mobile handsets. Hence, Figure 3.7 investigates the attainable BER performance of the BPSK-modulated DOSTBC scheme having $M = 2$ and $N = 1$ antennas, when communicating over spatially correlated Rayleigh fading channels encountering a normalized Doppler frequency of $f_d = 10^{-3}$. The spatial correlation model proposed in [113] was adopted, where the inter-

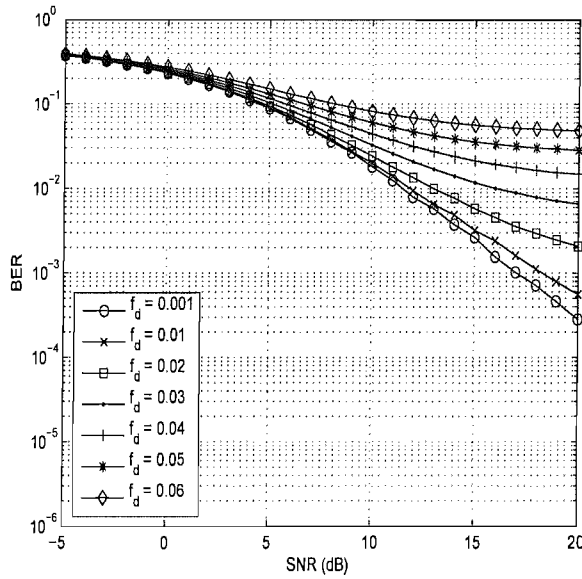


Figure 3.6: BER of a BPSK modulated DOSTBC scheme of Figure 3.2 using the generator matrix of Equation (3.13), when communicating over i.i.d. Rayleigh fading channels having various normalized Doppler frequencies f_d . All the system parameters were summarized in Table 3.1.

antenna correlation is determined by the correlation coefficient δ . Furthermore, $\delta = 1$ implies that the two antennas's signals are perfectly correlated, while $\delta = 0$ represents the channels that are independently faded. Observe in Figure 3.7 that when we have $\delta = 0$, the best BER performance is observed. When the channel's fading correlation becomes higher, the associated BER degradation becomes more significant. When the spatial channels become identical as characterized by $\delta = 1$, the associated BER performance becomes identical to a single-antenna aided scheme using the Differential-BPSK constellation.

3.3.6 Summary

At this stage, it is beneficial to summarize the advantages and drawbacks of DOSTBCs detailed in Sections 3.3.1 to 3.3.4, before we move on to the more general structure of Differential Linear Dispersion Codes (DLDCs). More explicitly, the benefits and constraints are summarized as follows:

- The number of time slots T used per transmission block has to be equal to M , a constraint which is imposed by the differential encoding structure of Equation (3.5);
- The number of symbols Q transmitted per space-time block is determined by the degree of orthogonality possessed by the space-time matrix \mathbf{S}_n ;

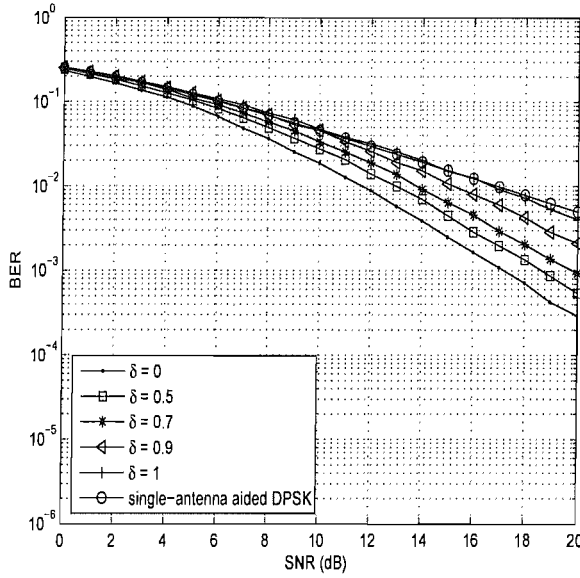


Figure 3.7: The effect of spatial correlation for a BPSK modulated DOSTBC scheme of Figure 3.2 using the generator matrix of Equation (3.13), when communicating over Rayleigh fading channels having a normalized Doppler frequency of $f_d = 10^{-3}$. All the system parameters were summarized in Table 3.1.

- The number of transmit antennas M used in Figure 3.2 is limited and this constraint was imposed by the orthogonal design;
- The number of receive antennas N in Figure 3.2 is unrestricted;
- The power-related expressions have to be estimated, as exemplified by the channel's output power in Section 3.3.1.1 and the normalization factors considered in Section 3.3.3.

Note that apart from the constraint of $T = M$, all the other constraints are imposed by the orthogonal structure, such as Equations (3.13) and (3.24). Based on the general LDC framework detailed in Chapter 2, in the following section we propose a family of DLDCs, which does not impose any constraints on the parameters Q and M of Figure 3.2 and avoids the estimation of the power-related factors in Sections 3.3.1.1 and 3.3.3.

3.4 Differential Linear Dispersion Codes

The family of DLDCs proposed in this section inherits the design flexibility of the LDCs by adopting a non-orthogonal structure for the space-time coding matrix. More particularly, in analogy to its non-differential counterpart, a DLDC($MNTQ$) scheme describes a differential coding scheme suitable for an $(M \times N)$ -element MIMO configuration, while having a symbol rate of $R_{DLDC} = \frac{Q}{T}$.

3.4.1 Evolution to a Linear Structure

One of the early attempts in the literature to address the challenge of designing a set of unitary matrices \mathbf{X}_n for the scheme of Figure 3.2 is constituted by the family of DUSTM schemes proposed simultaneously in [20] [37] and [29]. A distinctive feature of DUSTM is that no orthogonality is imposed on the space-time coded matrix. The DUSTM schemes proposed in [37] and [29] were shown to have a good BER performance [30], when the constellation of matrices used for transmission form a group under the matrix multiplication of Equation (3.5). However, the philosophy of the DUSTMs is to directly design $F = L^Q$ number of space-time matrices \mathbf{X}_n by maximizing the *rank criterion* of Equation (2.26) and the *determinant criterion* of Equation (2.27). Hence, this design problem becomes intractable, since the objective function may be non-convex and the associated search space increases exponentially with both the constellation size and the number of antennas. Although substantial efforts have been made [30] [114] to simplify the design of differential space-time constellation matrices, the optimization of high-order DUSTM schemes remains a challenging problem.

In Chapter 2, we have demonstrated that the family of LDCs transforms the design of $F = L^Q$ number of space-time matrices to the design of a single Dispersion Character Matrix (DCM) χ , as seen in Equation (2.16). The DCM fully and uniquely specifies the characteristics of a particular LDC scheme. Similarly, by introducing the linear dispersion structure of Equation (3.46) into the design of differential space-time transmission schemes, the resultant DLDCs can also be fully described by a single DCM χ . Therefore, the problem of designing F number of space-time matrices for describing the DUSTMs can be simplified to that of designing a single matrix χ for the DLDCs.

Furthermore, Figure 3.8 illustrates the classification of various DSTBCs and highlights that the design of STBCs and DSTBCs is linked by the unitary constraint of Equation (3.5). Provided the discussions of Section 2.3, it is straightforward to show that DLDCs subsume the family of DOSTBCs, which impose different degrees of orthogonality on the space-time matrix. With the aid of the non-orthogonal structure of Equation (3.46), DLDCs become capable of supporting arbitrary $(M \times N)$ element MIMO antenna configurations and of supporting flexible throughput. More explicitly, given a symbol vector $\mathbf{K}_n = [s_n^1, \dots, s_n^Q]^T$, the linear dispersion structure of the space-time coded matrix $\tilde{\mathbf{X}}_n \in \zeta^{M \times M}$ can be written as:

$$\tilde{\mathbf{X}}_n = \sum_{q=1}^Q \mathbf{A}_q s_n^q, \quad (3.46)$$

which is a weighted superposition of the corresponding dispersion matrices $\mathbf{A}_q \in \zeta^{M \times M}$. The resultant linearly combined matrix $\tilde{\mathbf{X}}_n$ has to be unitary. All the \mathbf{A}_q matrices can be specified using

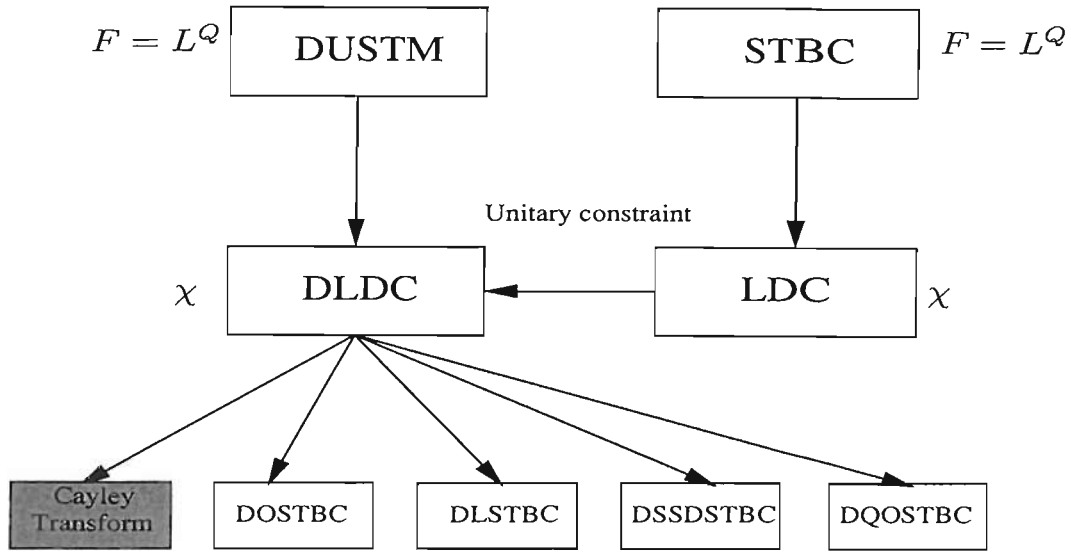


Figure 3.8: Classification of DSTBC techniques. The corresponding coherently detected schemes were classified in Figure 2.16.

the DCM χ defined by:

$$\chi = [vec(\mathbf{A}_1), vec(\mathbf{A}_2), \dots, vec(\mathbf{A}_Q)]. \quad (3.47)$$

However, the construction of a unitary matrix $\tilde{\mathbf{X}}_n$ obeying the linear combination structure of Equation (3.46) is challenging, because even if each individual dispersion matrix A_q is a unitary matrix, there is no guarantee that their weighted sum $\tilde{\mathbf{X}}_n$ will automatically be a unitary matrix.

3.4.2 Differential LDCs Based on the Cayley Transform

The challenge of constructing a set of unitary matrices for differential encoding was addressed in [33] [115], where the Cayley transform was employed. In Figure 3.9, we show the schematic of the DLDC scheme based on the Cayley transform. Compared to the general DSTBC framework of Figure 3.2, the Cayley transform [33] [116] of Figure 3.9 provides an efficient way of projecting the linearly-structured matrix $\tilde{\mathbf{X}}_n$ into a unique unitary matrix \mathbf{X}_n , which potentially facilitates the differential encoding. Hence, the DLDCs generated using the Cayley transform remain a subset of the family of DLDCs, as seen in Figure 3.8.

3.4.2.1 The Cayley Transform

The philosophy behind DLDCs based on the Cayley transform is to design a set of linear-structured Hermitian space-time matrices $\tilde{\mathbf{X}}_n$ obeying Equation (3.46) and to uniquely map the resultant Hermitian matrices to the unitary matrices \mathbf{X}_n of Figure 3.9. Designing Hermitian space-time matrices is attractive, since they are linear and hence the weighted sum of a number of Hermitian matrices

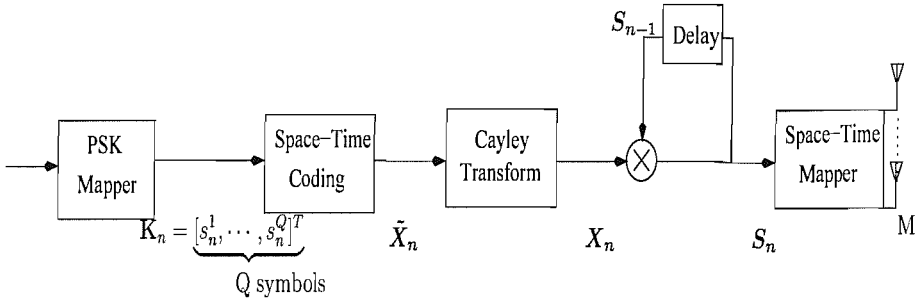


Figure 3.9: Schematic of a DLDC($MNTQ$) scheme equipped M transmit and N receive antennas employs Cayley transform, while transmitting Q symbols over T time slots using \mathbf{S}_n .

remains also a Hermitian matrix, provided that the weighting coefficients are real-valued.

The Cayley transform creates a unique mapping between a Hermitian matrix and a unitary matrix. More explicitly, the Cayley transform of the complex-valued $(M \times M)$ -element matrix $\tilde{\mathbf{X}}_n$ of Equation (3.46) is defined as [33]:

$$\mathbf{X}_n = (\mathbf{I} - j\tilde{\mathbf{X}}_n)(\mathbf{I} + j\tilde{\mathbf{X}}_n)^{-1}, \quad (3.48)$$

where \mathbf{I} is the $(M \times M)$ -element identity matrix and $j\tilde{\mathbf{X}}_n$ is assumed to have no eigenvalues at -1 in order to ensure that the $(\mathbf{I} + j\tilde{\mathbf{X}}_n)^{-1}$ item of Equation (3.48) exists. Note that $(\mathbf{I} - j\tilde{\mathbf{X}}_n)$, $(\mathbf{I} + j\tilde{\mathbf{X}}_n)$, $(\mathbf{I} - j\tilde{\mathbf{X}}_n)^{-1}$ and $(\mathbf{I} + j\tilde{\mathbf{X}}_n)^{-1}$ all commute. Hence, there are other equivalent ways to write this transform. The resultant matrix \mathbf{X}_n is unitary, because

$$\begin{aligned} \mathbf{X}_n \mathbf{X}_n^H &= (\mathbf{I} - j\tilde{\mathbf{X}}_n)(\mathbf{I} + j\tilde{\mathbf{X}}_n)^{-1}[(\mathbf{I} - j\tilde{\mathbf{X}}_n)(\mathbf{I} + j\tilde{\mathbf{X}}_n)^{-1}]^H \\ &= (\mathbf{I} - j\tilde{\mathbf{X}}_n)(\mathbf{I} + j\tilde{\mathbf{X}}_n)^{-1}(\mathbf{I} - j\tilde{\mathbf{X}}_n)^{-1}(\mathbf{I} + j\tilde{\mathbf{X}}_n) \\ &= \mathbf{I}, \end{aligned} \quad (3.49)$$

where we exploit the fact that $\tilde{\mathbf{X}}_n$ is Hermitian. The employment of the Cayley transform appears promising, because it is a unique one-to-one transform, which can be inverted to yield

$$j\tilde{\mathbf{X}}_n = (\mathbf{I} - \mathbf{X}_n)(\mathbf{I} + \mathbf{X}_n)^{-1}, \quad (3.50)$$

provided that the inverse exists or, equivalently, assuming that $j\tilde{\mathbf{X}}_n$ has no eigenvalue at -1 . Some important properties of the Cayley transform are listed as follows [33]:

- (Unique mapping) A matrix with no eigenvalues at -1 , such as $j\tilde{\mathbf{X}}_n$ of Equation (3.48), is unitary if and only if its Cayley transform is a skewed-Hermitian matrix¹. For the proof of this property please refer to [33];

¹A square matrix \mathbf{A} is said to be skewed-Hermitian if it satisfies the relation $\mathbf{A}^H = -\mathbf{A}$. A skewed-Hermitian matrix can be obtained by $j\mathbf{A}$, provided that \mathbf{A} is a Hermitian matrix.

- (Eigenvalues) The matrix $j\tilde{\mathbf{X}}_n$ and its Cayley transform \mathbf{X}_n commute. Hence they have the same eigenvectors, while their eigenvalues denoted by μ_i and ∇_i obey:

$$\mu_i = \frac{1 - \nabla_i}{1 + \nabla_i}. \quad (3.51)$$

For the proof of this property please refer also to [33];

- (Diversity) A set of unitary matrices \mathbf{X}_n is referred to as fully diverse, which hence satisfies the *rank criterion* of Equation (2.26), if and only if its Cayley transform $j\tilde{\mathbf{X}}_n$ is also fully diverse. This allows the resultant DLDC schemes to achieve full diversity. Again, for the proof of this property please refer to [33].

Hence, the Cayley transform is capable of preserving the characteristics of the Hermitian space-time matrices, when projecting them to unitary matrices.

It is necessary to point out a constraint imposed by designing in the Hermitian space. More precisely, real-valued modulated symbols s_q have to be employed in Equation (3.46) to ensure that the Cayley transformed Hermitian space-time matrix does result in a linear unitary matrix.

3.4.2.2 Differential Encoding/Decoding

With the aid of the Cayley transform introduced in Section 3.4.2.1, the differential encoding / decoding process can be further refined. More explicitly, when we have a real-valued modulated symbol vector $\mathbf{K}_n = [s_1, \dots, s_Q]^T$, the Hermitian space-time coded matrix $\tilde{\mathbf{X}}_n$ of Equation (3.46) is projected to a unitary matrix using the Cayley transform of Equation (3.48). Thus, the resultant unitary matrix \mathbf{X}_n becomes suitable for the differential encoding process of Equation (3.5).

Given the received signal matrix \mathbf{Y}_n and assuming that the channel's envelope remains constant over two consecutive transmission blocks, the resultant differential relationship can be expressed as:

$$\begin{aligned} \mathbf{Y}_n &= \mathbf{H}_n \mathbf{S}_{n-1} \mathbf{X}_n + \mathbf{V}_n \\ &= (\mathbf{Y}_{n-1} - \mathbf{V}_{n-1}) \mathbf{X}_n + \mathbf{V}_n \\ &= \mathbf{Y}_{n-1} \mathbf{X}_n + \mathbf{V}_n - \mathbf{V}_{n-1} \mathbf{X}_n. \end{aligned} \quad (3.52)$$

Then, conventional ML estimation can be performed as:

$$\tilde{\mathbf{X}}_n = \arg \left\{ \min_{\mathbf{X}_n \in F} (||\mathbf{Y}_n - \mathbf{Y}_{n-1} \mathbf{X}_n||^2) \right\}. \quad (3.53)$$

The above detection method requires the receiver to carry out the Cayley transform in order to generate the candidate unitary matrix \mathbf{X}_n , which may impose an excessive decoding complexity at the receiver.

However, we can avoid the calculation of the Cayley transform of Equation (3.48) upon multiplying both sides of Equation (3.52) by $(\mathbf{I} + j\tilde{\mathbf{X}}_n)$, yielding

$$\begin{aligned} \mathbf{Y}_n(\mathbf{I} + j\tilde{\mathbf{X}}_n) &= \mathbf{Y}_{n-1}(\mathbf{I} - j\tilde{\mathbf{X}}_n) + \mathbf{V}_n(\mathbf{I} + j\tilde{\mathbf{X}}_n) - \mathbf{V}_{n-1}(\mathbf{I} - j\tilde{\mathbf{X}}_n) \\ \underbrace{\mathbf{Y}_n - \mathbf{Y}_{n-1}}_{\hat{\mathbf{Y}}_n} &= \underbrace{-(\mathbf{Y}_n + \mathbf{Y}_{n-1})i\tilde{\mathbf{X}}_n}_{\hat{\mathbf{H}}_n\tilde{\mathbf{X}}_n} + \underbrace{-\mathbf{V}_n(\mathbf{I} + j\tilde{\mathbf{X}}_n) - \mathbf{V}_{n-1}(\mathbf{I} - j\tilde{\mathbf{X}}_n)}_{\hat{\mathbf{V}}_n}, \end{aligned} \quad (3.54)$$

The equivalent received signal matrix $\hat{\mathbf{Y}}_n$ and the equivalent CIR matrix $\hat{\mathbf{H}}_n$ in Equation (3.54) are both determined by the pair of consecutive received signal matrices \mathbf{Y}_n and \mathbf{Y}_{n-1} . The corresponding noise matrix $\hat{\mathbf{V}}_n$ has independent columns with a covariance of:

$$\hat{N}_0 = 2\sigma_0^2(\mathbf{I} + \tilde{\mathbf{X}}_n^2). \quad (3.55)$$

Furthermore, the linearity of the Hermitian matrix $\tilde{\mathbf{X}}_n$ of Equation (3.46) enables us to apply the vertical stacking operation $\text{vec}()$ to Equation (3.54), which results in:

$$\hat{\mathbf{Y}}_n = \bar{\mathbf{H}}_n\chi\mathbf{K}_n + \bar{\mathbf{V}}_n, \quad (3.56)$$

where $\hat{\mathbf{Y}}_n \in \zeta^{NT \times 1}$, $\bar{\mathbf{H}}_n \in \zeta^{NT \times MT}$, $\chi \in \zeta^{MT \times Q}$, $\mathbf{K}_n \in \zeta^{Q \times 1}$, $\bar{\mathbf{V}}_n \in \zeta^{NT \times 1}$ and $\bar{\mathbf{H}}_n$ in Equation (3.56) is given by:

$$\bar{\mathbf{H}}_n = \mathbf{I} \otimes \hat{\mathbf{H}}_n. \quad (3.57)$$

Thus, the simplified differential ML detection becomes:

$$\bar{\mathbf{K}}_n = \arg \left\{ \min_{\mathbf{K}_n \in F} (||\hat{\mathbf{Y}}_n - \bar{\mathbf{H}}_n\chi\mathbf{K}_n||)^2 \right\}. \quad (3.58)$$

This is commonly referred to as the 'linearized ML detector' in the literature [33]. Since the resultant noise variance of Equation (3.55) becomes $\hat{N}_0 > 2\sigma_0^2\mathbf{I}$, the 'linearized ML detector' suffers from a further performance loss compared to the conventional differential ML detection of Equation (3.53).

We have argued in Section 3.2.3 that the main challenge of designing DSTBCs is to construct a set of space-time matrices obeying the unitary constraint of Equation (3.5). From this point of view, the problem of designing DSTBCs is related to that of STBCs. Therefore, it is straightforward to show that the LDCs' diversity property formulated in Theorem 3 is directly applicable to the DLDCs, where the maximum achievable diversity is $N \cdot \min(M, T)$. Since the differential encoding process restricts us to $T = M$, the maximum achievable spatial diversity order of the DLDCs becomes $D = NM$. The optimization of the DSTBCs from the capacity maximization perspective is challenging, because the capacity also depends on the temporal correlation of the channel. Therefore, the conventional *rank criterion* of Equation (2.26) and the *determinant criterion* of Equation (2.27) detailed in Section 2.3.1 are adopted in order to optimize the DLDCs based

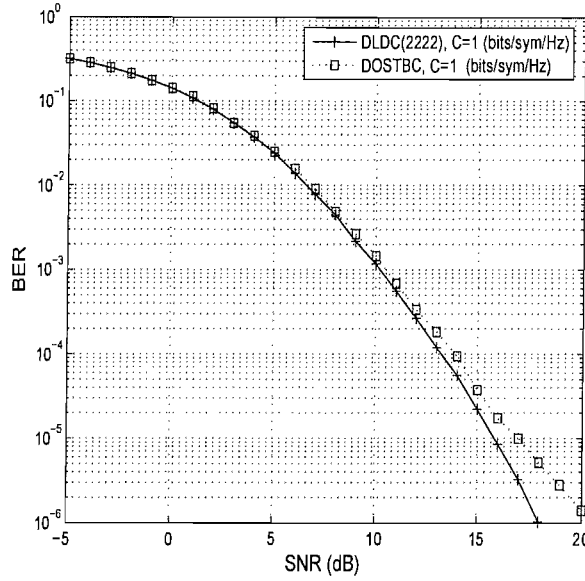


Figure 3.10: BER comparison of the DLDC(2222) of Figure 3.9 and the DOSTBC of [26] using BPSK modulation as well as an ML detector, when transmitting over i.i.d. Rayleigh fading channels having $f_d = 10^{-2}$.

on the Cayley transform. More explicitly, we randomly generate Q number of Hermitian dispersion matrices, where each matrix element obeys the Gaussian distribution. Hence, the achievable diversity order and coding gain of this particular DLDC($MNTQ$) scheme, which was portrayed in Figure 3.9, are examined after the Cayley transform. The specific code having the highest diversity order as well as coding gain is selected for the particular DLDC($MNTQ$) scheme. Throughout our investigations, we found that typically 100,000 random dispersion matrix search steps are required to generate a DLDC having a good BER performance.

3.4.2.3 Examples of DLDCs Based on the Cayley Transform

Let us consider a simple system equipped with $M = 2$ transmit as well as $N = 2$ receive antennas and having an effective throughput of $C = 1$ (bits/sym/Hz). Hence, a DLDC(2222) scheme obeying Figure 3.9 and transmitting $Q = 2$ BPSK modulated symbols during $T = 2$ channel uses, is required to achieve the target throughput. According to the optimization method outlined in Section 3.4.2.2, a particular choice of two Hermitian dispersion matrices are

$$\mathbf{A}_1 = \begin{pmatrix} -0.580 & -0.262 + j0.308 \\ -0.262 - j0.308 & 0.580 \end{pmatrix}, \quad (3.59)$$

and

$$\mathbf{A}_2 = \begin{pmatrix} 0.404 & -0.366 + j0.450 \\ -0.366 - j0.450 & -0.404 \end{pmatrix}. \quad (3.60)$$

Therefore, the n -th space-time coded matrices $\tilde{\mathbf{X}}_n$ of Figure 3.9 becomes:

$$\tilde{\mathbf{X}}_n = \mathbf{A}_1 s_n^1 + \mathbf{A}_2 s_n^2, \quad (3.61)$$

where we have $s_n^1, s_n^2 \in [-1, 1]$. Hence, the Cayley transform of Equation (3.48) is employed to project the weighted Hermitian matrix $\tilde{\mathbf{X}}_n$ into a unitary matrix. The resultant four candidate unitary space-time coded matrices \mathbf{X}_n^i ($i = 1, 2, 3, 4$) of Figure 3.9 are:

$$\begin{aligned} \mathbf{X}_n^1 &= \begin{pmatrix} 0 - j0.176 & -0.758 - j0.628 \\ 0.758 - j0.629 & 0 + j0.176 \end{pmatrix}, \\ \mathbf{X}_n^2 &= \begin{pmatrix} 0 + j0.176 & 0.758 + j0.628 \\ -0.758 + j0.629 & 0 - j0.176 \end{pmatrix}, \\ \mathbf{X}_n^3 &= \begin{pmatrix} 0 - j0.984 & 0.142 + j0.104 \\ -0.142 + j0.103 & 0 + j0.984 \end{pmatrix}, \\ \mathbf{X}_n^4 &= \begin{pmatrix} 0 + j0.984 & -0.142 - j0.104 \\ 0.142 - j0.103 & 0 - j0.984 \end{pmatrix}. \end{aligned} \quad (3.62)$$

For comparison, we may consider the set of space-time coded matrices \mathbf{X}_n^i ($i = 1, 2, 3, 4$) based on orthogonal designs, as illustrated in Equation (3.15) of Section 3.3.1, which are given by:

$$\begin{aligned} \mathbf{X}_1 &= \frac{1}{\sqrt{2}} \begin{pmatrix} 1 & -1 \\ 1 & 1 \end{pmatrix}, & \mathbf{X}_2 &= \frac{1}{\sqrt{2}} \begin{pmatrix} 1 & 1 \\ -1 & 1 \end{pmatrix}, \\ \mathbf{X}_3 &= \frac{1}{\sqrt{2}} \begin{pmatrix} -1 & 1 \\ 1 & 1 \end{pmatrix}, & \mathbf{X}_4 &= \frac{1}{\sqrt{2}} \begin{pmatrix} -1 & -1 \\ -1 & -1 \end{pmatrix}. \end{aligned}$$

Figure 3.10 plots the BER performance of both the DLDC(2222) scheme based on the Cayley transform using Equation (3.62) and that of the DOSTBC scheme of Equation (3.63), when communicating over i.i.d. Rayleigh fading channels having $f_d = 10^{-2}$. Figure 3.10 demonstrates that at $\text{BER} = 10^{-5}$ the DLDC's performance gain over the identical-throughput DOSTBC scheme is approximately 0.9dB. This example shows that there are good codes within the DLDC structure based on the Cayley transform at low rates. Even more importantly, the power of the DLDCs lies in its flexibility to accommodate diverse antenna configurations as well as in its ability to achieve high throughput, which will be further demonstrated in Section 3.4.3.

Table 3.2: System parameters for the DLDCs of Figure 3.9 based on the Cayley transform.

Modulation	2PAM
Mapping	Gray mapping
Number of transmitters (M)	2
Number of receivers (N)	2
Normalized Doppler frequency	$f_d = 10^{-2}$
Detector	ML of Equation (3.53)

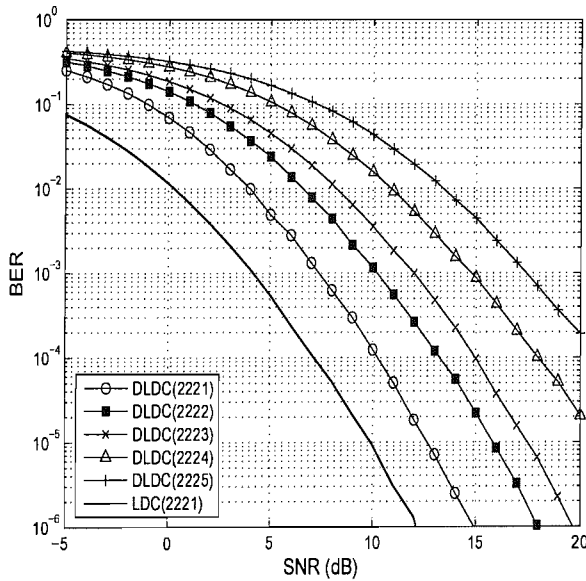


Figure 3.11: BER comparison of a family of DLDCs of Figure 3.9 having $M = 2$, $N = 2$, $T = 2$ and $Q = 1, 2, 3, 4, 5$, when transmitting over i.i.d. Rayleigh fading channels having $f_d = 10^{-2}$. All the system parameters were summarized in Table 3.9.

3.4.3 Performance Results

This section presents the simulation results for a group of DLDCs based on the Cayley transform, which are associated with various parameter ($MNTQ$) combinations. All the system parameters are listed in Table 3.9, unless otherwise specified.

Figure 3.11 characterizes the BER performance of a family of DLDCs having the parameters of $M = 2$, $N = 2$, $T = 2$ and $Q = 1, 2, 3, 4, 5$ using an ML detector, when transmitting over i.i.d. Rayleigh fading channels having a normalized Doppler frequency of $f_d = 10^{-2}$. The coherently detected LDC(2221) scheme of Figure 2.5 is plotted as the benchmark. Observe in Figure 3.11 that the DLDC(2221) scheme suffers from an approximately 3dB performance loss compared to its

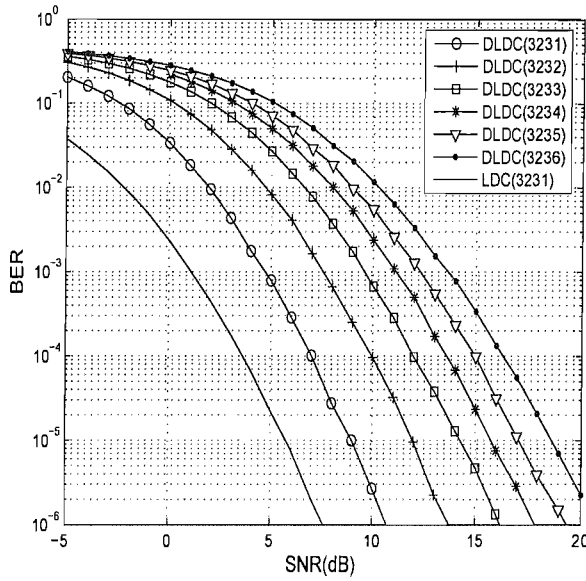


Figure 3.12: BER comparison of a family of DLDCs of Figure 3.9 having $M = 3$, $N = 2$, $T = 3$ and $Q = 1, 2, 3, 4, 5, 6$, when transmitting over i.i.d. Rayleigh fading channels having a normalized Doppler frequency of $f_d = 10^{-2}$. All the system parameters were summarized in Table 3.9.

coherently detected counterpart, where perfect CSI was assumed. We also observe in Figure 3.11 that all the curves exhibit similar shape, which implies that the maximum attainable diversity order of $D = 4$ has been achieved.

Figure 3.12 portrays the BER performance for a family of DLDCs having $M = 3$, $N = 2$, $T = 3$ and $Q = 1, 2, 3, 4, 5, 6$ using the differential ML detector of Equation (3.9), when transmitting over i.i.d. Rayleigh fading channels having a normalized Doppler frequency of $f_d = 10^{-2}$. This family of DLDCs is capable of achieving the maximum diversity order of $D = 6$. Similarly, the BER performance of the coherently detected LDC(3231) optimized using the method in Chapter 2 is given as a benchmark, where the usual 3dB performance difference is observed, as a result of requiring no CSI.

Figure 3.13 further demonstrates the DLDCs' capability of achieving full spatial diversity upon employing $M = 2$ transmit and $N = 1, 2, 3$ receive antennas, when transmitting over i.i.d. Rayleigh fading channels encountering a normalized Doppler frequency of $f_d = 10^{-2}$. Upon increasing N , the total spatial diversity order achieved becomes $D = 2, 4, 6$, respectively.

A distinctive feature of the differentially encoded schemes is that the attainable BER performance is affected by the rate of fluctuation experienced by the MIMO channels, since the differential decoding of Equation (3.7) requires the channel's envelope to be constant over two consecutive transmission blocks. Figure 3.14 quantifies the SNR required for the DLDCs having $M = 2$,

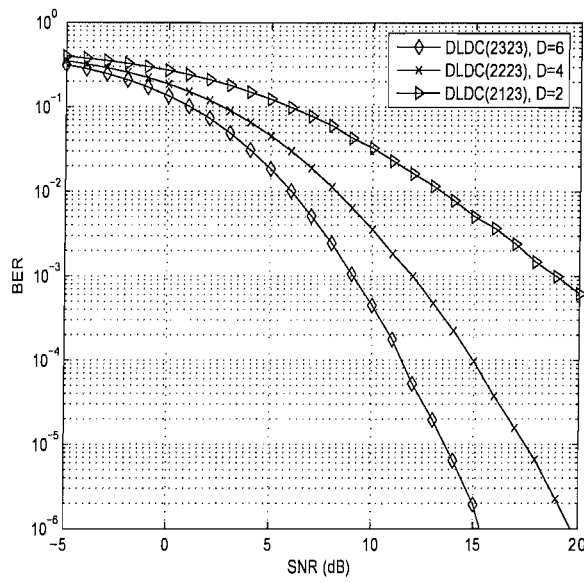


Figure 3.13: BER comparison of a family of DLDCs of Figure 3.9 having $M = 2$, $N = 1, 2, 3$, $T = 2$ and $Q = 3$, when transmitting over i.i.d. Rayleigh fading channels having $f_d = 10^{-2}$. All the system parameters were summarized in Table 3.9.

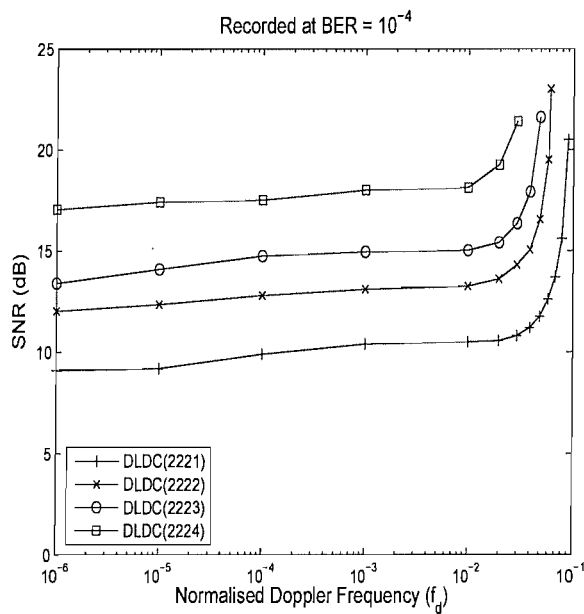


Figure 3.14: SNR required for a family of DLDCs of Figure 3.9 having $M = 2$, $N = 2$, $T = 2$ and $Q = 1, 2, 3, 4$ to maintain $\text{BER} = 10^{-4}$, when transmitting over i.i.d. Rayleigh fading channels encountering various normalized Doppler frequency of f_d . All the system parameters were summarized in Table 3.9.

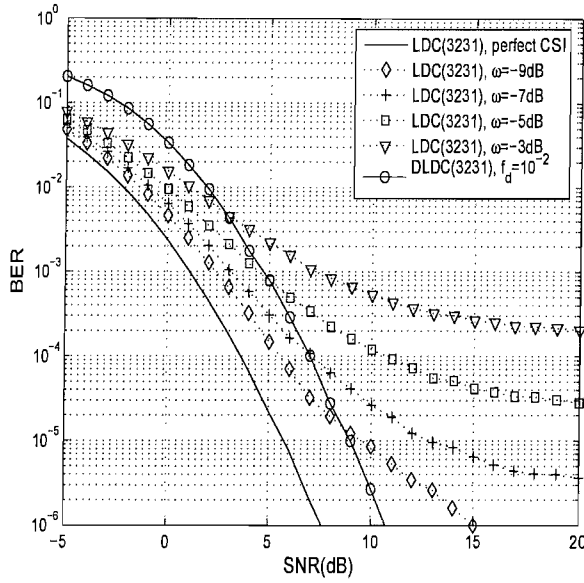


Figure 3.15: BER comparison of a LDC(3231) scheme of Figure 2.3 having imperfect CSI governed by ω and a non-coherent DLDC(3231) arrangement of Figure 3.9, when transmitting over i.i.d. Rayleigh-fading channels having a normalized Doppler frequency of $f_d = 10^{-2}$. All the system parameters were summarized in Table 3.9.

$N = 2$, $T = 2$ and $Q = 1, 2, 3, 4$ in order to maintain $\text{BER} = 10^{-4}$, when transmitting over i.i.d. Rayleigh fading channels encountering different normalized Doppler frequencies f_d . As expected, a higher transmission power is required for a DLDC scheme to maintain a specific BER level, when the channel envelope fluctuates more rapidly. More specifically, an extra SNR of 11.4dB is necessary for the DLDC(2221) scheme of Figure 3.9 to maintain $\text{BER} = 10^{-4}$, when f_d increases from 10^{-6} to 0.09. When we have $f_d > 0.09$, an error floor higher than $\text{BER} = 10^{-4}$ is observed. Also observe in Figure 3.14 that the achievable robustness against a high rate of channels' envelope fluctuation is reduced, when the throughput of the DLDC schemes increases by transmitting more symbols per space-time block. For example, an error floor higher than $\text{BER} = 10^{-4}$ occurred for the DLDC(2224) scheme having $f_d = 0.02$, whereas the DLDC(2221) arrangement is capable of maintaining the BER of 10^{-4} until the $f_d = 0.09$ value is exceeded.

The coherently detected LDCs detailed in Chapter 2 assume that the receiver has perfect CSI. Under this assumption, the differentially encoded schemes normally exhibit a 3dB SNR performance loss, as shown in Figures 3.11 and 3.12. However, this assumption is unrealistic, owing to the inevitable channel estimation errors. Figure 3.15 explicitly quantifies the BER comparison of a LDC(3231) scheme having different degrees of channel estimation errors and the corresponding DLDC(3231) arrangement. We assume that the channel estimation errors obey the Gaussian distribution and the degree of the CSI estimation errors is governed by ω (dB) with respect to the

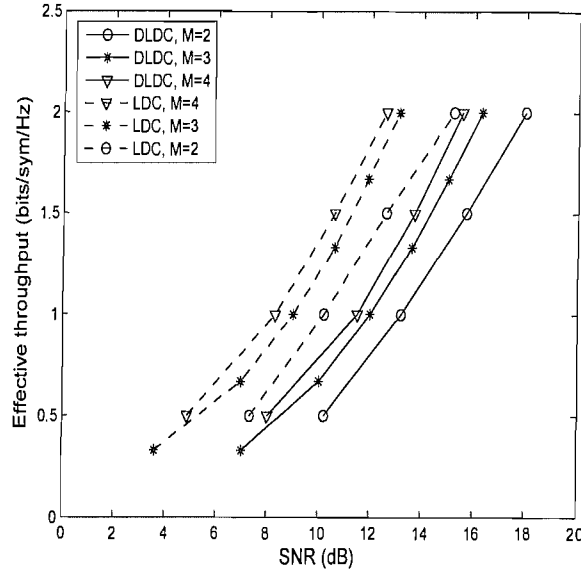


Figure 3.16: Effective throughput comparison of a family of DLDC schemes of Figure 3.9 employing $M = 2, 3, 4$ transmit and $N = 2$ receive antennas and the corresponding coherently detected LDC counterparts, when communicating over i.i.d. Rayleigh-fading channels having $f_d = 10^{-2}$. All the system parameters were summarized in Table 3.9.

received signal power. Hence, the perfect CSI scenario corresponds to $\omega = -\infty$. Observe in Figure 3.15 that the BER performance gradually degrades upon increasing ω . Also observe that there exists a crossover point between the BER curve of the DLDC(3231) scheme and that of its coherently detected counterpart LDC(3231) having different ω values. For example, when we have $\omega = -7$ dB, the crossover occurs at $\rho = 7$ dB. This implies that the DLDC(3231) scheme is capable of outperforming its coherently detected counterpart for SNR values in excess of $\rho > 7$ dB without the typically high complexity of MIMO channel estimation.

3.4.4 Summary

In this section, we summarize the performance trends of the DLDCs presented in Sections 3.3 and 3.4.3 in terms of their effective throughput and their coding gain, where the latter was defined as the SNR difference, expressed in dBs, at a BER of 10^{-4} between various DLDCs and single-antenna aided DPSK systems having the identical effective throughput.

Figure 3.16 characterizes the effective throughput of a family of DLDCs employing $M = 2, 3, 4$ transmit and $N = 2$ receive antennas, when transmitting over i.i.d. Rayleigh-fading channels having $f_d = 10^{-2}$. The increase of effective throughput was achieved by transmitting more symbols (Q) per space-time block, while 2PAM modulation was employed for all the schemes. The effective

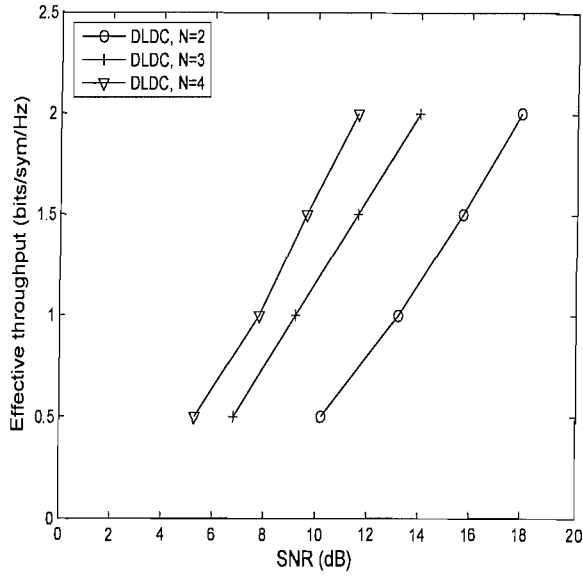


Figure 3.17: Effective throughput of a class of DLDC schemes of Figure 3.9 employing $N = 2, 3, 4$ receive and $M = 2$ transmit antennas, when communicating over i.i.d. Rayleigh-fading channels having $f_d = 10^{-2}$. All the system parameters were summarized in Table 3.9.

throughput achieved by their coherently-detected LDC counterparts was also shown in Figure 3.16. Observe that an approximately 3dB SNR gap exists between the corresponding DLDC and LDC schemes.

Furthermore, Figure 3.17 characterizes the effective throughput achieved by a family of 2PAM modulated DLDCs employing $M = 2$ transmit and $N = 2, 3, 4$ receive antennas, when communicating over i.i.d. Rayleigh-fading channels having a normalized Doppler frequency of $f_d = 10^{-2}$. Naturally, a certain throughput can be achieved using less power, when increasing the receive diversity order from $D_{rx} = 2$ to $D_{rx} = 4$. By comparing Figures 3.16 and 3.17, it becomes clear that for a given total diversity order receive diversity provides a more substantial improvement than the corresponding transmit diversity scheme, because the former improves the SNR by gleaning a high received signal power, whereas the transmit diversity shares the same total power over several antennas.

The coding gains of a family of DLDCs having an effective throughput of 1 or 2 (bits/sym/Hz) are listed in Table 3.3. The highest coding gains were recorded for the DLDC schemes employing 2PAM. Compared to the coding gains achieved by their LDC counterparts listed in Tables 2.1 and 2.2, the DLDCs are capable of attaining similar coding gain over the single-antenna-aided systems, which was found to be approximately 23dB. Again, the DLDCs' achievable throughput characterized in Figures 3.16 and 3.17 as well as the coding gains recorded in Table 3.3 demonstrated the flexibility of the DLDCs of Figure 3.9, which lead to their reconfigurable system structures, while

Table 3.3: Coding gains of a family of DLDCs of Figure 3.9 having an effective throughput of 1 or 2 (bits/sym/Hz).

DLDC	Throughput	Modulation	Coding Gain
DLDC(2221)	1	4PAM	18.1dB
DLDC(2222)	1	2PAM	23.3dB
DLDC(2221)	2	16PAM	11.4dB
DLDC(2222)	2	4PAM	18.7dB
DLDC(2224)	2	2PAM	21.5dB

achieving full diversity.

3.5 RSC-Coded Precoder-Aided DOSTBCs

One crucial issue in the context of iteratively-detected schemes [117] is the design of constellation mapping, which was studied in [118] [119]. All the results indicate that the specific arrangement of the bits to the modulated signal constellation has substantial effect on the iterative system's performance. In [98], Sphere Packing (SP) modulation was proposed for improving the performance of DOSTBCs [26], where the symbols transmitted in two time slots were jointly designed. As a result, the size of the new SP modulated constellation became $L = 16$, if originally QPSK symbols were transmitted.

Section 2.4.2 has demonstrated that the employment of the precoder is capable of rendering the channels to appear recursive to the receiver, which potentially facilitates a high interleaver gain [100]. There are other methods of rendering the impulse response duration infinite. For example, the differential encoding process of DOSTBC schemes potentially renders the CIR-duration infinite, but unfortunately the conventional DOSTBC decoding strategy of Equations (3.17) and (3.18) is incapable of exploiting the recursion, hence rendering the DSTBC system more or less a diversity combiner. Another method of introducing recursion is the employment of differential constellations, such as DPSK. In [120], it has been argued that turbo-detected DPSK has the potential of outperforming coherent PSK, although this requires a number of iterative detection steps, which increases the detector's complexity. Therefore, unity-rate precoder remains to be the most flexible method of controlling the spreading of the extrinsic information using different feedback polynomials and various precoder memory sizes with the aid of EXIT chart analysis [57].

Based on the above discussions, in this section a RSC-coded SP-aided DOSTBC design was

proposed. The novelty and rationale can be summarized as follows:

- The proposed scheme is capable of achieving both spatial and temporal diversity, without the high complexity of channel estimation in coherent detection;
- The employment of SP modulation allows us to intelligently amalgamate *inner* DOSTBC scheme and *outer* RSC code, where we jointly rather than separately design the space-time signals of two time-slots;
- Various rate-1 precoder designs are investigated. The spread of extrinsic information across the transmitted bit stream is governed by the precoder's memory. We will demonstrate that the shape of the EXIT curve, which determines the convergence threshold, is controlled by the precoder's memory;
- We further improve the performance of the proposed serial concatenated receiver relying on classic convolutional codes by invoking IRCCs [60] [69] as an *outer* code. We jointly consider the flexibility provided by the specifically tailored EXIT characteristics of the IRCCs and the precoder. As a result, an even lower SNR convergence threshold is attainable in comparison to the system using regular convolutional codes.

3.5.1 DOSTBC Design With Sphere Packing Modulation

It was shown in [121] that the diversity product quantifying the coding advantage of a STBC scheme is determined by the minimum Euclidean distance of the vectors $\mathbf{K}_n = [s_n^1, s_n^2, \dots, s_n^Q]^T$. Therefore, it was proposed in [121] to use sphere packing schemes that have the best known minimum Euclidean distance in the $2Q$ -dimensional real-valued Euclidean space \mathfrak{R}^{2Q} .

In this section, DOSTBC schemes obeying the structure of Figure 3.2 and employing two transmit antennas are considered, where the symbols are differentially encoded using the generator matrix \mathbf{G}_2 of Equation (3.13). It has been demonstrated in Section 3.3.1 that when the DSTBC design is based on the orthogonal design, the received signals after the linear combination will be scaled versions of the transmitted symbols s_n^1 and s_n^2 as seen in Equations (3.17) and (3.18), which are corrupted by complex AWGN. This observation implies that the diversity product of DOSTBC scheme is also determined by the minimum Euclidean distance of all legitimate vectors $[s_n^1, s_n^2]$.

For the sake of generalizing our treatment, let us assume that there are L legitimate twin-time-slot vectors $[s_n^1, s_n^2]$, where L represents the number of sphere-packed modulated symbols. The encoder, then, has to choose the modulated symbol associated with each block of bits from these L legitimate symbols. In contrast to the independent DOSTBC signalling pulses s_n^1 and s_n^2 , our aim

is to design s_n^1 and s_n^2 jointly, so that they have the best minimum Euclidean distance from all other $(L - 1)$ legitimate SP symbols, since this minimizes the system's SP symbol error probability.

Let $(a_{l,1}, a_{l,2}, a_{l,3}, a_{l,4}), l = 0, \dots, L - 1$, be SP phasor points selected from the four-dimensional real-valued Euclidean space \Re^4 , where each of the four elements $a_{l,1}, a_{l,2}, a_{l,3}, a_{l,4}$ gives one coordinate of the twin-time-slot complex-valued phasor points. Hence, s_n^1 and s_n^2 can be written as:

$$\{s_n^1, s_n^2\} = SP(a_{l,1}, a_{l,2}, a_{l,3}, a_{l,4}) = \{a_{l,1} + ia_{l,2}, a_{l,3} + ia_{l,4}\}. \quad (3.63)$$

In the four-dimensional real-valued Euclidean space \Re^4 , the lattice \Re^4 is defined as a sphere packing having the best minimum Euclidean distance from all other $(L - 1)$ legitimate SP constellation points in \Re^4 [122]. More specifically, \Re^4 may be defined as a lattice that consists of all legitimate SP constellation points having integer coordinates $[a_1 \ a_2 \ a_3 \ a_4]$ uniquely and unambiguously describing the legitimate combinations of the DOSTBC modulated symbols s_n^1 and s_n^2 of each time slot, but subjected to the sphere packing constraint of the sum of $[a_1 \ a_2 \ a_3 \ a_4]$ equals to an integer constant. Let us assume that $\Re^4 \{[a_{l,1}, a_{l,2}, a_{l,3}, a_{l,4}] \in \Re^4 : 0 \leq l \leq L - 1\}$ constitutes a set of L legitimate constellation points selected from the lattice \Re^4 having a total energy of $\tilde{E} \triangleq \sum_{l=0}^{L-1} (|a_{l,1}|^2 + |a_{l,2}|^2 + |a_{l,3}|^2 + |a_{l,4}|^2)$, and introduce the set of complex constellation symbols, $\{SP^l : 0 \leq l \leq L - 1\}$

$$SP_l = \sqrt{\frac{2L}{\tilde{E}}} (s_n^1, s_n^2), \quad l = 0, 1, \dots, L - 1. \quad (3.64)$$

whose diversity product is determined by the minimum Euclidean distance of the set of L legitimate constellation points in \Re^4 . For example, at the first layer of the SP lattice there are 24 constellation points according to all possible constellations of the values $[\pm 1; \pm 1, 0, 0]$ and the constellation set of $L = 16$ points was found by computer search upon maximizing their Euclidean distance at a given total power \tilde{E} .

In contrast to Alamouti's approach, our SP aided DOSTBC allowed us to jointly design all the space and time dimensions available. Hence, more extrinsic information can be obtained compared to conventional QPSK modulation. Furthermore, the best SP mapping that enables the creation of an open convergence tunnel can be chosen for the iteratively detected system. For the proposed scheme of Figure 3.18, Gray labelling is chosen, since there are no *inner* iterations between SP demapper and precoder. The exact choice of the $L = 16$ SP constellation points is given in [103].

3.5.2 System Description

The block diagram of the three-stage scheme is shown in Figure 3.18, which employs two transmit and one receive antenna, although the concept may be readily applied to an arbitrary number of

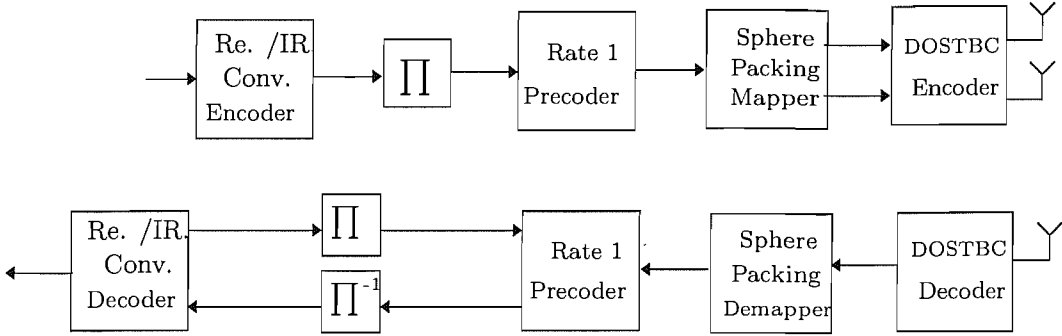


Figure 3.18: Schematic of the precoded SP aided DOSTBC design using regular/irregular convolutional codes.

receive antennas.

First, a frame of information bits is encoded by a regular/irregular *outer* half-rate convolutional channel encoder. Then, the *outer* channel encoded bits of Figure 3.18 are permuted by a random interleaver. The interleaved bits are then encoded by a rate-1 recursive precoder, which contributes towards achieving a high iteration gain. Initially a memory-one precoder is considered. Then, the sphere packing mapper of Figure 3.18 maps each block of encoded bits to a legitimate constellation point $SP_n^l \in \Re^{\dagger}$. The same mapper then represents the constellation point SP_l by two complex DOSTBC symbols s_n^1 and s_n^2 of the two time slots using Equations (3.63) and (3.64). Subsequently, the DOSTBC encoder of Figure 3.18 calculates the transmitted symbols using Equation (3.19), as detailed in Section 3.3.1. Furthermore, instead of directly transmitting the differentially encoded symbols, the proposed system may also be amalgamated with differential Space-Time Spreading (STS) [123]. Since each spreading sequence of the STS scheme spans two symbol periods and transmitting two symbols, which is identical to the philosophy of DOSTBC, it can be argued that the employment of STS allows the system to accommodate two users without affecting the achievable single-user throughput. Similarly, multiple users maybe supported with the aid of multiple antennas and longer spreading sequences.

The structure of the receiver is shown in Figure 3.18, where the DOSTBC decoder decouples the symbol stream according to Equations (3.21) and (3.22) then we have:

$$\bar{s}_n^1 = (|h_{1,1}|^2 + |h_{1,2}|^2) \cdot \theta \cdot s_n^1 + \bar{v}_n^1, \quad (3.65)$$

$$\bar{s}_n^2 = (|h_{1,1}|^2 + |h_{1,2}|^2) \cdot \theta \cdot s_n^2 + \bar{v}_n^2, \quad (3.66)$$

where θ is given in Equation (3.23). Recall in Equations (3.63) and (3.64) that one SP constellation point is represented by s_n^1 and s_n^2 , thus we can derive:

$$\bar{SP}_n^l = (|h_{1,1}|^2 + |h_{1,2}|^2) \cdot \theta \cdot SP_n^l + \bar{v}_n^l. \quad (3.67)$$

Table 3.4: System parameters for the precoded SP aided DOSTBC system of Figure 3.18.

Modulation	SP ($L = 16$)
Mapping	Gray mapping
Number of Transmit Antennas	2
Number of Receive Antennas	1
Normalized Doppler Frequency	$f_d = 0.01$
Regular Outer Channel Code	RSC(2,1,5)
IRCC	Half-rate
Interleaver Length	10^6 bits
Precoder Rate	1
Precoder Memory	1
Throughput	1 bit per channel use

Then, the decoded symbols of Equation (3.67) are passed to the SP demapper of Figure 3.18, where they are demapped to their LLR representation for each of the convolutional coded bits in a SP symbol. The rate-1 precoder's decoder processes the *a priori* information fed back from the *outer* decoder and the output of the sphere packing demapper of Figure 3.18. Then the extrinsic information is exchanged between the *outer* decoder and precoder's decoder for a consecutive number of iterations (k). Note that the SP demapper combined with the DOSTBC decoder does not involve in the iteration decoding process.

3.5.3 EXIT Chart Analysis

The EXIT chart of the precoded system of Figure 3.18 is shown in Figure 3.19, when using a memory-one precoder together with RSC(215) code and the system parameters outlined in Table 3.4. This scheme is compared to a non-precoded system, when operating at SNR $\rho = 6$ dB. The non-precoded system also employs iterative decoding between the soft SP demapper and the *outer* channel decoder as described in [64] [103], where the best anti-Gray mapping scheme that matches the *outer* code's EXIT curve was chosen as in [98].

Observe in Figure 3.19 that the precoded system reaches the point $I_E \approx 0.998$, where a convergence tunnel has taken shape, hence resulting in an infinitesimally low BER. By contrast, the non-precoded scheme reaches $I_E \approx 0.79$, as shown in Figure 3.19, hence only modest BER advantage can be achieved. In other words, it is expected that the precoded system is capable of reaching

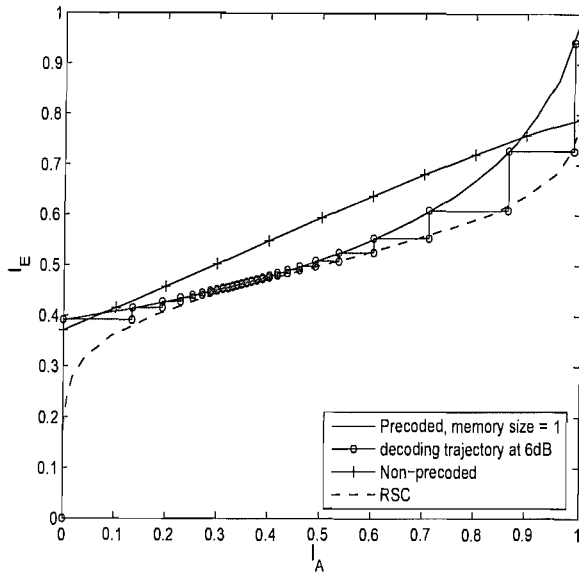


Figure 3.19: EXIT chart comparison of both a non-precoded and of the precoded system of Figure 3.18 employing a single-stage precoder, when using the system parameters outlined in Table 3.4, where the monte-carlo simulation based decoding trajectory was recorded at $\rho = 6\text{dB}$.

the typical turbo-cliff, when considering the BER versus SNR performance, as it will be shown in Section 3.5.4.

Figure 3.20 shows the EXIT curves of the *inner* decoder operating at $\rho = 6\text{dB}$, when using various precoder memory sizes. The *inner* decoder is constituted by the precoder's decoder, SP demapper and DOSTBC decoder of Figure 3.18. The precoder's structure is shown in Figure 2.30. When the memory size of the precoder is increased, the EXIT curves of the *inner* decoder tend to start at lower I_E values, but rise more rapidly. For $\rho = 6\text{dB}$, a memory-one precoded system has an open convergence tunnel, whereas a higher precoder memory tends to require a higher SNR value for an open convergence tunnel to take shape. However, once an open convergence tunnel was formed, less iterations are required to reach the point of intersection by the systems employing precoders having a higher memory size. Hence, for this particular system employing an RSC(215) *outer* code, a precoder memory size of one is capable of achieving an infinitesimally low BER at the lowest possible SNR value. Note that the area under all the EXIT curves recorded for various precoder memory sizes is constant, which indicates that the achievable channel capacity is not affected [68] [99] by changing the shape of the EXIT curves. Note that the same phenomenon has also been recorded for the coherently detected precoded STBCs of Figure 2.24, as justified in Figure 2.31.

The open EXIT tunnel area between the *inner* and *outer* decoder's curves in Figure 3.19 is not necessarily an unambiguous characteristic of the system, since the convergence tunnel is only

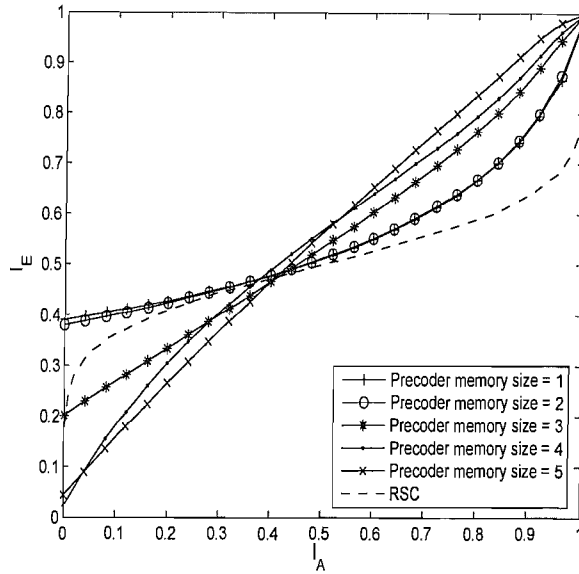


Figure 3.20: EXIT characteristics of precoded system of Figure 3.18 using Gray mapping for different precoder memory sizes, when employing the system parameters outlined in Table 3.4 and operating at $\rho = 6\text{dB}$.

narrow within a certain range. By shaping both the *inner* and *outer* EXIT curves, it is potentially possible to create an even narrower tunnel in conjunction with a lower SNR requirement. Since IRCCs exhibit flexible EXIT characteristics as extensively demonstrated in Section 2.5.2, we adopt an IRCC as our *outer* code, while keeping the overall code rate the same as that of our previous RSC code. The IRCC scheme constituted by a set of $P_{out} = 12$ component codes was employed, where the corresponding weighting coefficient vector is $\gamma = [\gamma_1, \dots, \gamma_{P_{out}}]$. The associated component rates of the IRCCs are $R_{i,IRCC} = [0.1, 0.15, 0.25, 0.4, 0.45, 0.55, 0.6, 0.7, 0.75, 0.8, 0.85, 0.9]$, respectively. Hence, γ is optimized with the aid of the iterative algorithm of [60], so that the EXIT curve of the resultant IRCC closely matches that of the *inner* code. Since the *inner* code's EXIT curve benefits from the flexibility provided by the precoder's memory size, as shown in Figure 3.20, the IRCC is optimized for all the different memory sizes featuring in Figure 3.20. Explicitly, our design objective is to find the lowest SNR value, where it is possible to form an open convergence tunnel.

Figure 3.21 illustrates both the EXIT curves of the IRCC optimized for the proposed system having a precoder memory of 3 as well as the bit-by-bit decoding trajectory at SNR $\rho = 5.5\text{dB}$, where the optimized weighting coefficients are as follows: $\gamma = [0, 0.0206, 0.0199, 0.1567, 0, 0.0811, 0.1803, 0.0835, 0.2757, 0.0302, 0.0326, 0.1194]$. Observe that an extremely narrow EXIT tunnel is formed, which exhibits a 0.5dB advantage over the RSC(215) coded scheme characterized in Figure 3.20.

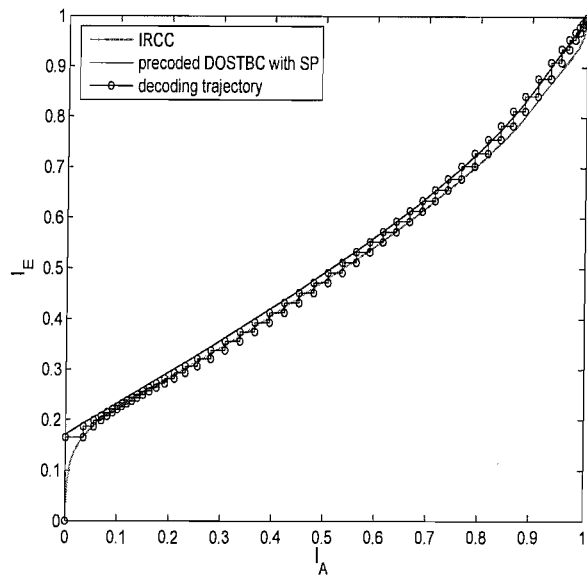


Figure 3.21: EXIT chart of the memory size = 3 precoded system of Figure 3.18 using IRCC, when using the system parameters outlined in Table 3.4 and the actual decoding trajectory at $\rho = 5.5\text{dB}$.

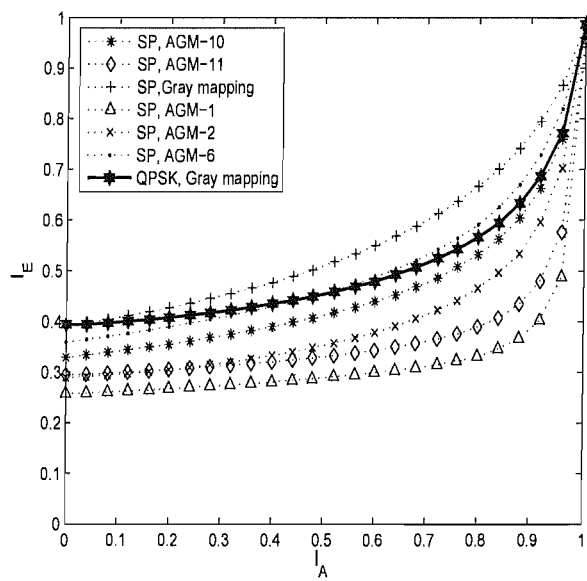


Figure 3.22: EXIT comparison of system of Figure 3.18 employing SP using various mappings and employing QPSK with Gray mapping at $\rho = 6\text{dB}$, when using the system parameters outlined in Table 3.4.

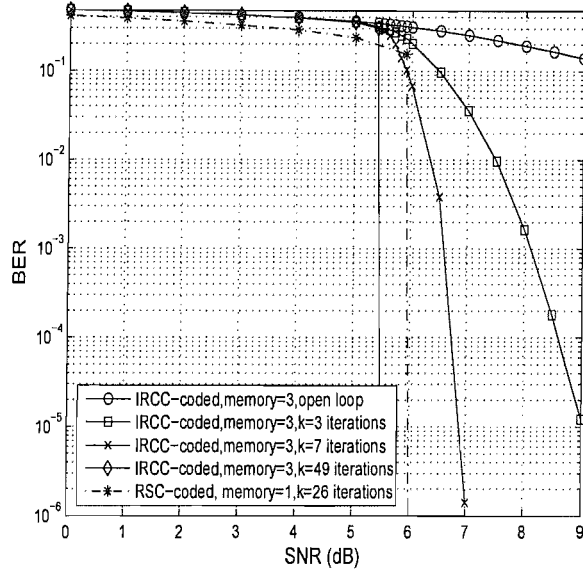


Figure 3.23: BER performance of a half-rate RSC/IRCC-coded SP aided DOSTBC scheme of Figure 3.18 with unity-rate precoder having a memory size of 1 or 3, when employing the system parameters outlined in Table 3.4.

Finally, the benefits of employing SP scheme over the conventional QPSK modulation recorded for the iteratively detected schemes are characterized in Figure 3.22, where SP modulation employing $L = 16$ constellation points and various mapping schemes is compared to classic QPSK at $\rho = 6\text{dB}$. Note that SP using Gray labelling is capable of generating higher extrinsic information than the various Anti-Gray Mapping (AGM) schemes, since there is no information exchange between the SP demapper and the precoder's decoder [124]. Since the SP aided DOSTBC facilitated the joint design of the space-time dimension available, more extrinsic information was obtained with the aid of the precoder compared to the conventional QPSK modulation. Therefore, the proposed SP-aided scheme using Gray labelling exhibited a larger area under the EXIT curve compared to its QPSK counterpart, as seen in Figure 3.22.

3.5.4 Performance Results

We now proceed to characterize the achievable BER performance of the turbo-detected precoded SP aided DOSTBC system of Figure 3.18. All the simulation parameters are listed in Table 3.4, unless otherwise specified.

Figure 3.23 demonstrates the BER performance of the half-rate RSC/IRCC-coded SP aided DOSTBC system. The precoding-aided RSC-coded system exhibits a turbo cliff at $\rho = 6\text{dB}$, where $k = 26$ iterations are required to reach the turbo-cliff region. This observation matches

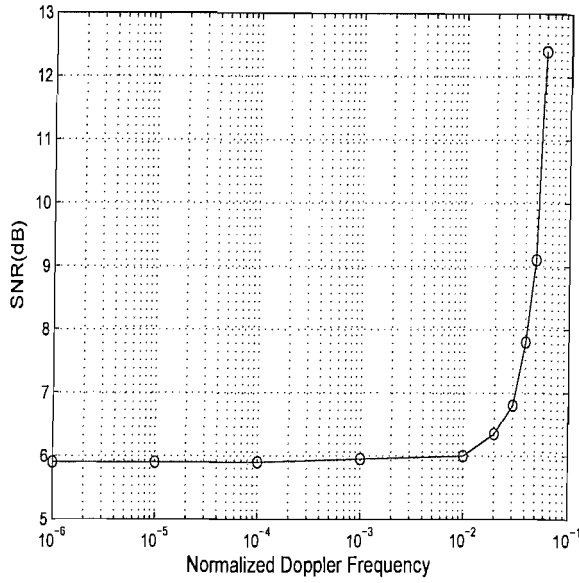


Figure 3.24: SNR required for the SP-aided RSC-coded DOSTBC of Figure 3.18 to achieve an infinitesimally low BER at different Doppler frequencies.

the prediction of the EXIT charts seen in Figure 3.19. Furthermore, the BER performance of the IRCC-coded scheme using a precoder memory of 3 is also shown in Figure 3.23. As predicted in Figure 3.21, the system achieved an infinitesimally low BER at $\rho = 5.5$ dB, where a 0.5dB SNR gain is observed over the RSC-coded scheme having a precoder memory size of 1. Naturally, a higher number of decoding iterations is needed in addition to the increased decoding complexity imposed by the precoder memory size of 3.

Figure 3.24 quantifies the SNR ρ required for maintaining an open convergence tunnel against the normalized Doppler frequency f_d , for the proposed RSC-coded SP-aided scheme of Figure 3.18 using a memory size-1 precoder. At this SNR an infinitesimally low BER may be attained. The success of differential decoding depends on the channel's variation between two consecutive transmission blocks. When the normalized Doppler frequency obeys $f_d \leq 0.01$, the proposed system is robust against the CIR tap fluctuations and achieves an infinitesimally low BER around $\rho = 6$ dB. When the CIR fluctuates faster, a higher transmit power is required for an open convergence tunnel to form, as seen in Figure 3.24. Our proposed scheme successfully supports normalized Doppler frequencies up to $f_d = 0.06$, where $\rho = 12.2$ dB is necessary as evidenced by Figure 3.24. A normalized Doppler frequency higher than $f_d = 0.06$ will render the errors after differential decoding non-recoverable.

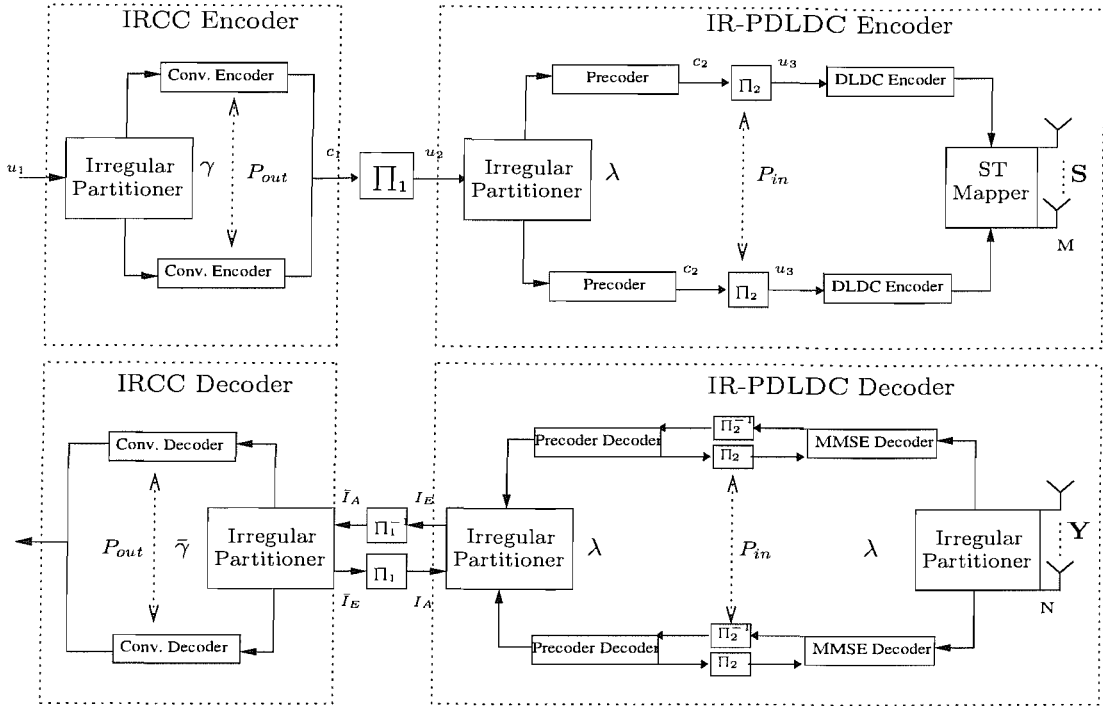


Figure 3.25: Schematic of the IRCC-coded IR-PDLDC using iterative decoding.

3.6 IRCC-Coded Precoder-Aided DLDCs

The schematic of the proposed scheme is illustrated in Figure 3.25, which again can be viewed as a differentially encoded version of the IRCC-coded coherently detected IR-PLDC scheme detailed in Section 2.5.3. By replacing the coherently detected LDC coding blocks of Figure 2.48 with the non-coherent DLDC block, the resultant irregular scheme of Figure 3.25 becomes capable of supporting high rates, while dispensing with high complexity MIMO channel estimation. Therefore, similar design methods to those presented in Section 2.5.3 can be adopted. Hence, this section will focus on the proposed irregular system's features imposed by the non-coherent detection, rather than on the similarities to the features of the irregular coherent-detection aided counterparts.

3.6.1 EXIT Chart Based IR-PDLDC Design

The family of DLDCs based on the Cayley transform of Equation (3.48) is employed as the *inner* space-time block, since they are capable of providing flexible rates and supporting arbitrary antenna configurations. We will demonstrate how to generate an *inner* IR-PDLDC coding scheme containing $P_{in} = 6$ components for a MIMO configuration having $M = 3$ transmit and $N = 2$ receive antennas. Since $T = M$ is imposed by the differential encoding process, the resultant DLDCs have the potential of achieving the maximum attainable spatial diversity order of $D = 6$, according to Theorem 3 in Section 2.2. By setting $Q = 1$, we have DLDC(3231), which can be optimized by

Table 3.5: The $P_{in} = 6$ component codes of the 2PAM modulated IR-PDLDC scheme of Figure 3.25 generated for a MIMO system having $M = 3$ and $N = 2$ antennas, where the complexity is quantified in terms of the number of addition and multiplication operations required to calculate a single LLR value in the logarithmic domain.

Index	M	N	T	Q	Rate	D	Inner Iterations	Complexity
0	3	2	3	1	0.33	6	0	2399
1	\vdots	\vdots	\vdots	2	0.67	6	1	6694
2	\vdots	\vdots	\vdots	3	1	6	1	8590
3	\vdots	\vdots	\vdots	4	1.33	6	1	10486
4	\vdots	\vdots	\vdots	5	1.67	6	1	12382
5	\vdots	\vdots	\vdots	6	2	6	1	14278

maximizing the diversity gain using the *rank criterion* of Equation (2.26) and maximizing the coding gain using the *determinant criterion* of Equation (2.27). Consequently, different-rate DLDCs can be generated by changing the value of Q . Hence, by increasing the value of Q and maximizing both the diversity gain and the coding gain for each resultant DLDC($MNTQ$) component of the IR-PDLDC scheme, a set of meritorious DLDCs can be generated. Since Q single-stream transmitted symbols are jointly detected, low Q values are desirable for the sake of maintaining a low complexity. The resultant $P_{in} = 6$ component codes designed for our IR-PDLDC scheme are listed in Table 2.7. Hence, *inner* Precoded Differential Linear Dispersion Codes (PDLDCs) can be directly obtained by combining memory-1 unity-rate precoders with DLDCs having the parameter combination ($MNTQ$).

Figure 3.26 quantifies the maximum achievable rates for three 2PAM-modulated PDLDCs of Table 3.5 having $j = 0, 1$ *inner* iterations using an MMSE detector, when communicating over i.i.d. Rayleigh fading channels having $f_d = 10^{-2}$. For each set of comparisons, the DLDC's maximum achievable rates quantified after the MMSE detector of Figure 3.25 is plotted as the upper bound. Observe in Figure 3.26 that there exists a gap between the maximum achievable rate quantified both *before* and *after* the rate-1 precoder, when employing no *inner* iterations for different values of Q . However, the gap can be eliminated, when employing $j = 1$ *inner* iterations. Therefore, the required number of *inner* iterations maximizing the achievable rate is listed in Table 3.5.

Figure 3.27 characterizes the maximum achievable rates for the PDLDCs of Table 3.5 communicating over Rayleigh fading channels having $f_d = 10^{-2}$, when using 2PAM modulation and an MMSE detector. Furthermore, the maximum achievable rates of the corresponding group of

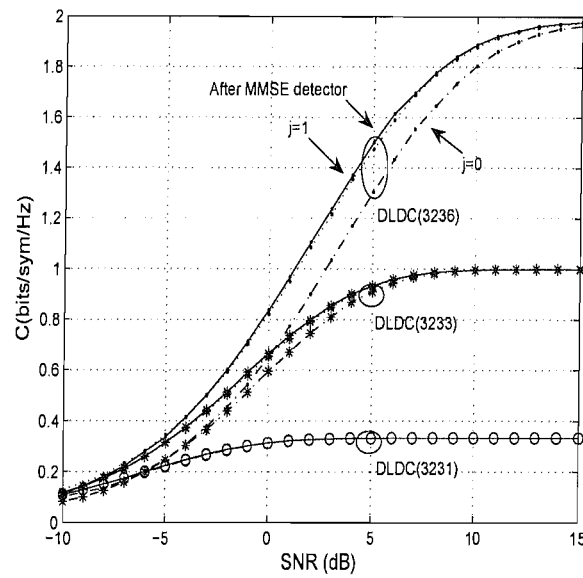


Figure 3.26: Maximum achievable rates for three 2PAM-modulated DLDC schemes of Table 3.5 having $j = 0, 1$ inner iterations using an MMSE detector, when communicating over i.i.d. Rayleigh fading channels having $f_d = 10^{-2}$.

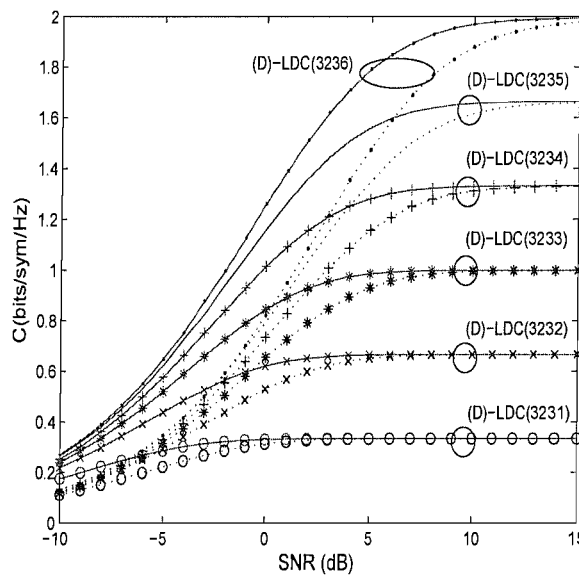


Figure 3.27: Maximum achievable rates for the 2PAM-modulated PDLDC schemes of Table 3.5 and their coherent counterparts PLDCs using an MMSE detector, when communicating over i.i.d. Rayleigh fading channels having $f_d = 10^{-2}$.

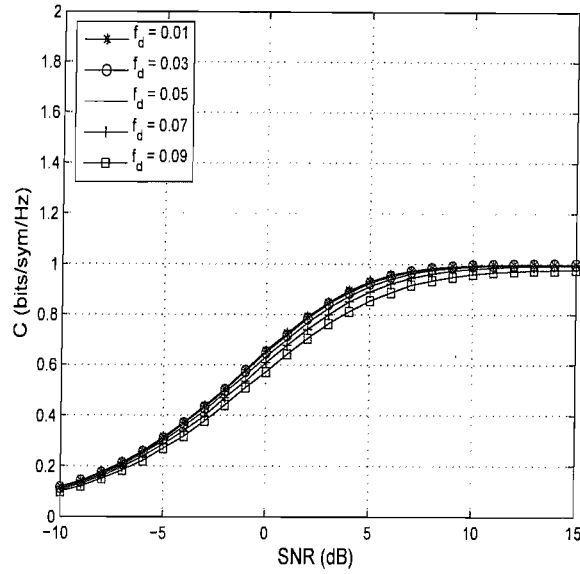


Figure 3.28: Maximum achievable rates of the 2PAM-modulated PDLDC(3233) scheme of Table 3.5 communicating over i.i.d. Rayleigh fading channels having different normalized Doppler frequencies f_d , when using an MMSE detector.

coherent PLDCs are also plotted under the same channel conditions as well as employing the same number of *inner* iterations. Observe in Figure 3.27 that PDLDCs require an approximately 3dB extra power in comparison to the corresponding PLDCs to achieve an infinitesimally low BER, when operating at a certain throughput. However, the associated performance gap can be closed in the high SNR region, where the noise variance becomes insignificant, compared to the signal's power.

Figure 3.28 characterizes the 2PAM-modulated PDLDC(3233) scheme's maximum achievable rates evaluated using Equation (2.47), when communicating over i.i.d. Rayleigh fading channels having different f_d values and employing an MMSE detector. Observe that the maximum achievable rate gradually dropped, when the channel's fluctuation became faster and the associated rate loss becomes more apparent in the high-SNR region. This observation is consistent with those recorded for the non-coherent MIMO channel's capacity given in Equation (3.12), which suggests a capacity reduction, when the corresponding coherence time \Im is reduced. Also note that the maximum achievable rate increase is modest, when we have $f_d < 0.03$.

Figure 3.29 characterizes the maximum achievable rates of the 2PAM-modulated PLDC(3233) having imperfect CSI governed by ω as well as that of the PDLDC(3233) scheme of Table 3.5, when encountering Rayleigh fading having $f_d = 10^{-2}$ and employing an MMSE detector. Observe in Figure 3.29 that at high SNRs the non-coherent PDLDC(3233) scheme is capable of achieving a higher throughput compared to its coherently detected counterparts, owing to the non-vanishing errors imposed by the imperfect CSI. More explicitly, when the channel estimation error power is

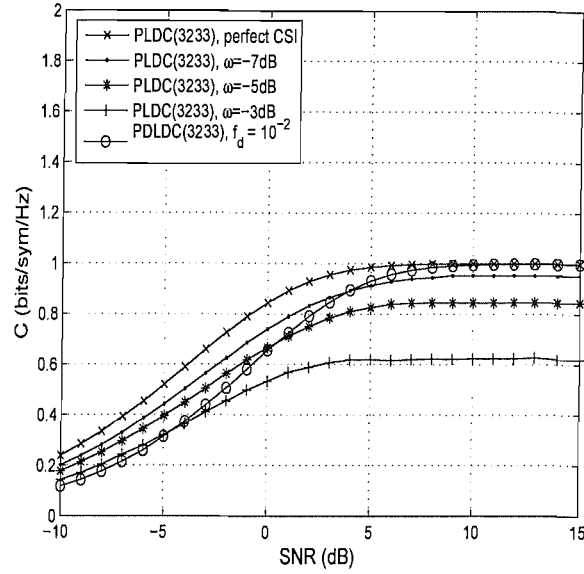


Figure 3.29: Maximum achievable rates of the 2PAM-modulated PDLDC(3233) scheme of Table 3.5 and the corresponding PLDC schemes having imperfect CSI governed by ω , when transmitting over i.i.d. Rayleigh-fading channels having $f_d = 10^{-2}$.

$\omega = -7\text{dB}$, the PDLDC(3233) scheme outperforms its coherent counterpart beyond the point of $\rho = 4\text{dB}$. When ω reaches -3dB , the coding advantage of the PDLDC(3233) scheme becomes promising for SNRs in excess of $\rho = -5\text{dB}$.

3.6.2 Performance Results

This section presents some further numerical results for the scheme of Figure 3.25 designed for maximizing the throughput for SNRs in excess of certain thresholds, while maintaining an infinitesimally low BER. For all the simulations, 2PAM modulation is employed and the first interleaver of Figure 3.25 is set to have a length of 10^6 bits. We employed a total number $P = 12$ component codes, where the IR-PDLDC scheme employs the $P_{in} = 6$ component codes of Table 3.5 and the IRCC contains $P_{out} = 6$ component codes having a rate of $R_{i,IRCC} = [0.1, 0.25, 0.4, 0.55, 0.7, 0.9]$. The weighting coefficient vectors γ and λ are optimized using the method presented in Section 2.5.3, which are summarized in Tables D.7 and D.8.

Figure 3.30 presents the associated EXIT charts and the corresponding decoding trajectory of our IRCC-coded IR-PDLDC scheme of Figure 3.25 designed for operating at $\rho = -2\text{dB}$ using an MMSE detector, when communicating over i.i.d. Rayleigh fading channels having $f_d = 10^{-2}$. The dashed lines represent the EXIT curves of the IR-PDLDC's component codes of Table 3.5 and the dotted lines denote the EXIT curves for the set of IRCC components. The solid lines represent

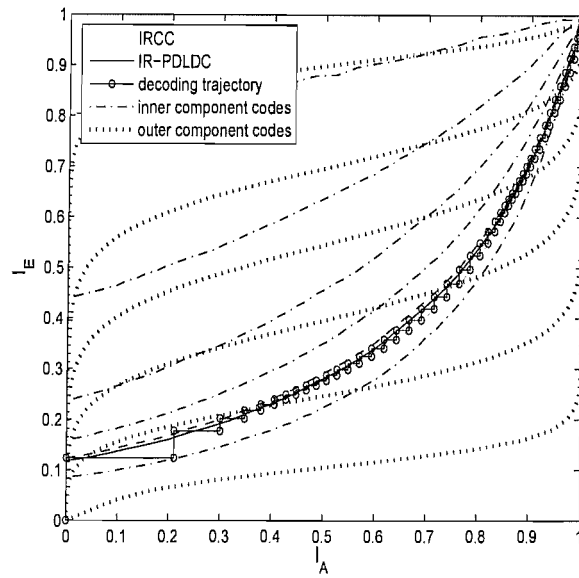


Figure 3.30: EXIT chart and the decoding trajectory of the IRCC-coded IR-PDLDC scheme of Figure 3.25 recorded at $\rho = -2\text{dB}$ using an MMSE detector and 2PAM modulation, when communicating over i.i.d. Rayleigh fading channels having $f_d = 10^{-2}$.

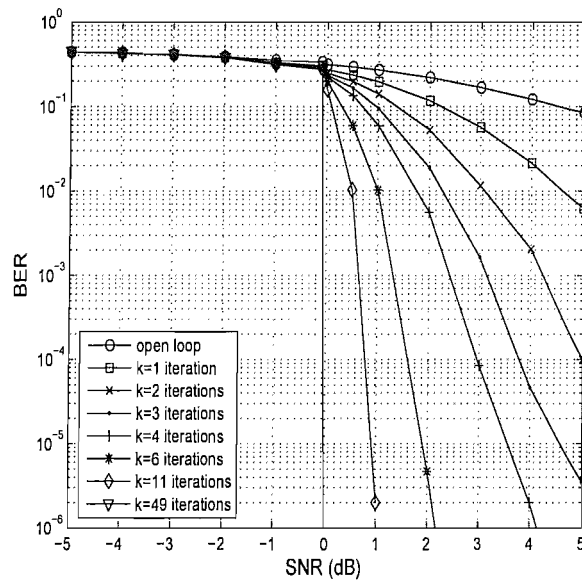


Figure 3.31: BER of the IRCC-coded IR-PDLDC scheme of Figure 3.25 designed for achieving an infinitesimally low BER at $\rho = -2\text{dB}$ using an MMSE detector and 2PAM modulation, when communicating over i.i.d. Rayleigh fading channels having $f_d = 10^{-2}$.

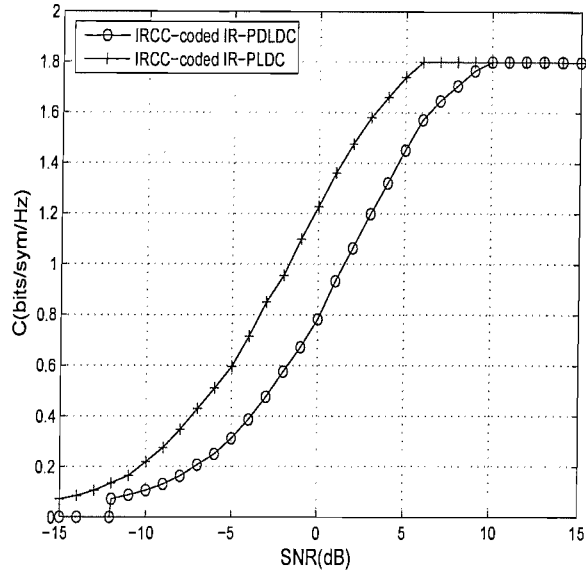


Figure 3.32: The maximum rates achieved by the IRCC-coded IR-P(D)LDC schemes of Figures 2.48 and 3.25 using an MMSE detector and 2PAM modulation according to Tables D.7, D.8, D.9 and D.10, when communicating over i.i.d. Rayleigh fading channels having $f_d = 10^{-2}$.

the aggregate EXIT curves of the IRCC and IR-PDLDC having the weighting coefficients listed in Tables D.7 and D.8. By simultaneously maximizing throughput and the EXIT tunnel area, the optimized EXIT curves of Figure 3.30 exhibit a narrow open tunnel, where the decoding trajectory shows that $k = 49$ *outer* iterations were required. The corresponding BER performance is shown in Figure 3.31.

Naturally, the same design process can be extended to a range of SNR values. Figure 3.32 plots the maximum rates achieved by the proposed IRCC-coded IR-PDLDC scheme of Figure 3.25 using an MMSE detector, when transmitting over i.i.d. Rayleigh fading channels having $f_d = 10^{-2}$. Each point of Figure 3.32 was designed to achieve the maximum throughput by adjusting the weighting coefficient vectors λ and γ , listed in Tables D.7 and D.8 of Appendix D. The maximum rates achieved using the corresponding set of coherently detected IR-PLDCs of Figure 2.48 having perfect CSI are plotted as the benchmark. Similar to the observations inferred from Figure 3.27, the SNR penalty owing to differential encoding is approximately 3dB. The proposed scheme is capable of operating in the SNR range in excess of $\rho = -12$ dB, while maintaining an infinitesimally low BER. However, the rate increase is limited to 1.8 (bits/sym/Hz) for SNRs beyond $\rho = 10$ dB. Clearly, a further rate increase can be achieved, when higher-rate DLDC components are employed.

3.7 Conclusion

In this chapter, firstly a universal structure have been established in order to describe all the existing DSTBCs found in the open literature. In Section 3.2, the challenge of designing DSTBCs obeying this general structure has been stated with the aim of designing a set of unitary space-time coded matrices. Section 3.3 outlined the philosophy of the class of DSTBCs based on various orthogonal designs, where different degrees of orthogonality have been imposed on the associated space-time matrices. Furthermore, in Section 3.4, we proposed the family of non-orthogonal DLDCs based on the Cayley transform, which is suitable for operating at high rates and for arbitrary antenna configurations.

In Section 3.5, the turbo principle was invoked for the proposed RSC-coded SP-aided DOSTBC scheme. The resultant scheme is capable of operating at an SNR of $\rho = 5.5\text{dB}$ at a throughput of 1 (bits/sym/Hz) with the aid of IRCCs. In Section 3.6, the performance of an irregular scheme is investigated, where the irregularity was imposed both at the *outer* code using the IRCC and at the *inner* code employing an IR-PDLDC. The amalgamated irregular differential scheme had a 3dB SNR loss, when compared to its coherently detected irregular counterpart, although this loss was reduced, when realistic imperfect CSI was used. More specifically, in Figures 3.15 and 3.29 we provided both a BER and a maximum achievable rate comparison between the DLDCs and the corresponding LDCs using realistic imperfect channel estimation. The results implied that DLDC schemes are more reliable for high rate communications at high SNRs, when the channel estimation error is non-negligible. As a benefit of the DLDCs, the typically high-complexity MIMO channel estimation can be eliminated.

Chapter 4

Cooperative Space-Time Block Codes

4.1 Introduction and Outline

The space time block coding techniques detailed in Chapters 2 and 3 provide promising solutions in the context of co-located MIMO systems requiring reliable wireless communications at high rates. However, it may not always be practical to accommodate multiple antennas at the mobile stations, owing to cost, size and other hardware limitations. A further limitation of having co-located MIMO elements is that even at relatively large element separations their elements may not benefit from independent fading, when subjected to shadow-fading imposed for example by large-bodied vehicles or other shadowing local paraphernalia. As a remedy, High Speed Downlink Packet Access (HSDPA) style adaptive modulation [125] as well as the concept of cooperative MIMOs [126] have been proposed for cellular systems as an attempt to attain a better communication efficiency beyond that permitted by a single node's resources. More specifically, a group of mobile nodes, known as relays, 'shares' their antennas with other users to create a virtual antenna array to provide spatial diversity gain. In order to deepen our discussion, Figure 4.1 illustrates the relay concept as well as potential applications of various cooperative MIMO systems in a cellular network. For example, when a user is behind buildings or underground, as seen in Figure 4.1, direct communication with the Base Station (BS) becomes unreliable, owing to severe shadow fading and path loss. In order to maintain reliable wireless communications, a group of users in each others' vicinity may form a virtual antenna array in order to reliably forward the data between the source node and the BS.

A ground-breaking paper of Cover and El Gamal [127] proposed several cooperation strategies for the relays and extensively investigated the information-theoretic properties based on the assumption of encountering Line-Of-Sight (LOS) Gaussian channels. More recent studies have fo-

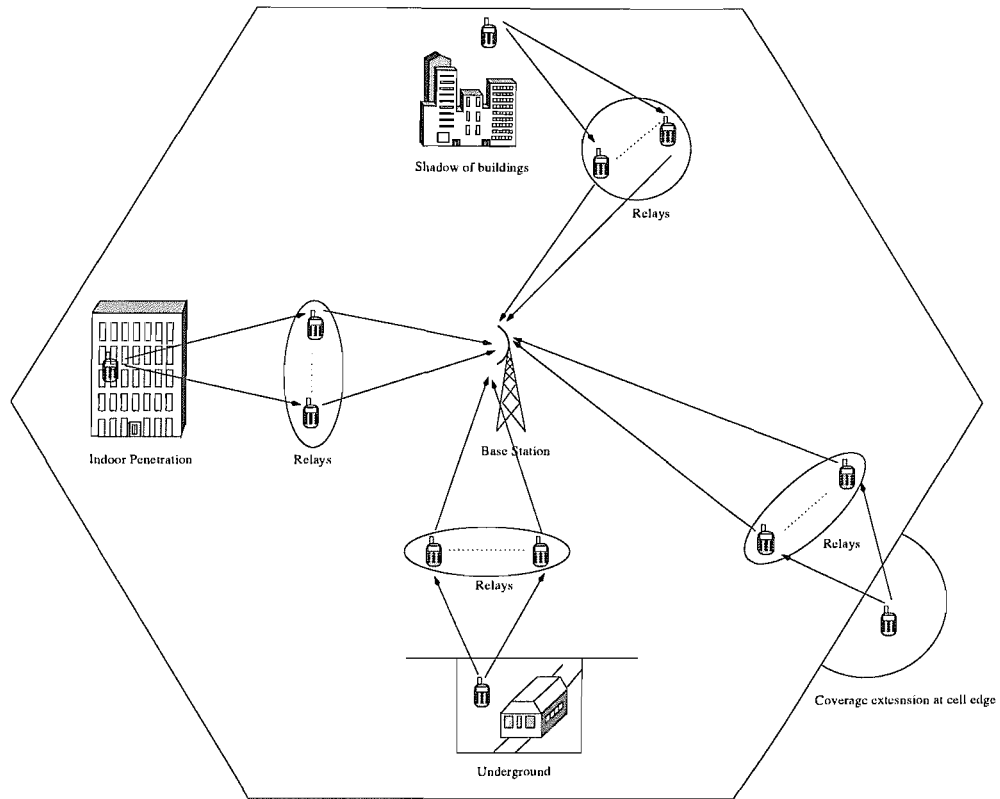


Figure 4.1: Cooperative MIMO systems in a cellular network.

cused on the more realistic assumptions of encountering fading channels [46] [52] and applied the relay-aided cooperation concept to wireless sensor networks [128]. It has been shown by several researchers [52] [129] that considerable benefits can be achieved as a result of relay-aided cooperation, including the reduction of the outage probability and a substantial diversity gain as well as throughput improvement.

Generally speaking, there are three types of cooperations [127], Amplify-and-Forward (AF), Decode-and-Forward (DF) as well as Compress-and-Forward (CF). When using the AF cooperation scheme, the relay nodes simply amplify the received signal waveforms, but they amplify the signal and noise jointly and hence are unable to improve the SNR. On the other hand, in the DF strategy, the signals received at the relays are decoded and possibly re-encoded using different Forward Error Correction (FEC) codes, before being forwarded to the destination. Finally, the CF arrangement is also referred to as an observe-forward or quantize-forward technique by some researchers [129]. In its original form [127], the relay compresses, estimates or quantizes its observations without decoding the information.

Owing to the philosophical similarities between the cooperative MIMO and the co-located MIMO systems, numerous space-time block coding techniques have been 'transplanted' into relay-aided schemes in order to achieve cooperative diversity, based on either AF strategies [40] [42] or

DF arrangements [46] [52]. It was Laneman and Wornell [40] who first proposed to employ orthogonal STBCs for cooperative MIMO systems, where each relay transmits according to a different column of the orthogonal STBC matrix. As argued in Chapter 2, the family of LDCs [1] constitutes a powerful design alternative to provide cooperative diversity gain for various relay-aided systems [44] [49] [50], owing to its remarkable design flexibility guaranteed by its linear structure. Furthermore, the authors of [43] [51] [45] exploited the diversity-multiplexing gain tradeoff as a means of evaluating the fundamental limitations of different cooperation strategies. In a similar manner, the same tradeoff was capitalized on by Zheng and Tse in the context of co-located MIMO systems [7].

In an effort to introduce channel coding schemes into cooperative MIMO systems for the sake of attaining near error-free transmission, the authors of [130] [131] developed the so-called 'coded-cooperative' schemes, where each relay contributes extrinsic information in a manner similar to the 'parallel-concatenated' component of classic turbo codes [64]. More explicitly, after receiving the channel-coded signals broadcast by the source node, the relays decode and interleave the information, before it is re-encoded by another channel encoder. Hence, the BS becomes capable of exploiting the extrinsic information gleaned from various interleaved replicas of the transmitted information by employing a conventional turbo detector [64]. In [132] [133], the coded-cooperative aided schemes have been further improved by forwarding the soft estimates of the transmitted bits from the relays, rather than forwarding the hard decoded bits. However, this family of coded-cooperative schemes inevitably imposes both a high complexity as well as a high delay at the relays. Furthermore, it increases the power consumption of the relays despite transmitting no source-data from themselves.

Since relay strategies typically consist of two-phase transmissions, namely the broadcast interval and the cooperation interval, in this chapter we propose a novel family of twin-layer Cooperative Linear Dispersion Codes (CLDCs), which allows us to explore each transmission interval's specific characteristics as well as to design them jointly. We also propose a novel serial concatenated coded-cooperative system and highlight its benefits in contrast to the coded-cooperative schemes of [130] [131] based on parallel concatenated philosophies. More explicitly, the novel features of the schemes proposed in this chapter are listed as follows:

- The proposed twin-layer CLDC schemes inherit the LDCs' flexible yet powerful structure, where similar diversity properties can be observed. Therefore, the CSTBCs listed in Table 1.3 remain subsets of the CLDC structure;
- The twin-layer CLDC schemes may be readily integrated with next-generation systems, such

as the Third Generation Partnership Project's Long Term Evolution (3GPP-LTE) proposals, while supporting an arbitrary number of relays equipped with single or multiple antennas;

- The power consumption as well as the complexity imposed by cooperation at the relays are insignificant, since only simple linear combination operations are performed;
- We propose a novel IRCC aided IrRegular Precoded Cooperative Linear Dispersion Code (IR-PCLDC) using iterative decoding, which is designed based on EXIT charts [55];
- The proposed IRCC-coded IR-PCLDC scheme becomes capable of providing a flexible throughput, which may be harmonized with the SNR encountered.

The rest of this chapter is structured in two parts. The first part commences by presenting a general system model for the CLDCs based on the AF protocol in Section 4.2.1 and outlines the associated assumptions in Section 4.2.2, followed by the mathematical characterization of the twin-layer CLDC scheme. Hence, the linkage between LDCs designed for co-located MIMO systems and CLDCs designed for cooperative MIMO systems is outlined in Section 4.2.4. In the second part of our investigations, Section 4.3 introduces the irregular design philosophy in the context of cooperative systems and proposes a novel IRCC-coded IR-PCLDC scheme in order to maintain high rates across a wide SNR range, while maintaining an infinitesimally low BER. We focus our attention on the irregular system's distinctive features in the context of the cooperative MIMO systems. The corresponding irregular co-located MIMO system detailed in Section 2.5.3 will be used as the benchmark. Finally, the findings of this chapter are summarized in Section 4.4.

4.2 Twin-Layer Cooperative Linear Dispersion Codes

4.2.1 System Model

In this section, we commence our discourse with the detailed description of the proposed twin-layer CLDCs based on the AF cooperation protocol, noting that this philosophy may be readily extended to DF and CF strategies. An UpLink (UL) scenario in a cellular network is considered, as exemplified in Figure 4.1, where a source node communicates with the BS having N receive antennas with the aid of M independent relays. For simplicity, each cooperating node is assumed to equip with a single transmit antenna, although multiple antenna aided nodes may also be incorporated into the proposed CLDCs.

Figure 4.2 portrays the schematic of the cooperation-aided uplink system based on the proposed twin-layer CLDCs. As seen in Figure 4.2, each transmission block consists of two intervals,

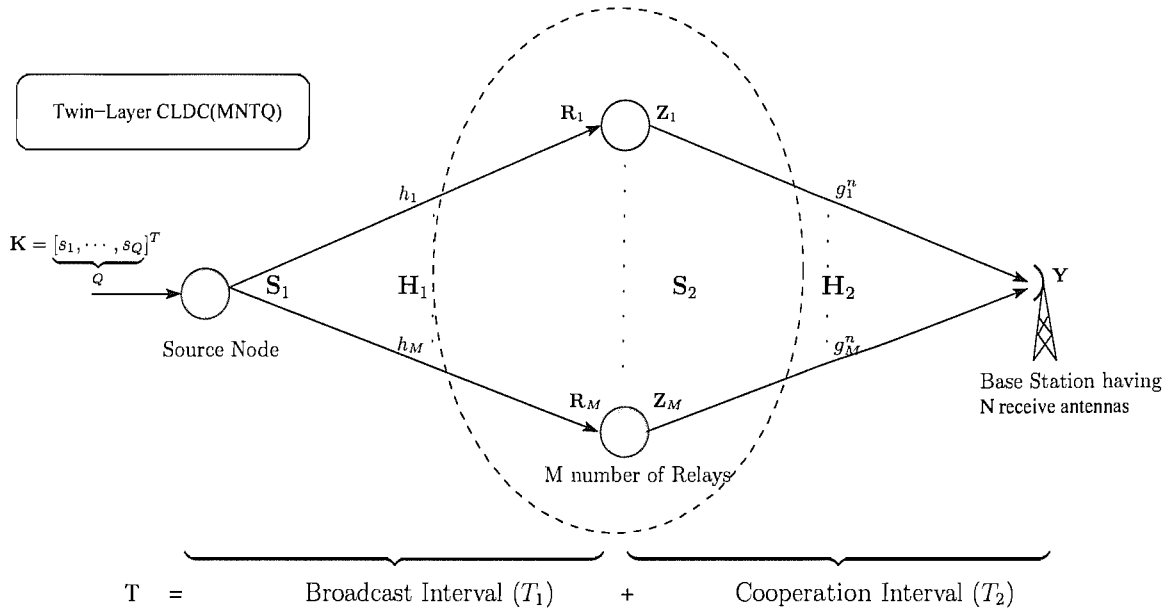


Figure 4.2: Schematic of the cooperation-aided uplink system employing the twin-layer Cooperative Linear Dispersion Codes (CLDCs).

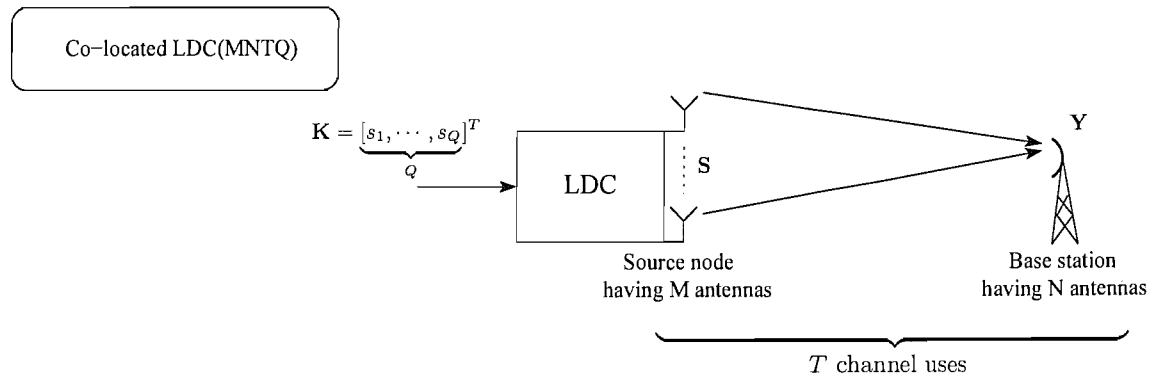


Figure 4.3: Schematic of a co-located uplink MIMO system using Linear Dispersion Codes (LDCs).

namely the broadcast interval and the cooperation interval. During the broadcast interval T_1 , the source broadcasts an UL information bearing vector $\mathbf{K} = [s_1, \dots, s_Q]^T$ containing Q L-PSK symbols to the relay nodes using CLDC's the first-layer dispersion matrix, which will be detailed in Section 4.2.3. During the cooperation interval T_2 , the relays form a virtual antenna array and cooperatively transmit a space-time codeword \mathbf{S}_2 of Figure 4.2 to the BS based on CLDC's second-layer dispersion matrices. Hence, the twin-layer CLDC scheme of Figure 4.2 based on the AF strategy can be fully specified by the parameters ($MNTQ$), provided that the total number of channel uses T obeys $T = T_1 + T_2$. Throughout our investigations, a side-by-side comparison of the twin-layer cooperative CLDC($MNTQ$) scheme and the corresponding co-located LDC($MNTQ$) arrangement of Figure 4.3 is provided.

4.2.2 System Assumptions

This section outlines the assumptions stipulated, in order to make the twin-layer CLDC scheme of Figure 4.2 as practical as possible. The assumptions and their rationale are summarized as follows:

- All the relays of Figure 4.2 are assumed to transmit synchronously. Quasi-synchronous transmissions can be accomplished, when the relative delays between the relays are significantly shorter than the symbol duration. Solutions designed for asynchronous cooperations have been proposed by a number authors [134] [135], but this issue is beyond the scope of our discussions;
- All the nodes of Figure 4.2 are assumed to have a single antenna and hence operate in half-duplex mode, i.e. at any point of time, a node can either transmit or receive. This constraint is imposed, in order to prevent the high-power transmit signal from contaminating the low-power received signal, for example, by the non-linear distortion-induced out-of-bound emissions routinely encountered at the transmitter. This may even potentially mislead the Automatic Gain Control (AGC) of the receiver into believing that a high-level signal was received, which would block the useful received signal arriving at a low power;
- All the relays of Figure 4.2 transmit and receive on the same frequency as the source node, in order to avoid wasting or occupying additional bandwidth;
- No communication is permitted between the relays, in an effort to minimize the total network traffic. The relays may use the same unallocated time-slot for their reception and transmission;
- Since the simple AF strategy is adopted, only linear combination operations are performed at the relays before retransmitting the signals dispersed to the cooperating MIMO elements to the BS, which will be explicitly shown in the context of Equation (4.13);
- The BS seen in Figure 4.2 is equipped with N receive antennas. Moreover, the BS is assumed to have the knowledge of perfect CSI for all the wireless links, i.e. it knows \mathbf{H}_1 and \mathbf{H}_2 of Figure 4.2 in order to facilitate coherent detection. More particularly, \mathbf{H}_1 and \mathbf{H}_2 are given by

$$\mathbf{H}_1 = [h_1, \dots, h_M]^T, \quad \mathbf{H}_2 = \begin{pmatrix} g_1^1 & \cdots & g_m^1 \\ \vdots & \ddots & \vdots \\ g_1^N & \cdots & g_m^N \end{pmatrix}, \quad (4.1)$$

where h_m denotes the CIR between the source and the m -th relay of the broadcast interval and g_m^n denotes the CIR between the m -th relay and the n -th receive antenna of the BS during the cooperation interval, and we have $m = (1, \dots, M)$ and $n = (1, \dots, N)$;

- All the channel matrices \mathbf{H}_1 and \mathbf{H}_2 of Figure 4.2 are assumed to be representing quasi-static Rayleigh-fading, i.e. the channel gains remain constant during T time slots and change independently at the beginning of the next. Furthermore, the channels gains are assumed to be spatially independent, while having a unit variance. Therefore, the resultant virtual antenna array elements can be considered to be subjected to perfectly independent fading. By contrast, the co-located MIMO elements of Figure 4.3 typically suffer from a certain degree of spatial correlation, owing to their insufficient spatial separation;
- We confine the total number of channel uses of the twin-layer CLDC scheme of Figure 4.2 to T , where $T = T_1 + T_2$. Hence, by appropriately adjusting the parameters T_1 or T_2 , different degrees of freedom can be provided for the broadcast interval as well as for the cooperation interval;
- At any given time, the total transmit power of the twin-layer CLDC scheme of Figure 4.2 is normalized to unity. More explicitly, the source transmits at unit power during the broadcast interval, but keeps silent during the cooperation interval. On the other hand, after listening for T_1 time slots, each relay transmits a signal vector with the power of $\frac{1}{M}$ in order to exploit the next unallocated T_2 time slots. Since M number of relays are involved in the cooperation, the total power remains unity during the cooperation interval.

4.2.3 Mathematical Representations

Based on the assumptions outlined in Section 4.2.2, we are now ready to provide a more insightful description of the twin-layer CLDC model of Figure 4.2. When a user intends to transmit data, the BS firstly functions as a control unit and selects a group of nearby users in order to assist the source node's UL transmission. More specifically, the BS assigns a dispersion matrix χ_1 obeying Equation (4.4) to the source node in order to enable its UL transmission during the broadcast interval. Each relay also receives a different dispersion matrix \mathbf{B}_m obeying Equation (4.13) from the BS in order to attain diversity during the cooperation interval. These control information transmissions are necessary for initializing the cooperation-aided UL transmission of the source node.

Since the distance between the relays is typically far lower than the distance to the source, we

could reasonably assume that the SNR between the source and the relays becomes:

$$\rho_{SR} = \frac{1}{\sigma_{SR}^2}, \quad (4.2)$$

where σ_{SR}^2 denotes the corresponding noise variance at the relays. During the cooperation interval, each relay transmits at a power of $\frac{1}{M}$, which implies that the total transmit power is evenly distributed across the M relays of Figure 4.2. Hence, the SNR at the BS can be written as:

$$\rho_{RB} = \frac{1}{\sigma_{RB}^2}, \quad (4.3)$$

where σ_{RB}^2 is the noise variance at the BS.

In the first stage of the cooperation-aided communication, namely the broadcast interval occupying T_1 time slots, the source node encodes each L -PSK modulated information vector $\mathbf{K} = [s_1, \dots, s_Q]^T$ to a transmission vector $\mathbf{S}_1 \in \zeta^{T_1 \times 1}$ based on

$$\underbrace{\begin{pmatrix} t^1 \\ \vdots \\ t^{T_1} \end{pmatrix}}_{\mathbf{S}_1} = \underbrace{\begin{pmatrix} x^{1,1} & \dots & x^{1,Q} \\ \vdots & \ddots & \vdots \\ x^{T_1,1} & \dots & x^{T_1,Q} \end{pmatrix}}_{\chi_1 \mathbf{K}} \underbrace{\begin{pmatrix} s_1 \\ \vdots \\ s_Q \end{pmatrix}}_{\mathbf{S}_1}, \quad (4.4)$$

where the first-layer dispersion matrix $\chi_1 \in \zeta^{T_1 \times Q}$ is responsible for dispersing the information vector \mathbf{K} to all the T_1 temporal dimensions. According to the power constraint, the transmission vector is normalized to $E\{tr(\mathbf{S}_1^H \mathbf{S}_1)\} = T_1$, which requires the dispersion matrix χ_1 to satisfy

$$tr(\chi_1^H \chi_1) = T_1. \quad (4.5)$$

At the m -th relay, the corresponding receive vector $\mathbf{R}_m = [r_m^1, \dots, r_m^{T_1}]^T$ becomes

$$\mathbf{R}_m = h_m \mathbf{S}_1 + \mathbf{V}_m. \quad (4.6)$$

By stacking the received signals from M relays, we arrive at

$$\underbrace{\begin{pmatrix} \mathbf{R}_1 \\ \vdots \\ \mathbf{R}_M \end{pmatrix}}_{\mathbf{R}} = \underbrace{\begin{pmatrix} h_1 \mathbf{I} \\ \vdots \\ h_M \mathbf{I} \end{pmatrix}}_{\bar{\mathbf{H}}_1 \mathbf{S}_1} \mathbf{S}_1 + \underbrace{\begin{pmatrix} \mathbf{V}_1 \\ \vdots \\ \mathbf{V}_M \end{pmatrix}}_{\bar{\mathbf{V}}_1}, \quad (4.7)$$

where $\mathbf{R} = [\mathbf{R}_1, \dots, \mathbf{R}_M]^T$ and $\bar{\mathbf{V}}_1 \in \zeta^{MT_1 \times 1}$ denotes the combined noise vector having a variance of σ_{SR}^2 . The equivalent channel matrix $\bar{\mathbf{H}}_1 \in \zeta^{MT_1 \times T_1}$ of Equation (4.7) can be represented by

$$\bar{\mathbf{H}}_1 = \mathbf{H}_1 \otimes \mathbf{I}, \quad (4.8)$$

where \mathbf{I} denotes an identity matrix having a size of $(T_1 \times T_1)$. Furthermore, by combining Equations (4.4) and (4.7), we have

$$\mathbf{R} = \bar{\mathbf{H}}_1 \chi_1 \mathbf{K} + \bar{\mathbf{V}}_1. \quad (4.9)$$

During the cooperation interval of Figure 4.2, the relays cooperatively construct a space-time codeword based on the pre-assigned dispersion matrices \mathbf{B}_m of Equation (4.13) using the received signal vectors \mathbf{R}_m of Equation (4.6). Firstly, the energy of the received signals has to be normalized during the broadcast interval. From Equation (4.6), we have

$$E\{\mathbf{R}_m^H \mathbf{R}_m\} = (1 + \sigma_{SR}^2)T_1. \quad (4.10)$$

Thus, before performing the second-layer dispersion operations, we multiply \mathbf{R}_m of Equation (4.6) by the normalization factor

$$\theta = \sqrt{\frac{T_1}{E\{\mathbf{R}_m^H \mathbf{R}_m\}}} = \sqrt{\frac{1}{1 + \sigma_{SR}^2}}, \quad (4.11)$$

so that we arrive at

$$\theta^2 E\{\mathbf{R}_m^H \mathbf{R}_m\} = T_1. \quad (4.12)$$

At the m -th relay, the second-layer dispersion matrices $\mathbf{B}_m \in \zeta^{T_2 \times T_1}$ are employed to disperse the normalized received vector $\theta \mathbf{R}_m$ to the T_2 available number of time slots. Hence, the m -th relay's transmitted vector is given by

$$\underbrace{\begin{pmatrix} z_m^1 \\ \vdots \\ z_m^{T_2} \end{pmatrix}}_{\mathbf{Z}_m} = \underbrace{\theta \begin{pmatrix} b_m^{1,1} & \dots & b_m^{1,T_1} \\ \vdots & \ddots & \vdots \\ b_m^{T_2,1} & \dots & b_m^{T_2,T_1} \end{pmatrix}}_{\theta \cdot \mathbf{B}_m} \underbrace{\begin{pmatrix} r_m^1 \\ \vdots \\ r_m^{T_1} \end{pmatrix}}_{\mathbf{R}_m}, \quad (4.13)$$

which should satisfy the power constraint of $E\{tr(\mathbf{Z}_m^H \mathbf{Z}_m)\} = \frac{T_2}{M}$ and z_m^i ($i = 1, \dots, T_2$) denotes the m -th relay's transmit signal of the i -th slot. Thus, the set of second-layer matrices \mathbf{B}_m should obey

$$tr(\mathbf{B}_m^H \mathbf{B}_m) = \frac{T_2}{M}. \quad (4.14)$$

Therefore, the 'virtual' space-time codeword $\mathbf{S}_2 \in \zeta^{M \times T_2}$ of Figure 4.2 can be formed by concatenating the dispersed vectors from all the relays, which is given by

$$\mathbf{S}_2 = \begin{pmatrix} \mathbf{Z}_1^T \\ \vdots \\ \mathbf{Z}_M^T \end{pmatrix} = \theta \begin{pmatrix} (\mathbf{B}_1 \mathbf{R}_1)^T \\ \vdots \\ (\mathbf{B}_M \mathbf{R}_M)^T \end{pmatrix}. \quad (4.15)$$

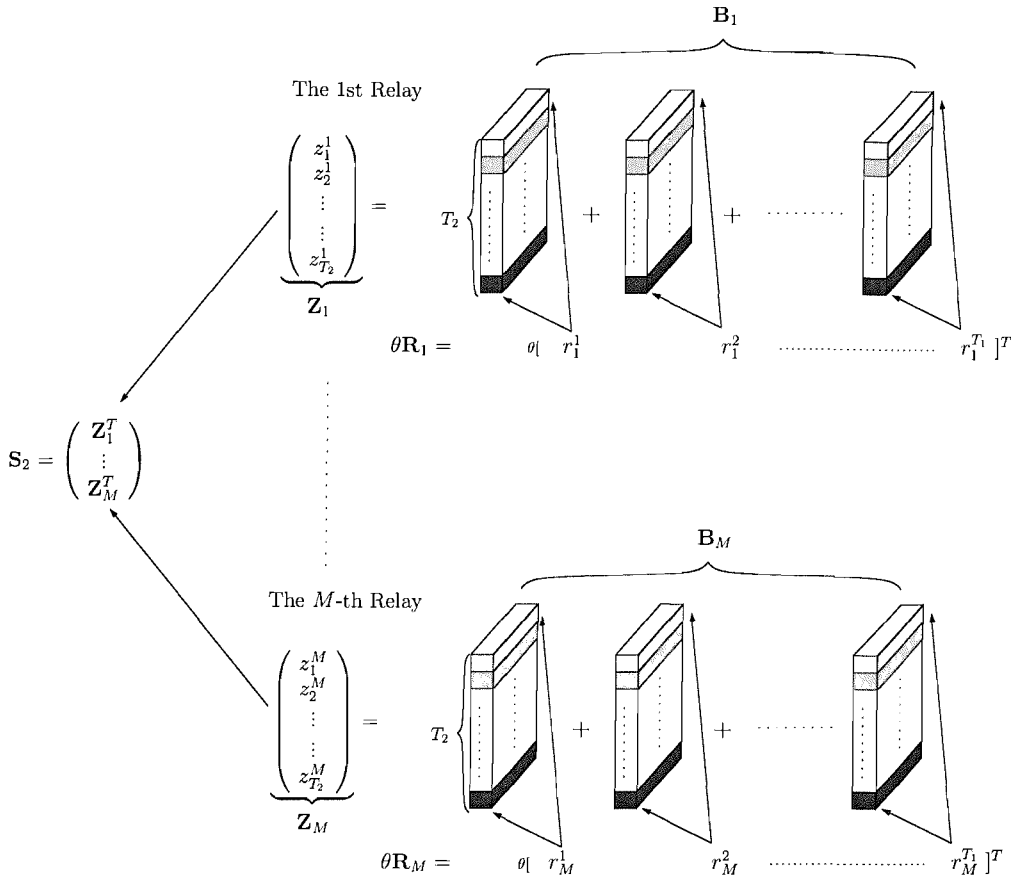


Figure 4.4: The cooperative space-time codeword \mathbf{S}_2 formulated based on Equations (4.13) and (4.15).

Observe in Equation (4.15) that each relay contributes one row of the second-layer space-time codeword \mathbf{S}_2 . Also note that each relay's received signal \mathbf{R}_m formulated in Equation (4.6) may experience quite different channel conditions, owing to experiencing i.i.d. Rayleigh fading. Furthermore, the process of forming the cooperative space-time codeword \mathbf{S}_2 for the cooperation interval is visualized in Figure 4.4. More explicitly, the m -th relay disperses the corresponding normalized received signal vector $\theta\mathbf{R}_m = \theta[r_m^1, \dots, r_m^{T_1}]^T$ to the T_2 temporal slots using the assigned dispersion matrix \mathbf{B}_m obeying Equation (4.13), as seen in Figure 4.4. The resultant signal vector \mathbf{Z}_m contributes one row the space-time codeword \mathbf{S}_2 of Equation (4.15).

At the BS, the received signal matrix $\mathbf{Y} \in \zeta^{N \times M}$ of Figure 4.2 becomes

$$\mathbf{Y} = \mathbf{H}_2 \mathbf{S}_2 + \mathbf{V}_2. \quad (4.16)$$

Define the *row()* operation as the vertical stacking of the rows of an arbitrary matrix. Subjecting both sides of Equation (4.16) to the *row()* operation gives the equivalent system matrix:

$$\bar{\mathbf{Y}} = \bar{\mathbf{H}}_2 \mathbf{Z} + \bar{\mathbf{V}}_2, \quad (4.17)$$

where $\bar{\mathbf{Y}} \in \zeta^{NT_2 \times 1}$ and $\bar{\mathbf{V}}_2 \in \zeta^{NT_2 \times 1}$ denotes the noise vector having a variance of σ_{RB}^2 . The

equivalent channel matrix $\bar{\mathbf{H}}_2 \in \zeta^{NT_2 \times MT_2}$ of Equation (4.17) is given by

$$\bar{\mathbf{H}}_2 = \mathbf{H}_2 \otimes \mathbf{I}, \quad (4.18)$$

and the equivalent transmission matrix $\mathbf{Z} \in \zeta^{MT_2 \times 1}$ of Equation (4.17) becomes

$$\underbrace{\begin{pmatrix} \mathbf{Z}_1 \\ \vdots \\ \mathbf{Z}_M \end{pmatrix}}_{\mathbf{Z}} = \underbrace{\begin{pmatrix} \mathbf{B}_1 & \mathbf{0} & \cdots & \mathbf{0} \\ \mathbf{0} & \mathbf{B}_m & \cdots & \mathbf{0} \\ \mathbf{0} & \mathbf{0} & \ddots & \mathbf{0} \\ \mathbf{0} & \cdots & \cdots & \mathbf{B}_M \end{pmatrix}}_{\chi_2 \cdot \theta \mathbf{R}} \cdot \theta \mathbf{R}, \quad (4.19)$$

where $\mathbf{0} \in \zeta^{T_2 \times T_1}$ denotes a zero matrix. The equivalent second-layer Dispersion Character Matrix (DCM) $\chi_2 \in \zeta^{MT_2 \times MT_1}$ defined in Equation (4.19) fully characterizes the transmissions during the cooperation interval.

Further combining Equations (4.9), (4.17) and (4.19) we arrive at

$$\begin{aligned} \bar{\mathbf{Y}} &= \bar{\mathbf{H}}_2 \mathbf{Z} + \bar{\mathbf{V}}_2 \\ &= \theta \bar{\mathbf{H}}_2 \chi_2 \mathbf{R} + \bar{\mathbf{V}}_2 \\ &= \theta \bar{\mathbf{H}}_2 \chi_2 (\bar{\mathbf{H}}_1 \chi_1 \mathbf{K} + \bar{\mathbf{V}}_1) + \bar{\mathbf{V}}_2 \\ &= \theta \underbrace{\bar{\mathbf{H}}_2 \chi_2 \bar{\mathbf{H}}_1 \chi_1}_{\bar{\mathbf{H}} \mathbf{K}} \mathbf{K} + \theta \underbrace{\bar{\mathbf{H}}_2 \chi_2 \bar{\mathbf{V}}_1 + \bar{\mathbf{V}}_2}_{\bar{\mathbf{V}}}. \end{aligned} \quad (4.20)$$

The combined noise $\bar{\mathbf{V}}$ becomes colored, with a covariance of $\sigma_0^2 = (\mathbf{I}_{T_2} \sigma_{RB}^2 + \theta^2 \bar{\mathbf{H}}_2 \chi_2 \chi_2^H \bar{\mathbf{H}}_2^H \sigma_{SR}^2)$, owing to the noise amplification and recombination experienced at the relays. The equivalent channel matrix $\bar{\mathbf{H}} \in \zeta^{NT_2 \times Q}$ of Equation (4.20) is known to the BS, since the BS has the knowledge of the CIR matrices \mathbf{H}_1 as well as \mathbf{H}_2 of Figure 4.2 and that of the DCM pair $\{\chi_1, \chi_2\}$. Most importantly, Equation (4.20) demonstrates that the twin-layer CLDC structure originally formulated in Equations (4.4) and (4.13) can be merged into a 'single' equivalent channel matrix.

In order to perform ML detection, we have to whiten the noise, which is achieved by multiplying with $\sigma_0^{2-\frac{1}{2}}$ on both sides of Equation (4.20). Hence, the ML estimation of the transmitted symbol vector $\mathbf{K} = [s_1, \dots, s_Q]^T$ can be written as

$$\bar{\mathbf{K}} = \arg \{ \min (||\sigma_0^{2-\frac{1}{2}} \mathbf{Y} - \sigma_0^{2-\frac{1}{2}} \bar{\mathbf{H}} \mathbf{K}_f||^2) \}, \quad (4.21)$$

where \mathbf{K}_f denotes all the possible combinations of the Q transmitted symbols.

Table 4.1: Comparison of the LDCs of Figure 4.3 and the CLDCs of Figure 4.2.

	LDCs of Figure 4.3	CLDCs of Figure 4.2
M	Number of transmit antennas	Number of relays
N	Number of receive antennas	Number of receive antennas
T	Time slots per LDC block	$T = T_1 + T_2$
Q	Number of symbols	Number of symbols
R	$R_{LDC} = Q/T$	$R_{CLDC} = Q/T$
\mathbf{K}	Perfect knowledge	Obtained using Equation (4.6)
DCM	χ	$\{\chi_1, \chi_2\}$
Equivalent channel matrix	$\bar{\mathbf{H}}\chi$ of Equation (2.15)	$\bar{\mathbf{H}}_2\chi_2\bar{\mathbf{H}}_1\chi_1$ of Equation (4.20)

4.2.4 Link Between CLDCs and LDCs

This section aims for characterizing the fundamental link between the LDCs designed for the co-located MIMO systems of Figure 4.3 and the CLDCs contrived for the cooperative MIMO systems of Figure 4.2. The similarities as well as the differences between the LDCs and the CLDCs are summarized in Table 4.1 and a range of remarks is offered as follows.

- The LDCs of Figure 4.3 employ M number of transmit antennas, whereas the CLDCs of Figure 4.2 form an identical-size virtual antenna array with the aid of M relays selected by the BS;
- In both scenarios, the UL receiver of the BS is assumed to have N receive antennas;
- The LDCs of Figure 4.3 occupy a total of T channel slots per space-time block. For the sake of a fair comparison, the twin-layer CLDCs also span $T = T_1 + T_2$ time slots per block. More explicitly, the broadcast interval having T_1 slots is employed for the relays to receive the source information, whereas T_2 time slots are used for the cooperation phase;
- The symbol rate of both the LDCs and CLDCs is defined as $R = \frac{Q}{T}$, where Q is the number of L -PSK symbols transmitted per space-time block;
- When constructing the symbol vector $\mathbf{K} = [s_1, \dots, s_Q]^T$, each transmit antenna element of the LDCs of Figure 4.3 has direct access to the Q number of L -PSK symbols. In contrast, the CLDCs of Figure 4.2 only have access to the potentially channel-contaminated version of \mathbf{K} received during the broadcast interval using Equation (4.6). We will characterize the CLDCs'

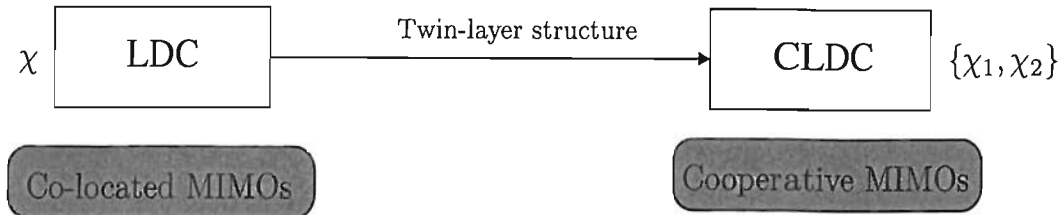


Figure 4.5: Link between LDCs designed for co-located MIMO systems and twin-layer CLDCs designed for cooperative MIMO systems.

BER performance in Figure 4.7, when the relays have differently contaminated information vectors of \mathbf{K} ;

- LDCs can be fully characterized by a single DCM χ , as extensively demonstrated in Chapter 2. By contrast, the CLDCs are characterized by a DCM pair $\{\chi_1, \chi_2\}$, which was given in Equations (4.4) and (4.19), respectively, owing to the twin-layer structure shown in Figure 4.2. The twin-layer structure portrays the fundamental design difference between LDCs and CLDCs, and this relationship is explicitly shown in Figure 4.5;
- The LDCs' equivalent channel model of Equation (2.15) implies transmitting the symbol vector \mathbf{K} through the channel characterized by the equivalent channel matrix $\bar{\mathbf{H}}\chi$. Similarly, Equation (4.20) indicates that the CLDCs transmit the symbol vector \mathbf{K} through the channel characterized by the equivalent channel matrix $\bar{\mathbf{H}}_2\chi_2\bar{\mathbf{H}}_1\chi_1$. More explicitly, the DCM χ_1 of Equation (4.4) together with the CIR matrix $\bar{\mathbf{H}}_1$ of Equation (4.8) characterizes the transmission during the broadcast interval, while the cooperation interval is characterized by the DCM χ_2 of Equation (4.19) as well as by $\bar{\mathbf{H}}_2$ of Equation (4.18).

Observe furthermore in Equations (2.15) and (4.20) that both LDCs and CLDCs obey a similar equivalent system structure, where the equivalent CIR matrix is determined by the channel CIR experienced and the specific DCM employed. Recall from Section 2.2.4 that we optimized the LDCs' DCM χ based on the DCMC capacity of Equation (2.23) using the corresponding equivalent channel matrix of Equation (2.15). Similarly, for a CLDC scheme, we are looking for the particular pair of DCMs $\{\chi_1, \chi_2\}$ that maximizes the DCMC capacity of Equation (2.23). Accordingly, all the DCM pairs $\{\chi_1, \chi_2\}$ used in this chapter are listed in Appendix C.

4.2.5 Performance Results

This section presents the simulation results for a number of CLDC schemes obeying the structure of Figure 4.2, which are associated with parameters $(MNTQ)$. In most of our simulations, we

Table 4.2: System parameters for the CLDC schemes of Figure 4.2.

Number of relays	M
Number of antenna per relay	1
Number of antennas at BS	N
Total channel uses	$T = T_1 + T_2$
Number of symbols per CLDC block	Q
SNR (dB)	$\rho_{SR} = \rho_{RB}$
Modulation	BPSK
Mapping	Gray mapping
Detector	ML of Equation (4.21)

set the SNR ρ_{SR} experienced at the relays to the SNR ρ_{RB} recorded at the BS and the resultant BER performance is plotted against ρ_{RB} . However, the scenarios where $\rho_{SR} \neq \rho_{RB}$ are also characterized in Figure 4.9. All the system parameters are listed in Table 4.2, unless otherwise stated.

Figure 4.6 characterizes the BER of a family of CLDCs having $M = 4$, $N = 1$, $T = 8$ and $T = 3$ as well as using different T_1 and T_2 values, when transmitting over uncorrelated i.i.d. Rayleigh-fading channels. Since the total number of channel uses per CLDC block is set to a relatively high value of $T = 8$, we are able to vary the resource allocation by employing different T_1 and T_2 values during the broadcast and cooperation intervals. Observe in Figure 4.6 that the best achievable BER performance was recorded, when we have $T_1 = 2$ and $T_2 = 6$. This phenomenon is related to the achievable cooperative diversity gain of the CLDC schemes of Figure 4.2.

More explicitly, observe in Figure 4.2 that during the broadcast interval, only first-order diversity can be achieved, because each cooperating node is equipped with a single antenna. During the cooperation interval, the space-time transmission matrix \mathbf{S}_2 of Equation (4.15) is formed across the relays, which potentially facilitates a spatial diversity order of $N \cdot \min(M, T_2)$ according to Theorem 3 of Chapter 2. Observe in Figure 4.6 that when we have $T_2 \geq (M = 4)$, the CLDCs achieve a cooperative diversity order of $D \approx 4$. The achievable performance is not exactly identical to that of fourth-order diversity, since the relays only have access to the noisy version of the transmitted information. When we have $(T_2 = 1, 2, 3) < M$, $D \approx 1, 2, 3$ can be observed from Figure 4.6, respectively. Again, observe in Figure 4.6 that the CLDC(4183) scheme having $T_1 = 2$ and $T_2 = 6$ exhibits the best BER performance, since it guaranteed the maximum achievable cooperative diversity order provided by the cooperation interval as well as protected the signals received by the

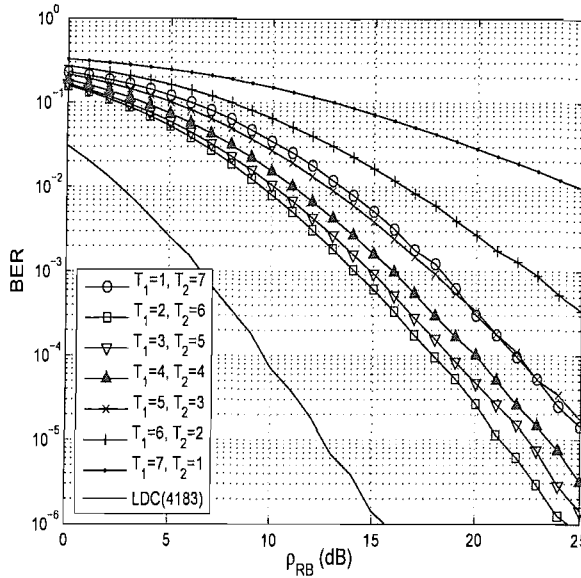


Figure 4.6: BER comparison of a group of CLDCs obeying the architecture of Figure 4.2 having $M = 4$, $N = 1$, $T = 8$ and $Q = 3$ while using different T_1 and T_2 values, when transmitting over uncorrelated i.i.d. Rayleigh-fading channels. All the system parameters were summarized in Table 4.2.

relays during the broadcast interval. Figure 4.6 also plots the BER of the LDC(4183) scheme of Figure 4.3 designed for the co-located MIMO system as our benchmarker. Observe in Figure 4.6 that an SNR gap of 8.3dB is recorded at $\text{BER} = 10^{-4}$ between the BER curves of the LDC(4183) scheme and the CLDC(4183) arrangement having $T_1 = 2$ and $T_2 = 6$. The non-cooperative LDC scheme outperformed its cooperative counterpart, which is predominantly owing to the imperfect reception of the source data by the relays during the broadcast phase. A further reason is that only a reduced number of slots is available for increasing the diversity gain during the cooperation phase owing to dedicating $T_1 = 2$ slots to the broadcast phase, which imposes further SNR penalties.

In order to further explain this SNR gap in more quantitative terms, Figure 4.7 plots the BER performance of the CLDC(4183) scheme having $T_1 = 2$ and $T_2 = 6$, when transmitting over perfect broadcast channels or AWGN as well as over noisy Rayleigh-faded source-to-relay channels. The channels between the relays and the BS are assumed to be uncorrelated i.i.d. Rayleigh-fading channels. When we have perfect source-to-relay links, namely the relays have access to the perfect source information, the CLDC(4183) scheme suffers about 1.8dB SNR penalty in comparison to the LDC(4183) benchmarker, since only $T_2 = 6$ time slots are employed for the cooperative transmission scenario compared to $T = 8$ slots available for the co-located MIMO systems. When the source-to-relay links are LOS AWGN channels, the associated SNR penalty in comparison to the LDC(4183) benchmarker increases only modestly to 3.3dB. Finally, when each relay's re-

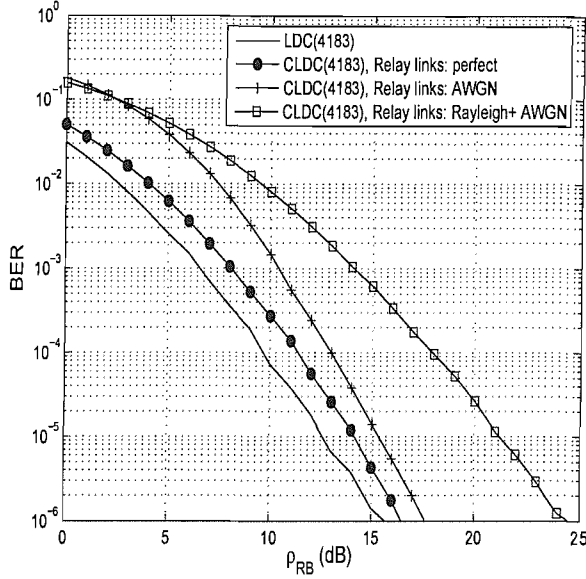


Figure 4.7: BER of the CLDC(4183) scheme of Figure 4.2 having $T_1 = 2$ and $T_2 = 6$. The source-to-relay channels were assumed to be either perfect, or a LOS AWGN or worse-case Rayleigh channels. The relay-to-BS channels remain uncorrelated i.i.d. Rayleigh-fading channels. All the system parameters were summarized in Table 4.2.

ceived signals \mathbf{R}_m formulated in Equation (4.6) suffers further, owing to experiencing independent Rayleigh fading, the SNR gap widens more dramatically to 8.3dB. It worth noting at this stage that owing to the crucial impact of the broadcast phase integrity on the overall BER performance, it is anticipated that the best combination of T_1 and T_2 has the potential of improving the overall BER performance.

The BER performance gap between the CLDCs and the corresponding LDCs illustrated in Figure 4.6 was investigated under small-scale Rayleigh fading conditions. However, when the transmitted signals are subjected to large-scale fading effects, i.e. shadow fading, the cooperative MIMO system has the potential to outperform its co-located MIMO system counterpart. More particularly, Figure 4.8 characterizes the BER performance of the LDC(4183) scheme following the schematic of Figure 4.3, when communicating over uncorrelated i.i.d. Rayleigh faded channels contaminated by large-scale shadow fading. The shadow fading effect is modelled to have log-normal distribution [136], which can be written as:

$$h_{slow} = 10^{\bar{h}_s/10}, \quad (4.22)$$

where \bar{h}_s is a random Gaussian variable with zero mean and standard deviation Ω (dB).

Observe in Figure 4.8 that when the shadow fading is insignificant, i.e. we have $\Omega = 0$ dB, the LDC(4183) scheme maintains the diversity order of $D \approx 4$, although suffering approximately

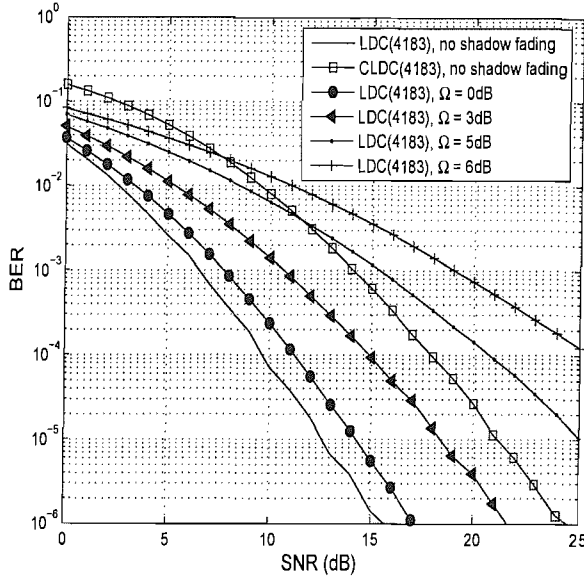


Figure 4.8: BER of the LDC(4183) scheme following the schematic of Figure 4.3, when communicating over uncorrelated i.i.d. Rayleigh faded channels contaminated by large-scale shadow fading governed by Ω .

1.4dB SNR penalty compared to the scenario in the absence of shadowing. When we have $\Omega = 6\text{dB}$, the achievable diversity order is reduced to $D = 1$, since all the communication channels tend to experience the same shadow fading. By contrast, the cooperative MIMO systems can eliminate the shadow fading effect by appropriately choosing a group of relays to assist their transmissions, as illustrated in Figure 4.1. Hence, Figure 4.8 demonstrates that the CLDC(4183) scheme is capable of offering more reliable transmissions than its co-located counterpart, when large-scale fading effects dominate the BER performance.

Figure 4.9 shows the BER performance of the CLDC(4183) scheme of Figure 4.2 having $T_1 = 2$ and $T_2 = 6$, when the source-to-relay Rayleigh fading channels have an SNR of ρ_{SR} , while the relay-to-BS Rayleigh fading channels have an SNR of ρ_{RB} . We use the BER curve of the CLDC(4183) scheme having $\rho_{SR} = \rho_{RB}$ as the benchmark, which was previously recorded in Figure 4.6. When we have $\rho_{SR} = \infty$, namely the source-to-relay links are Rayleigh fading channels without AWGN, the resultant BER curve exhibits 1.2dB SNR gain over the benchmark. When we gradually decrease the value of ρ_{SR} , an error floor begins to emerge, owing to the noise of the broadcast interval formulated in Equation (4.20). Again, Figure 4.9 evidences the importance of the received signals' integrity at relays.

Figure 4.10 quantifies the BER performance of a group of CLDCs having $M = 4$, $N = 1$, $T = 8$ and $Q = 1, 2, 3, 4, 5$, when transmitting over uncorrelated i.i.d. Rayleigh-fading channels. Previously, Figure 4.6 has demonstrated that the achievable BER performance is seriously affected

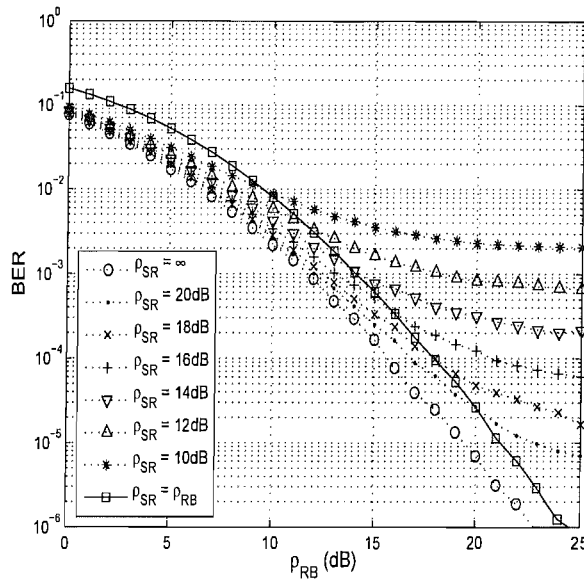


Figure 4.9: BER of the CLDC(4183) scheme of Figure 4.2 having $T_1 = 2$ and $T_2 = 6$, when communicating over uncorrelated i.i.d. Rayleigh faded channels at an SNR of ρ_{SR} and ρ_{RB} , respectively. All the system parameters were summarized in Table 4.2.

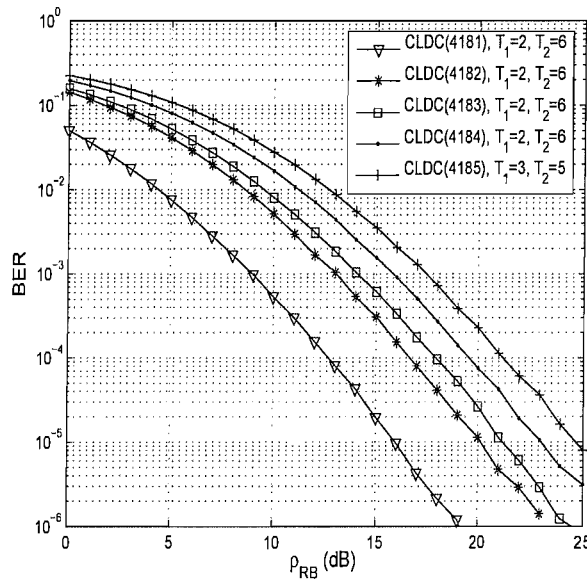


Figure 4.10: BER comparison of a group of CLDCs obeying the structure of Figure 4.2 having $M = 4$, $N = 1$, $T = 8$ and $Q = 1, 2, 3, 4, 5$, when transmitting over uncorrelated i.i.d. Rayleigh-fading channels. All the system parameters were summarized in Table 4.2.

Table 4.3: The best combination of T_1 and T_2 values for a group of CLDCs obeying the structure of Figure 4.2 having $M = 4$, $N = 1$, $T = 8$ and $Q = 1, 2, 3, 4, 5$.

	T	T_1	T_2	Diversity
CLDC(4181)	8	2	6	≈ 4
CLDC(4182)	8	2	6	≈ 4
CLDC(4183)	8	2	6	≈ 4
CLDC(4184)	8	2	6	≈ 4
CLDC(4185)	8	3	5	≈ 4

by the integrity of the source-to-relay channels, depending on the specific choice of T_1 and T_2 values. Similar to Figure 4.6, we are capable of appropriately configuring a specific CLDC(418Q) scheme by characterizing all the possible T_1 and T_2 combinations and then choosing the particular configuration exhibiting the best achievable BER performance. A group of CLDCs configured using this method is listed in Table 4.3, while their BER performance is shown in Figure 4.10. Furthermore, observe in Table 4.3 that all the CLDCs maintain $T_2 > M$, which potentially enables the CLDCs to achieve the maximum cooperative diversity order. When the value of Q is gradually increased, more time slots are necessary for the broadcast interval T_1 in order to increase the level of protection provided for the symbols received at the relays.

Figure 4.11 characterizes a group of CLDCs obeying the structure of Figure 4.2 having $M = 4$, $N = 1$, $T = 2, 4, 6, 8$ and $Q = 3$, when transmitting over uncorrelated i.i.d. Rayleigh-fading channels. Observe in Figure 4.11 that when the total number of slots available decreased from $T = 8$ to 4, the CLDC(4143) scheme having $T_1 = 1$ and $T_2 = 3$ exhibits a maximum diversity order of $D \approx 3$, since the cooperative diversity order is bounded by $N \cdot \min(M, T_2)$. When we have $T_1 = 1$ and $T_2 = 1$ corresponding to $T = 2$, the resultant CLDC(4123) scheme can only attain a cooperative diversity order of $D = 1$, despite the fact that $M = 4$ relays were employed to assist the cooperation-aided transmission. Again, Figure 4.11 demonstrates that the maximum achievable cooperative diversity order of a CLDC($MNTQ$) scheme is determined by both the total number of time slots T available and the number of relays M .

Figure 4.12 characterizes a group of CLDCs obeying the structure of Figure 4.2 having $M = 4$, $N = 1, 2, 3$, $T = 8$ and $Q = 3$ using $T_1 = 2$ as well as $T_2 = 6$, when communicating over uncorrelated i.i.d. Rayleigh-fading channels. As expected, when the BS employs more receive antennas, the maximum achievable diversity order can be significantly improved as a benefit of the well-known receive diversity gain. In fact, for this family of CLDCs, Figure 4.12 suggests that a

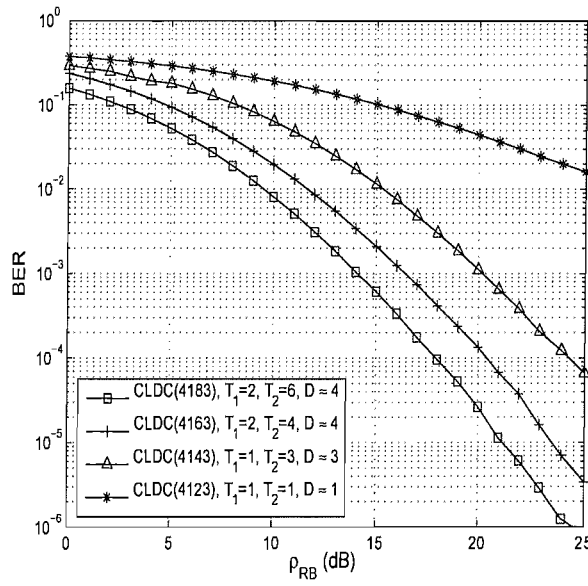


Figure 4.11: BER comparison of a group of CLDCs obeying the structure of Figure 4.2 and using $M = 4$, $N = 1$, $T = 2, 4, 6, 8$ and $Q = 3$, when transmitting over uncorrelated i.i.d. Rayleigh-fading channels. All the system parameters were summarized in Table 4.2.

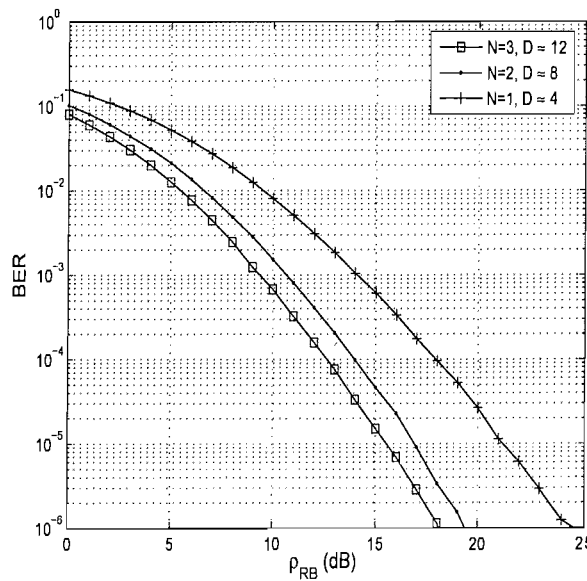


Figure 4.12: BER comparison of a group of CLDCs following the schematic of Figure 4.2 having $M = 4$, $N = 1, 2, 3$, $T = 8$ and $Q = 3$ using $T_1 = 2$ as well as $T_2 = 6$, when transmitting over uncorrelated i.i.d. Rayleigh-fading channels. All the system parameters were summarized in Table 4.2.

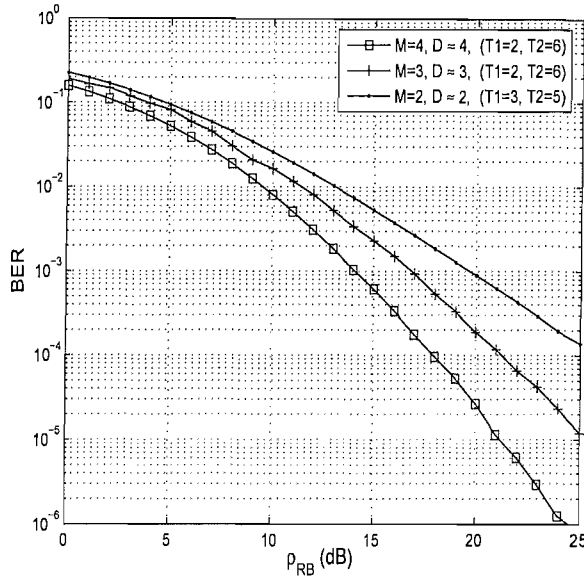


Figure 4.13: BER comparison of a group of CLDCs obeying the structure of Figure 4.2 having $M = 2, 3, 4, N = 1, T = 8$ and $Q = 3$, when transmitting over uncorrelated i.i.d. Rayleigh-fading channels. All the system parameters were summarized in Table 4.2.

cooperative diversity order of $D \approx 4, 8, 12$ can be achieved, when increase the value of N from 1 to 3.

Figure 4.13 attempts to characterize CLDCs' ability to provide cooperative diversity for the configuration of $M = 2, 3, 4, N = 1, T = 8$ and $Q = 3$, when transmitting over uncorrelated i.i.d. Rayleigh-fading channels. Observe in Figure 4.13 that a diversity order of $D \approx 2, 3, 4$ can be achieved with the aid of $M = 2, 3, 4$ relays, respectively, provided that maintaining $T_2 > M$ is guaranteed. Recall from Figure 4.6 that the CLDC(4183) scheme of Table 4.3 constitutes the best configuration, when we have $T_1 = 2$ and $T_2 = 6$. On the other hand, observe in Figure 4.13 that the CLDC(2183) scheme achieves the best performance, when we have $T_1 = 3$ and $T_2 = 5$.

In Figure 4.14, we characterize the effective throughput of a family of CLDCs employing the parameter of $M = 2, 3, 4, N = 1, T = 8$ and $Q = 1, 2, 3, 4$ recorded at $\text{BER} = 10^{-4}$, when transmitting over uncorrelated i.i.d. Rayleigh-fading channels, where the throughput is calculated as $C = \log_2(L) \cdot R_{CLDC}$. The increase of the effective throughput was achieved by transmitting more symbols Q per CLDC block and BPSK modulation was employed by all the schemes. The effective throughput achieved by the corresponding group of LDCs with/without shadowing is also shown as the benchmarker. Similarly, the effective throughput achieved by a group of CLDCs employing different number of receive antennas $N = 1, 2, 3$, while having the parameter of $M = 4, T = 8$ and $Q = 1, 2, 3, 4$ is quantified in Figure 4.15. Observe in Figures 4.14 and 4.15 that CLDCs outperform the corresponding LDCs, when encountering large-scale shadowing governed

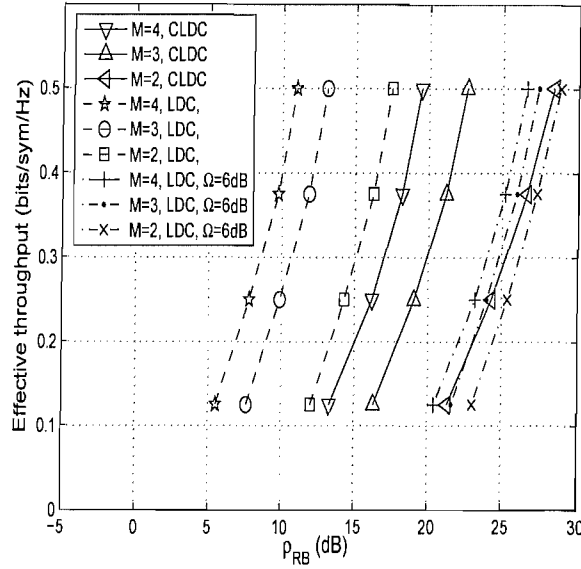


Figure 4.14: Effective throughput of a family of CLDCs obeying the structure of Figure 4.2 having $M = 2, 3, 4$, $N = 1$, $T = 8$ and $Q = 1, 2, 3, 4$ and the corresponding LDCs with/without shadowing, when transmitting over uncorrelated i.i.d. Rayleigh-fading channels. All the system parameters were summarized in Table 4.2.

by $\Omega = 6\text{dB}$.

Finally, Table 4.4 lists the coding gains of a family of CLDCs obeying the structure of Figure 4.2 and the corresponding LDCs having the structure of Figure 4.3, when having an effective throughput of 0.5 (bits/sym/Hz) as well as using BPSK modulation. The coding gain was defined as the SNR difference, at a BER of 10^{-4} between various LDCs/CLDCs and a single-antenna aided system having the same effective throughput. Observe in Table 4.4 that the achieve coding gains gradually increase with the number of relays and the family of LDCs having co-located MIMO elements suffers a substantial SNR penalty in the presence of shadowing.

4.3 IRCC-coded Precoder-Aided CLDCs

The 'coded-cooperative' schemes proposed in [130] and [132] were based on the DF cooperation strategy, which require the relays to perform either hard or soft decoding. However, the DF-based coded-cooperative schemes have two impediments. Firstly, the power consumption of the relays used for the decoding as well as for transmitting the re-encoded data may be quite significant. Secondly, the resultant overall delay at the final destination may become excessive, which renders the support of delay-sensitive real-time interactive applications, such as video telephony infeasible.

In this section, we propose a novel IRCC aided IrRegular Precoded Cooperative Linear Disper-

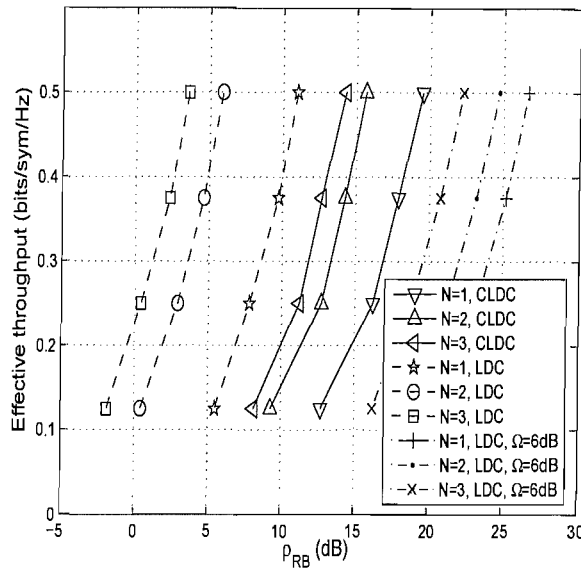


Figure 4.15: Effective throughput of a family of CLDCs obeying the structure of Figure 4.2 having $M = 4$, $N = 1, 2, 3$, $T = 8$ and $Q = 1, 2, 3, 4$ and the corresponding LDCs with/without shadowing, when transmitting over uncorrelated i.i.d. Rayleigh-fading channels. All the system parameters were summarized in Table 4.2.

Table 4.4: Coding gain comparison of a family of CLDCs obeying the structure of Figure 4.2 and the corresponding LDCs having the structure of Figure 4.3, which are extracted from Figures 4.14 and 4.15, when having an effective throughput of 0.5 (bits/sym/Hz) as well as using BPSK modulation.

CLDC				Coding Gain	LDC				Coding Gain no shadowing	Coding Gain with $\Omega = 6\text{dB}$
M	N	T	Q		M	N	T	Q		
2	1	8	4	2.7dB	2	1	8	4	13.5dB	2.1dB
3	:	:	:	8.4dB	3	:	:	:	17.9dB	3.5dB
4	:	:	:	11.5dB	4	:	:	:	20.0dB	4.3dB
4	2	8	4	15.3dB	4	2	8	4	25.1dB	8.5dB
:	3	:	:	16.7dB	:	3	:	:	27.5dB	11.0dB

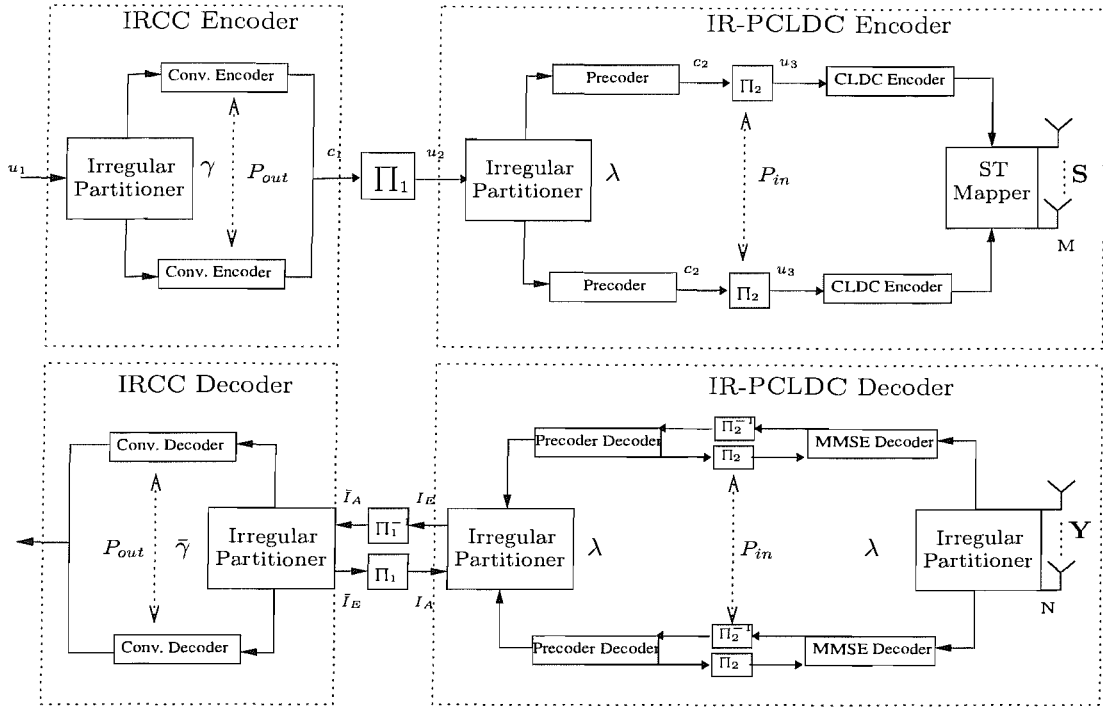


Figure 4.16: Schematic of the IRCC-coded IR-PCLDC scheme using iterative decoding.

sion Code (IR-PCLDC) scheme based on the AF protocol [127]. The proposed scheme becomes capable of operating at reduced SNRs as a benefit of adopting the sophisticated irregular near-capacity code-design principles of Section 2.5. More explicitly, we have demonstrated in Section 2.5.2 that the irregular design principles are applicable to both the *inner* and *outer* code. However, if only the *inner* code employs the irregular design, the resultant scheme may fail to closely approach the achievable capacity. Hence, we argued in the context of Figures 2.48 and 3.25 that irregularity should be imposed on both the *inner* code and the *outer* code, in order to achieve the best possible performance at an acceptable complexity.

The proposed scheme only requires the relays to perform low-complexity, low-delay linear combining according to Equation (4.13), rather than DF operations. Figure 4.16 portrays the schematic of the proposed IRCC-coded IR-PCLDC scheme using iterative decoding, where memory-1 unit-rate precoders are employed. Compared to the IRCC-coded IR-PLDC scheme of Figure 2.48 designed for co-located MIMO systems, the schematic of Figure 4.16 employs a group of CLDCs for the relay-aided system's twin-phase transmissions. Owing to the striking similarity observed in Figures 4.16 and 2.48, our design methodology will be similar to that described in Section 2.5.3, which is appropriately adopted for the IRCC-coded IR-PCLDCs employing in a cooperative MIMO system. Hence, in this section we will focus our attention on the proposed irregular system's features imposed by the twin-layer structure, rather than on the similarities with respect to the irregular co-located MIMO systems.

Table 4.5: The $P_{in} = 4$ component codes of the BPSK modulated IR-PCLDC scheme of Figure 4.16 generated for the cooperative MIMO system of Figure 4.2 having $M = 4$ and $N = 1$.

Index	M	N	T	T_1	T_2	Q	Rate	D	Inner Iterations (j)
0	4	1	8	2	6	1	0.125	≈ 4	0
1	\vdots	\vdots	8	2	6	2	0.25	≈ 4	1
2	\vdots	\vdots	8	2	6	3	0.375	≈ 4	1
3	\vdots	\vdots	8	2	6	4	0.5	≈ 4	2

Table 4.6: The $P_{in} = 4$ component codes of the BPSK modulated IR-PLDC scheme of Figure 2.48 generated for the co-located MIMO system of Figure 4.3 having $M = 4$ and $N = 1$ antennas.

Index	M	N	T	Q	Rate	D	Inner Iterations (j)
0	4	1	8	1	0.125	4	0
1	\vdots	\vdots	\vdots	2	0.25	4	1
2	\vdots	\vdots	\vdots	3	0.375	4	1
3	\vdots	\vdots	\vdots	4	0.5	4	2

4.3.1 EXIT Chart Based IR-PCLDC Design

This section describes the BPSK-modulated IRCC-coded IR-PCLDC scheme of Figure 4.16 having $P = 10$ component codes, where the IRCC employs $P_{out} = 6$ *outer* and the IR-PCLDC has $P_{in} = 4$ *inner* component codes, respectively. More explicitly, an IRCC scheme having a component rate of $R_{i,IRCC} = [0.1, 0.25, 0.4, 0.55, 0.7, 0.9]$ is adopted, where the corresponding EXIT characteristics have been shown in Figure 2.46. The BS is assumed to have $M = 4$ relays to assist the source node and it employs $N = 1$ receive antennas, as seen in Figure 4.2. All the system parameters are listed in Table 4.7. As usual in irregular code design, we have to determine the specific fraction of the input bits to be encoded by each of the component codes, so that the corresponding *inner* and *outer* code's EXIT curves match each other as closely as possible. This design philosophy was detailed in the context of Figures 2.49 of Section 2.5.2.

Table 4.5 lists the group of CLDCs used as the component codes of the IR-PCLDC scheme obeying the structure of Figure 4.16. The number of *inner* iterations (j) listed in Table 4.5 refers to the iterations carried out between the unity-rate precoder's decoder and the MMSE detector of Figure 4.16. Accordingly, Precoded Cooperative Linear Dispersion Codes (PCLDCs) of Figure 4.16

Table 4.7: System parameters of the IRCC-coded IR-PCLDC scheme of Figure 4.16.

Number of relays	$M = 4$
Number of antennas per relay	1
Number of antennas at the BS	$N = 1$
Total number of slots	$T_1 + T_2 = 8$
Number of symbols per CLDC block	Q
SNR at the relays (dB)	$\rho_{SR} = 20$
SNR at the BS (dB)	ρ_{RB}
Modulation	BPSK
Mapping	Gray mapping
Detector	MMSE

are constituted by memory-1 unity-rate precoders and CLDCs having parameters $(MNTQ)$. Furthermore, Table 4.6 constructs a group of LDCs having identical parameters to the CLDCs of Table 4.5, which will be employed as the component codes of the IRCC-coded IR-PLDC scheme of Figure 2.48. Hence, we are able to carry out a fair comparison between the irregular system of Figure 4.16 invoked in cooperative MIMO systems and the corresponding irregular system of Figure 2.48 designed for co-located MIMO systems.

Figure 4.17 characterizes the EXIT charts of the BPSK-modulated PCLDC(4183) scheme of Table 4.5 obeying the structure of Figure 4.2, when communicating over i.i.d. Rayleigh fading channels. Assume that the *inner* code's EXIT curves can be perfectly matched by the EXIT curves of an *outer* code at any SNR ρ_{RB} , then the **maximum achievable rate** of a serial concatenated scheme can be approximated by evaluating the area under the EXIT curves. Given the rate of the *inner* block R_{in} , the maximum achievable rate is expressed as:

$$C(\rho_{RB}) = \log_2(L) \cdot R_{in} \cdot R_{out}, \quad (4.23)$$

where R_{out} is approximated by the area under the *inner* code's EXIT curve [68] and L -PSK modulation is used. Note that in Sections 2.4.2 and 3.6.1, we have explicitly shown that there may be a potential maximum achievable rate gap, when it is measured before and after the unit-rate precoder. The associated gap can be closed by employing *inner* iterations (j), which has been shown in Figures 2.27 and 3.26. Similarly, there may be a potential gap between the maximum achievable rates recorded for CLDCs and PCLDCs based on each component code's EXIT characteristic and the associated gap can be eliminated by increasing the value of j , which will be discussed in more detail below.

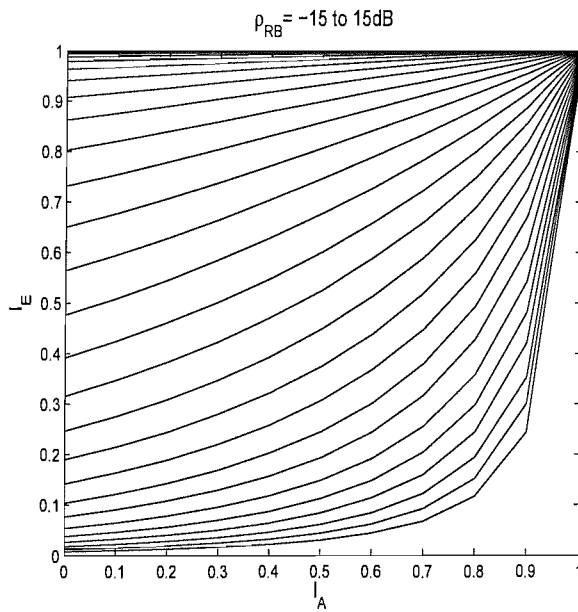


Figure 4.17: EXIT charts of the PCLDC(4183) scheme of Table 4.5 obeying the structure of Figure 4.2, when communicating over i.i.d. Rayleigh fading channels. All the system parameters were summarized in Table 4.7

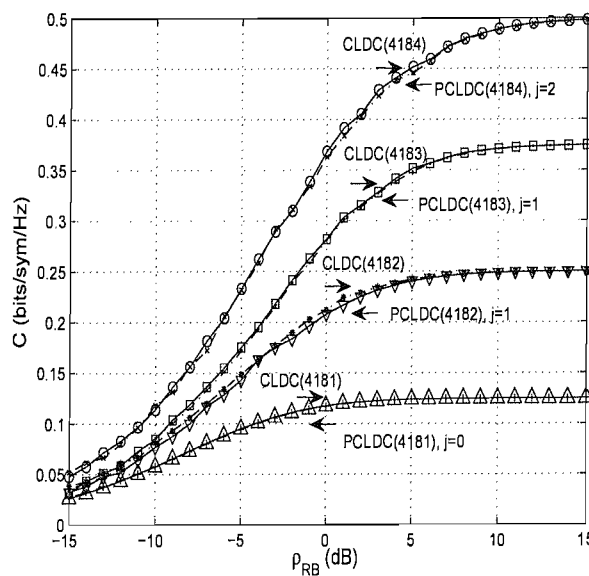


Figure 4.18: Maximum achievable rates of the CLDC and PCLDC schemes of Table 4.5 having different number of inner iterations j using an MMSE detector, when communicating over i.i.d. Rayleigh fading channels. All the system parameters were summarized in Table 4.7.

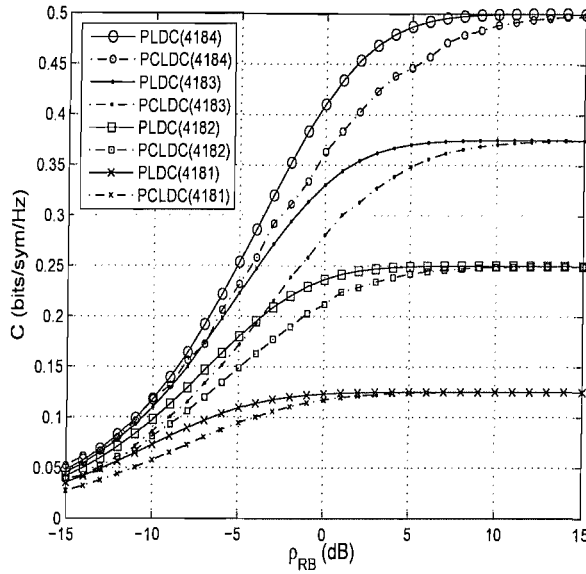


Figure 4.19: Maximum achievable rates of the PCLDC schemes of Table 4.5 and PLDC schemes of Table 4.6 using an MMSE detector, when communicating over i.i.d. Rayleigh fading channels. All the system parameters were summarized in Table 4.7.

Figure 4.18 plots the maximum achievable rates of the CLDCs of Table 4.5 and the corresponding PCLDCs having different number of *inner* iterations j , when communicating over i.i.d. Rayleigh fading channels. The maximum achievable rates are measured based on the EXIT charts using Equation (4.23). When we use the PCLDC(4181) scheme, the employment of the precoder does not decrease the maximum achievable rates compared to the CLDC(4181) scheme even without *inner* iterations, i.e. at $j = 0$. When more symbols have to be transmitted per CLDC block, i.e. when Q is increased, more *inner* iterations are necessary for the PCLDCs to approach the maximum achievable rates of the corresponding CLDCs. More particularly, we found from Figure 4.18 that $j = 1$ is adequate for both the PCLDC(4182) as well as for the PCLDC(4183) schemes and $j = 2$ is suitable for the PCLDC(4183) scheme. Again, the number of *inner* iterations necessary to close the maximum achievable rate gap is listed in Table 4.5.

Figure 4.19 characterizes the maximum achievable rates of the PCLDCs of Table 4.5 and the PLDC schemes of Table 4.6, when communicating over i.i.d. Rayleigh fading channels. Observe in Figure 4.19 that the family of PCLDCs summarized in Table 4.5 suffers from a substantial maximum rate loss compared to the class of its PLDC aided counterparts. Recall that the CLDC's equivalent system model of Equation (4.20) suggests that the combined noise term \bar{V} consists of the noise variance σ_{SR}^2 of the broadcast phase and that of the cooperation interval, namely σ_{RB}^2 . In contrast, the PLDC scheme using identical parameters is only affected by the noise encountered at the BS. Again, it is the linear combination and amplification operations of Equation (4.13) carried

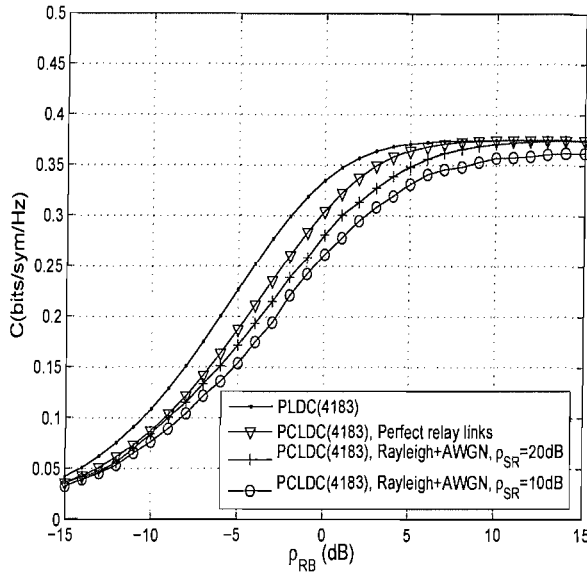


Figure 4.20: Maximum achievable rates of the PCLDC(4183) scheme of Table 4.5, when communicating over perfect channels, noisy media or Rayleigh-faded source-to-relay channels having an SNR of ρ_{SR} . All the system parameters were summarized in Table 4.7.

out at the relays, which impose the additional noise encountered during the broadcast interval. Naturally, the degradation imposed during the broadcast phase as characterized by σ_{SR}^2 can be eliminated by adopting DF related cooperation strategies, which may be able to ensure that the relays will have access to the perfect source information.

In order to elaborate a little further, Figure 4.20 characterizes the maximum achievable rates of the PCLDC(4183) schemes of Table 4.5, when transmitting over perfect broadcast channels, over noisy AWGN or Rayleigh-faded source-to-relay channels having an SNR of ρ_{SR} . The relay-to-BS channels are modelled as uncorrelated i.i.d. Rayleigh-fading channels. More explicitly, even when the source-to-relay channels are perfect, which implies that the relays have perfect source information, there exist a maximum achievable rate gap between the PCLDC(4183) schemes of Table 4.5 and the PLDC(4183) arrangements of Table 4.6. This is because the PCLDC(4183) scheme has to employ $T_1 = 2$ time slots to broadcast the source information to the relays. In other words, only $T_2 = 6$ slots or channel uses are available for the effective transmission of the data, whereas the PLDC(4183) scheme is capable of exploring all the dimensions provided by the $T = 8$ time slots.

Observe in Figure 4.20 that when we have more realistic Rayleigh-faded source-to-relay channels having a finite SNR of $\rho_{SR} = 20$ dB, a further maximum rate loss can be observed in Figure 4.20. Since each source-to-relay channel is independently faded and additionally corrupted by AWGN, each relay's received information inevitably becomes different, which implies that each

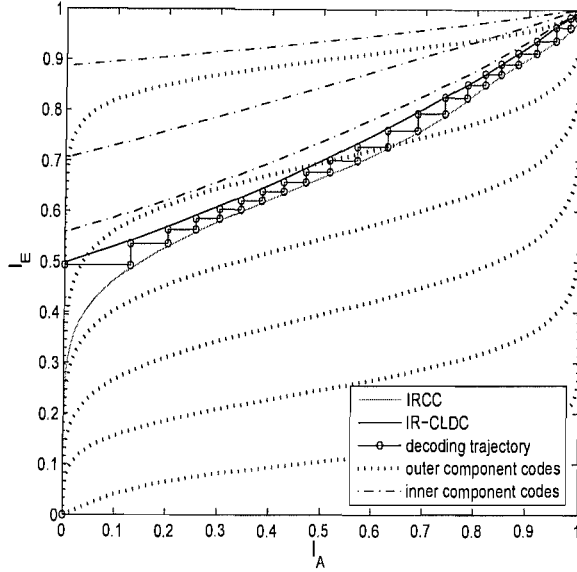


Figure 4.21: EXIT charts and the simulation-based decoding trajectory of the IRCC-coded IR-PCLDC scheme of Figure 4.16 recorded at $\rho_{RB} = 0\text{dB}$, when communicating over i.i.d. Rayleigh fading channels. All the system parameters were summarized in Table 4.7.

relay will disperse potentially quite different information to the T_2 time slots, when relaying based on Equation (4.13). When the SNR of the source-to-relay links is reduced further to $\rho_{SR} = 10\text{dB}$, the associated maximum achievable rate suffers an additional loss compared to that recorded for $\rho_{SR} = 20\text{dB}$. Observe in Figure 4.20 that the associated rate reduction persists even in the high SNR region, owing to the inherent noise imposed during the broadcast interval.

4.3.2 Performance Results

For all the simulations, the first interleaver of Figure 4.16 is set to a length of 10^6 bits and all the simulation parameters are listed in Table 4.7. Again, we construct an identical IRCC-coded IR-PLDC scheme using Table 4.6 as the benchmark to quantify the achievable performance.

Our design objective is to maximize the effective throughput across the widest possible SNR range, which can be achieved by adaptively adjusting the weighting coefficient vectors $\gamma = [\gamma_1, \dots, \gamma_{P_{out}}]$ of the IRCC scheme of Figure 2.46 and $\lambda = [\lambda_1, \dots, \lambda_{P_{in}}]$ of the IR-PCLDC scheme, respectively. More explicitly, an exhaustive search operation is carried out for all the possible combinations of γ and λ in order to maximize the throughput $C(\rho) = \log_2(L) \cdot R_{in} \cdot R_{out}$ of Equation (4.23) under the following constraints:

- $\gamma_1 + \gamma_2 + \dots + \gamma_{P_{out}} = 1$ and $\lambda_1 + \lambda_2 + \dots + \lambda_{P_{in}} = 1$;

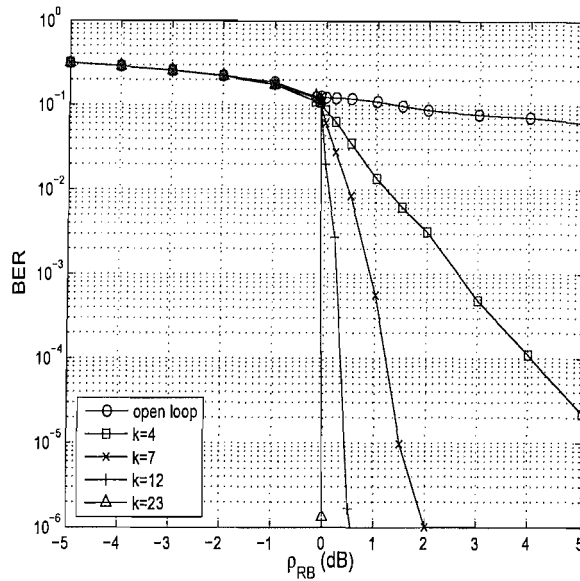


Figure 4.22: BER of the IRCC-coded IR-PCLDC scheme of Figure 4.16 designed for achieving an infinitesimally low BER at $\rho_{RB} = 0\text{dB}$, when communicating over i.i.d. Rayleigh fading channels. All the system parameters were summarized in Table 4.7.

- An open convergence tunnel must exist in the EXIT chart, which enables the irregular system to achieve an infinitesimally low BER using iterative decoding;
- The open EXIT tunnel area is maximized, for the sake of minimizing the number *outer* iterations required.

Figure 4.21 presents the associated EXIT charts and the corresponding decoding trajectory of our IRCC-coded IR-PCLDC scheme designed for operating at $\rho_{RB} = 0\text{dB}$, when communicating over i.i.d. Rayleigh fading channels. The dashed lines represent the EXIT curves of the IR-PCLDC's components of Table 4.5, while the dotted lines denote the EXIT curves for the set of IRCC components. The solid lines represent the aggregate EXIT curves of the IRCC scheme having the weighting coefficient vector of $\gamma = [0, 0, 0, 0.2374, 0.5036, 0.2590]$ and the IR-PCLDC scheme having the weighting coefficient vector of $\lambda = [0, 0, 0, 1]$. By simultaneously maximizing the achievable throughput and the open EXIT tunnel area at $\rho_{RB} = 0\text{dB}$, the proposed scheme becomes capable of achieving $C(0\text{dB}) = 0.3475$ (bits/sym/Hz) and the optimized EXIT curves of Figure 4.21 exhibit a narrow but still open tunnel, where the decoding trajectory shows that $k = 23$ *outer* iterations were required. The corresponding BER performance is portrayed in Figure 4.22.

By repeating the same design process as that used in Figures 4.21 and 4.22, we are able to design the IRCC-coded IR-PCLDC scheme of Figure 4.16 for other operating SNRs. Figure 4.23 portrays the maximum achievable rates attained by the IRCC-coded IR-PCLDC scheme of Figure 4.16.

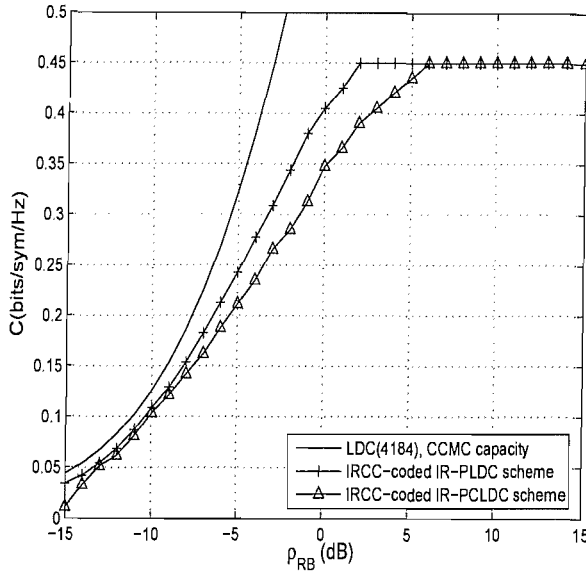


Figure 4.23: The maximum rates achieved by the IRCC-coded IR-PCLDC scheme of Figure 4.16 according to Tables D.11 and D.12 and the corresponding IRCC-coded IR-PLDC scheme of Figure 2.48 using Tables D.13 and D.14. All the system parameters were summarized in Table 4.7.

Each component of Figure 4.16 was designed to achieve the maximum effective throughput using specific weighting coefficient vectors λ and γ listed in Tables D.11 and D.12. Furthermore, we also plot the maximum rates achieved by the IRCC-coded IR-PLDC scheme of Figure 2.48 designed for co-located MIMO systems according to Tables D.13 and D.14. Observe in Figure 4.23 that there is an effective throughput discrepancy between the irregular system designed for the co-located MIMO system of Figure 4.3 and the corresponding irregular scheme designed for the cooperative MIMO arrangement of Figure 4.2. Finally, the LDC(4184) scheme's CCMC capacity obtained using Equation (2.9) is also provided in order to give us an idea as to how far we are operating from the capacity limit.

4.4 Conclusion

In this chapter, the concept of LDCs designed for co-located MIMO systems was extended to cooperative MIMO systems. Our key findings may be summarized as follows:

- In Sections 4.2.1 to 4.2.3, a general framework was established for the cooperative MIMO systems of Figure 4.2;
- Correspondingly, Section 4.2.4 emphasized that the fundamental difference between co-located MIMO systems and cooperative MIMO systems is that the latter relies on a twin-

Table 4.8: Characteristics of Co-located MIMO systems using LDCs and Cooperative MIMO arrangements using CLDCs.

		Co-located MIMO	Cooperative MIMO
Similarity	($MNTQ$)	arbitrary	arbitrary
	Modulation	arbitrary	arbitrary
	Diversity	$N \cdot \min(M, T)$	$\approx N \cdot \min(M, T_2)$
Uncoded	Small-scale fading	better than CLDCs	trends in Figure 4.7
	Large-scale fading	trends in Figure 4.8	better than LDCs
Coded	Small-scale fading	better than CLDCs	explained in Figure 4.20
	Throughput	compared in Figure 4.23	

phase transmission regime, which provides us with a high grade of freedom in terms of appropriately share the total number of slots between the broadcast- and cooperation-phase;

- Section 4.2.5 demonstrated the achievable BER performance of CLDC schemes having various parameter combinations. The effective throughput have been summarized in Figures 4.14 and 4.15 and the achievable coding gains were listed in Table 4.4;
- In Section 4.3, irregularity is imposed on the relay-aided system based on the AF cooperation protocol. The resultant IRCC-coded IR-PCLDC scheme of Figure 4.16 becomes capable of operating at a throughput, which is close to the corresponding IR-PLDC benchmark as seen in Figure 4.23, while maintaining an infinitesimally low BER. The associated weighting coefficient vectors λ, γ were listed in Tables D.11 and D.12, respectively.
- Finally, we summarized the characteristics of both co-located MIMO systems using LDCs and those of cooperative MIMO schemes using CLDCs in Table 4.8. Both of the schemes are capable of supporting arbitrary ($MNTQ$) parameter combinations as well as employing arbitrary modulation schemes. Furthermore, the achievable total diversity order is jointly determined by the minimum spatial and temporal dimensions. For uncoded systems, the LDCs outperform the CLDCs, when encountering a small-scale fading environment. By contrast, the CLDCs tend to function more reliably than the LDCs in the context of large-scale fading, i.e. shadowing. The corresponding trends have been further explained in Figures 4.7 and 4.8. As far as near-capacity coded systems are concerned, which are implemented using IR-PLDCs/IR-PCLDCs, again, the effective throughput gap between co-located MIMO schemes and cooperative MIMO systems has been explicitly detailed in Figure 4.20.

Chapter 5

Conclusions and Future Research

The contribution of this thesis includes the following two aspects. Firstly, a novel LDC structure is introduced in order to design a block code that is capable of fully exploiting the degrees of freedom provided by both the spatial and temporal dimensions. This simple yet powerful architecture provides a unified framework, which not only subsumes all the major STBC representatives found in the open literature but reveals further insightful STBC design principles. Secondly, we proposed novel 'irregular' wireless coding schemes and their design methodologies, in the pursuit of near-capacity operation across a wide range of SNRs. Three particular applications of linear-structure based irregular schemes were investigated in this thesis, namely the IR-PLDCs of co-located MIMO systems of Chapter 2, the IR-PDLDCs of co-located MIMO schemes outlined in Chapter 3 and the IR-PCLDCs of cooperative MIMO arrangements discussed in Chapter 4. These are detailed in the following sections, together with a discussion of our future work.

5.1 IR-PLDCs of Co-located MIMO Systems

Chapter 2 exemplified the application of the LDCs designed for coherently detected co-located MIMO systems. This application was motivated by the fundamental challenge of effectively exploiting the additional spatial dimensions offered by the multiple antennas employed at both the transmitter and the receiver. The concept of LDCs introduced in Section 2.2 is radical, since their inherent linearity simplifies the challenge of designing a potentially excessive number of space-time codewords. As an explicit benefit, it allows us to design a single DCM χ defined in Equation (2.16), regardless of the number of antennas employed as well as of the modulation schemes used. Two LDC models were investigated in Sections 2.2.2 and 2.2.3, which are suitable for describing orthogonal STBCs and non-orthogonal STBCs, respectively. Furthermore, Section 2.2.4

Table 5.1: BER and capacity characteristics of the family of $LDC(MNTQ)$ schemes of Figure 2.3, when employing QPSK modulation as well as the ML detector of Equation (2.18).

$LDC(MNTQ)$	BER	Capacity
Changing the value of Q	Figure 2.5	Figures 2.6,2.7
Changing the value of T	Figure 2.8	Figure 2.9
Changing the value of M or N	Figure 2.12	Figure 2.13
Changing the DCM χ	Figure 2.10	Figure 2.11

proposed to optimize the DCM χ from a capacity maximization perspective, which was achieved by maximizing the LDCs' DCMC capacity using Equation (2.23). Section 2.2.5 characterized the BER performance as well as the associated achievable capacity of a family of LDCs, which are summarized in Table 5.1.

Section 2.3.1 examined the existing STBC design philosophies found in the open literature, including the rank criterion [10], the determinant criterion [10] as well as the diversity-rate tradeoffs and the diversity-multiplexing gain tradeoffs. Furthermore, Section 2.3.1 summarized the STBC's beneficial property of Transmit Symbol Separability (TSS). As explicitly shown in Table 2.3, the grade of TSS serves as an indicator of the specific tradeoff struck in terms of the achievable rate, diversity, complexity, orthogonality and design flexibility. If full TSS is guaranteed, the performance of the associated STBC is bounded by the rate-diversity tradeoff. In contrast, if partial TSS or non-TSS is observed, the resultant STBC arrangement could simultaneously achieve both a high throughput and full-diversity using a non-orthogonal structure. In other words, the LDCs' ability of encompassing the entire spectrum of TSS by simply applying the corresponding DCM χ allows the family of LDCs to meet various design objectives. Even more appealingly, the choice of χ is non-unique, since the solution to Equation (2.23) is non-unique. In Sections 2.3.2 to 2.3.7, we explicitly characterized the mathematical representation as well as the design philosophy of STBCs characterized in the literature and those of LDCs. In fact, the LDCs subsume all the known STBC schemes by imposing various restrictions on the set of the dispersion matrices.

As far as serial-concatenated channel-coded STBC schemes are concerned, Section 2.4 analyzed various iteratively-detected RSC-coded LDCs with/without a unity-rate precoder using EXIT charts [55] [57]. For the non-precoded scheme of Figure 2.17, we demonstrated in Figures 2.18 and 2.22 that the corresponding scheme was unable to operate near the capacity, since the *inner* code's EXIT curves became near-horizontal and hence the resultant BER performance improved only modestly. The employment of the unity-rate precoder potentially allows the associated scheme

of Figure 2.24 to achieve an infinitesimally low BER, since the *inner* and *outer* EXIT curves reach at the $(1.0, 1.0)$ point of the EXIT chart, as exemplified in Figures 2.26 and 2.29. However, the precoded scheme of Figure 2.24 still operates far from the MIMO channel's capacity, since the open EXIT tunnel area remains relatively high. Table 2.6 explicitly characterized the coding gains achieved by the precoded/non-precoded schemes discussed in Section 2.4.

In order to achieve near-capacity operation associated with an infinitesimally low BER, Section 2.5 employed the sophisticated irregular design principle for serial-concatenated systems. More explicitly, we proposed the novel RSC-coded IR-PLDC scheme of Figure 2.32, where the irregularity was imposed on the *inner* code. The maximum achievable rates of Figure 2.40 showed that this scheme becomes capable of operating as close as 2.5dB from the MIMO channel's capacity for SNRs in excess of a certain threshold. The open EXIT tunnel area was maximized at the target SNR, under the condition that the system's effective throughput was maximized. Maximizing the effective throughput in order to operate near the attainable capacity is our prime concern. On the other hand, the open EXIT tunnel area also has to be maximized in order to reduce the associated decoding complexity, which was justified in Figures 2.36 and 2.37. Section 2.5.1.3 demonstrated that the system of Figure 2.32 is capable of maintaining a moderate complexity, if we allow the system to operate further away from the achievable capacity.

In Section 2.5.2, the irregular design principle was applied solely to the *outer* code. The resultant IRCC-coded LDC scheme operated approximately 0.9dB from the MIMO channel's capacity within a limited SNR region, as seen in Figure 2.47. This was because the irregular *outer* code is capable of shaping the EXIT curve more flexibly than the irregular *inner* code, provided that an open EXIT tunnel existed. By contrast, the irregular *inner* IR-PLDC scheme of Figure 2.32 was capable of creating open EXIT tunnels based on the SNR encountered by employing different-rate LDC component codes. Figure 2.47 clearly demonstrated the above-mentioned observations by comparing the maximum achievable rates of the IRCC-coded PLDCs and RSC-coded IR-PLDCs, when employing the same number of component codes. Accordingly, Section 2.5.3 investigated the scenario, where the irregularity was imposed on both the *inner* and *outer* codes. The resultant IRCC-coded IR-PLDC scheme of Figure 2.48 became capable of operating within approximately 0.9dB of the capacity across a wide SNR region, as demonstrated in Figures 2.49 and 2.50.

Section 2.5.5 summarized the potential methods of constructing a near-capacity scheme using the irregular principle. More explicitly, the irregularity of the *outer* code can be created by employing different rate component codes [60] [69]. By contrast, there are diverse ways of creating a set of EXIT curves having distinguished characteristics for the *inner* code, such as using different code-rates, as well as diverse mapping and modulation schemes, as portrayed in Figure 2.53. In-

evitably, near-capacity operation imposes a high decoding complexity as well as a high interleaver delay, since high-complexity component codes have to be employed and the associated number of iterations to achieve an infinitesimally low BER is also high. In conclusion, the proposed irregular scheme of Figure 2.48 can operate near the attainable capacity across diverse SNRs at a potentially high complexity and high delay.

5.2 IR-PDLDCs of Co-located MIMO Systems

Chapter 3 considered the application of linear-dispersion style system structures and the irregular transceiver design philosophy in the context of non-coherently detected DSTBCs. The motivation behind DSTBCs stated in Section 3.1 is to dispense with the burden of high-complexity MIMO channel estimation required by the coherently detected STBCs of Chapter 2, while still achieving a beneficial diversity gain.

Section 3.2 characterized the DSTBC's structure of Figure 3.2 from two different perspectives. Firstly, we examined the principles that facilitate the employment of differential encoding/decoding for a single-antenna aided scheme and then demonstrated that the same design philosophy can be applied to multiple-antenna aided systems. Secondly, the schematic of Figure 3.2 was portrayed from a specific perspective, demonstrating that DSTBCs can be considered as STBCs combined with a differential encoder. This perspective allowed us to bridge the design of STBCs and DSTBCs, since the challenge of designing DSTBCs can be described as that of designing a family of STBCs, where all the space-time matrices are unitary.

Hence, in Section 3.3 we were able to investigate various DOSTBC schemes found in the open literature using the general framework of Figure 3.2. Since DOSTBCs are based on various orthogonal matrices, the unitary constraint of Equation (3.5) is automatically satisfied. The orthogonality of the resultant designs also enables the receiver to perform low-complexity ML detection, since the symbol streams can be decoupled into separately decoded groups. Unfortunately, the orthogonal design principle imposes numerous constraints on the DOSTBCs. For example, the number of antennas that may be employed is limited and the number of symbols transmitted per space-time block is also restricted. As expected, the BER performance of the family of DOSTBCs typically suffers a 3dB SNR penalty as the result of the doubled noise variance of the differential detection formulated in Equation (3.9), when compared to the corresponding LDCs of Chapter 2. Although the 3dB difference is reduced, when realistic CIR estimation is used at the receiver.

In order to eliminate the constraints imposed by the orthogonal structure, Section 3.4 proposed the class of DLDCs based on the Cayley transform [33]. In other words, DLDCs offer an alternative

Table 5.2: BER summary of the family of DLDC($MNTQ$) schemes of Figure 3.2 based on the Cayley transform, when employing 2PAM modulation and the ML detector of Equation (3.53).

DLDC($MNTQ$)	BER
Changing the value of Q	Figure 3.11
Changing the value of T or M	Figure 3.12
Changing the value of N	Figure 3.13
The effect of fading	Figure 3.14
Compared to LDCs with perfect CSI	Figures 3.11, 3.12
Compared to LDCs with imperfect CSI	Figure 3.15

method of designing a set of unitary space-time matrices, instead of employing the set of orthogonal matrices detailed in Section 3.3. More explicitly, the linear dispersion structure of Equation (3.46) can be employed in the Hermitian space, so that the weighted sum of a number of Hermitian matrices remains also a Hermitian matrix, provided that the weighting coefficients are real-valued. Furthermore, the Cayley transform [33] detailed in Section 3.4.2 provides an efficient way of projecting the weighted Hermitian matrix to a unique unitary matrix, which facilitates the differential encoding of Equation (3.5). Recall from Section 2.3 that we classified the various STBC techniques in Figure 2.16 and demonstrated that LDCs subsume all the members of the entire family. Similarly, it is straightforward to derive the family of DSTBCs from the DLDCs by simply imposing different degrees of orthogonality on the dispersion matrices, which was portrayed in Figure 3.8.

Table 5.2 summarized the BER performances presented in Section 3.4.3 for the family of DLDCs based on the Cayley transform. The DLDCs' ability of accommodating flexible antenna configurations as well as facilitating various parameter combinations was demonstrated in Figures 3.11 to 3.13. Note that the unitary matrix constraint shown in Section 3.2.3 and the restriction of employing real-valued modulation are imposed by the differential encoding process and by the Cayley transform, respectively. Additionally, Figure 3.14 investigated the DLDCs' achievable performance under different fading conditions, since the success of differential decoding relies on the degree of the channels' stationarity. As expected, a substantial performance degradation was observed in Figure 3.14, when the channels' fluctuation became severe. Figures 3.11 and 3.12 verified the 3dB SNR difference between the DSTBCs based on the Cayley transform and the corresponding LDCs having perfect CSI. However, when more realistic channel estimation scenarios were considered, the DLDCs became capable of outperforming their coherently detected LDC counterparts, as explicitly shown in Figure 3.15. These findings remained valid even when the channels were

experiencing moderately rapid Rayleigh fading having $f_d = 10^{-2}$. The achievable coding gain of the DLDCs based on the Cayley transform was recorded in Table 3.3. Similar coding advantages have been observed also in Tables 2.1 and 2.2, when employing the corresponding LDCs.

In Section 3.5, we proposed a novel RSC-coded Sphere Packing (SP) aided DOSTBC scheme employing unity-rate precoder and using iterative decoding, as an attempt to jointly design the space-time block coding and the modulation scheme. The philosophy behind SP is that the symbols transmitted during a space-time codeword should be designed jointly, rather than chosen separately from the modulation constellations. Hence, the SP modulation potentially requires all the transmitted symbols to experience identical fading, which can be satisfied by the DSTBC schemes of Section 3.3, which were based on orthogonal designs. By contrast, the DSTBCs of Section 3.4 were based on the non-orthogonal structure, and the resultant DLDCs were less applicable to SP modulation. The joint STBC-SP design is particularly attractive, since the SP modulation is capable of gleaning more extrinsic information than that of the conventional L -PSK modulation schemes, which allows the *inner* code to create a larger open tunnel in the EXIT chart, as seen in Figure 3.22. Accordingly, this coding advantage comes at the price of increasing the decoding complexity.

Furthermore, Section 3.5 investigated the achievable BER performance of the regular/irregular-coded precoded DOSTBC schemes using SP modulation at a throughput of 1 (bits/sym/Hz). Since the irregular *outer* scheme provides a higher grade of flexibility in shaping the *outer* code's EXIT curve, the resultant IRCC-coded DOSTBC scheme becomes capable of achieving an infinitesimally low BER at $\rho = 5.5$ dB in comparison to the SNR of $\rho = 6$ dB required by the regular coding aided scheme, as seen in Figure 3.23.

Section 3.6 further extended the irregular principle in the context of non-coherently detected systems, where the irregularity was imposed on both the *inner* code and the *outer* code. The design method of the resultant IRCC-coded IR-PDLDC scheme is similar to that of its coherently detected counterpart detailed in Section 2.5.3. Hence, we focused our attention on the distinctive features imposed by the differential encoding structure of Section 3.4.2. Firstly, we investigated the maximum achievable rates of the IR-PDLDGs of Figure 3.25 and that of the IR-PLDCs of Figure 2.48 associated with perfect CSI. Figure 3.27 explicitly demonstrated the well-known 3dB SNR between the coherently detected and non-coherently detected schemes, as a result of the doubled noise variance of Equation (3.7). Furthermore, Figure 3.29 recorded the maximum achievable rates of the IR-PLDCs of Figure 2.48 in the presence of channel estimation errors, as governed by the value of ω . Observe in Figure 3.29 that the IR-PDLDC scheme of Figure 3.25 was capable of achieving a higher throughput than its coherently detected IR-PLDC counterpart in the high-SNR region, when the channel estimation was imperfect. The maximum achievable rates of

the IR-PDLDC scheme of Figure 3.25 under various fading conditions were also investigated. As expected, Figure 3.28 suggested that the maximum achievable rates gradually decreased, when the channel conditions fluctuated rapidly. Finally, the effective throughput achieved by the IRCC-coded IR-PDLDC scheme was shown in Figure 3.32. Again, a 3dB SNR difference was observed, when compared to the corresponding IRCC-coded IR-PLDC benchmark.

5.3 IR-PCLDCs of Cooperative MIMO Systems

The application of the linear dispersion structure as well as of the irregular design philosophy of cooperative MIMO systems was demonstrated in Chapter 4. The employment of relay-aided transmissions was motivated by the realistic propagation scenario, where the wireless links between the source and the destination suffer from severe shadowing effects or from path loss. Hence, a group of relays can be employed to invoke cooperation transmissions in order to overcome these large-scale fading effects, which may dramatically erode the benefits of co-located MIMO elements, as exemplified in Figure 4.1. In general, there are three types of cooperation strategies, namely DF, AF and CF. However, Chapter 4 focused on the AF arrangement, which requires low-complexity relays.

Accordingly, Section 4.2.1 proposed a novel twin-layer CLDC scheme, which was specifically tailored to the two-phase transmission regime employed by the AF relay protocol. Furthermore, in Section 4.2.2 we outlined the assumptions stipulated, in order to make the twin-layer CLDC scheme of Figure 4.2 applicable to the 3GPP-LTE system. The mathematical model of the twin-layer CLDC scheme presented in Section 4.2.3 revealed that the CLDCs have a similar system structure as that of the LDCs of Chapter 2. Recall that the LDC's equivalent channel matrix of Equation (2.15) is characterized by the DCM χ . In contrast, the CLDC's equivalent channel matrix of Equation (4.20) is determined by a pair of DCMs (χ_1, χ_2) in order to describe their twin-phase transmission. More specifically, Section 4.2.4 listed the similarities and differences between the LDCs obeying the structure of co-located MIMO systems outlined in Figure 4.3 and the CLDCs having the structure of cooperative MIMO systems as seen in Figure 4.2.

Table 5.3 summarized the achievable BER performance quantified in Section 4.2.5 for a family of CLDCs obeying the structure of Figure 4.2 as well as having various $(MNTQ)$ parameter combinations. Similar to the LDCs of Chapter 2 and to the DLDCs of Chapter 3, the flexible linear dispersion matrix based structure formulated in Equations (4.4) and (4.13) allows the CLDCs to support arbitrary $(MNTQ)$ parameter combinations, as listed in Table 5.3. Particularly, we exploited the CLDC's special characteristics inherited from the twin-phase transmission of the co-

Table 5.3: BER performance summary of the family of CLDC($MNTQ$) schemes of Figure 4.2, when employing BPSK modulation as well as the ML detector of Equation (4.21).

CLDC($MNTQ$)	BER
Changing the value of Q	Figure 4.10
Changing the value of T_1 or T_2	Figure 4.6
Changing the value of T	Figure 4.11
Changing the value of M	Figure 4.13
Changing the value of N	Figure 4.12
Changing the value of ρ_{SR}	Figure 4.9
Compared to LDCs without shadowing	Figure 4.7
Compared to LDCs with shadowing	Figure 4.8

operative MIMO systems. More explicitly, Figure 4.6 demonstrated that the number of time slots used for the broadcast/cooperation interval has a dominant impact on the achievable BER performance, since it determines the symbol's integrity received at the relays and the achievable diversity gains at the destination. Furthermore, when the source-to-relay links experienced different SNRs ρ_{SR} , the corresponding CLDC's performance was characterized in Figure 4.9.

Table 5.3 also compared the performance of the CLDCs and the LDCs having identical parameters, when the channels were subjected to both small-scale Rayleigh fading and to large-scale shadowing. In the context of Rayleigh fading environments, the LDCs of co-located MIMO schemes outperformed the corresponding CLDCs of cooperative MIMO systems, since the noise introduced at the relays dominates the attainable performance, which was analyzed in Figure 4.7. However, in the presence of large-scale shadowing, where all the LDC's wireless channels tend to fade together, the CLDCs exhibited a significant advantage, as seen in Figure 4.8. The effective throughput of a class of CLDCs as well as of the corresponding group of LDCs operating with/without shadowing was characterized in Figures 4.14 and 4.15. The corresponding coding gains were extracted from these figures, which are listed in Table 4.4.

Section 4.3 demonstrated that the irregular design principle applied to the co-located MIMO systems of Chapters 2 and 3 can also be applied to the cooperative MIMO systems. Hence, the resultant IRCC-coded IR-PCLDC scheme of Figure 4.16 based on the AF cooperation protocol became capable of achieving a flexible effective throughput according to the SNR encountered. Throughout the investigations, an IRCC-coded IR-PLDC scheme of Figure 2.48 having identical parameters was constructed as the benchmark, when communicating over small-scale Rayleigh

Table 5.4: The suitable application scenarios and the characteristics of the LDCs of Chapter 2, the DLDCs of Chapter 3 and the CLDCs of Chapter 4.

	LDC	DLDC	CLDC
Application	co-locate MIMO	co-locate MIMO	cooperative MIMO
Suitable fading	Small-scale	Small-scale	Large-scale
CSI requirement	Perfect CSI	Non-CSI	Perfect CSI
Dispersion based on	Equation(2.12)	Equation(3.46)	Equations(4.4), (4.13)
Visualized dispersion	Figure 2.4	Figure 2.4	Figure 4.4
DCM listed in	Appendix A	Appendix B	Appendix C
Schematic of the uncoded system	Figure 2.3	Figure 3.2	Figure 4.2
Uncoded BER	Table 5.1	Table 5.2	Table 5.3
Coding gain	Tables 2.1,2.2	Table 3.3	Table 4.4
Uncoded throughput	Figures 2.14,2.15	Figures 3.16,3.17	Figures 4.14, 4.15
Schematic of the irregular system	Figure 2.48	Figure 3.25	Figure 4.16
Coded throughput	Figure 2.49	Figure 3.32	Figure 4.23
Weighting coefficient	Appendix D	Appendix D	Appendix D

fading channels. Figure 4.19 have shown that there was a maximum achievable rate gap between the IR-PCLDCs and the corresponding IR-PLDCs, since the relays only have access to imperfect source information, as highlighted in Figure 4.20. The effective throughput of the IRCC-coded IR-PCLDC scheme of Figure 4.16 was characterized in Figure 4.23, where a similar rate gap was recorded compared to the co-located MIMO benchmark.

5.4 Linking LDCs, DLDCs and CLDCs

Although, each individual link between the LDCs and the DLDCs/CLDCs has been characterized in Figures 3.8 and 4.5, respectively, Figure 5.1 portrays the fundamental design guidelines of the LDC, DLDC and CLDC techniques investigated in this thesis. As shown in Chapter 2, the LDCs characterized by a single DCM χ provide a unified solution to the design of STBCs used in co-located MIMO systems. The linear dispersion matrix based design philosophy can be projected to the differential encoding domain with the aid of the unitary constraint of Section 3.2.3, as seen

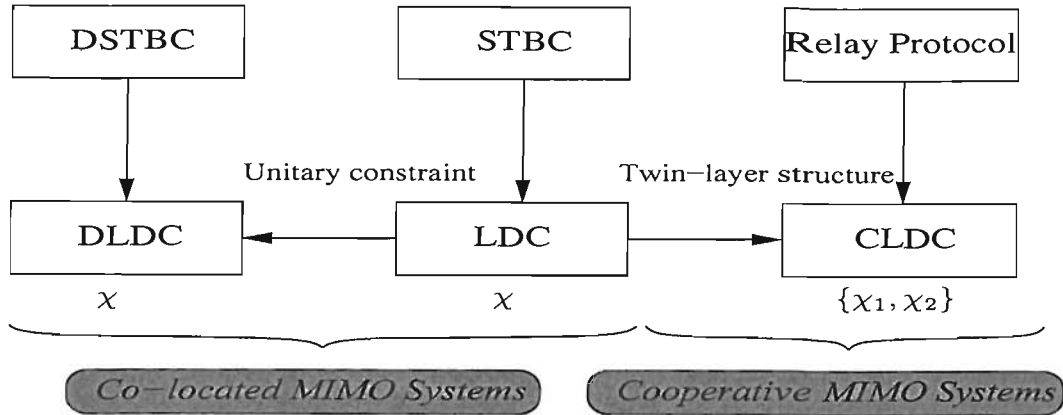


Figure 5.1: Link between the LDCs/DLDCs designed for co-located MIMO systems and the twin-layer CLDCs designed for cooperative MIMO systems.

in Figure 5.1. The resultant DLDCs of Chapter 3 also can be characterized by the DCM χ of Equation (3.56). Furthermore, in the context of the relay-aided networks, the concept of the linear dispersion structure remains applicable, provided that the DCM pair $\{\chi_1, \chi_2\}$ of Equation (4.20) is available to the CLDCs in order to characterize the twin-phase transmission regime required by the cooperative MIMO systems of Figure 4.2.

Table 5.4 summarized the appropriate application scenarios and the characteristics of the LDCs of Chapter 2, those of the DLDCs of Chapter 3 and those of the CLDCs of Chapter 4. Since co-located MIMO systems have access to all the spatial and temporal dimensions at the transmitter, each L -PSK symbol is dispersed to all the slots and the aggregate space-time codeword is the weighted sum of all the dispersed symbols. Hence, we refer to this operation as 'symbol-based' linear dispersion, which has been visualized in Figure 2.4. By contrast, for a cooperative MIMO system, each relay functions as a virtual element of a MIMO antenna array, where only T_2 number of temporal dimensions are accessible. Hence, each relay disperses all the received signals to the temporal dimensions and each relay contributes one row of the aggregate space-time codeword formulated in Equation (4.15). Therefore, we refer to it as 'relay-based' linear dispersion, where the dispersion process was shown graphically in Figure 4.4.

Finally, we constructed a set of comparisons between the family of LDCs, DLDCs and CLDCs in order to evaluate their advantages as well as limitations, when communicating in *small*-scale or *large*-scale fading scenarios as well as when having *perfect* or *imperfect* CSI at the receiver. All the simulation parameters were listed in Table 5.5. Observe in Table 5.5 that we set $M = T$ and assume that the channels were subjected to Rayleigh fading having $f_d = 10^{-2}$ in order to enable the adequate operations of the DLDCs. Hence, the group of LDCs and DLDCs have the potential to achieve the full diversity order of $D = N \cdot \min(M, T)$ in comparison to the reduced maximum

Table 5.5: Comparison of the LDCs of Figure 2.3, the DLDCs of Figure 3.2 and the CLDCs of Figure 4.2, when communicating over small-scale/large-scale fading channels and having perfect/imperfect CSI at the receiver.

	LDC	DLDC	CLDC
M	3	3	3
N	2	2	2
T	3	3	$T_1 = 1, T_2 = 2$
Q	1,2,3	1,2,3	1,2,3
Modulation	BPSK	BPSK	BPSK
Mapping	Gray mapping	Gray mapping	Gray mapping
ML detector	Equation (2.18)	Equation (3.9)	Equation (4.21)
Doppler frequency	$f_d = 10^{-2}$	$f_d = 10^{-2}$	$f_d = 10^{-2}$
Diversity	$D = 6$	$D = 6$	$D \approx 4$
Comparison A	<i>Small-scale Rayleigh fading, perfect CSI in Figure 5.2</i>		
Comparison B	<i>Small-scale Rayleigh fading, imperfect CSI in Figure 5.3</i>		
Comparison C	<i>Large-scale shadowing, perfect CSI in Figure 5.4</i>		

diversity order $D \approx N \cdot \min(M, T_2)$ of the CLDCs.

- For Comparison A of Table 5.5, Figure 5.2 characterized the achievable throughput of the group of LDCs, DLDCs and CLDCs recorded at $\text{BER}=10^{-4}$, when the wireless channels were subjected to *small-scale Rayleigh fading* and *perfect CSI* was available at the receiver. Observe in Figure 5.2 that the class of LDCs is capable of operating at the lowest SNR at a certain throughput. The group of DLDCs suffers from a 3dB SNR penalty in comparison to that of the LDCs, since no CSI was exploited. The family of CLDCs operates at SNRs further away from that of the LDCs, owing to the reduced achievable diversity order as well as due to the reasons detailed in Section 4.2.5.
- For Comparison B of Table 5.5, Figure 5.3 characterized the effective throughput of the LDCs, the DLDCs and the CLDCs of Table 5.5 recorded at $\text{BER}=10^{-4}$, when the wireless channels were subjected to *small-scale Rayleigh fading* and the receiver has *imperfect CSI* governed by the parameter ω (dB). Observe in Figure 5.3 that the family of DLDCs demonstrated a significant advantage over the LDCs at a high throughput, even when the channel estimation errors were as low as $\omega = -10$ dB. Since the group of CLDCs has an error floor

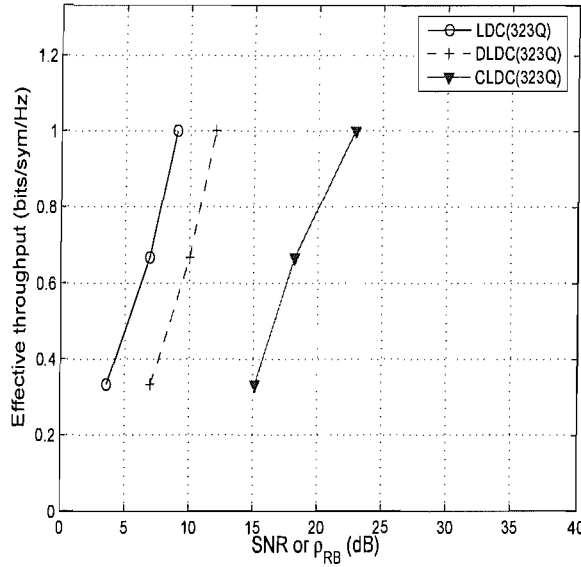


Figure 5.2: Throughput comparison for the LDCs of Figure 2.3, the DLDCs of Figure 3.2 and the CLDCs of Figure 4.2 recorded at $BER=10^{-4}$, when communicating over *small-scale* Rayleigh fading channels and assuming that the *perfect* CSI was known by the receiver. All the system parameters were summarized in Table 5.5.

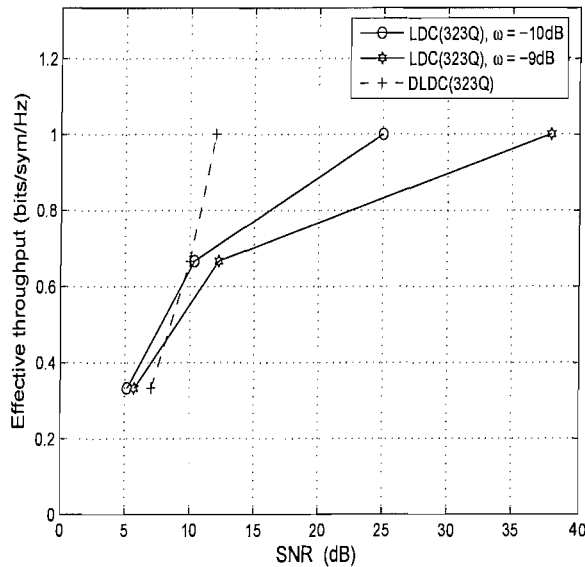


Figure 5.3: Throughput comparison for the LDCs of Figure 2.3, the DLDCs of Figure 3.2 and the CLDCs of Figure 4.2 recorded at $BER=10^{-4}$, when communicating over *small-scale* Rayleigh fading channels and having *imperfect* CSI governed by ω (dB). All the system parameters were summarized in Table 5.5.

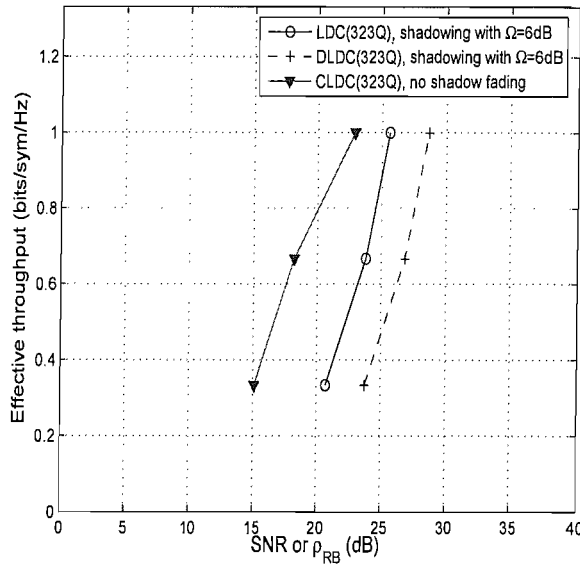


Figure 5.4: Throughput comparison for the LDCs of Figure 2.3, the DLDCs of Figure 3.2 and the CLDCs of Figure 4.2 recorded at $\text{BER}=10^{-4}$, when the channels were subjected to *large-scale shadowing* and assuming that the *perfect CSI* was known at the receiver. All the system parameters were summarized in Table 5.5.

higher than $\text{BER}=10^{-4}$, the associated throughput curve was omitted from Figure 5.3. This phenomenon suggested that the CLDCs are more sensitive to the channel estimation errors than the LDCs. This is because the CLDCs require the knowledge of $M(N + 1)$ number of channels in comparison to MN number of links necessitated by the LDCs designed for co-located MIMO systems.

- Finally in Comparison C of Table 5.5, Figure 5.4 characterized the throughput of the LDCs, of the DLDCs and of the CLDCs of Table 5.5 recorded at $\text{BER}=10^{-4}$, when the communication channels were subjected to *shadowing* and the receiver had access to *perfect CSI*. Observe in Figure 5.4 that the family of CLDCs designed for cooperative MIMO systems has the best ability to combat the effect of large-scale shadowing with the aid of relays. Compared to the small-scale Rayleigh fading performance curves of Figure 5.2, the SNR required for the group of LDCs in Table 5.5 to maintain a BER of 10^{-4} increased by about 17dB, even though the receiver had access to perfect CSI.

Note that the above-mentioned observations based on Figures 5.2, 5.3 and 5.4 are consistent with the results recorded in Table 5.4. Again, our investigations indicate that the LDCs obeying the structure of Figure 2.3 are ideal for small-scale fading environments, when near-perfect CSI is available. On the other hand, the DLDCs having the structure of Figure 3.2 constitute the most appropriate solution, when the CSI is unavailable or the channel estimation imposes severe errors.

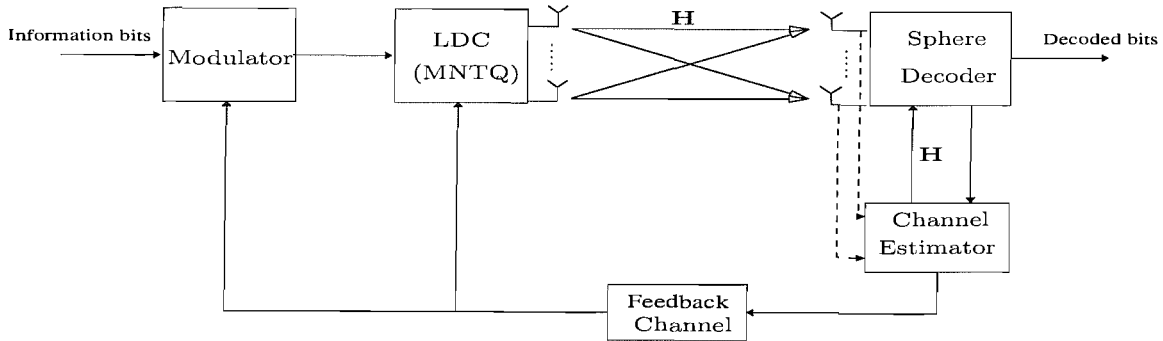


Figure 5.5: Schematic of the adaptive co-located MIMO system using Linear Dispersion Codes.

When large-scale shadowing dominates the achievable performance, the family of CLDCs obeying the structure of Figure 4.2 remains capable of maintaining reliable wireless communications.

5.5 Future Work

5.5.1 Adaptive Closed-loop Co-located MIMO Systems

In this thesis, we demonstrated that substantial performance improvements may be attained by co-located MIMO elements using a group of LDCs, when only the receiver has the knowledge of CSI. On the other hand, when the transmitter has access to full or partial CSI, we have a closed-loop MIMO system. The CSI available at the transmitter has been shown to be beneficial for optimizing STBC schemes in terms of their achievable link capacity and throughput [137]. Closed-loop MIMO systems can be implemented by employing a dedicated CSI feedback channel using frequency-division duplexing or sharing the same wireless channels in time-division duplexing systems.

Hence, we propose the adaptive MIMO scheme portrayed in Figure 5.5 for further study in order to exploit the CSI information at the transmitter, which jointly considers the design of modulation, space-time coding and the decoding complexity. The main idea is to dynamically adjust the system's throughput based on the near-real-time channel condition as well as the affordable complexity at the receiver. More explicitly, the channel estimator of Figure 5.5 provides the CSI required by a sphere decoder [138] [139] [140] and determines the number of CSI bits feedback to the transmitter. For example, a single bit can be used to indicate the transmitter of Figure 5.5, whether to increase or decrease the throughput by adjusting the modulation order or by changing the value of Q of the LDCs. Alternatively, if the receiver's affordable complexity is limited, for example by its battery consumption, a single bit can be transmitted to inform the transmitter of Figure 5.5 to reduce the throughput, to employ antenna selection [141] or even to decrease the value of T . Naturally, more precise control of the transmitter is attainable based on the near-instantaneous

channel quality and on the affordable complexity at the receiver, when more feedback bits are provided by the channel estimator of Figure 5.5.

5.5.2 Improved Performance Cooperative MIMO Systems

The CLDCs proposed in Chapter 4 were design for cooperative MIMO systems based on the AF cooperation protocol [127]. We offer the following suggestions in order to address some of the unresolved design issues as well as to improve the system's achievable performance. More explicitly:

- Observe in Figure 4.7 that the system's performance is gravely affected by the integrity of the signals received at the relays. Unfortunately, the source-to-relay links have to operate without diversity assistance, as seen in Figure 4.2. Hence, we expect the code design of the broadcast interval to be improved by increasing the achievable detection reliability at the relays, which can be achieved, for example, by Luby Transform (LT) codes [142] [143] [144].
- Figure 5.3 demonstrated that the CLDCs of Figure 4.2 are sensitive to the channel estimation errors, since both the source-to-relay and the relay-to-BS channels have to be estimated. Therefore, differential encoding schemes [145] [146] are desirable to eliminate the impediments imposed by the channel estimation process.
- The DF cooperation strategy can be employed instead of the AF protocol investigated in Chapter 4 in order to eliminate the ambiguity imposed by the relays. However, if the relays make an erroneous decision concerning the source information, the errors may be propagated further at the BS. Hence, the DF protocol is suitable for the scenarios, where the source-to-relay links are highly reliable and the BS has the knowledge of which relay is involved in the cooperation.
- Finally, owing to the distributed nature of the cooperative MIMO systems, it is straightforward to employ the multi-function MIMO concept originally designed for the co-located MIMO systems [147]. For example, we can configure a group of relays to form a beam [148] or configure another group of relays to employ space-time coding [44], according to their specific geographic distributions.

Appendix A

LDCs' χ for QPSK Modulation

$$\chi_{2212} = \begin{pmatrix} & \\ -0.405864+j0.401752 & 0.266975-j0.320303 \\ -0.373855-j0.184668 & -0.533834-j0.20286 \end{pmatrix}$$

$$\chi_{2221} = \begin{pmatrix} & \\ -0.92995-j0.166142 & \\ -0.0493851-j0.269278 & \\ 0.0470708-j0.056298 & \\ 0.0470708-j0.056298 & \end{pmatrix}$$

$$\chi_{2222} = \begin{pmatrix} & \\ -0.37759-j0.481206 & -0.0903934+j0.4462 \\ 0.283719-j0.242103 & -0.515433+j0.18240 \\ -0.0725764+j0.3777 & -0.443492+j0.2987 \\ 0.571661+j0.1095 & 0.336265+j0.30786 \end{pmatrix}$$

$$\chi_{2223} = \begin{pmatrix} & & \\ -0.246026-j0.27331 & 0.513074+j0.18723 & -0.05485+j0.0888 \\ -0.0256093-j0.3472 & -0.323245-j0.091157 & -0.50436+j0.3351 \\ 0.261717+j0.34385 & 0.238277-j0.1696 & -0.20259+j0.49595 \\ 0.119714-j0.45733 & 0.36222-j0.19698 & 0.04141+j0.01799 \end{pmatrix}$$

$$\chi_{2224} =$$

$$\begin{pmatrix} -0.02667-j0.3869 & 0.3181-j0.1179 & -0.1357-j0.3378 & 0.2356+j0.2157 \\ 0.02776-j0.2499 & 0.3341+j0.0361 & -0.3109+j0.1713 & -0.2236+j0.3845 \\ 0.18745-j0.11353 & 0.1395+j0.4161 & -0.3828+j0.0743 & 0.03857-j0.325 \\ -0.48671+j0.0384 & 0.0176+j0.2812 & -0.01802-j0.298 & -0.3046-j0.0097 \end{pmatrix}$$

 $\chi_{2225} =$

$$\begin{pmatrix} 0.0995-j0.1970 & -0.1595+j0.2814 & -0.2239-j0.2483 & -0.0999+j0.4198 & 0.1881-j0.115 \\ -0.1929-j0.1008 & -0.2018-j0.2046 & 0.25229-j0.1654 & 0.1984-j0.09254 & 0.0275-j0.4799 \\ 0.2651+j0.08348 & 0.1991-j0.2574 & -0.1421+j0.0309 & -0.2946+j0.211 & -0.1925-j0.3569 \\ -0.3677+j0.0415 & -0.2348-j0.2526 & -0.3051+j0.2967 & -0.2156-j0.0704 & 0.1069+j0.0135 \end{pmatrix}$$

 $\chi_{2226} =$

$$\begin{pmatrix} -0.0118453+j0.176595 & -0.166926+j0.18957 & -0.21592-j0.278066 & 0.05431+j0.29694 \\ 0.271779+j0.155392 & -0.243656-j0.32982 & 0.08774+j0.089246 & -0.16584+j0.26809 \\ -0.025031-j0.40389 & 0.13664+j0.237754 & 0.0384657-j0.0742 & -0.34909+j0.11268 \\ 0.0695421+j0.142181 & 0.215694+j0.04254 & 0.363479-j0.360688 & 0.13103+j0.08859 \\ -0.35861-j0.18914i & -0.0552-j0.14966 & & \\ -0.00187+j0.22265 & -0.26267+j0.01512 & & \\ -0.01572+j0.13145 & -0.26573-j0.17709 & & \\ -0.00548+j0.31543 & 0.17058-j0.10373 & & \end{pmatrix}$$

 $\chi_{2231} =$

$$\begin{pmatrix} -0.180116-j0.437363 \\ 0.0607185-j1.08843 \\ 0.569829-j0.398904 \\ -0.578465+j0.03283 \\ 0.754848-j0.265569 \\ 0.355719-j0.039016 \end{pmatrix}$$

 $\chi_{2232} =$

$$\begin{pmatrix} -0.135059+j0.67473 & 0.613496+j0.16956 \\ -0.439605+j0.294438 & -0.648091-j0.135779 \\ -0.22639-j0.0018267 & -0.499265-j0.121784 \\ 0.44635+j0.440015 & -0.183282-j0.203973 \\ -0.42659+j0.0988857 & 0.24671-j0.464298 \\ 0.327112+j0.0607891 & -0.196041-j0.0474298 \end{pmatrix}$$

$\chi_{2233} =$

$$\left(\begin{array}{ccc} -0.197896-j0.397516 & 0.447064-j0.556957 & -0.233644-j0.268266 \\ -0.169231-j0.569433 & -0.289421+j0.173695 & -0.0991308+j0.0559252 \\ 0.406543+j0.205873 & -0.221729+j0.0415185 & -0.26662+j0.10425 \\ -0.253797-j0.115446 & -0.446467+j0.257081 & 0.119519-j0.58575 \\ -0.160325+j0.34845 & 0.165754-j0.115912 & 0.530789-j0.137715 \\ 0.0136372-j0.131207 & -0.0164136+j0.136043 & 0.101885-j0.33176 \end{array} \right)$$

 $\chi_{2234} =$

$$\left(\begin{array}{cccc} -0.38169+j0.20106 & -0.1807+j0.3158 & -0.2639-j0.1252 & -0.111+j0.0384 \\ -0.20817-j0.26138 & -0.2739-j0.04583 & 0.14763+j0.3791 & 0.4402-j0.1636 \\ 0.32969+j0.07748 & 0.0083+j0.2443 & -0.1939-j0.01956 & 0.3213-j0.5498 \\ 0.0757-j0.51343 & -0.1736+j0.3061 & -0.1701-j0.2706 & -0.0333+j0.087 \\ 0.1787-j0.1289 & 0.06474+j0.326 & -0.2501+j0.1633 & 0.0441+j0.0789 \\ -0.1390-j0.01618 & 0.2131-j0.4481 & -0.3875-j0.3456 & 0.1384-j0.2716 \end{array} \right)$$

 $\chi_{2235} =$

$$\left(\begin{array}{ccccc} -0.1654-j0.0065 & -0.1782-j0.2422 & 0.5564-j0.1301 & -0.0665-j0.2825 & 0.0651-j0.0545 \\ 0.2076-j0.4481 & 0.1119-j0.0566 & 0.0511-j0.1929 & 0.0484-j0.1940 & 0.0041-j0.3703 \\ -0.1103-j0.1275 & -0.0387+j0.1548 & -0.1579+j0.0478 & -0.2659-j0.034 & 0.5917-j0.1534 \\ 0.3900-j0.1748 & -0.0481-j0.3926 & -0.1776-j0.12803 & -0.0648+j0.1935 & -0.0529+j0.0267 \\ 0.1113+j0.2462 & -0.3847+j0.0538 & -0.1801-j0.0061 & 0.3683-j0.2535 & -0.0440-j0.2628 \\ 0.2079-j0.0364 & -0.3899+j0.0948 & 0.2835+j0.2138 & -0.2471+j0.3183 & -0.0813-j0.0314 \end{array} \right)$$

 $\chi_{2241} =$

$$\left(\begin{array}{c} -0.221114-j0.494598 \\ 0.0980142+j0.226399 \\ -0.746841+j0.225963 \\ 0.373998+j0.912255 \\ 0.536852+j0.584814 \\ -0.263779+j0.21009 \\ 0.691621-j0.683595 \\ 0.39136+j0.47113 \end{array} \right)$$

 $\chi_{2243} =$

-0.453242+j0.374656	-0.126301-j0.282369	-0.0967778+j0.139826
0.273518+j0.0266982	-0.467402-j0.2064	-0.172853+j0.411392
-0.420225+j0.141066	-0.22024+j0.25243	-0.048435+j0.275407
-0.321455+j0.242619	0.365645-j0.23303	0.0147895+j0.105005
-0.241918+j0.0266229	0.264479+j0.165391	-0.25357+j0.77101
-0.117268+j0.602912	-0.0038704+j0.523916	-0.0801905-j0.248962
-0.212304+j0.171448	-0.0686492-j0.465512	-0.094808-j0.327579
0.181526+j0.0970578	0.263082-j0.118006	-0.359276+j0.208113

 $\chi_{2245} =$

-0.0494-j0.0683	0.1747+j0.1919	0.155907-j0.07955	-0.0702-j0.1889	0.2557-j0.2321
-0.2073+j0.2180	-0.1061+j0.1024	0.150372-j0.14881	0.3176+j0.1941	-0.0581-j0.2098
0.1671+j0.0559	-0.2076+j0.3527	-0.374529+j0.01133	0.0323+j0.0361	-0.3035-j0.1819
-0.1159+j0.3092	-0.2626+j0.1096	-0.0287448+j0.49359	0.0487+j0.338	0.1980-j0.1296
0.0581-j0.1775	-0.0212+j0.491	0.170009-j0.240328	-0.4753+j0.3518	-0.0558+j0.0209
0.2598+j0.0239	0.2756-j0.2007	-0.138142+j0.14911	-0.2003+j0.0388	0.0203-j0.5863
-0.0128-j0.4441	0.0879-j0.0186	0.193049+j0.292598	0.1077-j0.0086	0.1329-j0.1430
-0.4211+j0.2911	0.2578+j0.1749	0.00639021+j0.2981	-0.2370-j0.2067	-0.2577-j0.0005

 $\chi_{2247} =$

-0.12986-j0.23838	-0.1156-j0.0763	-0.0329-j0.19681	-0.2163-j0.25286
0.10971-j0.4252	-0.34448+j0.011	-0.0039-j0.0972	0.37495+j0.0361
0.2896+j0.0998	-0.1052-j0.0735	-0.3172-j0.2053	-0.09719-j0.2700
-0.04043-j0.1204	-0.0581-j0.0706	0.251-j0.02953	-0.2822+j0.18163
0.07016-j0.0673	-0.0223-j0.4401	0.262-j0.2702	-0.111+j0.1022
-0.11586+j0.052	-0.0511-j0.1605	-0.0376-j0.2777	-0.027+j0.08845
-0.10619+j0.3817	-0.2639+j0.07324	0.156+j0.074	0.1380-j0.1307
0.111-j0.0041	0.1363+j0.30387	-0.093+j0.2368	0.2099+j0.110

$$\begin{array}{ccc}
 0.0846305-j0.180206 & -0.250361+j0.228041 & -0.273297-j0.0244441 \\
 -0.219413+j0.0949425 & 0.0424736+j0.078488 & 0.0242912+j0.129786 \\
 0.0758912+j0.0340755 & 0.229038-j0.1981 & 0.0925592+j0.317003 \\
 -0.0318609+j0.517846 & 0.104264+j0.0231903 & 0.0330019+j0.0672416 \\
 -0.150191-j0.307028 & 0.157935-j0.169761 & 0.020939-j0.0485428 \\
 -0.0483534-j0.106107 & -0.197735+j0.244426 & 0.505831+j0.0244521 \\
 -0.22209+j0.053245 & -0.270766-j0.157822 & 0.104142+j0.0777363 \\
 0.126008-j0.00882476 & -0.13067+j0.27887 & -0.0235858+j0.295523
 \end{array}$$

 $\chi_{2324} =$

$$\begin{pmatrix}
 -0.01049+j0.349 & -0.3895+j0.00368 & -0.2532+j0.10835 & 0.2535+j0.2935 \\
 0.10824-j0.4266 & 0.0331+j0.2476 & -0.42283-j0.0105 & -0.064+j0.247 \\
 -0.03331+j0.272 & 0.3437+j0.00559 & -0.42152-j0.207 & 0.12481-j0.2643 \\
 -0.2982+j0.1408 & -0.1849+j0.365 & -0.0832+j0.1318 & -0.3952-j0.2074
 \end{pmatrix}$$

 $\chi_{3224} =$

$$\begin{pmatrix}
 -0.2425-j0.1850 & -0.2895+j0.0503 & -0.3121-j0.08697 & -0.14691-j0.27664 \\
 0.05667-j0.3875 & -0.1549-j0.0539 & -0.0144+j0.3689 & -0.0822+j0.2394 \\
 0.04526-j0.0398 & -0.0516-j0.2582 & -0.2578+j0.0461 & 0.03451+j0.2839 \\
 -0.1681-j0.2590 & 0.16140+j0.1316 & -0.0037-j0.31776 & -0.146+j0.3754 \\
 -0.0712+j0.2685 & -0.2593-j0.3806 & 0.2515-j0.03864 & -0.2128+j0.1755 \\
 -0.0902+j0.2629 & -0.1638+j0.187 & -0.1553-j0.0118 & -0.105+j0.0808
 \end{pmatrix}$$

 $\chi_{3324} =$

$$\begin{pmatrix}
 -0.0562-j0.361 & 0.0629-j0.2637 & 0.146287-j0.1437 & 0.05466+j0.3514 \\
 0.2767-j0.122 & -0.214-j0.3854 & -0.07529+j0.183 & 0.2074-j0.1908 \\
 -0.147+j0.185 & 0.058-j0.3382 & -0.2978-j0.0407 & -0.316-j0.07860 \\
 0.1720+j0.168 & -0.143-j0.088 & 0.28631-j0.3333 & -0.166+j0.1585 \\
 0.2228-j0.1502 & -0.098-j0.005 & -0.1803-j0.2818 & -0.244-j0.2426 \\
 0.281+j0.0958 & 0.0990+j0.257 & -0.1367+j0.0672 & 0.1262+j0.0167
 \end{pmatrix}$$

Appendix

B

DLDCs' χ for 2PAM Modulation

$$\chi_{3231} = \begin{pmatrix} -0.370502+j0 \\ 0.167623+j0.701519 \\ -0.255219-j0.524332 \\ 0.167623-j0.701519 \\ -0.173728-j0 \\ -0.659946+j0.162501 \\ -0.255219+j0.524332 \\ -0.659946-j0.162501 \\ -0.433707-j0 \end{pmatrix}$$

$$\chi_{3232} = \begin{pmatrix} -0.0549+j0 & 0.1476-j0 \\ -0.26993+j0.676 & -0.3309-j0.3760 \\ -0.1187-j0.0593 & 0.0868-j0.4113 \\ -0.2699-j0.676 & -0.3309+j0.376 \\ -0.039712-j0 & 0.0493+j0 \\ 0.09487-j0.1667 & -0.3406-j0.2528 \\ -0.1187+j0.0593 & 0.0868+j0.4113 \\ 0.0949+j0.1667 & -0.3406+j0.2528 \\ 0.5718+j0 & 0.5105+j0 \end{pmatrix}$$

$\chi_{3233} =$

$$\left(\begin{array}{ccc} -0.2498+j0 & 0.0754-j0 & 0.3885-j0 \\ 0.2403+j0.01 & -0.1796-j0.3199 & 0.11496-j0.1835 \\ -0.0634+j0.4061 & 0.2034-j0.2178 & -0.1827+j0.3217 \\ 0.2403-j0.01 & -0.1796+j0.3199 & 0.11496+j0.1835 \\ -0.385619-j0 & -0.4054+j0 & 0.2958+j0 \\ -0.3044+j0.2739 & 0.0656+j0.3614 & 0.388977+j0.20423 \\ -0.0634-j0.4061 & 0.2034+j0.2178 & -0.1827-j0.3217 \\ -0.3044-j0.2739 & 0.0656-j0.3614 & 0.3889-j0.20423 \\ 0.00019+j0 & -0.3367+j0 & -0.0898-j0 \end{array} \right)$$

 $\chi_{3234} =$

$$\left(\begin{array}{cccc} -0.1158+j0 & -0.1032+j0 & -0.3165+j0 & -0.530825+j0 \\ -0.0123+j0.3571 & -0.0046+j0.1659 & -0.1119+j0.0726 & -0.0613-j0.1763 \\ 0.4215+j0.0889 & -0.1255+j0.2798 & 0.0538+j0.0852 & -0.1628+j0.2166 \\ -0.0123-j0.3571 & -0.0046-j0.1659 & -0.1119-j0.0726 & -0.0613+j0.1763 \\ -0.227013-j0 & -0.3148+j0 & 0.452988-j0 & -0.2747-j0 \\ -0.0655-j0.1575 & 0.2654+j0.3468 & -0.0263+j0.1942 & -0.0749-j0.279 \\ 0.4215-j0.089 & -0.1255-j0.2798 & 0.0538-j0.085 & -0.1627-j0.21661 \\ -0.0656+j0.1575 & 0.265-j0.347 & -0.0263-j0.1942 & -0.0748+j0.279 \\ 0.01569+j0 & -0.1254-j0 & 0.5585+j0 & 0.0956-j0 \end{array} \right)$$

 $\chi_{3235} =$

$$\left(\begin{array}{ccccc} -0.2309+j0 & 0.086+j0 & -0.0066-j0 & 0.4227-j0 & 0.0989-j0 \\ -0.185-j0.0977 & -0.011-j0.0934 & 0.1107+j0.317 & -0.2262+j0.0991 & 0.3942-j0.0362 \\ 0.1390+j0.230 & -0.3061+j0.3981 & 0.0569+j0.1810 & 0.1893+j0.0475 & 0.0065-j0.0236 \\ -0.1853+j0.0977 & -0.011+j0.093 & 0.110-j0.317 & -0.2262+j0.0991 & 0.3942-j0.0362 \\ -0.3457-j0 & 0.1243+j0 & -0.4062-j0 & 0.0413+j0 & -0.2193+j0 \\ -0.0037-j0.1011 & 0.0217+j0.1582 & -0.033-j0.0552 & 0.3123+j0.1146 & 0.1821+j0.1746 \\ 0.1390+j0.230 & -0.3061+j0.3981 & 0.0569+j0.1810 & 0.1893+j0.0475 & 0.0065-j0.0236 \\ -0.0037-j0.1011 & 0.0217+j0.1582 & -0.033-j0.0552 & 0.3123+j0.1146 & 0.1821+j0.1746 \\ 0.4168+j0 & -0.0622-0 & -0.3593+j0 & -0.0039-j0 & 0.3163+j0 \end{array} \right)$$

$$\chi_{3236} =$$

$$\begin{pmatrix} -0.2857+j0 & 0.0504628+j0 & -0.342589+j0 & 0.0572714+j0 \\ 0.06459-j0.1708 & -0.0988-j0.2411 & 0.1939+j0.064 & -0.0722+j0.0244 \\ -0.03706+j0.0443 & -0.3769+j0.0992 & 0.0474+j0.102 & -0.01643-j0.3795 \\ 0.06459-j0.1708 & -0.0988-j0.2411 & 0.1939+j0.064 & -0.0722+j0.0244 \\ 0.220344+j0 & 0.0480425-j0 & 0.00109-j0 & 0.2958-j0 \\ -0.1052-j0.1247 & 0.0599-j0.05052 & 0.0105-j0.274 & 0.1271-j0.1936 \\ -0.03706+j0.0443 & -0.3769+j0.0992 & 0.0474+j0.102 & -0.01643-j0.3795 \\ -0.1052-j0.1247 & 0.0599-j0.05052 & 0.0105-j0.274 & 0.1271-j0.1936 \\ 0.4931+j0 & -0.2078-j0 & -0.35099-j0 & -0.041168+j0 \\ 0.143171-j0 & -0.109684+j0 \\ 0.0774-j0.387 & -0.395-j0.02217 \\ 0.2569-j0.047 & 0.15752+j0.0851 \\ 0.0774-j0.387 & -0.395-j0.02217 \\ -0.1186-j0 & 0.1071-j0 \\ 0.0513-j0.0326 & -0.1857-j0.0782 \\ 0.2569-j0.047 & 0.15752+j0.0851 \\ 0.0513-j0.0326 & -0.1857-j0.0782 \\ 0.0999088-j0 & -0.13375+j0 \end{pmatrix}$$

$$\chi_{2221} =$$

$$\begin{pmatrix} -0.404626+j0 \\ 0.820031+j0.404755 \\ 0.820031-j0.404755 \\ 0.404626+j0 \end{pmatrix}$$

$$\chi_{2222} =$$

$$\begin{pmatrix} -0.5802+j0 & 0.404212-j0 \\ -0.2624-j0.3077 & -0.366-j0.45 \\ -0.2624+j0.3077 & -0.366+j0.45 \\ 0.579896+j0 & -0.40439+j0 \end{pmatrix}$$

$$\chi_{2223} = \begin{pmatrix} -0.328116+j0 & -0.469847-j0 & 0.0222762+j0 \\ 0.0913+j0.46418 & -0.0892-j0.3194 & -0.5631+j0.1259 \\ 0.0913-j0.46418 & -0.0892+j0.3194 & -0.5631-j0.1259 \\ 0.333784+j0 & 0.475327+j0 & -0.0202509-j0 \end{pmatrix}$$

$$\chi_{2224} = \begin{pmatrix} -0.372+j0 & 0.4744+j0 & 0.0984-j0 & -0.3559+j0 \\ -0.4041-j0.091 & -0.1984-j0.2643 & -0.1903+j0.3864 & 0.1056-j0.1499 \\ -0.4041+j0.091 & -0.1984+j0.2643 & -0.1903-j0.3864 & 0.1056+j0.1499 \\ 0.1348+j0 & -0.2377-j0 & -0.3454+j0 & -0.5532+j0 \end{pmatrix}$$

$$\chi_{2225} = \begin{pmatrix} -0.1415+j0 & -0.4042-j0 & 0.4097-j0 & -0.2627+j0 & 0.2824+j0 \\ 0.0316+j0.0217 & -0.1391+j0.3455 & -0.3227+j0.1897 & -0.3517-j0.3026 & -0.0422-j0.0512 \\ 0.0316-j0.0217 & -0.1391-j0.3455 & -0.3227-j0.1897 & -0.3517+j0.3026 & -0.0422+j0.0512 \\ -0.6517+j0 & 0.0119-j0 & -0.0283-j0 & -0.0047+j0 & -0.27265-j0 \end{pmatrix}$$

Appendix C

CLDCs' χ_1 and χ_2 for BPSK Modulation

Recall from Section 4.2.3 that we defined the DCM $\chi_1 \in \zeta^{T_1 \times Q}$ for the broadcast interval and analogous matrix $\chi_2 \in \zeta^{MT_2 \times MT_1}$ for characterizing the cooperation interval, which is given by:

$$\chi_2 = \begin{pmatrix} \mathbf{B}_1 & \mathbf{0} & \cdots & \mathbf{0} \\ \mathbf{0} & \mathbf{B}_m & \cdots & \mathbf{0} \\ \mathbf{0} & \mathbf{0} & \ddots & \mathbf{0} \\ \mathbf{0} & \cdots & \cdots & \mathbf{B}_M \end{pmatrix}, \quad (\text{C.1})$$

where $\mathbf{B}_m \in \zeta^{T_2 \times T_1}$ and $\mathbf{0} \in \zeta^{T_2 \times T_1}$ denotes a zero matrix.

Since the size of the DCM χ_2 is often quite large, we define another matrix $\bar{\chi}_2$ having a size of $(T_1 T_2 \times M)$ in order to present the dispersion matrices in a more compact form, which is given as follows

$$\bar{\chi}_2 = [vec(\mathbf{B}_1), vec(\mathbf{B}_2), \dots, vec(\mathbf{B}_M)]. \quad (\text{C.2})$$

$$\chi_1(4181, T_1 = 2, T_2 = 6) = \begin{pmatrix} \chi_1(4181, T_1 = 2, T_2 = 6) \\ -0.8054+j0.9896 \\ 0.4786+j0.3782 \end{pmatrix}$$

$$\bar{\chi}_2(4181, T_1 = 2, T_2 = 6) =$$

$$\left(\begin{array}{cccc} -0.2925+j0.3594 & -0.1667-j0.1819 & -0.392-j0.0055i & -0.4077+j0.0371 \\ 0.1738+j0.1374 & -0.2843-j0.2997 & -0.0778+j0.225 & -0.0721-j0.0102 \\ 0.2104-j0.0556 & 0.0098+j0.005 & -0.1882+j0.3942 & 0.0884-j0.3008 \\ 0.1120+j0.5111 & 0.1562-j0.1450 & 0.4430-j0.1178 & 0.3282+j0.3345 \\ 0.0622-j0.3963 & 0.1381-j0.1562 & 0.2122+j0.1585 & 0.0442-j0.3906 \\ 0.0388-j0.0508 & -0.3664+j0.5434 & i 0.0146-j0.2605 & 0.2845+j0.1540 \\ 0.3884-j0.0272 & -0.2456-j0.3130 & 0.1882+j0.0160 & 0.2412-j0.2033 \\ -0.2449+j0.5105 & -0.0337+j0.2887 & -0.3098+j0.1832 & 0.0047+j0.2537 \\ -0.0747-j0.01823 & 0.3680-j0.1673 & -0.0550+j0.1429 & 0.1947-j0.2236 \\ 0.0187+j0.1511 & -0.0563+j0.5262 & 0.004+j0.3746 & 0.4934-j0.0909 \\ -0.0406-j0.057 & -0.1773-j0.1177 & 0.1378-j0.1408 & 0.0713+j0.4279 \\ 0.4732+j0.1411 & -0.1312+j0.03579 & -0.6160+j0.0524 & 0.0756+j0.2294 \end{array} \right)$$

$$\chi_1(4182, T_1 = 2, T_2 = 6) =$$

$$\left(\begin{array}{cc} -0.4838 - j0.5383 & 0.0551 - j0.6878 \\ 0.6889 - j0.0394 & -0.5271 - j0.4959 \end{array} \right)$$

$$\bar{\chi}_2(4182, T_1 = 2, T_2 = 6) =$$

$$\left(\begin{array}{cccc} -0.3545 - j0.3944 & -0.0045 + j0.6001 & -0.2679 + j0.1594 & -0.0344 + j0.1286 \\ 0.5047 - j0.0289 & -0.1781 + j0.2782 & 0.3350 - j0.2350 & -0.0116 - j0.0919 \\ 0.0884 - j0.0396 & -0.0583 - j0.1296 & -0.1513 - j0.0147 & -0.0293 + j0.5856 \\ -0.1015 + j0.0157 & -0.1118 + j0.2598 & -0.0291 - j0.3369 & 0.0869 + j0.1181 \\ 0.0281 - j0.0831 & -0.0895 - j0.3184 & 0.1179 + j0.3124 & -0.0375 + j0.3506 \\ -0.3200 + j0.2884 & 0.2563 - j0.0737 & 0.0302 + j0.4853 & 0.1793 + j0.4494 \\ -0.2509 - j0.2475 & 0.1173 + j0.2456 & 0.0007 - j0.0166 & 0.0695 - j0.4795 \\ -0.0898 - j0.1111 & -0.2637 - j0.2359 & -0.0459 + j0.4471 & -0.0289 + j0.3445 \\ -0.3867 - j0.1989 & 0.1538 + j0.1944 & 0.3467 - j0.2887 & 0.0147 - j0.0058 \\ -0.0959 - j0.2959 & 0.2651 - j0.1216 & -0.3553 + j0.1135 & -0.0917 - j0.4221 \\ 0.3866 + j0.3213 & 0.3797 - j0.1122 & 0.0699 + j0.3765 & 0.2363 + j0.0601 \\ 0.1384 - j0.2185 & -0.2572 - j0.4259 & 0.1976 + j0.1392 & -0.1166 + j0.3687 \end{array} \right)$$

$$\chi_1(4183, T_1 = 2, T_2 = 6) =$$

$$\left(\begin{array}{ccc} -0.0128 + j0.1408 & -0.1711 - j0.6604 & -0.0316 - j0.7167 \\ 0.6999 - j0.1752 & -0.0823 - j0.5151 & 0.1068 + j0.4426 \end{array} \right)$$

$$\bar{\chi}_2(4183, T_1 = 2, T_2 = 6) =$$

$$\left(\begin{array}{cccc} -0.0085 + j0.0936 & -0.2769 - j0.3746 & -0.0056 - j0.3750 & -0.3079 - j0.1600 \\ -0.1138 - j0.4392 & 0.2488 - j0.0769 & 0.3535 + j0.0142 & 0.1272 - j0.1987 \\ -0.0210 - j0.4766 & 0.1693 - j0.2010 & -0.2999 + j0.4355 & -0.4265 - j0.0862 \\ 0.3327 - j0.0510 & 0.0353 - j0.4967 & -0.1331 + j0.0459 & -0.3847 + j0.0256 \\ -0.0484 - j0.4290 & -0.0961 - j0.1811 & -0.0457 - j0.0633 & 0.2161 - j0.2943 \\ 0.0827 + j0.0342 & 0.1226 - j0.3019 & -0.4175 - j0.0662 & -0.2331 + j0.2198 \\ -0.0546 + j0.0046 & 0.4167 - j0.0401 & 0.0030 - j0.5396 & 0.2180 + j0.0096 \\ -0.1339 + j0.3918 & -0.1557 - j0.1280 & -0.2019 + j0.0647 & -0.2823 - j0.0337 \\ -0.3404 - j0.0024 & -0.0704 - j0.1223 & -0.0780 - j0.0001 & -0.4304 - j0.1147 \\ 0.3968 + j0.1526 & -0.2195 - j0.2403 & 0.1937 + j0.4835 & -0.3821 - j0.1044 \\ 0.3512 - j0.0938 & 0.3787 - j0.4351 & 0.1464 + j0.0522 & -0.2407 + j0.1828 \\ -0.1449 + j0.3546 & -0.2746 + j0.0123 & 0.3319 + j0.0466 & 0.3085 - j0.2824 \end{array} \right)$$

$$\chi_1(4184, T_1 = 2, T_2 = 6) = \left(\begin{array}{cccc} -0.3439 - j0.1960 & -0.2670 + j0.5943 & 0.0378 - j0.2339 & -0.5589 - j0.2244 \\ 0.4529 + j0.3324 & -0.2748 + j0.2500 & -0.2868 + j0.6279 & -0.2585 - j0.0544 \end{array} \right)$$

$$\bar{\chi}_2(4184, T_1 = 2, T_2 = 6) = \left(\begin{array}{cccc} -0.2136 - j0.1217 & -0.1473 + j0.2378 & -0.5139 + j0.2171 & -0.4358 + j0.1618 \\ -0.1658 + j0.3691 & 0.1116 + j0.3585 & -0.0132 + j0.1322 & 0.1501 - j0.2588 \\ 0.0235 - j0.1452 & 0.1192 - j0.1431 & -0.0742 - j0.0147 & -0.0530 - j0.2310 \\ -0.3471 - j0.1394 & -0.2079 - j0.1048 & -0.0224 - j0.2400 & -0.2920 - j0.0522 \\ 0.4673 + j0.3173 & -0.2050 + j0.3654 & 0.1226 + j0.3303 & 0.3573 + j0.3383 \\ 0.0140 - j0.2121 & 0.5133 + j0.0535 & -0.4051 + j0.2629 & -0.0502 + j0.2359 \\ -0.1735 + j0.4573 & -0.1149 + j0.0692 & -0.1740 + j0.4664 & -0.2181 - j0.2347 \\ 0.1287 + j0.0947 & -0.3074 + j0.2104 & -0.1755 + j0.2553 & -0.4391 - j0.1735 \\ -0.2762 + j0.2484 & -0.1262 + j0.5668 & -0.2510 - j0.2168 & -0.3286 + j0.2278 \\ 0.2131 - j0.3684 & -0.2299 + j0.2989 & 0.1540 + j0.1193 & -0.2135 + j0.1627 \\ 0.1405 + j0.0502 & 0.3103 + j0.0011 & -0.1605 - j0.3728 & -0.2639 - j0.0263 \\ 0.3712 + j0.0784 & 0.1318 + j0.0128 & -0.0165 - j0.3054 & -0.3214 + j0.1372 \end{array} \right)$$

$$\chi_1(4185, T_1 = 3, T_2 = 5) = \left(\begin{array}{cccc} -0.0085 + j0.5196 & -0.1005 - j0.1172 & -0.0170 - j0.1127 & -0.5283 + j0.3177 \\ -0.0616 + j0.2309 & -0.6130 - j0.1501 & -0.2593 + j0.6090 & -0.0591 - j0.2384 \\ 0.5568 + j0.0553 \\ -0.1480 - j0.1556 \end{array} \right)$$

$$\bar{\chi}_2(4185, T_1 = 3, T_2 = 5) =$$

$$\left(\begin{array}{cccc} -0.2598 + j0.1219 & -0.1623 + j0.1250 & -0.1791 - j0.0678 & -0.0977 - j0.2066 \\ -0.2342 - j0.0991 & -0.1540 - j0.0662 & 0.0046 + j0.2690 & -0.4254 + j0.1552 \\ 0.2079 + j0.4125 & 0.0601 - j0.0075 & -0.0954 + j0.2249 & 0.1165 - j0.1197 \\ -0.0114 - j0.2283 & 0.1254 - j0.1603 & 0.3015 - j0.2845 & -0.2112 + j0.1640 \\ 0.0598 - j0.0215 & -0.5079 + j0.2087 & -0.0836 - j0.2628 & 0.2362 - j0.0650 \\ 0.0140 - j0.2674 & -0.1948 - j0.0350 & 0.1646 + j0.3185 & 0.4048 + j0.1807 \\ -0.2124 + j0.0197 & -0.1559 + j0.1745 & -0.2042 + j0.0061 & -0.0278 - j0.0694 \\ -0.0334 - j0.1312 & -0.0408 + j0.3978 & -0.2833 - j0.2402 & -0.1846 + j0.0142 \\ -0.0684 - j0.3077 & 0.2902 - j0.1976 & -0.1323 - j0.2358 & 0.0374 + j0.1211 \\ -0.4062 - j0.1295 & 0.1988 - j0.0065 & -0.0100 - j0.1876 & 0.2910 - j0.2820 \\ 0.0248 + j0.2084 & 0.0558 + j0.0024 & 0.1346 + j0.1628 & 0.0678 - j0.1194 \\ -0.1086 - j0.2842 & 0.4243 + j0.1725 & -0.0048 + j0.0181 & 0.2355 + j0.0890 \\ -0.0351 - j0.2917 & 0.1414 + j0.0171 & -0.1205 + j0.1984 & -0.1622 + j0.2352 \\ 0.1008 - j0.2576 & 0.3358 + j0.1943 & 0.1748 - j0.2001 & -0.4138 + j0.2568 \\ 0.0755 + j0.3339 & -0.0599 + j0.1712 & 0.2218 + j0.4450 & -0.0264 + j0.1221 \end{array} \right)$$

$$\chi_1(4163, T_1 = 2, T_2 = 4) =$$

$$\left(\begin{array}{ccc} -0.3303 - j0.3193 & -0.2146 - j0.4589 & -0.5325 + j0.4987 \\ 0.6794 - j0.2491 & -0.1937 + j0.4730 & -0.2186 + j0.4090 \end{array} \right)$$

$$\bar{\chi}_2(4163, T_1 = 2, T_2 = 4) =$$

$$\left(\begin{array}{cccc} -0.2298 - j0.2221 & -0.2837 - j0.3488 & -0.3169 + j0.2518 & -0.0656 + j0.0739 \\ -0.1493 - j0.3193 & 0.2514 + j0.2502 & 0.0231 - j0.2635 & 0.5389 + j0.1393 \\ -0.3705 + j0.3470 & 0.0860 - j0.3256 & -0.4126 - j0.2860 & 0.1674 + j0.3785 \\ -0.1218 + j0.0339 & 0.0393 - j0.2390 & -0.1148 + j0.0319 & -0.0071 + j0.0954 \\ 0.1353 - j0.2457 & -0.1822 + j0.2684 & -0.3193 + j0.0761 & -0.1773 - j0.2913 \\ -0.0005 - j0.3831 & -0.0257 + j0.1558 & -0.3253 - j0.3234 & -0.1483 - j0.0600 \\ 0.3018 - j0.0231 & -0.1419 + j0.0838 & 0.3821 + j0.1380 & 0.0475 + j0.0984 \\ 0.2990 + j0.3059 & 0.5750 - j0.1099 & 0.0423 + j0.1229 & 0.1575 + j0.5669 \end{array} \right)$$

$$\chi_1(4143, T_1 = 1, T_2 = 3) =$$

$$\left(\begin{array}{ccc} -0.6323 + j0.2230 & -0.1558 - j0.5720 & 0.4167 + j0.1593 \end{array} \right)$$

$$\bar{\chi}_2(4143, T_1 = 1, T_2 = 3) =$$

$$\begin{pmatrix} -0.5476 + j0.1931 & -0.5760 + j0.2573 & -0.2554 - j0.2909 & -0.3169 + j0.3566 \\ -0.1349 - j0.4953 & 0.5261 - j0.0371 & -0.0629 + j0.7045 & -0.3277 - j0.3445 \\ 0.3609 + j0.1380 & -0.2679 + j0.0463 & 0.2362 + j0.2100 & -0.1683 + j0.5176 \end{pmatrix}$$

Weighting Coefficient Vectors λ and γ

This Appendix presents all the weighting coefficient vectors λ of the *inner* irregular scheme and γ of the *outer* irregular scheme used in Sections 2.5, 3.6 and 4.3 of this thesis. More explicitly,

- Tables D.1 shows λ of the RSC(213)-coded **IR-PLDC** scheme of Figure 2.32.
- Tables D.2 shows λ of the RSC(215)-coded **IR-PLDC** scheme of Figure 2.32.
- Tables D.3 shows γ of the **IRCC**-coded PLDC(2224) scheme of Figure 2.24.
- Tables D.4 shows γ of the **IRCC**-coded PLDC(2221) scheme of Figure 2.24.
- Tables D.5 shows γ of the **IRCC**-coded IR-PLDC scheme of Figure 2.48.
- Tables D.6 shows λ of the **IRCC**-coded **IR-PLDC** scheme of Figure 2.48.
- Tables D.7 shows γ of the **IRCC**-coded IR-PDLDC scheme of Figure 3.25.
- Tables D.8 shows λ of the **IRCC**-coded **IR-PDLDC** scheme of Figure 3.25.
- Tables D.9 shows γ of the **IRCC**-coded IR-PLDC scheme of Figure 2.48.
- Tables D.10 shows λ of the **IRCC**-coded **IR-PLDC** scheme of Figure 2.48.
- Tables D.11 shows γ of the **IRCC**-coded IR-PCLDC scheme of Figure 4.16.
- Tables D.12 shows λ of the **IRCC**-coded **IR-PCLDC** scheme of Figure 4.16.
- Tables D.13 shows γ of the **IRCC**-coded IR-PLDC scheme of Figure 2.48.
- Tables D.14 shows λ of the **IRCC**-coded **IR-PLDC** scheme of Figure 2.48.

Table D.1: The weighting coefficient vector λ for the QPSK-modulated **IR-PLDC** scheme of Figure 2.32 designed for achieving maximum rates, while using an RSC(213) code.

SNR (dB)	Max Rate	R_{in}	(2241) =0.25	(2231) =0.33	(2221) =0.5	(2232) =0.67	(2243) =0.75	(2222) =1.0
-7	0.26	0.26	0.447	0.553	0	0	0	0
-6	0.31	0.31	0	0.777	0.223	0	0	0
-5	0.45	0.45	0	0.222	0.778	0	0	0
-4	0.54	0.54	0	0	0.637	0.363	0	0
-3	0.67	0.67	0	0	0.0209	0.9539	0	0
-2	0.80	0.80	0	0	0.25	0	0	0.75
-1	1.009	1.009	0	0	0	0	0	0.99
0	1.1392	1.1392	0	0	0	0.146	0.034	0
1	1.402	1.402	0	0	0	0	0	0.1402
2	1.65	1.65	0	0	0	0	0	0
3	1.88	1.88	0	0	0	0	0	0
4	2.0	2.0	0	0	0	0	0	0

SNR (dB)	Max Rate	R_{in}	(2245) =1.25	(2234) =1.33	(2223) =1.5	(2235) =1.67	(2224) =2.0
-7	0.26	0.26	0	0	0	0	0
-6	0.31	0.31	0	0	0	0	0
-5	0.45	0.45	0	0	0	0	0
-4	0.54	0.54	0	0	0	0	0
-3	0.67	0.67	0.0252	0	0	0	0
-2	0.80	0.80	0	0	0	0	0
-1	1.009	1.009	0	0	0	0	0.01
0	1.1392	1.1392	0	0.82	0	0	0
1	1.402	1.402	0	0	0.8598	0	0
2	1.65	1.65	0	0	0.5314	0.1889	0.2797
3	1.88	1.88	0	0	0	0.08	0.92
4	2.0	2.0	0	0	0	0	1

Table D.2: The weighting coefficient vector λ for the QPSK-modulated **IR-PLDC** scheme of Figure 2.32 designed for achieving maximum rates, while using an RSC(215) code.

SNR (dB)	Max Rate	R_{in}	(2241) =0.25	(2231) =0.33	(2221) =0.5	(2232) =0.67	(2243) =0.75	(2222) =1.0
-7	0.26	0.26	0.7729	0.2271	0	0	0	0
-6	0.306	0.306	0.069	0.8469	0.0841	0	0	0
-5	0.41	0.41	0	0.381	0.619	0	0	0
-4	0.51	0.51	0	0	0.847	0.153	0	0
-3	0.622	0.622	0	0	0.216	0.784	0	0
-2	0.74	0.74	0	0	0	0.8	0	0
-1	0.9315	0.9315	0	0	0	0.1472	0	0.8528
0	1.065	1.065	0	0	0	0.2511	0	0
1	1.296	1.296	0	0	0	0	0	0.5335
2	1.55	1.55	0	0	0	0	0	0
3	1.765	1.765	0	0	0	0	0	0
4	2.0	2.0	0	0	0	0	0	0

SNR (dB)	Max Rate	R_{in}	(2245) =1.25	(2234) =1.33	(2223) =1.5	(2235) =1.67	(2224) =2.0
-7	0.26	0.26	0	0	0	0	0
-6	0.306	0.306	0	0	0	0	0
-5	0.41	0.41	0	0	0	0	0
-4	0.51	0.51	0	0	0	0	0
-3	0.622	0.622	0	0	0	0	0
-2	0.74	0.74	0	0	0.2	0	0
-1	0.9315	0.9315	0	0	0	0	0
0	1.065	1.065	0	0.7489	0	0	0
1	1.296	1.296	0.0179	0	0	0	0.4486
2	1.55	1.55	0	0	0.8573	0	0.1427
3	1.765	1.765	0	0	0	0.693	0.307
4	2.0	2.0	0	0	0	0	1

Table D.3: The weighting coefficient vector γ of the **IRCC** for the IRCC-coded PLDC(2224) scheme of Figure 2.24 designed for achieving maximum rates, while using the QPSK modulation in conjunction with an MMSE detector.

SNR (dB)	Max Rate	R_{out}	$R_{ircc,1}$ =0.10	$R_{ircc,2}$ =0.15	$R_{ircc,3}$ =0.25	$R_{ircc,4}$ =0.40	$R_{ircc,5}$ =0.45
-3	0.940	0.235	0.255	0	0.182	0	0.268
-2	1.124	0.281	0.075	0.198	0	0.161	0.108
-1	1.310	0.328	0	0.186	0.164	0.215	0
0	1.550	0.388	0.006	0.06	0.233	0.152	0
1	1.764	0.436	0	0	0.244	0.179	0
2	2.0	0.5	0	0	0.181	0.178	0

SNR (dB)	Max Rate	R_{out}	$R_{ircc,6}$ =0.55	$R_{ircc,7}$ =0.6	$R_{ircc,8}$ =0.7	$R_{ircc,9}$ =0.75	$R_{ircc,10}$ =0.85	$R_{ircc,11}$ =0.9
-3	0.940	0.235	0	0	0.183	0	0	0.112
-2	1.124	0.281	0.175	0	0	0.208	0.032	0.043
-1	1.310	0.328	0.126	0.042	0.136	0.075	0	0.056
0	1.550	0.388	0.168	0.054	0.169	0	0	0.158
1	1.764	0.436	0.195	0	0.209	0	0.075	0.098
2	2.0	0.5	0.114	0.09	0.237	0	0.033	0.167

Table D.4: The weighting coefficient vector γ of the IRCC for the IRCC-coded PLDC(2221) scheme of Figure 2.24 designed for achieving maximum rates, while using the QPSK modulation in conjunction with an MMSE detector.

SNR (dB)	Max Rate	R_{out}	$R_{ircc,1}$ =0.10	$R_{ircc,2}$ =0.15	$R_{ircc,3}$ =0.25	$R_{ircc,4}$ =0.40	$R_{ircc,5}$ =0.45
-10	0.136	0.136	0.5705	0.0439	0.2553	0.1303	0
-9	0.256	0.256	0.0467	0.2843	0.1405	0.2517	0
-8	0.322	0.322	0.0098	0.1364	0.2722	0	0.2336
-7	0.38	0.38	0	0.0062	0.3765	0.1320	0
-6	0.445	0.445	0	0	0.2804	0.2494	0
-5	0.492	0.492	0.0054	0	0	0.2395	0.1033
-4	0.581	0.581	0	0	0	0	0.2795
-3	0.642	0.642	0.0026	0	0	0	0
-2	0.715	0.715	0	0	0	0	0
-1	0.772	0.772	0.0019	0	0	0	0
0	0.824	0.824	0	0	0	0	0
1	0.881	0.881	0	0	0	0	0
2	0.9	0.9	0	0	0	0	0

SNR (dB)	Max Rate	R_{out}	$R_{ircc,6}$ =0.55	$R_{ircc,7}$ =0.6	$R_{ircc,8}$ =0.7	$R_{ircc,9}$ =0.75	$R_{ircc,10}$ =0.85	$R_{ircc,11}$ =0.9
-10	0.136	0.136	0	0	0	0	0	0
-9	0.256	0.256	0	0.1111	0.1657	0	0	0
-8	0.322	0.322	0.0749	0	0.1589	0	0	0.1142
-7	0.38	0.38	0.2514	0	0	0.1664	0	0.0675
-6	0.445	0.445	0.0686	0.087	0.2008	0	0	0.1138
-5	0.492	0.492	0.0599	0	0.2387	0.0643	0.0569	0.232
-4	0.581	0.581	0.3589	0	0	0.2058	0.0038	0.1556
-3	0.642	0.642	0.2984	0.2497	0.2158	0	0.0808	0.1527
-2	0.715	0.715	0	0.1801	0.655	0	0	0.1649
-1	0.772	0.772	0	0	0	0.7381	0.0457	0.2143
0	0.824	0.824	0	0	0	0.41	0.176	0.414
1	0.881	0.881	0	0	0	0	0.3691	0.6309
2	0.9	0.9	0	0	0	0	0	1

Table D.5: The weighting coefficient vector γ of the **IRCC** for the IRCC-coded IR-PLDC scheme of Figure 2.48, when using QPSK modulation in conjunction with an MMSE detector.

SNR (dB)	Max Rate	R_{out}	$R_{ircc,1}$ =0.10	$R_{ircc,3}$ =0.25	$R_{ircc,4}$ =0.40	$R_{ircc,6}$ =0.55	$R_{ircc,8}$ =0.70	$R_{ircc,11}$ =0.90
-12	0.1316	0.1975	0.3544	0.0633	0.3038	0.2785	0	0
-11	0.175	0.2275	0.2418	0.2747	0.0879	0.2453	0.1503	0
-10	0.222	0.2275	0.2418	0.2747	0.0879	0.2453	0.1503	0
-9	0.2762	0.235	0.234	0.2128	0.2553	0	0.2979	0
-8	0.3418	0.235	0.234	0.2128	0.2553	0	0.2979	0
-7	0.4272	0.235	0.234	0.2128	0.2553	0	0.2979	0
-6	0.532	0.235	0.234	0.2128	0.2553	0	0.2979	0
-5	0.6558	0.235	0.234	0.2128	0.2553	0	0.2979	0
-4	0.7894	0.25	0.2	0.25	0.16	0.11	0.28	0
-3	0.97	0.245	0.2245	0.2041	0.1633	0.1224	0.2857	0
-2	1.12	0.28	0.1429	0.2679	0.1429	0.1964	0.2499	0
-1	1.3258	0.3425	0.073	0.2555	0.1752	0.1606	0.2044	0.1313
0	1.55	0.3875	0.0387	0.2258	0.2065	0.1419	0.2710	0.1161
1	1.76	0.44	0	0.2273	0.2273	0.1250	0.3182	0.1022
2	1.98	0.495	0	0.101	0.3232	0.1111	0.2828	0.1819
3	2.23	0.5575	0	0.0224	0.3229	0.0987	0.3139	0.2421
4	2.45	0.6125	0	0	0.1959	0.2245	0.2857	0.2939
5	2.65	0.6623	0	0	0.0302	0.4567	0.1057	0.4074
6	2.87	0.7175	0	0	0	0.2683	0.2927	0.4390
7	3.07	0.7675	0	0	0	0.1075	0.3648	0.5277
8	3.24	0.81	0	0	0	0	0.3889	0.6111
9	3.32	0.83	0	0	0	0	0.2952	0.7048
10	3.4	0.85	0	0	0	0	0.2059	0.7941
11	3.52	0.88	0	0	0	0	0.0795	0.9205
12	3.6	0.89	0	0	0	0	0	1

Table D.6: The weighting coefficient vector λ of the IR-PLDC for the IRCC-coded IR-PLDC scheme of Figure 2.48, when using QPSK modulation in conjunction with an MMSE detector.

SNR (dB)	Max Rate	R_{in}	(2231) =0.33	(2221) =0.5	(2232) =0.67	(2222) =1.0	(2223) =1.5	(2224) =2.0
-12	0.1316	0.337	1	0	0	0	0	0
-11	0.175	0.3846	0.6	0.4	0	0	0	0
-10	0.222	0.4878	0.1	0.8	0.1	0	0	0
-9	0.2762	0.5882	0	0.4	0.6	0	0	0
-8	0.3418	0.7273	0	0	0.75	0.25	0	0
-7	0.4272	0.9091	0	0	0.2	0.8	0	0
-6	0.532	1.1321	0	0	0	0.7	0.2	0.1
-5	0.6558	1.3954	0	0	0	0.3	0.4	0.3
-4	0.7894	1.5789	0	0	0	0	0.2	0.8
-3	0.97	2	0	0	0	0	0	1
-2	1.12	2	0	0	0	0	0	1
-1	1.3258	1.9355	0	0	0	0	0.1	0.9
0	1.55	2	0	0	0	0	0	1
1	1.76	2	0	0	0	0	0	1
2	1.98	2	0	0	0	0	0	1
3	2.23	2	0	0	0	0	0	1
4	2.45	2	0	0	0	0	0	1
5	2.65	2	0	0	0	0	0	1
6	2.87	2	0	0	0	0	0	1
7	3.07	2	0	0	0	0	0	1
8	3.24	2	0	0	0	0	0	1
9	3.32	2	0	0	0	0	0	1
10	3.4	2	0	0	0	0	0	1
11	3.52	2	0	0	0	0	0	1
12	3.6	2	0	0	0	0	0	1

Table D.7: The weighting coefficient vector γ of the **IRCC** for the IRCC-coded IR-PDLDC scheme of Figure 3.25 transmitting over Rayleigh fading channels having $f_d = 10^{-2}$, when using 2PAM or, equivalently, BPSK modulation in conjunction with an MMSE detector.

SNR (dB)	Max Rate	R_{out}	$R_{ircc,1}$ =0.10	$R_{ircc,3}$ =0.25	$R_{ircc,4}$ =0.40	$R_{ircc,6}$ =0.55	$R_{ircc,8}$ =0.70	$R_{ircc,11}$ =0.90
-12	0.0708	0.2125	0.3059	0.1765	0.0941	0.2588	0.1647	0
-11	0.087	0.235	0.234	0.2128	0.2553	0	0.2979	0
-10	0.1058	0.2275	0.2637	0.1648	0.2637	0	0.3078	0
-9	0.1302	0.2275	0.2637	0.1648	0.2637	0	0.3078	0
-8	0.1621	0.2675	0.1682	0.2804	0.0748	0.3084	0	0.1682
-7	0.2064	0.29	0.1379	0.2586	0.1379	0.1897	0.1207	0.1552
-6	0.3113	0.2825	0.1592	0.2212	0.1416	0.1947	0.1239	0.1594
-5	0.3113	0.2825	0.1592	0.2212	0.1416	0.1947	0.1239	0.1594
-4	0.3857	0.2825	0.1592	0.2212	0.1416	0.1947	0.1239	0.1594
-3	0.4754	0.29	0.1379	0.2586	0.1379	0.1897	0.1207	0.1552
-2	0.5755	0.305	0.1311	0.2049	0.1967	0.0902	0.2295	0.1476
-1	0.6716	0.3425	0.0876	0.2189	0.1168	0.2409	0.2044	0.1314
0	0.7822	0.395	0.0506	0.1582	0.2531	0.0696	0.3544	0.1141
1	0.9320	0.48	0	0.1823	0.1667	0.1719	0.2917	0.1874
2	1.0627	0.5425	0	0.0691	0.2581	0.1014	0.3226	0.2488
3	1.1980	0.605	0	0	0.2645	0.0909	0.3471	0.2975
4	1.32	0.66	0	0	0.1515	0.0833	0.4243	0.3409
5	1.45	0.725	0	0	0	0.2276	0.3379	0.4345
6	1.57	0.785	0	0	0	0.0701	0.3567	0.5732
7	1.645	0.8225	0	0	0	0.0334	0.2553	0.7113
8	1.705	0.8525	0	0	0	0.0323	0.1232	0.8445
9	1.765	0.8825	0	0	0	0.0312	0	0.9688
10	1.8	0.9	0	0	0	0	0	1

Table D.8: The weighting coefficient vector λ of the **IR-PDLDC** for the IRCC-coded IR-PDLDC scheme of Figure 3.25 transmitting over Rayleigh fading channels having $f_d = 10^{-2}$, when using 2PAM or, equivalently, BPSK modulation in conjunction with an MMSE detector.

SNR (dB)	Max Rate	R_{in}	(3231) =0.33	(3232) =0.67	(3233) =1.0	(3234) =1.33	(3235) =1.67	(3236) =2.0
-12	0.0708	0.3333	1	0	0	0	0	0
-11	0.0870	0.3703	0.8	0.2	0	0	0	0
-10	0.1058	0.4651	0.5	0.3	0.2	0	0	0
-9	0.1302	0.5722	0.25	0.6	0	0.05	0.1	0
-8	0.1621	0.6061	0.1	0.9	0	0	0	0
-7	0.2064	0.7117	0	0.9	0	0	0.05	0.05
-6	0.2489	0.8811	0	0.35	0.55	0	0.1	0
-5	0.3113	1.1019	0	0.15	0.3	0.35	0.2	0
-4	0.3857	1.3652	0	0.1	0.05	0.15	0.7	0
-3	0.4754	1.6393	0	0	0	0.1	0.85	0.05
-2	0.5755	1.887	0	0	0	0	0.3	0.7
-1	0.6716	1.9608	0	0	0	0	0.1	0.9
0	0.7822	1.9802	0	0	0	0	0.05	0.95
1	0.9320	1.9418	0	0	0	0	0.15	0.85
2	1.0627	1.9608	0	0	0	0	0.1	0.9
3	1.1980	1.9802	0	0	0	0	0.05	0.95
4	1.32	2.0	0	0	0	0	0	1
5	1.45	2.0	0	0	0	0	0	1
6	1.57	2.0	0	0	0	0	0	1
7	1.645	2.0	0	0	0	0	0	1
8	1.705	2.0	0	0	0	0	0	1
9	1.765	2.0	0	0	0	0	0	1
10	1.8	2.0	0	0	0	0	0	1

Table D.9: The weighting coefficient vector γ of the **IRCC** for the IRCC-coded IR-PLDC scheme of Figure 2.48 transmitting over Rayleigh fading channels having $f_d = 10^{-2}$, when using 2PAM or, equivalently, BPSK modulation in conjunction with an MMSE detector.

SNR (dB)	Max Rate	R_{out}	$R_{ircc,1} = 0.10$	$R_{ircc,3} = 0.25$	$R_{ircc,4} = 0.40$	$R_{ircc,6} = 0.55$	$R_{ircc,8} = 0.70$	$R_{ircc,11} = 0.90$
-15	0.0675	0.1975	0.3544	0.1266	0.1013	0.4177	0	0
-14	0.0879	0.235	0.234	0.1228	0.2553	0.09	0.2979	0
-13	0.1104	0.2125	0.2823	0.2353	0.1882	0.1294	0.1648	0
-12	0.14	0.2275	0.2418	0.2747	0.0879	0.2418	0.1538	0
-11	0.1774	0.235	0.234	0.1228	0.2553	0.09	0.2979	0
-10	0.2186	0.235	0.234	0.1228	0.2553	0.09	0.2979	0
-9	0.2749	0.235	0.234	0.1228	0.2553	0.09	0.2979	0
-8	0.3469	0.235	0.234	0.1228	0.2553	0.09	0.2979	0
-7	0.4292	0.235	0.234	0.1228	0.2553	0.09	0.2979	0
-6	0.5099	0.2575	0.1748	0.2913	0.1553	0.1068	0.2718	0
-5	0.5958	0.3575	0.042	0.3147	0.1678	0.1538	0.1958	0.1259
-4	0.715	0.3575	0.042	0.3147	0.1678	0.1538	0.1958	0.1259
-3	0.85	0.425	0	0.2647	0.1882	0.1941	0.2471	0.1059
-2	0.955	0.4775	0	0.1047	0.377	0.0576	0.3665	0.0942
-1	1.099	0.555	0	0	0.3243	0.1982	0.3153	0.1622
0	1.223	0.6175	0	0	0.1296	0.3117	0.3401	0.2186
1	1.36	0.68	0	0	0	0.3235	0.4118	0.2647
2	1.475	0.745	0	0	0	0.0738	0.5638	0.3624
3	1.58	0.79	0	0	0	0	0.4873	0.5127
4	1.66	0.83	0	0	0	0	0.2952	0.7048
5	1.74	0.87	0	0	0	0	0.1207	0.8793
6	1.8	0.9	0	0	0	0	0	1

Table D.10: The weighting coefficient vector λ of the **IR-PLDC** for the IRCC-coded IR-PLDC scheme of Figure 2.48 transmitting over Rayleigh fading channels having $f_d = 10^{-2}$, when using 2PAM or, equivalently, BPSK modulation in conjunction with an MMSE detector.

SNR (dB)	Max Rate	R_{in}	(3231) =0.33	(3232) =0.67	(3233) =1.0	(3234) =1.33	(3235) =1.67	(3236) =2.0
-15	0.0675	0.3419	0.95	0.05	0	0	0	0
-14	0.0879	0.3738	0.8	0.15	0.05	0	0	0
-13	0.1104	0.5195	0.45	0.05	0.5	0	0	0
-12	0.14	0.6154	0.1	0.85	0.05	0	0	0
-11	0.1774	0.7547	0	0.65	0.35	0	0	0
-10	0.2186	0.9302	0	0.15	0.85	0	0	0
-9	0.2749	1.1696	0	0	0.45	0.5	0.05	0
-8	0.3469	1.476	0	0	0.05	0.45	0.4	0.1
-7	0.4292	1.8265	0	0	0	0.05	0.35	0.6
-6	0.5099	1.9802	0	0	0	0	0.05	0.95
-5	0.5958	1.6667	0	0	0	0	1	0
-4	0.715	2	0	0	0	0	0	1
-3	0.85	2	0	0	0	0	0	1
-2	0.955	2	0	0	0	0	0	1
-1	1.099	2	0	0	0	0	0	1
0	1.223	2	0	0	0	0	0	1
1	1.36	2	0	0	0	0	0	1
2	1.475	2	0	0	0	0	0	1
3	1.58	2	0	0	0	0	0	1
4	1.66	2	0	0	0	0	0	1
5	1.74	2	0	0	0	0	0	1
6	1.8	2	0	0	0	0	0	1

Table D.11: The weighting coefficient vector γ of the **IRCC** for the IRCC-coded IR-PCLDC scheme of Figure 4.16 transmitting over i.i.d. Rayleigh fading channels, when using BPSK modulation in conjunction with an MMSE detector.

SNR (dB)	Max Rate	R_{out}	$R_{ircc,1} = 0.10$	$R_{ircc,3} = 0.25$	$R_{ircc,4} = 0.40$	$R_{ircc,6} = 0.55$	$R_{ircc,8} = 0.70$	$R_{ircc,11} = 0.90$
-15	0.0171	0.13	0.7308	0	0	0	0.2692	0
-14	0.0329	0.1975	0.3797	0	0.3038	0.1392	0.1773	0
-13	0.0513	0.205	0.3415	0.0610	0.2927	0.1341	0.1707	0
-12	0.0671	0.235	0.234	0.2128	0.2553	0	0.2979	0
-11	0.0810	0.235	0.234	0.2128	0.2553	0	0.2979	0
-10	0.1034	0.2275	0.2637	0.1648	0.2637	0	0.3078	0
-9	0.1213	0.2425	0.2062	0.3093	0	0.3402	0.1443	0
-8	0.1488	0.2975	0.1176	0.2941	0.1345	0.1849	0.1176	0.1513
-7	0.1638	0.3275	0.0763	0.3053	0.1221	0.2519	0.1069	0.1375
-6	0.1975	0.395	0	0.3481	0.1013	0.3481	0.0886	0.1139
-5	0.2238	0.4475	0	0.1676	0.3575	0.0615	0.3128	0.1006
-4	0.235	0.47	0	0.1064	0.4255	0	0.3723	0.0958
-3	0.2813	0.5625	0	0.0222	0.2133	0.2933	0.3111	0.1601
-2	0.285	0.57	0	0	0.2807	0.1930	0.3684	0.1579
-1	0.3125	0.625	0	0	0.128	0.264	0.392	0.216
0	0.3475	0.695	0	0	0	0.2374	0.5036	0.2590
1	0.3763	0.7525	0	0	0	0.0365	0.6047	0.3588
2	0.39	0.78	0	0	0	0	0.5385	0.4615
3	0.405	0.81	0	0	0	0	0.3889	0.6111
4	0.42	0.84	0	0	0	0	0.25	0.75
5	0.435	0.87	0	0	0	0	0.1207	0.8793
6	0.45	0.9	0	0	0	0	0	1

Table D.12: The weighting coefficient vector λ of the IR-PCLDC for the IRCC-coded IR-PCLDC scheme of Figure 4.16 transmitting over i.i.d. Rayleigh fading channels, when using BPSK modulation in conjunction with an MMSE detector.

SNR (dB)	Max Rate	R_{in}	(4181) =0.125	(4182) =0.25	(4183) =0.375	(4184) =0.5
-15	0.0171	0.01316	0.9	0.1	0	0
-14	0.0329	0.16667	0.5	0.5	0	0
-13	0.0513	0.25	0	1	0	0
-12	0.0671	0.2857	0	0.75	0	0.25
-11	0.0810	0.3448	0	0.45	0	0.55
-10	0.1034	0.4545	0	0.1	0.1	0.8
-9	0.1213	0.5	0	0	0	1
-8	0.1488	0.5	0	0	0	1
-7	0.1638	0.5	0	0	0	1
-6	0.1975	0.5	0	0	0	1
-5	0.2238	0.5	0	0	0	1
-4	0.235	0.5	0	0	0	1
-3	0.2813	0.5	0	0	0	1
-2	0.285	0.5	0	0	0	1
-1	0.3125	0.5	0	0	0	1
0	0.3475	0.5	0	0	0	1
1	0.3763	0.5	0	0	0	1
2	0.39	0.5	0	0	0	1
3	0.405	0.5	0	0	0	1
4	0.42	0.5	0	0	0	1
5	0.435	0.5	0	0	0	1
6	0.45	0.5	0	0	0	1

Table D.13: The weighting coefficient vector γ of the IRCC for the IRCC-coded IR-PLDC scheme of Figure 2.48 transmitting over Rayleigh fading channels, when using BPSK modulation in conjunction with an MMSE detector.

SNR (dB)	Max Rate	R_{out}	$R_{ircc,1}$ =0.10	$R_{ircc,3}$ =0.25	$R_{ircc,4}$ =0.40	$R_{ircc,6}$ =0.55	$R_{ircc,8}$ =0.70	$R_{ircc,11}$ =0.90
-15	0.0338	0.2275	0.2418	0.2747	0.0879	0.2418	0.1538	0
-14	0.0422	0.2125	0.2824	0.2353	0.1882	0.1294	0.1647	0
-13	0.0542	0.235	0.2340	0.2128	0.2553	0	0.2979	0
-12	0.0684	0.235	0.2340	0.2128	0.2553	0	0.2979	0
-11	0.0870	0.235	0.2340	0.2128	0.2553	0	0.2979	0
-10	0.1085	0.235	0.2340	0.2128	0.2553	0	0.2979	0
-9	0.1288	0.2575	0.1748	0.2913	0.1553	0.1068	0.2718	0
-8	0.1537	0.3125	0.08	0.4	0	0.264	0.112	0.144
-7	0.1825	0.365	0.0273	0.3425	0.1096	0.3014	0.0959	0.1233
-6	0.2127	0.4325	0	0.2023	0.3237	0.1272	0.2428	0.1040
-5	0.2425	0.485	0	0.0773	0.3711	0.1701	0.2887	0.0928
-4	0.2775	0.555	0	0	0.3243	0.1982	0.3153	0.1622
-3	0.3088	0.6175	0	0.0202	0.0324	0.4453	0.2834	0.2187
-2	0.3438	0.6875	0	0	0	0.28	0.4582	0.2618
-1	0.38	0.76	0	0	0	0	0.6447	0.3553
0	0.395	0.79	0	0	0	0	0.4873	0.5127
1	0.415	0.83	0	0	0	0	0.2952	0.7048
2	0.45	0.9	0	0	0	0	0	1

Table D.14: The weighting coefficient vector λ of the IR-PLDC for the IRCC-coded IR-PLDC scheme of Figure 2.48 transmitting over Rayleigh fading channels, when using BPSK modulation in conjunction with an MMSE detector.

SNR (dB)	Max Rate	R_{in}	(4181) =0.125	(4182) =0.25	(4183) =0.375	(4184) =0.5
-15	0.0338	0.1485	0.7	0.25	0.05	0
-14	0.0422	0.1987	0.4	0.3	0.05	0.25
-13	0.0542	0.2308	0.1	0.85	0.05	0
-12	0.0684	0.2913	0	0.65	0.2	0.15
-11	0.0870	0.3704	0	0.05	0.9	0.05
-10	0.1085	0.4615	0	0.05	0.1	0.85
-9	0.1288	0.5	0	0	0	1
-8	0.1537	0.4918	0	0	0.05	0.95
-7	0.1825	0.5	0	0	0	1
-6	0.2127	0.4918	0	0	0.05	0.95
-5	0.2425	0.5	0	0	0	1
-4	0.2775	0.5	0	0	0	1
-3	0.3088	0.5	0	0	0	1
-2	0.3438	0.5	0	0	0	1
-1	0.38	0.5	0	0	0	1
0	0.395	0.5	0	0	0	1
1	0.415	0.5	0	0	0	1
2	0.45	0.5	0	0	0	1

Glossary

3GPP-LTE Third Generation Partnership Project's Long Term Evolution

ACS Add-Compare-Select

AF Amplify-and-Forward

AGC Automatic Gain Control

AGM Anti-Gray Mapping

APP *A Posteriori* Probability

AWGN Additive White Gaussian Noise

BECs Binary Erasure Channels

BER Bit Error Ratio

BICM-ID Bit-Interleaved Coded Modulation using Iterative Decoding

BLAST Bell Labs' Layered-Space-Time

BPSK Binary Phase Shift Keying

BS Base Station

CCMC Continuous-input Continuous-output Memoryless Channel

CF Compress-and-Forward

CIR Channel Impulse Response

CLDCs Cooperative Linear Dispersion Codes

CSI Channel State Information

CSTBCs Cooperative Space-Time Block Codes

DCM Dispersion Character Matrix

DCMC Discrete-input Continuous-output Memoryless Channel

DF	Decode-and-Forward
DLDCs	Differential Linear Dispersion Codes
DLSTBCs	Differential Linear Space-Time Block Codes
DOSTBCs	Differential Orthogonal Space-Time Block Codes
DPSK	Differential Phase Shift Keying
DQOSTBCs	Differential Quasi-Orthogonal Space-Time Block Codes
DSSD-STBCs	Differential Single-Symbol-Decodable Space-Time Block Codes
DSTBCs	Differential Space-Time Block Codes
DUSTM	Differential Unitary Space-Time Modulation
EGC	Equal Gain Combining
EXIT	EXtrinsic Information Transfer
FEC	Forward Error Correction
HSDPA	High Speed Downlink Packet Access
i.i.d.	independent and identically distributed
IIR	Infinite Impulse Response
IR-PCLDCs	IrRegular Precoded Cooperative Linear Dispersion Codes
IR-PDLDCs	IrRegular Precoded Differential Linear Dispersion Codes
IR-PLDCs	IrRegular Precoded Linear Dispersion Codes
IR-VLCs	IrRegular Variable Length Codes
IRCCs	IrRegular Convolutional Codes
LDCs	Linear Dispersion Codes
LDPC	Low Density Parity Check
LLR	Log-Likelihood Ratio
LOS	Line-Of-Sight
LSTBCs	Linear Space-Time Block Codes
LT	Luby Transform
MIMO	Multiple Input Multiple Output
ML	Maximum Likelihood

MMSE	Minimum Mean Squared Error
MRC	Maximal Ratio Combining
MSDDs	Multiple Symbol Differential Detectors
OFDM	Orthogonal Frequency-Division Multiplexing
OSTBCs	Orthogonal Space-Time Block Codes
PAM	Pulse Amplitude Modulation
PCLDCs	Precoded Cooperative Linear Dispersion Codes
PDF	Probability Density Function
PDLDCs	Precoded Differential Linear Dispersion Codes
PIC	Parallel Interference Cancellation
PLDCs	Precoded Linear Dispersion Codes
PSEP	Pairwise Symbol Error Probability
PSK	Phase-Shift Keying
QAM	Quadrature Amplitude Modulation
QOSTBCs	Quasi-Orthogonal Space-Time Block Codes
QPSK	Quadrature Phase Shift Keying
RSC	Recursive Systematic Convolutional
SC	Selection Combining
SCCs	Serial Concatenated Codes
SDM	Spatial Division Multiplexing
SDMA	Space-Division Multiple Access
SIC	Serial Interference Cancellation
SISO	Soft Inputs and Soft Outputs
SNR	Signal-to-Noise Ratio
SP	Sphere Packing
SSD-STBCs	Single-Symbol-Decodable Space-Time Block Codes
ST	Space-Time
STBCs	Space-Time Block Codes
STC	Space-Time Coding

STS	Space-Time Spreading
STTCs	Space-Time Trellis Codes
TASTBCs	Threaded Algebraic Space-Time Block Codes
TCM	Trellis Coded Modulation
TSS	Transmit Symbol Separability
TVLT	Time Variant Linear Transformation
UL	UpLink
USTM	Unitary Space-Time Modulation

Bibliography

- [1] B. Hassibi and B. M. Hochwald, “High-rate codes that are linear in space and time,” *IEEE Transactions on Information Theory*, vol. 48, pp. 1804–1824, July 2002.
- [2] R. W. J. Heath and A. Paulraj, “Linear dispersion codes for MIMO systems based on frame theory,” *IEEE Transactions on Signal Processing*, vol. 50, pp. 2429–2441, October 2002.
- [3] G. J. Foschini, “Layered space-time architecture for wireless communication in fading environments when using multiple antennas,” *Bell Labs Technical Journal*, vol. 2, pp. 41–59, 1996.
- [4] G. J. Foschini and M. J. Gans, “On limits of wireless communications in a fading environment when using multiple antennas,” *Wireless Personal Communications*, vol. 6, no. 3, pp. 311–335, 1998.
- [5] I. E. Telatar, “Capacity of multi-antenna Gaussian channels,” *European Transactions on Telecommunications*, vol. 10, pp. 585–595, November 1999.
- [6] M. Yuksel and E. Erkip, “Multiple-antenna cooperative wireless systems: A diversity-multiplexing tradeoff perspective,” *IEEE Transactions on Information Theory*, vol. 53, pp. 3371–3393, October 2007.
- [7] L. Z. Zheng and D. Tse, “Diversity and multiplexing: a fundamental tradeoff in multiple-antenna channels,” *IEEE Transactions on Information Theory*, vol. 49, pp. 1073–1096, May 2003.
- [8] A. Goldsmith, *Wireless Communications*. Cambridge University Press, August 2005.
- [9] Y. Zhu and H. Jafarkhani, “Punctured super-orthogonal space-time trellis codes,” *IEEE Transactions on Wireless Communications*, vol. 6, pp. 4494–4503, December 2007.

- [10] V. Tarokh, N. Seshadri, and A. R. Calderbank, "Space-time codes for high data rate wireless communication: performance criterion and code construction," *IEEE Transactions on Information Theory*, vol. 44, no. 2, pp. 744–765, 1998.
- [11] G. Ungerboeck, "Channel coding with multilevel/phase signals," *IEEE Transactions on Information Theory*, vol. 28, pp. 55–67, January 1982.
- [12] A. Wittneben, "Base station modulation diversity for digital simulcast," in *IEEE Vehicular Technology Conference*, (St. Louis), pp. 848–853, May 1991.
- [13] N. Seshadri and J. H. Winters, "Two signaling schemes for improving the error performance of frequency-division-duplex (FDD) transmission systems using transmitter antenna diversity," in *IEEE Vehicular Technology Conference*, (Secaucus), pp. 508–511, May 1993.
- [14] S. M. Alamouti, "A simple transmit diversity technique for wireless communications," *IEEE Journal on Selected Areas in Communications*, vol. 16, no. 8, pp. 1451–1458, 1998.
- [15] V. Tarokh, H. Jafarkhani, and A. R. Calderbank, "Space-time block codes from orthogonal designs," *IEEE Transactions on Information Theory*, vol. 45, no. 5, pp. 1456–1467, 1999.
- [16] G. Ganesan and P. Stoica, "Space-time diversity using orthogonal and amicable orthogonal designs," in *IEEE International Conference on Acoustics, Speech, and Signal Processing*, vol. 5, (Istanbul), pp. 2561–2564, June 2000.
- [17] H. Jafarkhani, "A quasi-orthogonal space-time block code," *IEEE Transactions on Communications*, vol. 49, no. 1, pp. 1–4, 2001.
- [18] H. E. Gamal and M. O. Damen, "Universal space-time coding," *IEEE Transactions on Information Theory*, vol. 49, pp. 1097–1119, May 2003.
- [19] B. M. Hochwald and T. L. Marzetta, "Unitary space-time modulation for multiple-antenna communications in Rayleigh flat fading," *IEEE Transactions on Information Theory*, vol. 46, no. 2, pp. 543–564, 2000.
- [20] B. M. Hochwald, T. L. Marzetta, T. J. Richardson, W. Sweldens, and R. Urbanke, "Systematic design of unitary space-time constellations," *IEEE Transactions on Information Theory*, vol. 46, no. 6, pp. 1962–1973, 2000.
- [21] J. C. Belfiore, G. Rekaya, and E. Viterbo, "The golden code: a 2×2 full-rate space-time code with nonvanishing determinants," *IEEE Transactions on Information Theory*, vol. 51, pp. 1432–1436, April 2005.

- [22] A. Sezgin, E. A. Jorswieck, and E. Costa, “LDC in MIMO Ricean channels: Optimal transmit strategy with MMSE detection,” *IEEE Transactions on Signal Processing*, vol. 56, pp. 313–328, January 2008.
- [23] C. Lin and V. V. Veeravalli, “Optimal linear dispersion codes for correlated MIMO channels,” *IEEE Transactions on Wireless Communications*, vol. 7, pp. 657–666, February 2008.
- [24] J. G. Proakis, *Digital Communications*. McGraw-Hill, 2nd ed., 1989.
- [25] L. Z. Zheng and D. Tse, “Communication on the Grassmann manifold: a geometric approach to the noncoherent multiple-antenna channel,” *IEEE Transactions on Information Theory*, vol. 48, pp. 359–383, February 2002.
- [26] V. Tarokh and H. Jafarkhani, “A differential detection scheme for transmit diversity,” *IEEE Journal on Selected Areas in Communications*, vol. 18, no. 7, pp. 1169–1174, 2000.
- [27] S. H. Nam, C. S. Hwang, J. Chung, and V. Tarokh, “Differential space time block codes using QAM for four transmit antennas,” in *IEEE International Conference on Communications*, vol. 2, pp. 952–956, June 2004.
- [28] Y. Zhu and H. Jafarkhani, “Differential modulation based on quasi-orthogonal codes,” *IEEE Transactions on Wireless Communications*, vol. 4, no. 6, pp. 3005–3017, 2005.
- [29] B. M. Hochwald and W. Sweldens, “Differential unitary space-time modulation,” *IEEE Transactions on Communications*, vol. 48, no. 12, pp. 2041–2052, 2000.
- [30] A. Shokrollahi, B. Hassibi, B. M. Hochwald, and W. Sweldens, “Representation theory for high-rate multiple-antenna code design,” *IEEE Transactions on Information Theory*, vol. 47, no. 6, pp. 2335–2367, 2001.
- [31] F. Oggier, “Cyclic algebras for noncoherent differential space-time coding,” *IEEE Transactions on Information Theory*, vol. 53, pp. 3053–3065, September 2007.
- [32] I. Stewart, *Galois Theory*. London, UK: Chapman and Hall, 1989.
- [33] B. Hassibi and B. M. Hochwald, “Cayley differential unitary space-time codes,” *IEEE Transactions on Information Theory*, vol. 48, no. 6, pp. 1485–1503, 2002.
- [34] V. Pauli and L. Lampe, “Tree-search multiple-symbol differential decoding for unitary space-time modulation,” *IEEE Transactions on Communications*, vol. 55, pp. 1567–1576, August 2007.

- [35] Y. Li and B. Vucetic, "Design of differential space-time trellis codes," *IEEE Transactions on Wireless Communications*, vol. 6, pp. 1631–1637, May 2007.
- [36] C. S. Hwang, S. H. Nam, J. Chung, and V. Tarokh, "Differential space time block codes using nonconstant modulus constellations," *IEEE Transactions on Signal Processing*, vol. 51, no. 11, pp. 2955–2964, 2003.
- [37] B. L. Hughes, "Differential space-time modulation," *IEEE Transactions on Information Theory*, vol. 46, no. 7, pp. 2567–2578, 2000.
- [38] W. Burnside, "On a general property of finite irreducible groups of linear substitutions," *Messenger of Mathematics*, vol. 35, pp. 51–55, 1905.
- [39] F. Oggier, G. Rekaya, J. C. Belfiore, and E. Viterbo, "Perfect space-time block codes," *IEEE Transactions on Information Theory*, vol. 52, pp. 3885–3902, September 2006.
- [40] J. N. Laneman and G. W. Wornell, "Distributed space-time-coded protocols for exploiting cooperative diversity in wireless networks," *IEEE Transactions on Information Theory*, vol. 49, pp. 2415–2425, October 2003.
- [41] Y. D. Jing and H. Jafarkhani, "Using orthogonal and quasi-orthogonal designs in wireless relay networks," *IEEE Transactions on Information Theory*, vol. 53, pp. 4106–4118, November 2007.
- [42] R. U. Nabar, H. Bolcskei, and F. W. Kneubuhler, "Fading relay channels: performance limits and space-time signal design," *IEEE Journal on Selected Areas in Communications*, vol. 22, pp. 1099–1109, August 2004.
- [43] E. Stauffer, O. Oyman, R. Narasimhan, and A. Paulraj, "Finite-SNR diversity-multiplexing tradeoffs in fading relay channels," *IEEE Journal on Selected Areas in Communications*, vol. 25, pp. 245–257, February 2007.
- [44] K. C. Liang, X. D. Wang, and I. Berenguer, "Minimum error-rate linear dispersion codes for cooperative relays," *IEEE Transactions on Vehicular Technology*, vol. 56, pp. 2143–2157, July 2007.
- [45] S. Yang and J. C. Belfiore, "Optimal space-time codes for the MIMO amplify-and-forward cooperative channel," *IEEE Transactions on Information Theory*, vol. 53, pp. 647–663, February 2007.
- [46] A. Sendonaris, E. Erkip, and B. Aazhang, "User cooperation diversity. Part I. system description," *IEEE Transactions on Communications*, vol. 51, pp. 1927–1938, November 2003.

- [47] V. Mahinthan, L. Cai, J. W. Mark, and X. M. Shen, "Partner selection based on optimal power allocation in cooperative-diversity systems," *IEEE Transactions on Vehicular Technology*, vol. 57, pp. 511–520, january 2008.
- [48] J. N. Laneman, D. Tse, and G. W. Wornell, "Cooperative diversity in wireless networks: Efficient protocols and outage behavior," *IEEE Transactions on Information Theory*, vol. 50, pp. 3062–3080, December 2004.
- [49] Y. D. Jing and B. Hassibi, "Distributed space-time coding in wireless relay networks," *IEEE Transactions on Wireless Communications*, vol. 5, no. 12, pp. 3524–3536, 2006.
- [50] S. Yiu, R. Schober, and L. Lampe, "Distributed space-time block coding," *IEEE Transactions on Communications*, vol. 54, pp. 1195–1206, July 2006.
- [51] K. Azarian, H. E. Gamal, and P. Schniter, "On the achievable diversity-multiplexing tradeoff in half-duplex cooperative channels," *IEEE Transactions on Information Theory*, vol. 51, no. 12, pp. 4152–4172, 2005.
- [52] A. Sendonaris, E. Erkip, and B. Aazhang, "User cooperation diversity. Part II. implementation aspects and performance analysis," *IEEE Transactions on Communications*, vol. 51, pp. 1939–1948, November 2003.
- [53] C. Berrou, A. Glavieux, and P. Thitimajshima, "Near-Shannon-limit error-correcting coding and decoding: Turbo-codes," in *IEEE International Conference on Communications*, vol. 2, (Geneva, Switzerland), pp. 1064–1070, May 1993.
- [54] S. Benedetto, D. Divsalar, G. Montorsi, and F. Pollara, "Serial concatenation of interleaved codes: performance analysis, design, and iterative decoding," *IEEE Transactions on Information Theory*, vol. 44, no. 3, pp. 909–926, 1998.
- [55] S. ten Brink, J. Speidel, and R. H. Yan, "Iterative demapping and decoding for multilevel modulation," in *IEEE Global Telecommunications Conference*, vol. 1, (Sydney), pp. 579–584, November 8–12, 1998.
- [56] D. Divsalar, S. Dolinar, and F. Pollara, "Serial concatenated trellis coded modulation with rate-1 inner code," in *IEEE Global Telecommunications Conference*, vol. 2, (San Francisco), pp. 777–782, November 2000.
- [57] S. ten Brink, "Designing iterative decoding schemes with the extrinsic information transfer chart," *AEU International Journal of Electronics and Communications*, vol. 54, pp. 389–398, 2000.

- [58] S. ten Brink, "Convergence behavior of iteratively decoded parallel concatenated codes," *IEEE Transactions on Communications*, vol. 49, pp. 1727 – 1737, October 2001.
- [59] M. Tüchler, "Convergence prediction for iterative decoding of threefold concatenated systems," in *IEEE Global Telecommunications Conference*, vol. 2, pp. 1358–1362, November 2002.
- [60] M. Tüchler and J. Hagenauer, "Exit charts of irregular codes," in *36th Conference on Information Sciences and Systems (CISS)*, (Princeton, NJ), pp. 748–753, March 2002.
- [61] R. G. Maunder, J. Wang, S. X. Ng, L. L. Yang, and L. Hanzo, "Iteratively decoded irregular variable length coding and trellis coded modulation," in *IEEE Workshop on Signal Processing Systems*, (Shanghai), pp. 222–227, October 2007.
- [62] B. M. Hochwald and S. ten Brink, "Achieving near-capacity on a multiple-antenna channel," *IEEE Transactions on Communications*, vol. 51, pp. 389–399, March 2003.
- [63] Y. Zhang, "Approaching V-BLAST capacity with adaptive modulation and LDPC encoding," *IEEE Transactions on Communications*, vol. 55, pp. 2261–2269, December 2007.
- [64] L. Hanzo, T. H. Liew, and B. L. Yeap, *Turbo Coding, Turbo Equalisation, and Space-Time Coding: For Transmission over Fading Channels*. Wiley-IEEE Press, July 2002.
- [65] G. Li, I. J. Fair, and W. A. Krzymien, "Low-density parity-check codes for space-time wireless transmission," *IEEE Transactions on Wireless Communications*, vol. 5, pp. 312–322, February 2006.
- [66] L. Goulet and H. Leib, "Serially concatenated space-time codes with iterative decoding and performance limits of block-fading channels," *IEEE Journal on Selected Areas in Communications*, vol. 21, pp. 765–773, June 2003.
- [67] A. Ashikhmin, G. Kramer, and S. ten Brink, "Extrinsic information transfer functions:a model and two properties," *36th Conference on Information Sciences and Systems (CISS)*, (Princeton University), vol. 1, pp. 742–747, March 2002.
- [68] A. Ashikhmin, G. Kramer, and S. ten Brink, "Extrinsic information transfer functions: model and erasure channel properties," *IEEE Transactions on Information Theory*, vol. 50, no. 11, pp. 2657–2673, 2004.
- [69] M. Tüchler, "Design of serially concatenated systems depending on the block length," *IEEE Transactions on Communications*, vol. 52, pp. 209–218, February 2004.

- [70] N. Wu, O. Alamri, S. X. Ng, and L. Hanzo, "Precoded sphere packing aided bit-interleaved differential space-time coded modulation using iterative decoding," *IEEE Transactions on Vehicular Technology*, vol. 57, pp. 1311–1316, March 2008.
- [71] N. Wu and L. Hanzo, "Near-capacity irregular convolutional-coding aided irregular precoded linear dispersion codes," *IEEE Transactions on Vehicular Technology*, submitted March 2008.
- [72] N. Wu and L. Hanzo, "Near-capacity irregular precoded linear dispersion codes," in *IEEE International Conference on Communications*, (Beijing, China), pp. 4501–4505, May 19–23, 2008.
- [73] N. Wu and L. Hanzo, "Irregular precoder-aided differential linear dispersion codes," in *Vehicular Technology Conference*, (Marina Bay, Singapore), pp. 285–289, May 2008.
- [74] P. W. Wolniansky, G. J. Foschini, G. D. Golden, and R. A. Valenzuela, "V-BLAST: an architecture for realizing very high data rates over the rich-scattering wireless channel," in *International Symposium on Signals, Systems, and Electronics*, (Pisa, Italy), pp. 295–300, September 1998.
- [75] M. O. Damen, H. E. Gamal, and N. C. Beaulieu, "Linear threaded algebraic space-time constellations," *IEEE Transactions on Information Theory*, vol. 49, pp. 2372–2388, October 2003.
- [76] H. J. Chen, A. Haimovich, and J. A. Sjogren, "Turbo space-time codes with time varying linear transformations," *IEEE Transactions on Wireless Communications*, vol. 6, pp. 486–493, February 2007.
- [77] X. L. Ma and G. B. Giannakis, "Full-diversity full-rate complex-field space-time coding," *IEEE Transactions on Signal Processing[see also IEEE Transactions on Acoustics, Speech, and Signal Processing]*, vol. 51, no. 11, pp. 2917–2930, 2003.
- [78] R. H. Gohary and T. N. Davidson, "Design of linear dispersion codes: asymptotic guidelines and their implementation," *IEEE Transactions on Wireless Communications*, vol. 4, pp. 2892–2906, November 2005.
- [79] I. Daubechies, *Ten Lectures on Wavelets*. SAIM, Philadelphia, PA, 1992.
- [80] Y. Hong, E. Viterbo, and J. C. Belfiore, "Golden space-time trellis coded modulation," *IEEE Transactions on Information Theory*, vol. 53, pp. 1689–1705, May 2007.

- [81] M. O. Damen, H. E. Gamal, and G. Caire, "On maximum-likelihood detection and the search for the closest lattice point," *IEEE Transactions on Information Theory*, vol. 49, pp. 2389–2402, October 2003.
- [82] S. X. Ng and L. Hanzo, "On the MIMO channel capacity of multidimensional signal sets," *IEEE Transactions on Vehicular Technology*, vol. 55, pp. 528–536, March 2006.
- [83] R. A. Horn and C. R. Johnson, *Matrix Analysis*. Cambridge University Press, 1985.
- [84] H. F. Lu and P. V. Kumar, "Rate-diversity tradeoff of space-time codes with fixed alphabet and optimal constructions for PSK modulation," *IEEE Transactions on Information Theory*, vol. 49, pp. 2747–2751, October 2003.
- [85] V. Tarokh, H. Jafarkhani, and A. R. Calderbank, "Space-time block coding for wireless communications: performance results," *IEEE Journal on Selected Areas in Communications*, vol. 17, no. 3, pp. 451–460, 1999.
- [86] H. F. Lu and P. V. Kumar, "A unified construction of space-time codes with optimal rate-diversity tradeoff," *IEEE Transactions on Information Theory*, vol. 51, pp. 1709–1730, May 2005.
- [87] M. O. Damen and N. C. Beaulieu, "On diagonal algebraic space-time block codes," *IEEE Transactions on Communications*, vol. 51, pp. 911–919, January 2003.
- [88] N. Sharma and C. B. Papadias, "Improved quasi-orthogonal codes through constellation rotation," *IEEE Transactions on Communications*, vol. 51, no. 3, pp. 332–335, 2003.
- [89] W. F. Su and X. G. Xia, "Quasi-orthogonal space-time block codes with full diversity," in *IEEE Global Telecommunications Conference*, vol. 2, pp. 1098–1102, November 2002.
- [90] W. F. Su and X. G. Xia, "Signal constellations for quasi-orthogonal space-time block codes with full diversity," *IEEE Transactions on Information Theory*, vol. 50, no. 10, pp. 2331 – 2347, 2004.
- [91] G. Ganesan and P. Stoica, "Space-time block codes: a maximum SNR approach," *IEEE Transactions on Information Theory*, vol. 47, no. 4, pp. 1650–1656, 2001.
- [92] S. Sandhu and A. Paulraj, "Space-time block codes: a capacity perspective," *IEEE Communications Letters*, vol. 4, no. 12, pp. 384–386, 2000.
- [93] S. Sandhu and A. Paulraj, "Unified design of linear space-time block codes," in *IEEE Global Telecommunications Conference*, vol. 2, (San Antonio), pp. 1073–1077, November 2001.

- [94] C. Yuen, Y. L. Guan, and T. T. Tjhung, "Algebraic relationship between amicable orthogonal designs and quasi-orthogonal STBC with minimum decoding complexity," in *IEEE International Conference on Communications*, vol. 11, (Istanbul), pp. 4882–4887, June 2006.
- [95] C. Yuen, Y. L. Guan, and T. T. Tjhung, "Quasi-orthogonal STBC with minimum decoding complexity," *IEEE Transactions on Wireless Communications*, vol. 4, pp. 2089–2094, September 2005.
- [96] H. E. Gamal and A. R. Hammons, "A new approach to layered space-time coding and signal processing," *IEEE Transactions on Information Theory*, vol. 47, pp. 2321–2334, September 2001.
- [97] V. Tarokh, A. Naguib, N. Seshadri, and A. R. Calderbank, "Space-time codes for high data rate wireless communication: performance criteria in the presence of channel estimation errors, mobility, and multiple paths," *IEEE Transactions on Communications*, vol. 47, pp. 199–207, February 1999.
- [98] O. Alamri, N. Wu, and L. Hanzo, "A differential turbo detection aided sphere packing modulated space-time coding scheme," in *Vehicular Technology Conference*, vol. 5, (Melbourne), pp. 2474–2478, May 2006.
- [99] A. Ashikhmin, G. Kramer, and S. ten Brink, "Code rate and the area under extrinsic information transfer curves," in *IEEE International Symposium on Information Theory*, pp. 115 – 115, 2002.
- [100] K. R. Narayanan and G. L. Stüber, "A serial concatenation approach to iterative demodulation and decoding," *IEEE Transactions on Communications*, vol. 47, no. 7, pp. 956–961, 1999.
- [101] J. Wang, S. X. Ng, L. L. Yang, and L. Hanzo, "Combined serially concatenated codes and MMSE equalization: An EXIT chart aided perspective," in *Vehicular Technology Conference*, (Montreal), pp. 1–5, September 2006.
- [102] F. Brannstrom, L. K. Rasmussen, and A. J. Grant, "Convergence analysis and optimal scheduling for multiple concatenated codes," *IEEE Transactions on Information Theory*, vol. 51, pp. 3354–3364, September 2005.
- [103] O. Alamri, B. L. Yeap, and L. Hanzo, "A turbo detection and sphere-packing-modulation-aided space-time coding scheme," *IEEE Transactions on Vehicular Technology*, vol. 56, pp. 575–582, March 2007.

- [104] S. Cheng, A. Nallanathan, and P. Y. Kam, "A new class of signal constellations for differential unitary space-time modulation (DUSTM)," *IEEE Communications Letters*, vol. 8, pp. 1–3, January 2004.
- [105] T. P. Soh, C. S. Ng, and P. Y. Kam, "Improved signal constellations for differential unitary space-time modulations with more than two transmit antennas," *IEEE Communications Letters*, vol. 9, pp. 7–9, January 2005.
- [106] T. Himsoon, W. F. Su, and K. J. R. Liu, "Differential unitary space-time signal design using matrix rotation structure," *IEEE Signal Processing Letters*, vol. 12, pp. 45–48, January 2005.
- [107] L. Hanzo, S. X. Ng, T. Keller, and W. Webb, *Quadrature Amplitude Modulation: From Basics to Adaptive Trellis-Coded, Turbo-EQUALISED and Space-Time Coded OFDM, CDMA and MC-CDMA Systems*. Wiley-IEEE Press, September 2004.
- [108] A. L. Moustakas., S. H. Simon, and T. L. Marzetta, "Capacity of differential versus nondifferential unitary space-time modulation for MIMO channels," *IEEE Transactions on Information Theory*, vol. 52, pp. 3622–3634, August 2006.
- [109] H. Jafarkhani and V. Tarokh, "Multiple transmit antenna differential detection from generalized orthogonal designs," *IEEE Transactions on Information Theory*, vol. 47, no. 6, pp. 2626–2631, 2001.
- [110] L. Y. Song and A. G. Burr, "Differential quasi-orthogonal space-time block codes," *IEEE Transactions on Wireless Communications*, vol. 6, pp. 64–68, January 2007.
- [111] G. Ganesan and P. Stoica, "Differential modulation using space-time block codes," *IEEE Signal Processing Letters*, vol. 9, pp. 57–60, February 2002.
- [112] C. Yuen, Y. L. Guan, and T. T. Tjhung, "Single-symbol-decodable differential space-time modulation based on QO-STBC," *IEEE Transactions on Wireless Communications*, vol. 5, no. 12, pp. 3329–3334, 2006.
- [113] R. Ertel and J. H. Reed, "Generation of two equal power correlated Rayleigh fading envelopes," *IEEE Communications Letters*, vol. 2, no. 10, pp. 276–278, 1998.
- [114] M. Hajiaghayi and C. Tellambura, "Unitary signal constellations for differential space-time modulation," *IEEE Communications Letters*, vol. 11, pp. 25–27, January 2007.
- [115] F. Oggier and B. Hassibi, "Algebraic Cayley differential space-time codes," *IEEE Transactions on Information Theory*, vol. 53, pp. 1911–1919, May 2007.

- [116] J. B. Wang, X. D. Wang, and M. Madihian, "Design of minimum error-rate Cayley differential unitary space-time codes," *IEEE Journal on Selected Areas in Communications*, vol. 23, pp. 1779–1787, September 2005.
- [117] X. D. Li and J. A. Ritcey, "Bit-interleaved coded modulation with iterative decoding using soft feedback," *Electronics Letters*, vol. 34, no. 10, pp. 942–943, 1998.
- [118] A. Chindapol and J. A. Ritcey, "Design, analysis, and performance evaluation for BICM-ID with square QAM constellations in Rayleigh fading channels," *IEEE Journal on Selected Areas in Communications*, vol. 19, no. 5, pp. 944–957, 2001.
- [119] Y. B. Li and X. G. Xia, "Constellation mapping for space-time matrix modulation with iterative demodulation/decoding," *IEEE Transactions on Communications*, vol. 53, no. 5, pp. 764–768, 2005.
- [120] P. Hoeher and J. Lodge, "Turbo DPSK: iterative differential PSK demodulation and channel decoding," *IEEE Transactions on Communications*, vol. 47, no. 6, pp. 837–843, 1999.
- [121] W. F. Su, Z. Safar, and K. J. R. Liu, "Space-time signal design for time-correlated Rayleigh fading channels," in *IEEE International Conference on Communications*, vol. 5, pp. 3175–3179, May 2003.
- [122] J. H. Conway and N. J. A. Sloane, *Sphere Packings, Lattices and Groups*. Springer-Verlag, 1998.
- [123] B. M. Hochwald, T. L. Marzetta, and C. B. Papadias, "A transmitter diversity scheme for wideband CDMA systems based on space-time spreading," *IEEE Journal on Selected Areas in Communications*, vol. 19, no. 1, pp. 48–60, 2001.
- [124] Y. H. Huang and J. A. Ritcey, "Optimal constellation labeling for iteratively decoded bit-interleaved space-time coded modulation," *IEEE Transactions on Information Theory*, vol. 51, pp. 1865–1871, May 2005.
- [125] L. Hanzo, J. Bologh, and S. Ni, *3G, HSPA and FDD versus TDD Networking: Smart Antennas and Adaptive Modulation*. Wiley-IEEE Press, 2 ed., February 2008.
- [126] Y. Fan and J. Thompson, "MIMO configurations for relay channels: Theory and practice," *IEEE Transactions on Wireless Communications*, vol. 6, pp. 1774–1786, May 2007.
- [127] T. Cover and A. E. Gamal, "Capacity theorems for the relay channel," *IEEE Transactions on Information Theory*, vol. 25, pp. 572–584, September 1979.

- [128] M. Dohler, Y. Li, B. Vucetic, A. H. Aghvami, M. Arndt, and D. Barthel, “Performance analysis of distributed space-time block-encoded sensor networks,” *IEEE Transactions on Vehicular Technology*, vol. 55, pp. 1776–1789, November 2006.
- [129] G. Kramer, M. Gastpar, and P. Gupta, “Cooperative strategies and capacity theorems for relay networks,” *IEEE Transactions on Information Theory*, vol. 51, pp. 3037–3063, September 2005.
- [130] M. Janani, A. Hedayat, T. E. Hunter, and A. Nosratinia, “Coded cooperation in wireless communications: space-time transmission and iterative decoding,” *IEEE Transactions on Signal Processing*, vol. 52, pp. 362–371, February 2004.
- [131] B. Zhao and M. C. Valenti, “Distributed turbo coded diversity for relay channel,” *Electronics Letters*, vol. 39, pp. 786–787, May 15 2003.
- [132] Y. Li, B. Vucetic, T. F. Wong, and M. Dohler, “Distributed turbo coding with soft information relaying in multihop relay networks,” *IEEE Journal on Selected Areas in Communications*, vol. 24, pp. 2040–2050, November 2006.
- [133] T. Y. Bui and J. H. Yuan, “A decode and forward cooperation scheme with soft relaying in wireless communication,” in *IEEE 8th Workshop on Signal Processing Advances in Wireless Communications*, (Helsinki), pp. 1–5, June 2007.
- [134] S. Wei, “Diversity-multiplexing tradeoff of asynchronous cooperative diversity in wireless networks,” *IEEE Transactions on Information Theory*, vol. 53, pp. 4150–4172, November 2007.
- [135] Y. Shang and X. G. Xia, “Shift-full-rank matrices and applications in space-time trellis codes for relay networks with asynchronous cooperative diversity,” *IEEE Transactions on Information Theory*, vol. 52, pp. 3153–3167, July 2006.
- [136] W. C. Jakes, *Microwave Mobile Communications*. John Wiley & Sons, 1974.
- [137] A. Maaref and S. Aissa, “Capacity of space-time block codes in MIMO Rayleigh fading channels with adaptive transmission and estimation errors,” *IEEE Transactions on Wireless Communications*, vol. 4, pp. 2568–2578, September 2005.
- [138] M. O. Damen, A. Chkeif, and J. C. Belfiore, “Lattice code decoder for space-time codes,” *IEEE Communications Letters*, vol. 4, pp. 161–163, May 2000.

- [139] K. K. Wong, A. Paulraj, and R. D. Murch, "Efficient high-performance decoding for overloaded MIMO antenna systems," *IEEE Transactions on Wireless Communications*, vol. 6, pp. 1833–1843, May 2007.
- [140] L. Zhang, H. P. Lei, X. Zhang, and D. C. Yang, "Efficient complex sphere decoding framework for linear dispersion space-time block codes," in *IEEE International Symposium on Personal, Indoor and Mobile Radio Communications*, (Greece), pp. 1–4, September 2007.
- [141] D. Deng, M. Zhao, and J. K. Zhu, "Transmit antenna selection for linear dispersion codes based on linear receiver," in *Vehicular Technology Conference*, vol. 6, (Melbourne), pp. 2927–2931, May 2006.
- [142] M. Luby, "LT codes," in *IEEE Symposium on Foundations of Computer Science*, (Vancouver, Canada), pp. 271–280, November 2002.
- [143] C. Y. Wei, T. Nguyen, N. Wu, J. Akhtman, L. L. Yang, and L. Hanzo, "Luby transform coding aided iterative detection for downlink SDMA systems," in *IEEE Workshop on Signal Processing Systems*, (Shanghai, China), pp. 397–402, October 2007.
- [144] N. Wu, T. D. Nguyen, C. Y. Wei, L. L. Yang, and L. Hanzo, "Integrated LT coding, bit interleaved differential space time coding and sphere packing modulation for the wireless internet," in *Vehicular Technology Conference*, (Marina Bay, Singapore), pp. 344–348, May 2008.
- [145] T. Kiran and B. S. Rajan, "Partially-coherent distributed space-time codes with differential encoder and decoder," *IEEE Journal on Selected Areas in Communications*, vol. 25, pp. 426–433, February 2007.
- [146] G. Y. Wang, Y. M. Zhang, and M. Amin, "Differential distributed space-time modulation for cooperative networks," *IEEE Transactions on Wireless Communications*, vol. 5, pp. 3097–3108, November 2006.
- [147] B. Hu, L. L. Yang, and L. Hanzo, "Performance of the smart antenna aided generalized multicarrier DS-CDMA downlink using both time-domain spreading and steered space-time spreading," in *Vehicular Technology Conference*, vol. 1, pp. 458–462, September 2005.
- [148] R. Mudumbai, G. Barriac, and U. Madhow, "On the feasibility of distributed beamforming in wireless networks," *IEEE Transactions on Wireless Communications*, vol. 6, pp. 1754–1763, May 2007.

Subject Index

Symbols

3GPP-LTE 143, 179

A

ACS 66

adaptive system 186

AF 141

AGC 145

AGM 130

Alamouti code 39

amicable orthogonal design 41

APP 9

AWGN 18

B

Beamforming 2

BECs 9

BER 2

BICM-ID 9

BLAST 9, 14

BPSK 36

broadcast channel 143, 187

BS 2, 140

C

capacity

coherent MIMO 21, 96

LDC 21, 23

non-coherent MIMO 96

Cayley transform 110

CCMC 5, 16

CF 141

CIR 19

CLDCs 11, 142, 146

coded cooperation 142

cooperative diversity 7

cooperative MIMO 1

CSI 3

CSTBCs 7

D

DCM 15, 23

DCMC 10, 16

determinant criterion 37

DF 141, 187

diversity gain 2

diversity-multiplexing gain tradeoff 38

DLDCs 10, 91, 108

DLSTBCs 102

DOSTBCs 90, 97

DPSK 12, 91, 92

DQOSTBCs 100

DSSD-STBCs 103

DSTBCs 5, 90

DUSTM 6, 90, 109

E

- EGC 3
EXIT 9

F

- FEC 141
flat fading 18, 94, 145
full diversity 37
full rate 37

G

- Gaussian distribution 16, 25, 27, 72, 113, 119

H

- Hermitian matrix 110
HSDPA 140

I

- i.i.d. 4
IIR 54
imperfect CSI 119, 135
IR-PCLDCs 13, 163
IR-PDLDCs 12, 91, 132
IR-PLDCs 12, 61
IR-VLCs 9, 88
IRCCs 9, 64, 80, 127
irregularity 9, 64

J

- joint modulation and space-time design . 123

L

- LDCs 5
coding gain 34
model 19, 22
optimization 25
LDPC 9
linearized ML detector 113

- LLR 63

- log-normal distribution 155

- LOS 140

- LSTBCs 41

- LT 187

M

- maximum achievable rate 49, 165
MIMO 1
ML 18, 23, 92, 95, 112, 150
MMSE 18
MRC 3
MSDDs 7
multiplexing gain 3

O

- OFDM 16
OSTBCs 5, 39

P

- PAM 100
PCLDCs 164
PDF 26
PDLDCs 133
PIC 88
PLDCs 54
PSEP 16
PSK 16

Q

- QAM 16
QOSTBCs 5, 40
QPSK 27

R

- rank criterion 37
rate-diversity tradeoff 38, 40–43
RSC 48

S

- SC 3
SCCs 9
SDM 14, 37
SDMA 2
shadowing 155, 172
SIC 88
SISO 9
skewed-Hermitian matrix 111
SNR 2
SP 12, 123, 178
SSD-STBCs 42
ST 19
STBCs 14
STC 1, 47
STS 125
STTCs 3, 47

T

- TASTBCs 15, 44
TCM 3
TSS 38, 40–43, 174
TVLT 15, 43

U

- UL 143
USTM 5, 14

Author Index

A

- Aazhang, B. [52] 8, 141, 142
Aazhang, B. [46] 7, 8, 141, 142
Aghvami, A.H. [128] 141
Aissa, S. [137] 186
Akhtman, J. [143] 187
Alamouti, S.M. [14] . 4–7, 19, 22, 39, 90, 97, 103

- Alamri, O. [103] 88, 124, 126
Alamri, O. [98] 48, 88, 122, 126
Alamri, O. [70] 9, 10, 12, 59, 91
Amin, M. [146] 187
Arndt, M. [128] 141
Ashikhmin, A. [67] 9, 63
Ashikhmin, A. [99] 49, 127
Ashikhmin, A. [68] . 9, 49, 63, 86, 127, 165
Azarian, K. [51] 8, 142

B

- Barriac, G. [148] 187
Barthel, D. [128] 141
Beaulieu, N.C. [87] 38
Beaulieu, N.C. [75] 15, 44
Belfiore, J.C. [21] 4–7, 10, 16
Belfiore, J.C. [138] 186
Belfiore, J.C. [80] 16
Belfiore, J.C. [39] 6
Belfiore, J.C. [45] 7, 142

- Benedetto, S. [54] 8, 9
Berenguer, I. [44] 7, 142, 187
Berrou, C. [53] 8, 9, 17
Blogh, J. [125] 140
Bolcskei, H. [42] 7, 8, 141
Brannstrom, F. [102] 63
Bui, T.Y. [133] 142
Burnside, W. [38] 6
Burr, A.G. [110] 100, 101

C

- Cai, L. [47] 7
Caire, G. [81] 20
Calderbank, A.R. [10] . 3, 5, 16, 19, 21, 22, 24, 25, 36, 37, 43, 45, 47, 174
Calderbank, A.R. [15] . 4, 5, 7, 10, 14, 39–41, 90, 99, 100
Calderbank, A.R. [97] 47
Calderbank, A.R. [85] 37, 90
Chen, H.J. [76] 15, 43, 45, 47
Cheng, S. [104] 91
Chindapol, A. [118] 122
Chkeif, A. [138] 186
Chung, J. [36] 6, 98, 99
Chung, J. [27] 6, 99, 100
Conway, J.H. [122] 124
Costa, E. [22] 4, 5
Cover, T. [127] 140, 141, 163, 187

D

- Damen, M.O. [138] 186
Damen, M.O. [87] 38
Damen, M.O. [81] 20
Damen, M.O. [75] 15, 44
Damen, M.O. [18] 4, 44, 45
Daubechies, I. [79] 16
Davidson, T.N. [78] 15, 16
Deng, D. [141] 186
Divsalar, D. [54] 8, 9
Divsalar, D. [56] 8, 9, 11, 53, 58
Dohler, M. [128] 141
Dohler, M. [132] 142, 161
Dolinar, S. [56] 8, 9, 11, 53, 58

E

- Erkip, E. [52] 8, 141, 142
Erkip, E. [46] 7, 8, 141, 142
Erkip, E. [6] 1
Ertel, R.B. [113] 106

F

- Fair, I.J. [65] 9
Fan, Y. [126] 140
Foschini, G.J. [3] 1
Foschini, G.J. [4] 1, 3, 4, 15, 21
Foschini, G.J. [74] 14

G

- Gamal, A.E. [127] 140, 141, 163, 187
Gamal, H.E. [51] 8, 142
Gamal, H.E. [81] 20
Gamal, H.E. [75] 15, 44
Gamal, H.E. [18] 4, 44, 45
Gamal, H.E. [96] 44
Ganesan, G. [16] 4, 5, 41, 42, 45
Ganesan, G. [91] 41, 102

- Ganesan, G. [111] 103
Gans, M.J. [4] 1, 3, 4, 15, 21
Gastpar, M. [129] 141
Giannakis, G.B. [77] 15, 38
Glavieux, A. [53] 8, 9, 17
Gohary, R.H. [78] 15, 16
Golden, G.D. [74] 14
Goldsmith, A. [8] 3
Goulet, L. [66] 9
Grant, A.J. [102] 63
Guan, Y.L. [95] 42
Guan, Y.L. [94] 42, 45
Guan, Y.L. [112] 103
Gupta, P. [129] 141

H

- Hagenauer, J. [60] 8, 9, 11, 17, 61, 63, 64, 69–71, 76, 80, 82, 88, 123, 128, 175
Haimovich, A. [76] 15, 43, 45, 47
Hajiaghayi, M. [114] 109
Hammons, A.R. [96] 44
Hanzo, L. [103] 88, 124, 126
Hanzo, L. [107] 92
Hanzo, L. [125] 140
Hanzo, L. [147] 187
Hanzo, L. [64] 9, 17, 47, 126, 142
Hanzo, L. [61] 8, 9, 88
Hanzo, L. [82] 26
Hanzo, L. [98] 48, 88, 122, 126
Hanzo, L. [101] 54
Hanzo, L. [143] 187
Hanzo, L. [72] 10, 17
Hanzo, L. [144] 187
Hanzo, L. [71] 10, 17
Hanzo, L. [73] 10, 91

- Hanzo, L. [70] 9, 10, 12, 59, 91
Hassibi, B. [1] 4, 5, 10, 15, 16, 19–22, 45,
142
Hassibi, B. [33] 6, 10, 91, 110–113, 176, 177
Hassibi, B. [49] 7, 142
Hassibi, B. [115] 110
Hassibi, B. [30] 6, 109
Heath, R.W.Jr. [2] 4, 5, 10, 15–17, 22, 24, 25,
38, 45, 47
Hedayat, A. [130] 142, 161
Himsoon, T. [106] 91
Hochwald, B.M. [1] 4, 5, 10, 15, 16, 19–22,
45, 142
Hochwald, B.M. [33] 6, 10, 91, 110–113,
176, 177
Hochwald, B.M. [20] 4, 5, 14, 90, 109
Hochwald, B.M. [29] 6, 90, 96, 109
Hochwald, B.M. [19] 4, 5, 14, 15, 96
Hochwald, B.M. [123] 125
Hochwald, B.M. [62] 8, 9, 11
Hochwald, B.M. [30] 6, 109
Hoehler, P. [120] 122
Hong, Y. [80] 16
Horn, R.A. [83] 27
Hu, B. [147] 187
Huang, Y.H. [124] 130
Hughes, B.L. [37] 6, 14, 15, 90, 109
Hunter, T.E. [130] 142, 161
Hwang, C.S. [36] 6, 98, 99
Hwang, C.S. [27] 6, 99, 100
- J**
Jafarkhani, H. [17] 4, 5, 7, 40, 41, 45, 101
Jafarkhani, H. [109] 99
Jafarkhani, H. [41] 7
- Jafarkhani, H. [15] 4, 5, 7, 10, 14, 39–41, 90,
99, 100
Jafarkhani, H. [85] 37, 90
Jafarkhani, H. [26] 6, 97, 98, 114, 122
Jafarkhani, H. [28] 6, 100, 102
Jafarkhani, H. [9] 3
Jakes, W.C. [136] 155
Janani, M. [130] 142, 161
Jing, Y.D. [49] 7, 142
Jing, Y.D. [41] 7
Johnson, C.R. [83] 27
Jorswieck, E.A. [22] 4, 5
- K**
Kam, P.Y. [104] 91
Kam, P.Y. [105] 91
Keller, T. [107] 92
Kiran, T. [145] 187
Kneubuhler, F.W. [42] 7, 8, 141
Kramer, G. [67] 9, 63
Kramer, G. [99] 49, 127
Kramer, G. [68] 9, 49, 63, 86, 127, 165
Kramer, G. [129] 141
Krzymien, W.A. [65] 9
Kumar, P.V. [84] 36, 38
Kumar, P.V. [86] 38, 43
- L**
Lampe, L. [34] 6, 7
Lampe, L. [50] 7, 142
Laneman, J.N. [40] 7, 10, 141, 142
Laneman, J.N. [48] 7
Lei, H.P. [140] 186
Leib, H. [66] 9
Li, G. [65] 9
Li, X.D. [117] 122

- Li, Y.B. [119] 122
Li, Y. [128] 141
Li, Y. [132] 142, 161
Li, Y. [35] 5
Liang, K.C. [44] 7, 142, 187
Liew, T.H. [64] 9, 17, 47, 126, 142
Lin, C. [23] 4, 5
Liu, K.J.R. [106] 91
Liu, K.J.R. [121] 123
Lodge, J. [120] 122
Lu, H.F. [84] 36, 38
Lu, H.F. [86] 38, 43
Luby, M. [142] 187
- M**
- Ma, X.L. [77] 15, 38
Maaref, A. [137] 186
Madhow, U. [148] 187
Madihian, M. [116] 110
Mahinthan, V. [47] 7
Mark, J.W. [47] 7
Marzetta, T.L. [20] 4, 5, 14, 90, 109
Marzetta, T.L. [19] 4, 5, 14, 15, 96
Marzetta, T.L. [123] 125
Marzetta, T.L. [108] 96
Maunder, R.G. [61] 8, 9, 88
Montorsi, G. [54] 8, 9
Moustakas., A.L. [108] 96
Mudumbai, R. [148] 187
Murch, R.D. [139] 186
- N**
- Nabar, R.U. [42] 7, 8, 141
Naguib, A. [97] 47
Nallanathan, A. [104] 91
Nam, S.H. [36] 6, 98, 99
Nam, S.H. [27] 6, 99, 100
Narasimhan, R. [43] 7, 8, 142
Narayanan, K.R. [100] 53, 122
Ng, C.S. [105] 91
Ng, S.X. [107] 92
Ng, S.X. [61] 8, 9, 88
Ng, S.X. [82] 26
Ng, S.X. [101] 54
Ng, S.X. [70] 9, 10, 12, 59, 91
Nguyen, T.D. [143] 187
Nguyen, T.D. [144] 187
Ni, S. [125] 140
Nosratinia, A. [130] 142, 161
- O**
- Oggier, F. [39] 6
Oggier, F. [31] 6
Oggier, F. [115] 110
Oyman, O. [43] 7, 8, 142
- P**
- Papadias, C.B. [123] 125
Papadias, C.B. [88] 41
Pauli, V. [34] 6, 7
Paulraj, A. [2] 4, 5, 10, 15–17, 22, 24, 25, 38, 45, 47
Paulraj, A. [92] 41
Paulraj, A. [93] 41
Paulraj, A. [43] 7, 8, 142
Paulraj, A. [139] 186
Pollara, F. [54] 8, 9
Pollara, F. [56] 8, 9, 11, 53, 58
Proakis, J.G. [24] 5, 16, 98
- R**
- Rajan, B.S. [145] 187
Rasmussen, L.K. [102] 63

- Reed, J.H. [113] 106
Rekaya, G. [21] 4–7, 10, 16
Rekaya, G. [39] 6
Richardson, T.J. [20] 4, 5, 14, 90, 109
Ritcey, J.A. [118] 122
Ritcey, J.A. [124] 130
Ritcey, J.A. [117] 122
- S**
- Safar, Z. [121] 123
Sandhu, S. [92] 41
Sandhu, S. [93] 41
Schniter, P. [51] 8, 142
Schober, R. [50] 7, 142
Sendonaris, A. [52] 8, 141, 142
Sendonaris, A. [46] 7, 8, 141, 142
Seshadri, N. [13] 4
Seshadri, N. [10] 3, 5, 16, 19, 21, 22, 24, 25, 36, 37, 43, 45, 47, 174
Seshadri, N. [97] 47
Sezgin, A. [22] 4, 5
Shang, Y. [135] 145
Sharma, N. [88] 41
Shen, X.M. [47] 7
Shokrollahi, A. [30] 6, 109
Simon, S.H. [108] 96
Sjogren, J.A. [76] 15, 43, 45, 47
Sloane, N.J.A. [122] 124
Soh, T.P. [105] 91
Song, L.Y. [110] 100, 101
Speidel, J. [55] 8, 9, 143, 174
Stüber, G.L. [100] 53, 122
Stauffer, E. [43] 7, 8, 142
Stewart, I. [32] 6
Stoica, P. [16] 4, 5, 41, 42, 45
Stoica, P. [91] 41, 102
Stoica, P. [111] 103
Su, W.F. [106] 91
Su, W.F. [89] 41, 102
Su, W.F. [121] 123
Su, W.F. [90] 41, 102
Sweldens, W. [20] 4, 5, 14, 90, 109
Sweldens, W. [29] 6, 90, 96, 109
Sweldens, W. [30] 6, 109
- T**
- Tüchler, M. [59] 8, 9
Tüchler, M. [69] 9, 17, 64, 80, 84, 88, 123, 175
Tüchler, M. [60] 8, 9, 11, 17, 61, 63, 64, 69–71, 76, 80, 82, 88, 123, 128, 175
Tarokh, V. [36] 6, 98, 99
Tarokh, V. [109] 99
Tarokh, V. [27] 6, 99, 100
Tarokh, V. [10] 3, 5, 16, 19, 21, 22, 24, 25, 36, 37, 43, 45, 47, 174
Tarokh, V. [15] 4, 5, 7, 10, 14, 39–41, 90, 99, 100
Tarokh, V. [97] 47
Tarokh, V. [85] 37, 90
Tarokh, V. [26] 6, 97, 98, 114, 122
Telatar, I.E. [5] 1, 4, 23
Tellambura, C. [114] 109
ten Brink, S. [67] 9, 63
ten Brink, S. [99] 49, 127
ten Brink, S. [68] 9, 49, 63, 86, 127, 165
ten Brink, S. [62] 8, 9, 11
ten Brink, S. [55] 8, 9, 143, 174
ten Brink, S. [57] 8, 9, 11, 51, 63, 86, 122, 174

- ten Brink, S. [58] 8, 11, 64, 86
Thitimajshima, P. [53] 8, 9, 17
Thompson, J. [126] 140
Tjhung, T.T. [95] 42
Tjhung, T.T. [94] 42, 45
Tjhung, T.T. [112] 103
Tse, D. [48] 7
Tse, D. [25] 5, 6, 96
Tse, D. [7] 3, 14, 36, 38, 142
- U**
- Ungerboeck, G. [11] 3
Urbanke, R. [20] 4, 5, 14, 90, 109
- V**
- Valenti, M.C. [131] 142
Valenzuela, R.A. [74] 14
Veeravalli, V.V. [23] 4, 5
Viterbo, E. [21] 4–7, 10, 16
Viterbo, E. [80] 16
Viterbo, E. [39] 6
Vucetic, B. [128] 141
Vucetic, B. [132] 142, 161
Vucetic, B. [35] 5
- W**
- Wang, G.Y. [146] 187
Wang, J.B. [116] 110
Wang, J. [61] 8, 9, 88
Wang, J. [101] 54
Wang, X.D. [44] 7, 142, 187
Wang, X.D. [116] 110
Webb, W. [107] 92
Wei, C.Y. [143] 187
Wei, C.Y. [144] 187
Wei, S. [134] 145
Winters, J.H. [13] 4

- Wittneben, A. [12] 4
Wolniansky, P.W. [74] 14
Wong, K.K. [139] 186
Wong, T.F. [132] 142, 161
Wornell, G.W. [40] 7, 10, 141, 142
Wornell, G.W. [48] 7
Wu, N. [98] 48, 88, 122, 126
Wu, N. [143] 187
Wu, N. [72] 10, 17
Wu, N. [144] 187
Wu, N. [71] 10, 17
Wu, N. [73] 10, 91
Wu, N. [70] 9, 10, 12, 59, 91
- X**
- Xia, X.G. [119] 122
Xia, X.G. [135] 145
Xia, X.G. [89] 41, 102
Xia, X.G. [90] 41, 102
- Y**
- Yan, R.H. [55] 8, 9, 143, 174
Yang, D.C. [140] 186
Yang, L.L. [147] 187
Yang, L.L. [61] 8, 9, 88
Yang, L.L. [101] 54
Yang, L.L. [143] 187
Yang, L.L. [144] 187
Yang, S. [45] 7, 142
Yeap, B.L. [103] 88, 124, 126
Yeap, B.L. [64] 9, 17, 47, 126, 142
Yiu, S. [50] 7, 142
Yuan, J.H. [133] 142
Yuen, C. [95] 42
Yuen, C. [94] 42, 45
Yuen, C. [112] 103

Yuksel, M. [6] 1

Z

Zhang, L. [140] 186

Zhang, X. [140] 186

Zhang, Y.M. [146] 187

Zhang, Y. [63] 8, 9

Zhao, B. [131] 142

Zhao, M. [141] 186

Zheng, L.Z. [25] 5, 6, 96

Zheng, L.Z. [7] 3, 14, 36, 38, 142

Zhu, J.K. [141] 186

Zhu, Y. [28] 6, 100, 102

Zhu, Y. [9] 3